

ARO

The Scientific Journal of Koya University

Design of a Branch-line Microstrip Coupler Using Spirals and Step Impedance Cells for WiMAX Applications.

Petrophysical Investigation of the Khurmala Formation in Taq Taq Oil Field, Zagros Folded Belt.

Evaluation of Oxidative Stress and some Biochemical Parameters in Normal Pregnant Women.

Industrial Assessment of the Carbonate Rocks of the Pila Spi Formation at Haibat Sultan Mountain, Iraqi Kurdistan Region.

Potato Peels and Mixed Grasses as Raw Materials for Biofuel Production.

Design and Performance of Microstrip Diplexers: A Review.

Automatic Recognition of Arabic Poetry Meter from Speech Signal using Long Short-term Memory and Support Vector Machine.

Moderate Range Static Magnetic Field Promoted Variation of Blood Parameters: An In vitro Study.

On Some Ve-Degree and Harmonic Molecular Topological Properties of Carborundum.

Theoretical Study of Diels-Alder Reaction of But-3-en-2-one with Hexa-1,2,4-triene: A Density Functional Theory Study.

Chemical and Structural Analysis of Rocks Using X-ray Fluorescence and X-ray Diffraction Techniques.

Effect of Modeling Techniques on the Simulation: Calculating the Stress Concentration Factors in Square Hollow Section T-Joints as a Case Study.

High Security and Capacity of Image Steganography for Hiding Human Speech Based on Spatial and Cepstral Domains.

Long-wavelength GaInNAs/GaAs Vertical-cavity Surface-emitting Laser for Communication Applications.

Energy Optimization Using a Pump Scheduling Tool in Water Distribution Systems.



ARO-The Scientific Journal of Koya University

The ARO (“Today” in Hewramí Kurdish), is an international scientific journal published by the Koya University with p-ISSN: 2410-9355, e-ISSN: 2307-549X and DOI: 10.14500/2307-549X. ARO is a journal of original scientific research, global news, and commentary. The ARO Scientific Journal is a peer-reviewed, open access journal that publishes original research articles as well as review articles in all areas of Science and Engineering.



ARO Executive Publisher

Dr. Wali M. Hamad; is the President of Koya University and the Executive Publisher of ARO.

ARO Editorial Board

The Editorial Board of ARO includes a thirteen-member Senior Executive Editorial Board and a six-member Associate Editorial Board that help in setting journal policy; a Board of Reviewing Editors consisting of more than 210 leading scientists.

ARO Editorial Group

Senior Executive Editors: Dilan M. Rostam, Salah I. Yahya, Basim M. Fadhil, Fahmi F. Muhammad, Mohammed H. S. Zangana, Jorge Correia., Fouad Mohammed, Jacek Binda, Nadhir Al-Ansari, Howri Mansurbeg, Tara Fuad Tahir, Yazan A. Khaleel.

Associate Editors: Hamed M. Jassim, Iqbal M.G. Tahir, Saddon T. Ahmad, Sahar B. Mahmood, Layth I. Abd Ali, Mohammed Gh. Faraj

This issue reviewers: Abdulqader Abdullah, Ahmed S. Mohammed, Ali K. D. Babani, Asaad M. Jassim, Fahmi F. Muhammad, Farhad Mustaffa, Faten A. Chaqmaqchee, Firas M. Zeki, Haider J. Ismail, Haitham K. Ali, Hamed M. Jassim, Jamal Fajoui, Jamil A. Juma, Jawad Kadhim, Kawis A. Faraj, Kayhan Zrar, Kharman A. Faraj, Kosrat N. Kaka, Kourosh Behzadian, Laith A. Najam, Mohammad A. Zarei, Mohammad G. Faraj, Mohammad R. Farahani, Mustafa N. Owaid, Nabel K. A. Ali, Qutaiba S. Al-Nema, Rafid Kadhim Abbas, Raghad Z. Yousif, Salah I. Yahya, Tola A. Mirza, Wa'el A. Hussien, Waqas Nazeer, Yazan A. Khaleel, Zakariya A. Hussein..

ARO Editorial Web and New Media: Dilan M. Rostam and Salah I. Yahya

Secretarial Office of the Journal: Haneen H. Falah

Journal Proofreader: Salah I. Yahya

Journal Copyeditor: Daban Q. H. Jaff

Journal Cover Designer: Othman Kamal Muhammad

ARO, the International journal of original scientific research and commentary is an online and published twice a year, as well, by Koya University. The journal has no article processing charge (APC). It is an online open access, distributed under the Creative Commons Attribution License (CC BY-NC-SA 4.0: <https://creativecommons.org/licenses/by-nc-sa/4.0/>). Responsibility of the content rests upon the authors and not upon ARO or Koya University.

ARO the Scientific Journal Office

Koya University, University Park
Danielle Mitterrand Boulevard, Koya KOY45
Kurdistan Region - F.R. Iraq

Tel.: +964 (0) 748 012 7423

Mobile: +964 (0) 750 187 5489

E-mail: aro.journal@koyauniversity.org

url: aro.koyauniversity.org

June - 2020 | Poshper – 2720

ARO

The Scientific Journal of Koya University

Vol VIII, No 1(2020)

Contents

ARO Editorial Words	iii
Sayed M. Hosseini, Abbas Rezaei	01
Design of a Branch-line Microstrip Coupler Using Spirals and Step Impedance Cells for WiMAX Applications	
Fraidoon Rashid, Devan O. Hussein, Hawar A. Zangana	05
Petrophysical Investigation of the Khurmala Formation in Taq Taq Oil Field, Zagros Folded Belt	
Musher I. Kakey, Kamaran K. Abdourahman, Gulbahar R. Uthman	17
Evaluation of Oxidative Stress and some Biochemical Parameters in Normal Pregnant Women	
Varoujan K. Sissakian, Mohammed J. Hamawandy, Rahel K. Ibrahim	24
Industrial Assessment of the Carbonate Rocks of the Pila Spi Formation at Haibat Sultan Mountain, Iraqi Kurdistan Region	
Shaaban Z. Omar, Ayad H. Hasan, Ivo Lalov	31
Potato Peels and Mixed Grasses as Raw Materials for Biofuel Production	
Salah I. Yahya, Abbas Rezaei, Leila Nouri	38
Design and Performance of Microstrip Diplexers: A Review	
Abdulbasit K. Al-Talabani	50
Automatic Recognition of Arabic Poetry Meter from Speech Signal using Long Short-term Memory and Support Vector Machine	
Bestoon T. Mustafa, Sardar P. Yaba, Asaad H. Ismail	55
Moderate Range Static Magnetic Field Promoted Variation of Blood Parameters: An In vitro Study	
Murat Cancan, Kerem Yamaç, Ziyattin Taş, Mehmet Şerif Aldemir	65
On Some Ve-Degree and Harmonic Molecular Topological Properties of Carborundum	

Rezan J. Hassan, Hassan H. Abdallah	74
Theoretical Study of Diels-Alder Reaction of But-3-en-2-one with Hexa-1,2,4-triene: A Density Functional Theory Study	
Mohammed M. Sabri	79
Chemical and Structural Analysis of Rocks Using X-ray Fluorescence and X-ray Diffraction Techniques	
Serwan S. M. Talabani, Ahmad T. Azeez, Silvio D. Barros, Basim M. Fadhil, Hewa H. Omer	88
Effect of Modeling Techniques on the Simulation: Calculating the Stress Concentration Factors in Square Hollow Section T-Joints as a Case Study	
Yazen A. Khaleel	95
High Security and Capacity of Image Steganography for Hiding Human Speech Based on Spatial and Cepstral Domains	
Faten A. Chaqmaqchee	107
Long-wavelength GaInNAs/GaAs Vertical-cavity Surface-emitting Laser for Communication Applications	
Karwan A. Muhammed, Raziye Farmani	112
Energy Optimization Using a Pump Scheduling Tool in Water Distribution Systems	
General information	125
Guide to Author	126
ARO Reviewer/Associate Editor Application Form	128

ARO Editorial Words

Dear reader,

ARO, the Scientific Journal of Koya University, is closing its Issue Fourteen (Vol VIII, No 1, 2020). It has been an exciting and yet progressive season for our journal. A major part of the world has gone into lockdown to face the threat of Corona Pandemic which has taken over our way of life, in particular, the educational communities. In this issue, ARO managed to peer-review 15 outstanding articles. ARO is publishing its 14th issue as an internationally listed Scientific Journal in Kurdistan Region of Iraq. Notably, ARO has been accepted for indexing in the Emerging Sources Citation Index (ESCI), a new edition of Web of Science™ as of Feb 2016. Content in this issue is under consideration by Clarivate to be accepted in the Science Citation Index Expanded™ (SCIE) during 2019. ARO's individual articles are currently listed by Clarivate using articles unique DOI numbers which is a historical achievement for our academic community. ARO is starting its eighth-year journey in leading the quality of regional scientific publications with global impact. The editorial team have been working tirelessly to keep the novel mission and sustain ARO's future publications with greater impacts and citations. It is exciting that ARO has been awarded to DOAJ Seal listing which is an indication of a trusted high standard open access scientific work. The upcoming new season will be an even more exciting period in ARO's life as Thomson Reuters will examine our journal for a full permanent listing.

ARO continues its mission to provide resources, support and advice for researchers in the process of publishing their scientific papers with a global standard quality for an internationally recognised scientific publication, while at the same time offering free public access to scientific research by open online access. This is a daunting task which we hope to advance in the years to come. Thus, in the sections to follow, we would like to share and elaborate on the core elements that constitute ARO.

ARO is a peer-reviewed, open-access journal that publishes original scientific research, global news, letters and commentary as well as review articles in areas of natural sciences and technology. In this issue, you will have access to original research papers in a variety of areas, such as Physics, Chemistry, Biology, Material Science, Civil Engineering, Architectural Engineering, Software Engineering, Electrical and Electronics Engineering, Petroleum Engineering and Geology.

The great responses from researchers, academics and professionals in the last seven years have made us create a wider Editorial Board which serves the wider submitted scientific manuscripts. However, it is clear that having a dedicated and well-organised editorial board for the journal is only one side of the coin. The other is the ability to attract submissions of quality research and scholarly work. We are thankful to all of those who put their trust in ARO and presented their original research work for publication in Vol VIII, No 1 (2020) of the journal, as well as, our thanks are extended to the 34 peer-reviewers from the Universities worldwide for their efforts in reviewing and enabling this issue of ARO.

Your support and feedback are invited and appreciated.

Dilan M. Rostam
Editor-in-Chief

Wali M Hamad
Executive Publisher

Dilan M. Rostam, Salah I. Yahya, Basim M. Fadhil, Fahmi F. Muhammad, Mohammed H. S. Zangana, Jorge Correia, Executive Editor, Fouad Mohammed, Jacek Binda, Nadhir Al-Ansari, Howri Mansurbeg, Tara Fuad Tahir, Yazen A. Khaleel.

Executive Editorial Board

Design of a Branch-line Microstrip Coupler Using Spirals and Step Impedance Cells for WiMAX Applications

Sayed M. Hosseini and Abbas Rezaei

Department of Electrical Engineering, Kermanshah University of Technology, Kermanshah, Iran

Abstract—A branch-line microstrip coupler is designed and fabricated in this paper. The proposed coupler operates at 3 GHz, which is suitable for WiMAX applications. The designed coupler has a high performance, that is, a low phase difference of 0.49° , low insertion loss, good coupling factor, and good isolation better than -30 dB. Another advantage of the designed coupler is its novel geometrical structure based on integrating the semi-circular and step impedance cells. The design process is based on introducing and analyzing an equivalent LC model to improve impedance matching and reduce losses. To verify the design process, the designed coupler is fabricated, where a good agreement between the simulation result and measurement is achieved.

Index Terms—Branch line, Coupler, Insertion loss, Microstrip, Phase shift.

I. INTRODUCTION

Modern wireless communication systems usually require high-performance microstrip devices to meet low cost and high performance (Noori and Rezaei, 2017a; Noori and Rezaei, 2017b; Noori and Rezaei, 2017c). Accordingly, several types of branch-line couplers in Kumar and Karthikeyan, 2015; Wang, et al., 2016; Salehi and Noori, 2014; Sa'ad, et al., 2014; Shukor and Seman, 2015; Jung, 2014; Sa'ad, et al., 2013; Zong, et al., 2014; Kumar, et al., 2016; Tsai, et al., 2014; Dwari and Sanyal, 2006; Salehi, et al., 2015; and Rezaei and Noori, 2018, have been proposed to be used in modern monolithic microwave integrated circuits. For examples, they can be used in balanced mixers, balanced amplifiers, and phase shifters. A microstrip coupler is designed in Kumar and Karthikeyan, 2015, which is based on open stubs and triple open complementary split-ring resonator. Utilizing this structure led to the size reduction. Using a substrate of integrated suspended line, a novel branch-line coupler has

been implemented by Wang, et al. (2016). To reduce the coupler size, Wang, et al. (2016) utilized several meander lines. The designed branch-line coupler by Salehi and Noori (2014) operates at 2.4 GHz for wireless local area networks. This coupler has good characteristics such as compact size, high isolation, and negligible phase imbalance. A novel transparent 3 dB branch-line coupler has been introduced by Sa'ad, et al. (2014) using a nanoparticle technology. A two-section microstrip-slot branch-line coupler for enhanced bandwidth performance has been presented in Shukor and Seman, 2015. In this structure, an overlapped $\lambda/4$ open-circuited line has been added to each port, whereas each branch of coupler is composed of a microstrip-slot line. Meanwhile, the shunt branches have been bended for size reduction. A branch-line coupler based on an interdigital capacitor and quarter-wavelength strips are reported by Jung (2014). Using this structure, wide bandwidth and compact size have been obtained. In Sa'ad, et al., 2013, a branch-line coupler using open cross stub meander lines technique with a symmetrical structure has been introduced. In Zong, et al., 2014, several interdigital capacitors have been utilized to design a microstrip branch-line coupler. It has compact size with low insertion and return losses and high isolation. In Kumar, et al., 2016, a branch-line coupler has been reported with multiple asymmetric π -shaped, cross-shaped, and T-shaped transmission lines to reduce the overall size of coupler. In Tsai, et al., 2014, a compact branch-line hybrid coupler with suppressed harmonics has been presented. It has the advantages of the 2nd harmonic suppression capability and good frequency selectivity. In Dwari and Sanyal, 2006, a high harmonic suppression microstrip coupler based on stopband characteristics of defected ground structure sections has been introduced. These reported couplers have some disadvantages. In Alhalabi, et al., 2018, a 3-dB branch-line coupler operating at 2.45 GHz has been proposed which is fabricated on a double-layer substrate to have a compact size. In Hosseinkhani and Roshani, 2018, a compact branch-line coupler operating at 1.5 GHz microstrip has been designed using microstrip meandered lines and low-pass resonators. In Letavin, 2019, the miniaturization of a microstrip branch-line coupler has been proposed by replacing the microstrip transmission line with the equivalent microstrip structures with the same phase shift. In Sha, et al., 2019, a novel compact branch-

ARO-The Scientific Journal of Koya University
Vol. VIII, No.1 (2020), Article ID: ARO.10606, 4 pages
DOI: 10.14500/aro.10606

Received 02 December 2019; Accepted 08 January 2020
Regular research paper: Published 20 February 2020

Corresponding author's e-mail: a.rezaei@kut.ac.ir

Copyright © 2020 Sayed M. Hosseini and Abbas Rezaei. Rashid.

This is an open-access article distributed under the Creative Commons Attribution License.



line microstrip coupler with wide suppression band has been presented. In Gholami and Yagoub, 2018, an innovative design of microstrip-to-waveguide transition integrated with a microstrip directional coupler has been introduced. In Tan and Yassin, 2017, a novel design of a microstrip planar coupler with enhancement of power coupling has been presented. In Chen and Yeo, 2007, a symmetrical four-port microstrip coupler has been presented for crossover application. In references (Kumar and Karthikeyan, 2015; Wang, et al., 2016; Shukor and Seman, 2015; Jung, 2014; Zong, et al., 2014; Kumar, et al., 2016; Tsai, et al., 2014; Dwari and Sanyal, 2006), the phase shifts are more than 1° . In Kumar and Karthikeyan, 2015; Wang, et al., 2016; Salehi and Noori, 2014; Sa'ad, et al., 2014; Sa'ad, et al., 2013; Zong, et al., 2014; Kumar, et al., 2016, the coupling factors and insertion losses are not good. The designed couplers in Shukor and Seman, 2015; Jung, 2014, have large return losses. In this paper, we propose a branch-line coupler based on analyzing a novel microstrip structure. The proposed coupler has the advantages of small phase imbalance, acceptable return loss, low insertion loss, high isolation, and good coupling factor. Our designed coupler works at 3 GHz. Hence, it is suitable to WiMAX applications. It can separate the desired WiMAX signals near 3 GHz from an antenna. Then, it transmits the desired signals to two separated ports and delivers them. The designing process is structured as follows: First, an equivalent LC circuit of a basic microstrip structure is presented. Then, the LC circuit is analyzed to obtain a perfect impedance matching. Finally, a microstrip coupler is designed using the presented basic structure and optimization method.

II. COUPLER DESIGN

Fig. 1(a) depicts the proposed basic microstrip structure. It consists of the steps, spiral lengths, and semi-circular cells. The presented basic structure is symmetric. An equivalent LC circuit of this basic structure is presented in Fig. 1(b). In this figure, the physical lengths l_a , l_b , l_c , l_d , and l_e are replaced by the inductors L_1 , L_2 , L_3 , L_4 , and L_5 , respectively. The input and output ports are connected to the wider cells with the equivalent capacitors C_1 . The effect of steps is significant at the frequencies higher than 10 GHz. Hence, in the LC model, the effect of steps is removed so the LC circuit is an approximated model.

The input impedance of the LC model can be calculated as follows:

$$Z_{in} = \frac{2}{j\omega C_1} + j2\omega L_1 + j\omega \frac{2L_2L_4}{L_2 + L_4} + j\omega \frac{L_3L_5}{L_3 + L_5} \quad (1)$$

Where, ω is an angular frequency. The transmission matrix of the proposed LC circuit is defined as follows: (Noori and Rezaei, 2017a; Noori and Rezaei, 2017b):

$$T = \begin{bmatrix} A & B \\ C & D \end{bmatrix} = \begin{bmatrix} 1 & Z_{in} \\ 0 & 1 \end{bmatrix} \quad (2)$$

To have a perfect impedance matrix, the reflection coefficient (Γ) must be zero. Therefore, it can be written as follows:

$$\begin{aligned} \Gamma &= \frac{A+B-C-D}{A+B+C+D} = 0 \Rightarrow Z_{in} = 0 \Rightarrow \\ \frac{2}{j\omega_r C_1} + j2\omega_r L_1 + j\omega_r \frac{2L_2L_4}{L_2 + L_4} + j\omega_r \frac{L_3L_5}{L_3 + L_5} &= 0 \Rightarrow \\ 2(L_3 + L_5)(L_2 + L_4) - \omega_r^2 C_1 [2L_1(L_3 + L_5)(L_2 + L_4) + & \\ L_3L_5(L_2 + L_4) + 2L_2L_4(L_3 + L_5)] &= 0 \Rightarrow \\ \omega_r &= \sqrt{\frac{2(L_3 + L_5)(L_2 + L_4)}{C_1 [2L_1(L_3 + L_5)(L_2 + L_4) + L_3L_5(L_2 + L_4) + 2L_2L_4(L_3 + L_5)]}} \quad (3) \end{aligned}$$

Since ω_r is obtained by $Z_{in}=0$, it is the angular resonance frequency (Noori and Rezaei, 2017c). We can put the target angular resonance frequency instead of ω_r . There is a high degree of freedom to tune the inductors and capacitor to have a defined ω_r . Accordingly, they can be obtained by optimization method. Meanwhile, we have a perfect impedance matching, which leads to improve losses. These inductors and capacitors must be selected so that the overall dimensions are miniaturized. Using this structure, a microstrip coupler with a symmetric geometry is designed, as shown in Fig. 2. The additional optimizations are carried out to get better performance. It consists of two basic structures integrated by the step impedance cells. The coupling factor and insertion loss are affected by the width of vertical stubs, whereas the other parameters are unchanged. Moreover, changing the physical lines (those are inside the semi-circles) leads to improve the return loss and isolation factor.

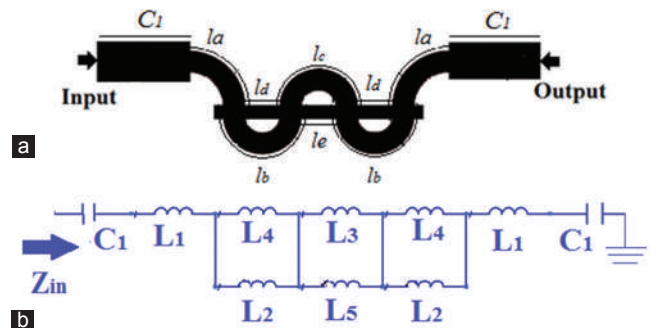


Fig. 1. The basic microstrip structure (a) layout, (b) equivalent LC circuit.

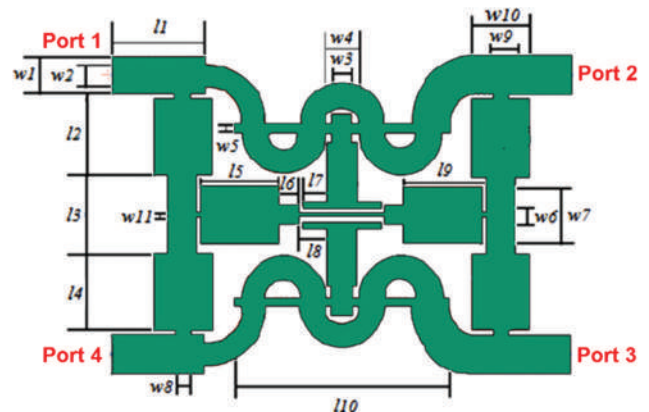


Fig. 2. Layout of the proposed coupler.

III. RESULTS AND DISCUSSION

The designed structure is simulated by electromagnetic simulator of advanced design system software. We used RT/duroid® 5880 substrate for simulation and fabrication of the proposed coupler. RT/duroid® 5880 substrate is used with the dielectric constant, dielectric thickness, and loss tangent of 2.2, 0.7874 mm, and 0.0009, respectively. Figs. 3a and b

show the frequency response of the designed coupler. The proposed coupler works at 3 GHz. A photograph of the fabricated circuit is provided in Fig. 3c.

The occupied area of the proposed coupler is $0.22 \lambda_g \times 0.32 \lambda_g$ (23.5 mm \times 16.5 mm) where λ_g is the guided wavelength calculated at the resonance frequency. At the center frequency of 3 GHz, the common port reflection coefficient ($|S_{11}|$) and isolation ($|S_{41}|$) are 17 dB and 34 dB, respectively. Meanwhile, the transmission coefficients ($|S_{21}|$ and $|S_{31}|$) are 3.07 and 3.17 dB, respectively. The fabricated structure is measured by an Agilent network analyzer N5230A. The simulated phase difference between the output ports is 270.49°. In Table I, the dimensions (in mm) of our branch-line coupler are presented. Table II depicts a comparison between this work and the previous reported couplers in terms of phase shift, common port return loss (S_{11}), insertion loss (S_{21}), coupling factor (S_{31}), isolation (S_{41}), and area. According to the comparison table, the proposed couplers in Kumar and Karthikeyan, 2015; Salehi and Noori, 2014; Jung, 2014; Sa'ad, et al., 2013; Zong, et al., 2014; Kumar, et al., 2016; Tsai, et al., 2014; and Dwari and Sanyal, 2006, are small, but we can see the large phase shifts and undesired isolation factors in Kumar and Karthikeyan, 2015; Jung, 2014; Sa'ad, et al., 2014; Kumar, et al., 2016; Tsai, et al., 2014; and Dwari and Sanyal, 2006. Moreover, there are the large insertion losses in the designs proposed in

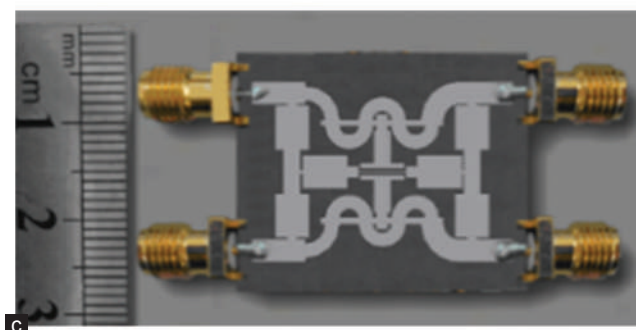
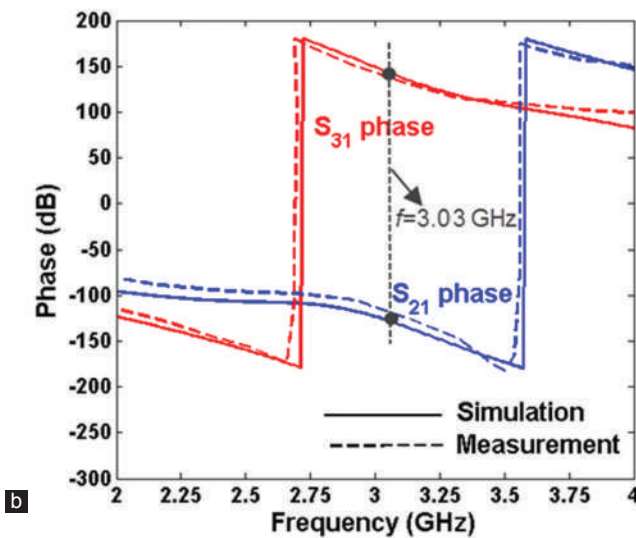
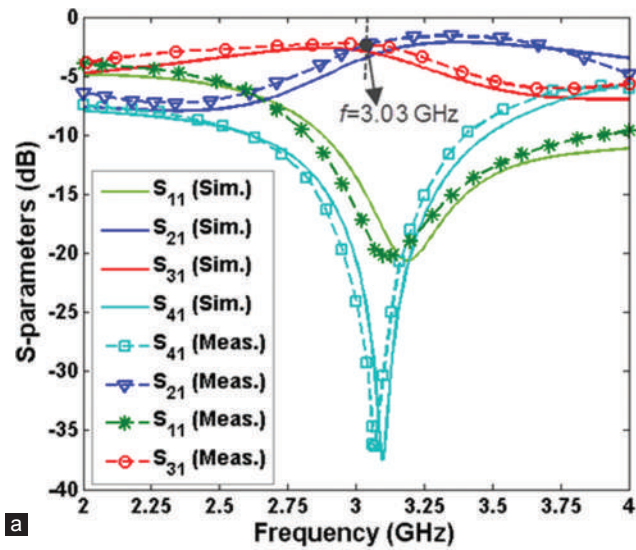


Fig. 3. (a) Simulated and measured frequency response of the proposed coupler, (b) simulated and measured phases of S_{21} and S_{31} , (c) fabricated coupler.

TABLE I
DIMENSIONS OF THE PROPOSED BRANCH-LINE COUPLER

Symbol	Value	Symbol	Value	Symbol	Value
l_1	4.75	l_8	1.42	w_5	0.5
l_2	4.2	l_9	4.2	w_6	1
l_3	4.1	l_{10}	11	w_7	3
l_4	4	w_1	2	w_8	0.8
l_5	4	w_2	1.25	w_9	1.5
l_6	1	w_3	1	w_{10}	3
l_7	1.25	w_4	1.5	w_{11}	0.3

TABLE II
COMPARISON WITH THE PREVIOUS DESIGNS

Refs.	S_{11} (dB)	S_{21} (dB)	S_{31} (dB)	S_{41} (dB)	Phase shift	Area ($\lambda_g \times \lambda_g$)
This work	17	3.05	3.16	34	0.49°	0.22 \times 0.32
Kumar and Karthikeyan, 2015	19.67	3.67	3.31	23.03	2.5°	0.41 \times 0.08
Wang, et al., 2016	30	3.75	3.85	20	1°	0.33 \times 0.33
Salehi and Noori, 2014	21.4	3.3	3.3	42.9	0.09°	0.23 \times 0.1
Sa'ad, et al., 2014	20.2	4.3	3.9	23.5	0.2°	0.45 \times 0.39
Shukor and Seman, 2015	10	3 \pm 2	3 \pm 1.6	10	5°	0.93 \times 0.35
Jung, 2014	10	-	-	30	2°	0.29 \times 0.20
Sa'ad, et al., 2013	20	3.51	3.36	20	0.5°	0.27 \times 0.25
Zong, et al., 2014	35	2.94	3.72	35	3°	0.1 \times 0.11
Kumar, et al., 2016	23.15	3.68	3.28	20.34	2.5°	0.20 \times 0.16
Tsai, et al., 2014	23.2	3.9	-	28.9	2°	0.077 \times 0.072
Dwari and Sanyal, 2006	22	3.2	3.1	17	2°	0.12 \times 0.12
Rezaei and Noori, 2018	29	3.3	2.8	31.3	0.97°	0.29 \times 0.26

Kumar and Karthikeyan, 2015; Salehi and Noori, 2014; Jung, 2014; Sa'ad, et al., 2013; Zong, et al., 2014; Kumar, et al., 2016; Tsai, et al., 2014; and Dwari and Sanyal, 2006.

Meanwhile, the lowest phase shift has been obtained in Sa'ad, et al., 2014, but it has large occupied area, low isolation factor, and large insertion loss.

IV. CONCLUSION

In this work, a 90° branch-line microstrip coupler is designed, fabricated, and measured to operate at 3 GHz for WiMAX applications. The proposed coupler is based on a symmetrical configuration, which consists of the semi-circular and step impedance cells. An *LC* approximate model of the basic microstrip structure is proposed to obtain the conditions for a good impedance matching. Meanwhile, we improved the coupler features using an optimization method, according to the presented theory method. Novel structure, low loss, low phase shift, and relatively good isolation are the advantages of the proposed microstrip coupler.

REFERENCES

- Alhalabi, H., Issa, H., Pistono, E. and Kaddour, D., 2018. Miniaturized branch-line coupler based on slow-wave microstrip lines. *International Journal of Microwave and Wireless Technologies*, 10(10), pp.1103-1106.
- Chen, Y. and Yeo, S.P., 2007. A symmetrical four-port microstrip coupler for crossover application. *IEEE Transactions on Microwave Theory and Techniques*, 55(11), pp.2434-2438.
- Dwari, S. and Sanyal, S., 2006. Size reduction and harmonic suppression of microstrip branch-line coupler using defected ground structure. *Microwave and Optical Technology Letters*, 48(10), pp.1966-1969.
- Gholami, M. and Yagoub, M.C.E., 2018. Integrated microstrip-to-waveguide transition with microstrip directional coupler. *IEEE Microwave and Wireless Components Letters*, 28(5), pp.389-391.
- Hosseinkhani, F. and Roshani, S., 2018. A compact branch-line coupler design using low-pass resonators and meandered lines open stubs. *Turkish Journal of Electrical Engineering and Computer Sciences*, 26, pp.1164-1170.
- Jung, Y., 2014. Wideband branch line coupler using symmetrical four-strip interdigitated coupler. *Electronics Letters*, 50(6), pp.452-454.
- Kumar, K., Barik, R. and Karthikeyan, S., 2016. A novel two section branch line coupler employing different transmission line techniques. *AEU-International Journal of Electronics and Communications*, 70, pp.738-742.
- Kumar, K. and Karthikeyan, S., 2015. Wideband three section branch line coupler using triple open complementary split ring resonator and open stubs. *AEU-International Journal of Electronics and Communications*, 69(10), pp.1412-1416.
- Letavin, D., 2019. Miniature microstrip branch line coupler with folded artificial transmission lines. *AEU-International Journal of Electronics and Communications*, 99, pp.8-13.
- Noori, L. and Rezaei, A., 2017a. Design of a microstrip diplexer with a novel structure for WiMAX and wireless applications. *AEU-International Journal of Electronics and Communications*, 77, pp.18-22.
- Noori, L. and Rezaei, A., 2017b. Design of a microstrip dual-frequency diplexer using microstrip cells analysis and coupled lines components. *International Journal of Microwave and Wireless Technologies*, 9(1), pp.1467-1471.
- Noori, L. and Rezaei, A., 2017c. Design of microstrip wide stopband quad-band bandpass filters for multi-service communication systems. *AEU-International Journal of Electronics and Communications*, 81, pp.136-142.
- Rezaei, A. and Noori, L., 2018. Microstrip hybrid coupler with a wide stop-band using symmetric structure for wireless applications. *Journal of Microwaves, Optoelectronics and Electromagnetic Applications*, 17(1), pp.23-31.
- Sa'ad, B., Rahim, S. and Dewan, R., 2013. Compact wide-band branch-line coupler with meander line, cross, and two-step stubs. *Microwave and Optical Technology Letters*, 55(8), pp.1810-1815.
- Sa'ad, B., Rahim, S., Peter, T., Rani, M., Ausordin, S., Zaidel, D. and Krishnan, C., 2014. Transparent branch-line coupler using micro-metal mesh conductive film. *IEEE Microwave and Wireless Components Letters*, 24(12), pp.857-859.
- Salehi, M., Noori, L. and Abiri, E., 2015. Novel tunable branch-line coupler for WLAN applications. *Microwave and Optical Technology Letters*, 57(5), pp.1081-1084.
- Salehi, M. and Noori, L., 2014. Novel 2.4 GHz branch-line coupler using microstrip cells. *Microwave and Optical Technology Letters*, 56(9), pp.2110-2113.
- Sha, S., Ye, Y. and Zhang, Z., 2019. A novel microstrip branch-line coupler with wide suppression band. *Progress in Electromagnetics Research Letters*, 83, pp.139-143.
- Shukor, N. and Seman, N., 2015. Enhanced design of two-section microstrip-slot branch line coupler with the overlapped $\lambda/4$ open circuited lines at ports. *Wireless Personal Communications*, 88(3), pp.467-478.
- Tan, B.K. and Yassin, G., 2017. Planar microstrip coupler with enhanced power coupling. *Electronics Letters*, 53(1), pp.34-36.
- Tsai, K., Yang, H., Chen, J. and Chen, Y., 2014. A miniaturized 3 dB branch-line hybrid coupler with harmonics suppression. *IEEE Microwave and Wireless Components Letters*, 21(10), pp.537-539.
- Wang, Y., Ma, K. and Mou, S., 2016. A compact branch line coupler using substrate integrated suspended line technology. *IEEE Microwave and Wireless Components Letters*, 26(2), pp.95-97.
- Zong, B., Wang, G., Zhang, C. and Wang, Y., 2014. Miniaturised branch-line coupler with ultra-wide high suppression stopband. *Electronics Letters*, 50(19), pp.1365-1367.

Petrophysical Investigation of the Khurmala Formation in Taq Taq Oil Field, Zagros Folded Belt

Fraidoon Rashid¹, Devan O. Hussein² and Hawar A. Zangana³

¹Department of Engineering, Kurdistan institution for Strategic Study and Scientific Research, Sulaimani, Kurdistan Region – F.R. Iraq

²Department of Geology, College of Science, University of Sulaimani, Sulaimani, Kurdistan Region – F.R. Iraq

³Department of Petroleum and Energy Engineering, College of Engineering, Sulaimani Polytechnic University, Sulaimani, Kurdistan Region – F.R. Iraq

Abstract– The Tertiary rocks of Khurmala Formation in the Taq Taq oil field have been studied using wireline log analysis, drilling cutting descriptions with integration of mud logging report, and test results for understanding reservoir potentiality and fluid distribution. The formation comprised dolostone and dolomitic limestone with an intercalation of clay layers between the recognized beds. The formation has variable thickness throughout the field, 99.8 m from the northeastern limb and 109 m in the southeastern plunge. The calculated shale volume in the studied interval shows a high rate of the clay contents which in some points the gamma ray has 100% of shale. The corrected log-derived bulk porosity subdivided the Khurmala Formation into 5 porosity units from the top to the bottom including (Kh-1, Kh-2, Kh-3, Kh-4, and Kh-5). The first (Kh-1), third (Kh-3), and fifth (Kh-5) porosity units have the average porosity ≥ 0.10 (10%) that can be considered as good reservoir unit in terms of porosity, whereas the shale contents reduced the reservoir quality of these units. However, well hydrocarbon entrapment through interconnected fractures and fault in the other Tertiary reservoir was recorded in Taq Taq field, but the weak connectivity of the pores in the Khurmala Formation caused this rock interval remains as water bearing zone.

Index Terms—Hydrocarbon, Khurmala, Porosity, Reservoir.

I. INTRODUCTION

Carbonate rocks are represented the dominant productive reservoir type in the Middle East (Hollis, 2011; Hollis et al., 2017; Jafarian et al., 2017; Adam et al., 2018) and this area holds nearly 15% of the world hydrocarbon reserves (Normi and Standen, 1997). The Iraqi Zagros basin is characterized by extension of different petroleum systems and heterogenous distribution of reservoir types including Triassic (Ryder Scott, 2011), Jurassic (Sherwani and Zangana, 2017), Cretaceous

(Al-Qayim and Rashid, 2012; Rashid, 2015; Rashid et al., 2015a and b; Rashid et al., 2017; Ghafur and Hasan, 2017; Rashid et al., 2020), and Tertiary reservoir rocks (Al-Qayim and Othman, 2012; Hussein, 2015; Hussein et al., 2017; and Hussein et al., 2018).

The Tertiary reservoir rocks have interrupted extensions and their availability was eliminated by local deposition of specific successions in a limited area. The tree dominant reservoir rocks in the Tertiary petroleum system in the Zagros folded zone are Kirkuk group, Euphrates, and Jeribe Formations (Jassim and Goff, 2006). However, in the Kirkuk oil field including Avanah and Khurmala domes, the Eocene Avanah Formation and Paleocene Sinjar Formation are considered as a productive reservoir rock (Aqrabi et al., 2010). Furthermore, the Eocene Pilaspi Formation identified as anisotropic reservoir rock units throughout the structures of Zagros basin in the Kurdistan region from Chamchamal block, Taq Taq and Tawke fields (Garland et al., 2010; Mackertich and Samarrai, 2015).

In contrast, the Paleocene Khurmala Formation has not recognized as a productive reservoir rock within the newly discovered fields in the Kurdistan region and also in the previously proved fields in the Kirkuk embayment. As a result, the rock evaluations of this formation were not analyzed and a very limited study about the reservoir characterization of this interval in the tertiary petroleum system has been considered, for understanding its reservoir potentiality. In this study, subsurface data sets from Taq Taq oil field were selected for evaluating the petrophysical properties and the reservoir quality of the Khurmala Formation to find out the logical reasons that influenced the rock ability for store hydrocarbon and production efficiency.

II. GEOLOGIC SETTING

Kurdistan region and Northern Iraq can be subdivided into three major structural unit areas, each unit has distinct structural characteristics and stratigraphic successions. Thrust Zone is characterized by highly complex tectonics with steep folds and over thrusts. The Folded Zone contains a series of anticlinal folds, having NW-SE trends, generally double plunging, in successive rows of parallel elongated closures, varying in axial



length and width. The Folded Zone enriched with a proved several oil and gas fields including Kirkuk, Khabaz, Bai Hassan, Jambur, Taq Taq, and Shaikan fields. The third zone is a narrow imbricated zone that appeared adjacent to the thrust belt front.

The Folded Zone can be subdivided into two areas (zones) based on geomorphologic criteria and geological distribution

of the sedimentary beds; High and Low Folded zones, (Ameen, 1992; Aqrawi et al., 2010, Jassim and Goff, 2006, Zebari and Burberry, 2015). These areas separated by the Mountain Front Fault, defined as the southern and southwestern, exposing of white limestone Pilaspi Formation, Fig. 1a. The High Mountains Zone is an intensely folded area north and

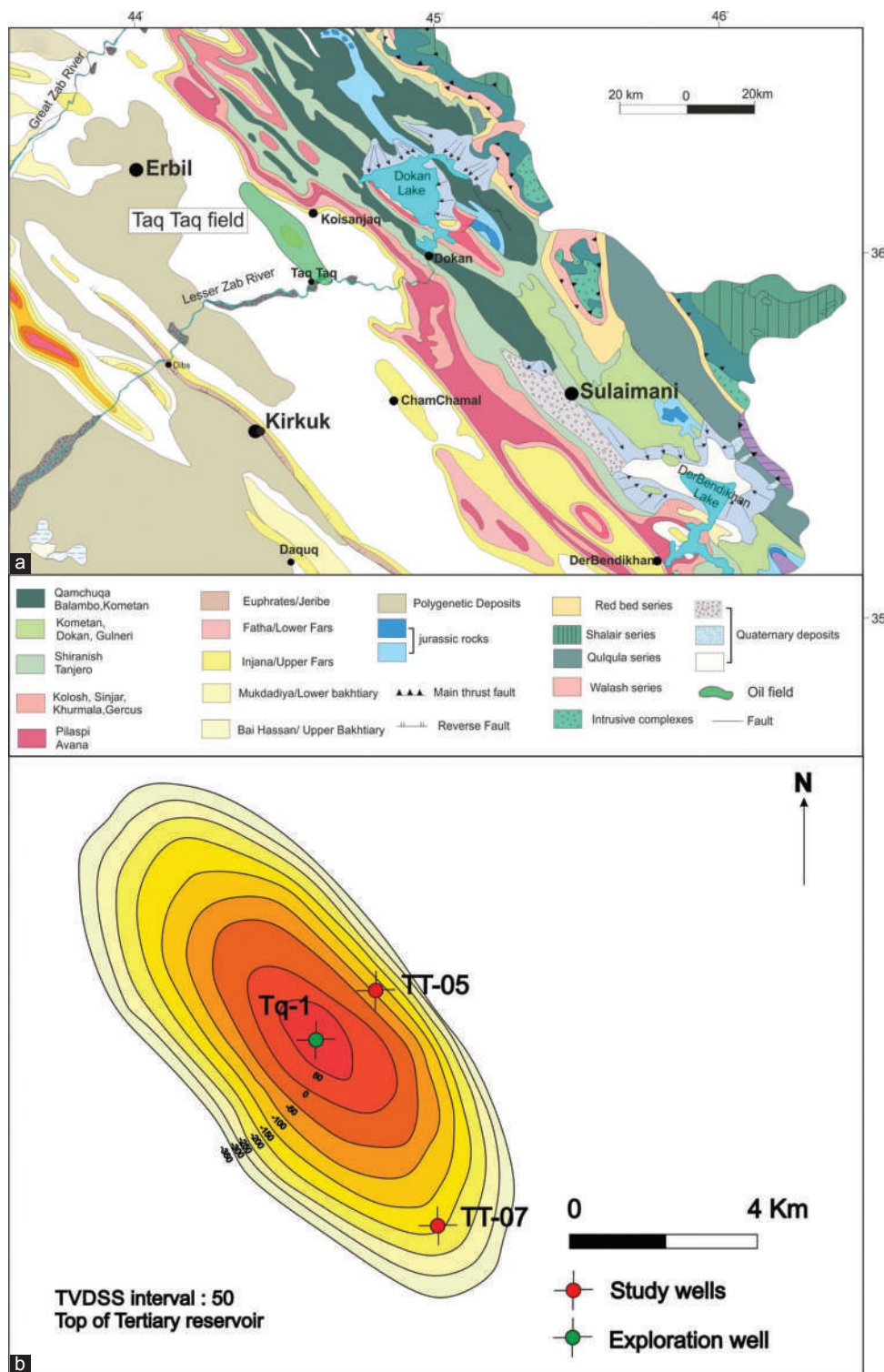


Fig. 1. (a). Geologic map of the Kurdistan region and north of Iraq shows the location of the Taq Taq oil field, modified from Sissakian et al., 2000. (b). Taq Taq field structure, contour on top of the Tertiary reservoir (NOC, 1987). The contours (contour interval = 50 m) measured from the ground surface. The selected well locates on the northeast and southwest of well Tq-1, crest of the Taq Taq anticline.

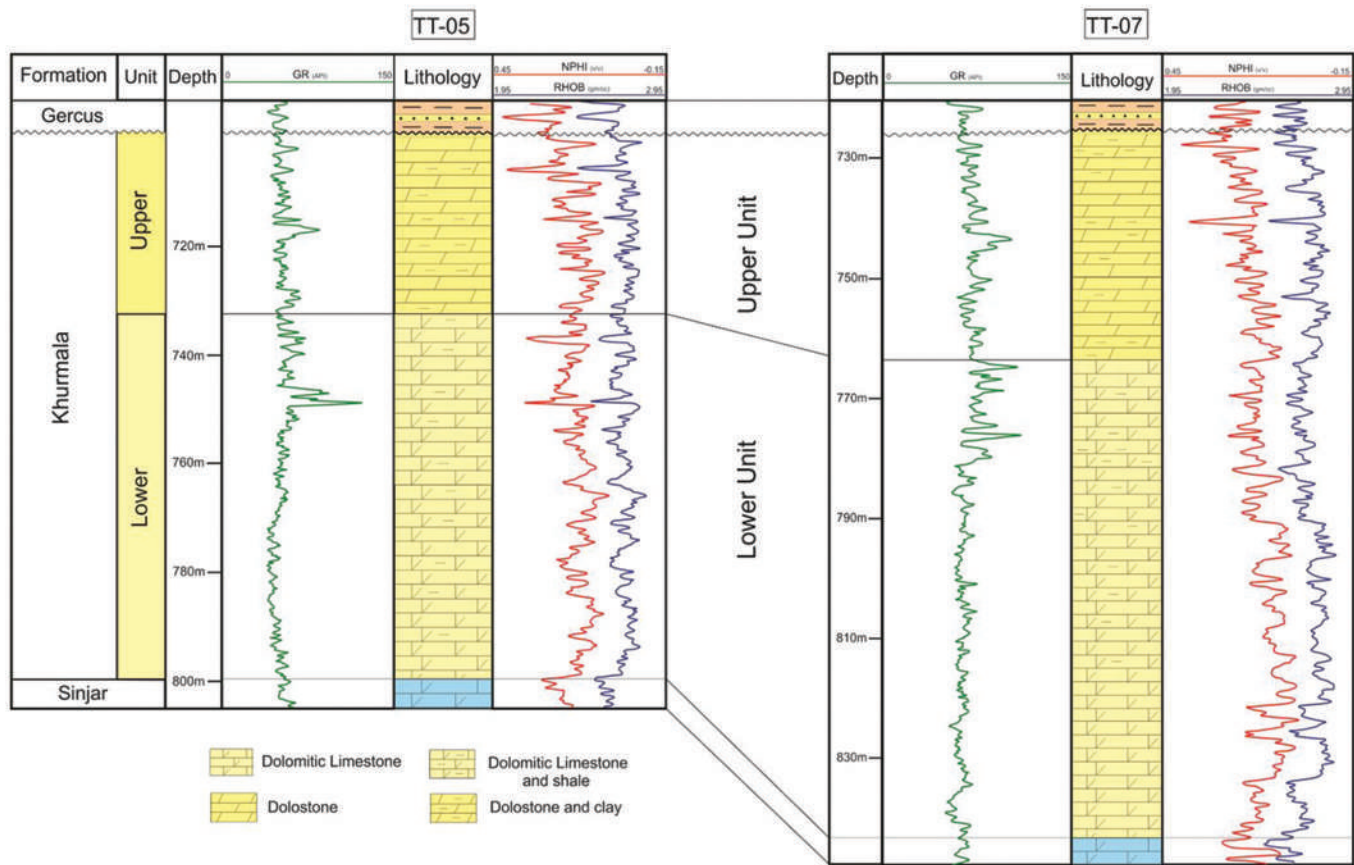


Fig. 2. Lithostratigraphic division of the Khurmala Formation in well TT-05 and TT-07 derived from wireline logs and lithologic description of cutting samples. The Khurmala Formation divided into two lithological units including upper unit (dolostone) and lower unit (dolomitic limestone). The calcareous clay and shale distributed within these two units.

northeast of the Mountain Front, in which different ages of rock units including Eocene, Palaeocene, and Cretaceous rocks were cropping out. The Low Folded Zone is the less intensely folded area located to the south and southwest of the Mountain Front, commonly Fars and Bakhtiari Formations can be seen at the exposure surfaces of this zone.

Taq Taq structure is a well-defined surface double-plunging anticline, oriented NW-SE parallel to the other structures in the Low Folded Zone of Zagros. The surface expression of the anticline has 27 km length of longitudinal axis and 11 km width, at an elevation of around 600 m above the sea level. The geological map of the area shows that the Pliocene-Pleistocene Upper Fars-Lower Bakhtiari Formations are cropped out at the surface on and surrounded area of the anticline. Toward the north, the older Eocene, Palaeocene, and Upper Cretaceous rocks equivalent to the Taq Taq reservoirs exposed in the mountains. The penetrated formations in the Taq Taq field starts from Miocene Lower Fars Formation at the Surface to the Jurassic Sargelu Formation in well Tq-1 and Upper Qamchuqa Formation in the most drilled wells, Fig. 1b. The dominant targets in this field were Cretaceous formation including Upper Qamchuqa Formation (Al-Qayim and Rashid, 2012), Kometan Formation (Rashid et al., 2015a), Shiranish Formation (Garland et al., 2010), and Tertiary Pilaspi Formation (Al-Qayim and Othman, 2010; Al-Qayim and Othman, 2012).

III. MATERIALS AND METHODOLOGIES

The data sets of this study were gathered from two drilled wells in the Taq Taq field including TT-05 and TT-07. The wells were penetrated all the targets and reached to the Upper Qamchuqa Formation successfully during the development program of the field. Well TT-05 is vertical developed well, located about 500 m of the northeast side of the first exploration well Tq-1 that was drilled on the crest of the structure. Well TT-07 is a deviated appraisal well which was drilled about 2500 m of the southeastern position of well Tq-1 on the southern plunge in the crestal part of the field.

The collected data for this research comprise a petrophysical wireline log covered the drilled Khurmala Formation intervals. The log data consist of porosity logs (sonic, density, and neutron), gamma ray logs, and resistivity logs. Besides the log data, drilling stem test, mud log, lithologs, and cutting samples have been used as a supporting evidence to enhance the quality of the study. A summary of the gathered data is shown in Table I.

The raw materials of the wireline logs have been used to identify the lithological distribution, mineralogical components, shale contents, porosity calculation, and fluid movability in the Khurmala Formation using Interactive Petrophysics. The petrophysical outcomes of the log data

TABLE I
SUMMARY OF THE COLLECTED DATA FROM THE TAQ TAQ FIELD

Data	TT-05	TT-07
Wireline log	Gamma ray (GR), sonic (DT), compensated density log (CDL), compensated neutron log (CNL)	Gamma ray (GR), sonic (DT), compensated density log (CDL), compensated neutron log (CNL)
Cutting sample	50	50
Well test	Drilling stem test	Drilling stem test
Mud log	Mud losses report	Mud losses report

TABLE II
STATISTICAL PARAMETERS OF THE CALCULATED SHALE VOLUME FROM GAMMA RAY LOGS

Well	Lithology Unit	Minimum	Maximum	Standard deviation	Mean	Mode
TT-05	Upper	0.011	0.262	0.039	0.055	0.038
	Lower	0.000	0.393	0.048	0.046	0.026
	Overall	0.000	0.393	0.045	0.049	0.038
TT-07	Upper	0.04	0.58	0.09	0.13	0.10
	Lower	0.01	1.00	0.10	0.10	0.06
	Overall	0.01	1.00	0.10	0.11	0.06

were dominantly achieved from the common equations and charts that have been used in wireline log analysis.

A. Lithology

The lithological description of the drilled cutting samples was integrated with the wireline lithology identification resulted from log combination method (Ellis and Singer, 2007; Asquith and Krygowski, 2004; Wiley and Pachett, 1990; Dahlberg, 1989), density-neutron log cross plot (Rider and Kennedy, 2011; Krygowski, 2003; Schlumberger, 1997). The conventional porosity logs are dependable on porosity change, lithology variation, and fluid contents. This criterion can be used to identify lithology composition and fluid type content in different rocks. The overlapping and crossover between the neutron and density logs are the dominant combination method for lithology determination. Furthermore, the cross plot between the neutron and a density log provides an essential result for continuous lithological variations in logged interval. This method gives single lithology component or a mixture between two types of rocks as limestone, dolostone, or dolomitic limestone.

B. Shale Volume

The gamma ray log can be used to calculate the volume of shale (clay) in a given interval. The estimated volume is usually shown as a decimal fraction or percentage is called shale volume (V_{sh}). In the carbonate rocks, the magnitude of the shale volume possibly affected by existence of organic matter because organic matter can concentrate uranium. The gamma ray index (I_{GR}) is the first step of the shale volume calculation using Equation (1), from the shale baseline (gamma reading = 100 API), clean sand line (gamma reading=0.0 API), and the gamma ray log reading from the selected interval (Bhuyan and Passey, 1994). The calculated gamma ray index (I_{GR}) then converts to shale volume with

using the most appropriate equation. In this study, we have used (Larionov, 1969) equation for calculating shale volume in Tertiary (young) rocks, Equation (2).

$$I_{GR} = \frac{GR_{log} - GR_{min}}{GR_{max} - GR_{min}} \quad (1)$$

$$V_{sh} = 0.083(2^{3.7I_{GR}} - 1) \quad (2)$$

I_{GR} : Gamma ray index

GR_{log} : Gamma ray reading from log, API

GR_{min} : Minimum gamma ray reading (clean sand or carbonate), API

GR_{max} : Maximum gamma ray reading (shale), API

V_{sh} : Shale volume.

C. Porosity

Sonic, density, and neutron logs are frequently referred to as porosity logs and they are widely used for calculating porosity in formation evaluation and reservoir quality assessment. Porosity must be calculated from the sonic slowness using Wiley time average Equation (3), (Wiley and Pachett, 1990; Asquith and Krygowski, 2004) and the apparent density knowing values for these parameters for the matrix and the fluids occupying the pores with applying Equation (4). In addition, the hydrogen concentration immediately transferred to neutron porosity while reading the logged interval (Rider and Kennedy, 2011; Schlumberger, 2012). The total porosity was achieved from the average value of the density derived porosity and neutron porosity.

$$f_s = \frac{(\Delta_{t\ bulk} - \Delta_{t\ ma})}{(\Delta_{t\ fl} - \Delta_{t\ ma})} \quad (3)$$

ϕ_s : Sonic porosity, fraction

$\Delta_{t\ bulk}$: Sonic log reading, $\mu\text{s}/\text{ft}$

$\Delta_{t\ ma}$: Transit time of matrix, $\mu\text{s}/\text{m}$

$\Delta_{t\ fl}$: Transit time of the mud filtrate, $\mu\text{s}/\text{m}$.

$$f_r = \frac{(r_{ma} - r_{bulk})}{(r_{ma} - r_{fl})} \quad (4)$$

ϕ_ρ : Density porosity, fraction

ρ_{ma} : Matrix density, g/cm^3

ρ_{bulk} : Log reading density, g/cm^3

ρ_{fl} : Fluid density, g/cm^3 .

Both the density and neutron tools use nuclear measurements, whereas the sonic tool measures the acoustic measure properties of the rock. Combination of three porosity logs in petrophysical measurement provides an accurate value of the calculated porosity from wireline logs. In this study, the estimated porosity was achieved from the porosity logs corrected for shale contents and environmental impaction.

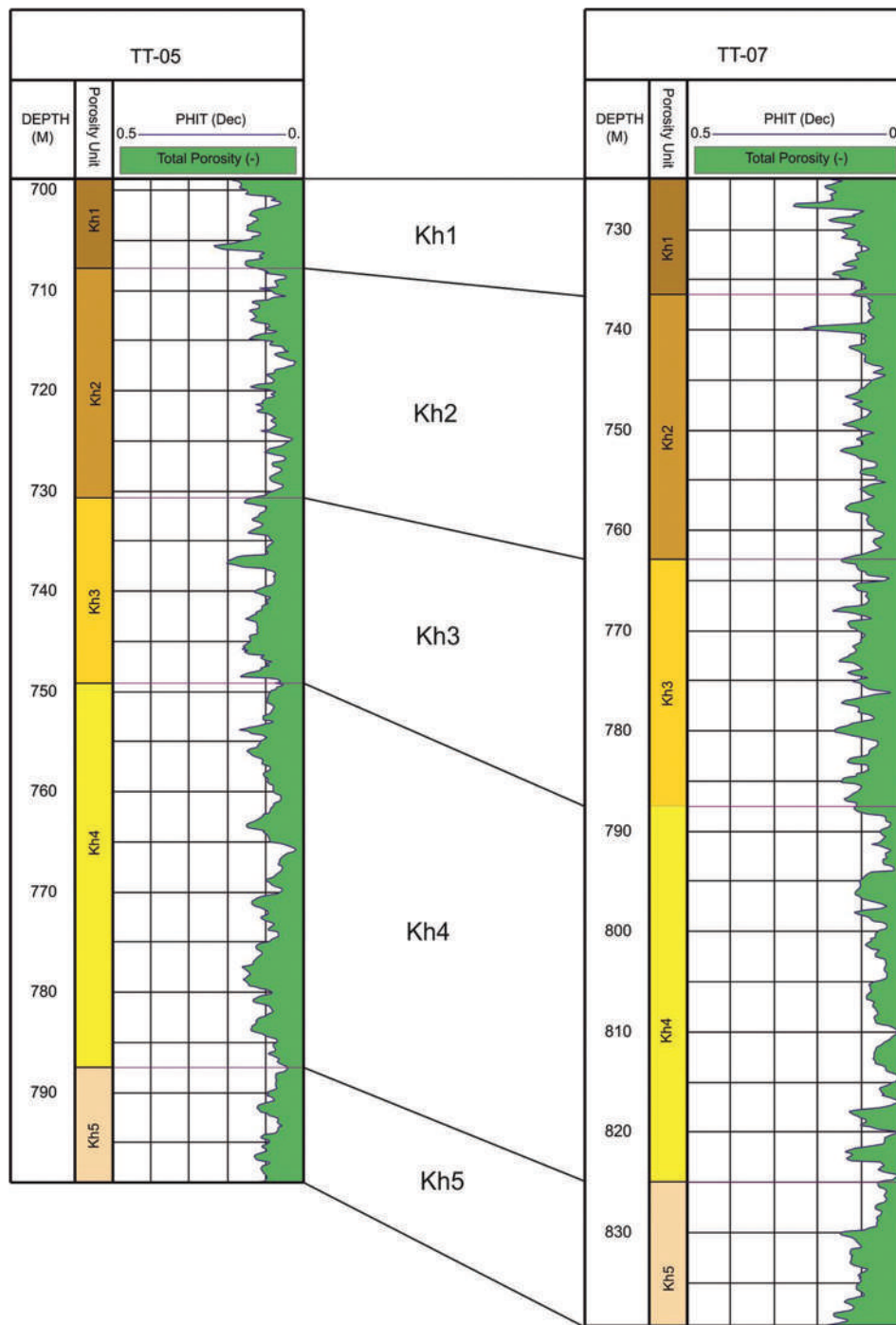


Fig. 3. Porosity distribution throughout the studied wells in the Taq Taq oil field, TT-05 and TT-07. The calculated total porosity was achieved from wireline logs and the studied interval subdivided into five porosity units from the top to the bottom of the formation.

IV. RESULTS

A. Lithology

The Khurmala Formation lithologically consists of dolostone and limestone beds in the well K-114 of Kirkuk oil field (Van Bellen et al., 1959). This composition changed to limestone successions with intercalation of argillaceous, gypsum, and anhydrate beds in the well Ch-2 from the Chamchamal block and argillaceous limestone and marls in the outcrop sections of the Zagros folded belt (Jassim and Goff, 2006; Aqrawi et al., 2010). The thickness of the formation is

adequately changeable throughout the Zagros folded belt in the subsurface and outcrops. The extension of gypsum and anhydrite within the carbonate beds is evidenced for restricted lagoon depositional environment of the Khurmala Formation.

The Khurmala Formation in the studied wells mostly comprises thick, fairly uniform, dolostone and dolomitic limestone with intercalation of clay beds and argillaceous limestone within the successions. The thickness of the formation is about 98.8 m in TT-05 and 113.8 m in TT07. These lithology components divided the Khurmala Formation in the Taq Taq

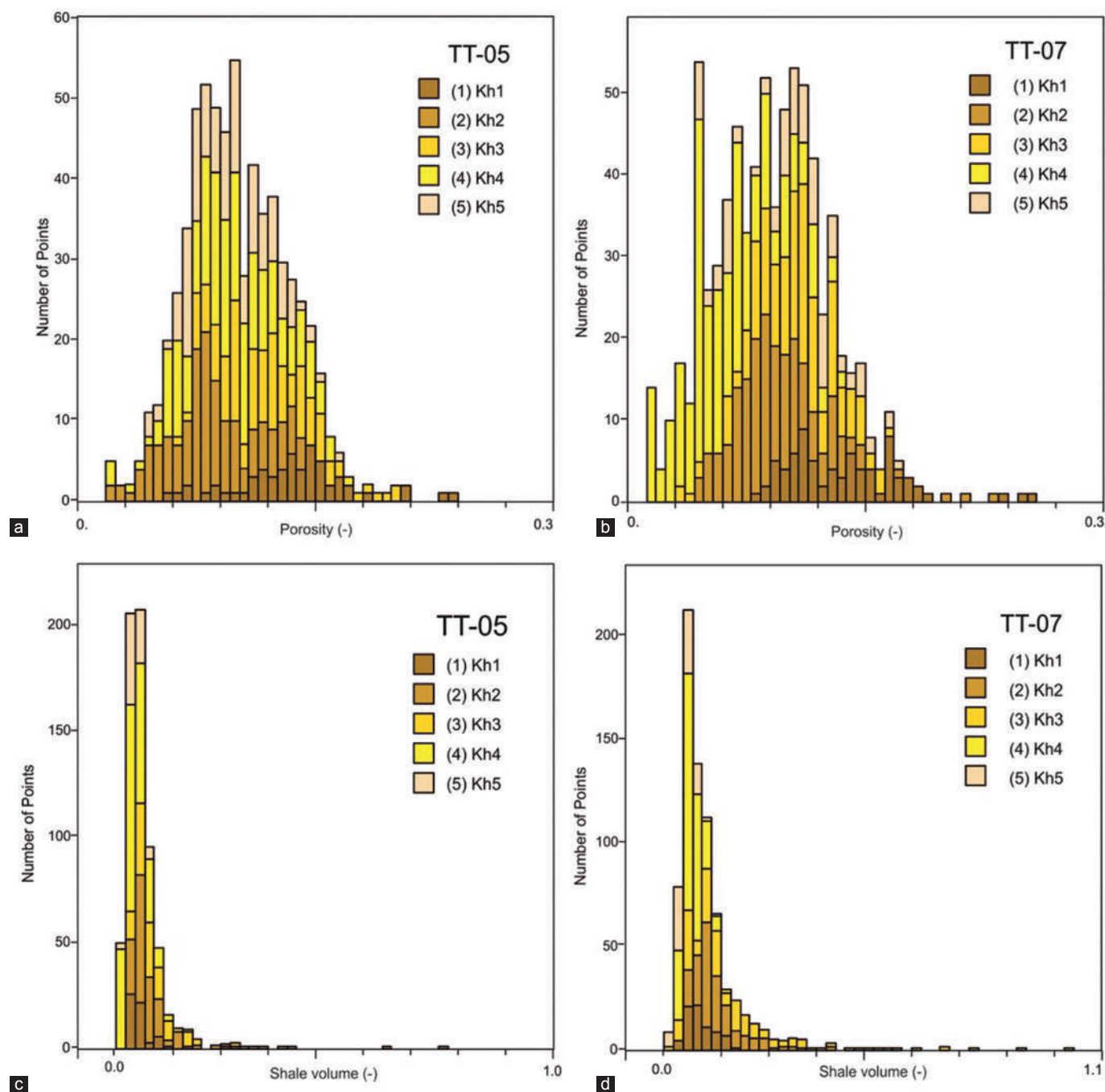


Fig. 4. Histograms of the total porosity and shale volume distribution throughout porosity units in the studied wells. (a) and (b) The total porosity distribution in the identified porosity units in well TT-05 and TT-07, respectively. (c) Shale volume distribution in well TT-05 and (d) shale volume distribution in TT-07.

field into two lithologic units; upper and lower lithologic units. The upper part is dominantly consisting of dolostone rocks with a calcareous clay (shale) contents. Thickness of this unit is about 31.3 m in TT-05, Fig. 2 and 37.6 m in TT-07 and overlaid by Gercus Formation. The dolostone rocks are characterized by light olive-gray to greenish-gray, firm to slightly hard, sub-blocky, locally crystalline texture. Visible pores cannot be investigated from the cutting samples.

Lower unit is comprised dolomitic limestone with intercalation of low amount shale layers in comparison to the upper part. Thickness of this unit is about 67.5 m

in TT-05 and 76.2 m in TT-07 and overlies by Sinjar Formation. The dolomitic limestone is pale gray to dark gray, hard blocky to angular, predominantly fine microcrystalline, occasionally micritic, microsucrosic texture. Very rare visible pores can be seen using naked eye observation. Occasionally, vuggy pores have been observed in the lower part of the formation. Dark gray to olive-gray calcareous shale intercalated with the dolomite and dolomitic beds that are characterized by platy to subplaty and fissile shape. In addition, moderately gray to dark and opaque and extremely hard and angular chert

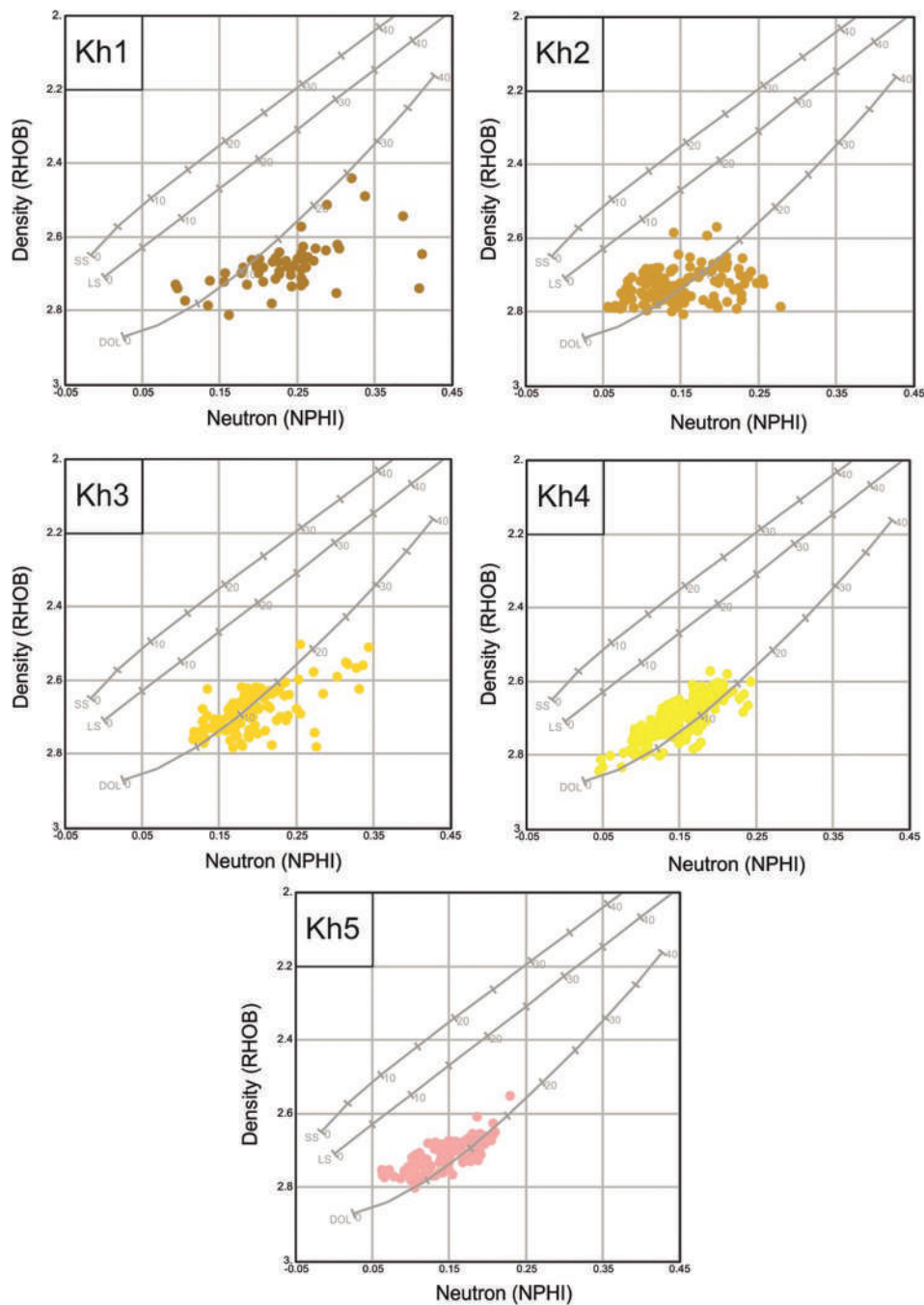


Fig. 5. Density-neutron cross plots of the Khurmala Formation in well TT-05 show different lithology components of the identified porosity units.

have been recorded in the lower part of the Khurmala Formation.

B. Shale Volume

The calculated volume of shale was obtained from the gamma ray log data using the Equations (1) and (2), respectively, for the studied intervals. The magnitude of the shale volume in the Khurmala Formations changed obviously from the top to the bottom and heterogeneous distribution of the shale percentage can be observed. Overall, the percentages of shale contents in the formation are quite high as reached

26% in the upper part of the formation in TT-05 and 57% in well TT-07. This magnitude was increased to 40% in TT-05 and 100% in shale-bearing interval in TT-07. The static results of the estimated shale volume of the studied wells are presented in Table II.

C. Porosity

The porosity distributions were achieved from the average values of the density log-derived porosity and the neutron-derived porosity of the Khurmala Formation presented as a total porosity. Based on the deflection of

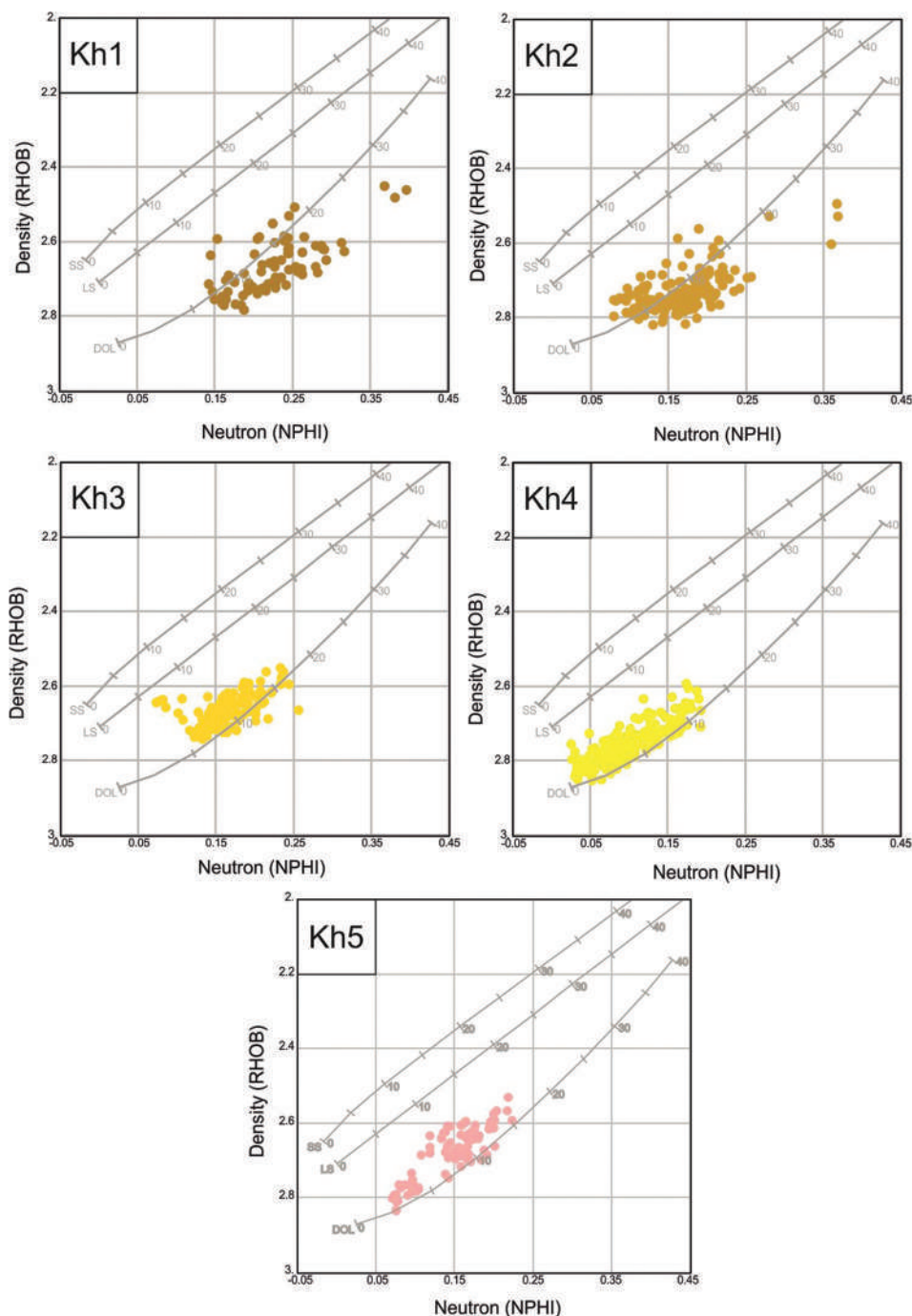


Fig. 6. Density-neutron cross plots of the Khurmala Formation in well TT-07 show different lithology components of the identified porosity units.

the total porosity curves, the total porosity distribution throughout the studied well can be subdivided into 5 units from the top to the bottom of the formation, respectively, Fig. 3.

Kh-1 Porosity Unit

The first unit is named Kh-1 covered the upper part of the Khurmala Formation in the Taq Taq oil field. The thickness of this unit is about 8.83 m in TT-05 and 11.5 m in TT-07, where Gercus Formation overlies this unit

throughout the field, Fig. 2. The magnitude of the average calculated total porosity in this unit is about 0.14, Fig. 4a and b, that is considered as the highest porosity value between the identified porosity units. The maximum clay volume in this unit is about 0.12 with an average of 0.04 throughout the unit, Fig. 4c and d. The lithology of this unit dominantly composed of dolostone (dolomite) as the plotted data from the density-neutron cross plot fall over the dolomite line with some movement toward the shale zone, Figs. 5 and 6.

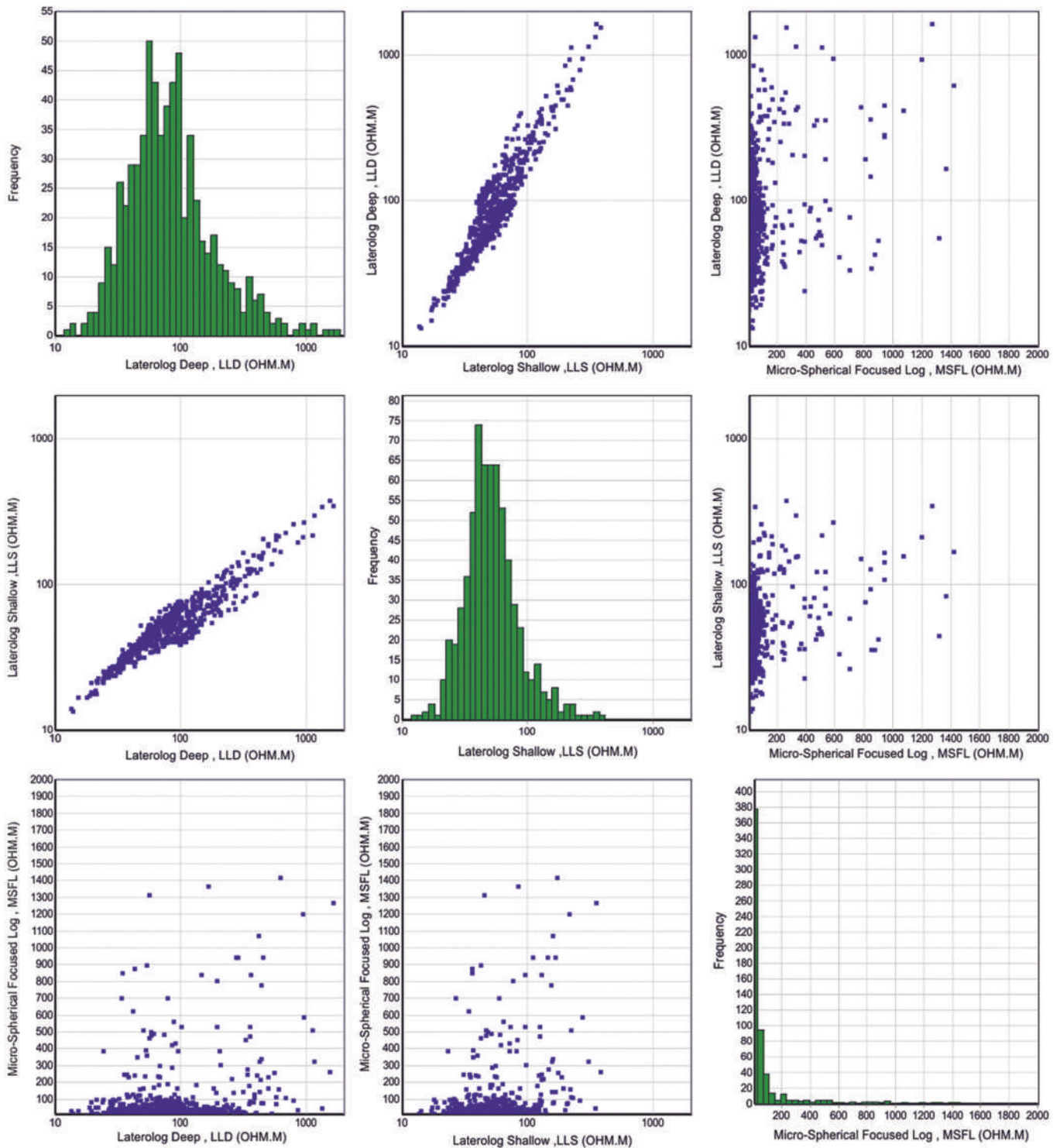


Fig. 7. Multicross plots of the resistivity logs including laterolog shallow (LLS), laterolog deep (LLD), and microspherically focused log (MSFL) of the Khurmala Formation in well TT-05. LLD and LLS readings are closed together, whereas the MSFL shows scattering readings for the same interval.

Kh-2 Porosity Unit

The second porosity unit (Kh-2) is located at the bottom of the first unit throughout the studied wells. The thickness of this unit is about 23 m in TT-05 and 26.7 m in TT-7. The magnitude of the average calculated total porosity was achieved from the wireline log in this unit which is about 0.09.

The maximum clay volume in this unit is 0.26 with an average of 0.06 throughout the unit in TT-05. The clay contents of this unit in TT-07 increased obviously and reached 0.57 as the maximum value and average is 0.14. The lithology of this unit dominantly composed of dolostone (dolomite) and dolomitic limestone in TT-05 and dolomite in well TT-07.

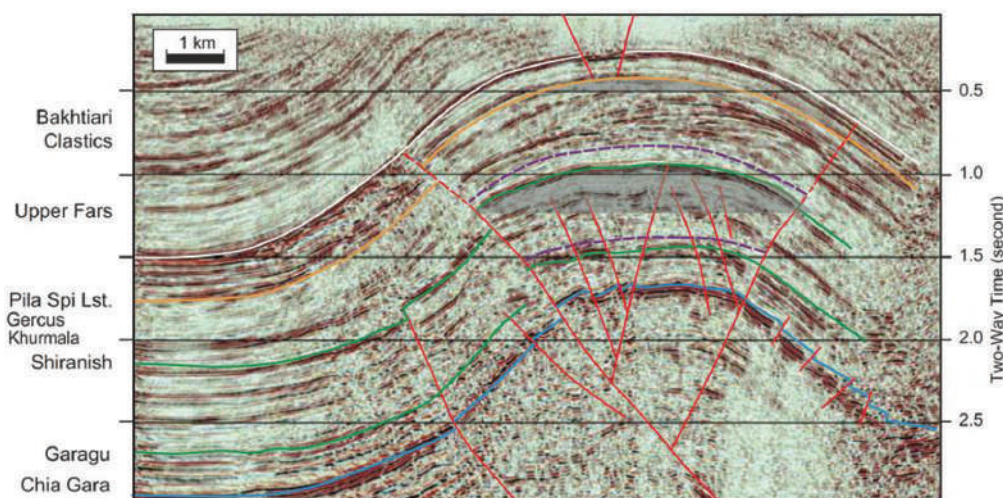


Fig. 8. Structural-seismic cross-section across the Taq Taq oil field with the stratigraphic succession and through going faults modified from Mackertich and Samarrai, 2015.

Kh-3 Porosity Unit

Kh-3 is the third porosity unit that is placed below the second unit (Kh-2) throughout the studied intervals in the Taq Taq field. The thickness of this unit is about 18.10 m in TT-05 and 23.4 m in TT-7. The magnitude of the average calculated total porosity was achieved from the wireline log in this unit which is 0.11. The shale volume within this porosity is much higher than the other units. The maximum clay volume in this unit is 0.39 with an average of 0.09 throughout the unit in TT-05. The clay contents of this unit in TT-07 increased obviously and reached 0.17 as the maximum value and average of 1.0. The lithology of this unit dominantly composed of dolostone rocks.

Kh-4 Porosity Unit

The fourth porosity unit (Kh4) in the Khurmala Formation has the thickest interval in the studied wells; 38.5 m thick in well TT-05 and TT-07. The average determined total porosity for this unit is 0.085, and the maximum shale volume in this unit is 0.15 with an average of 0.050. The clay content in this unit is much lower than the two previous units. The lithological composition of this unit as drawn from the density-neutron cross plot is dominantly composed of dolomitic limestone and the majority of the plotted data fall between the calcite and dolomite lines.

Kh-5 Porosity Unit

The last porosity unit (Kh-5) is located at the bottom of the Khurmala Formation and its thickness is 11.58 m in well TT-05 and 13.23 m in well TT-07. The average corrected total porosity in this unit is 0.10, and the percentage of shale volume reached 0.085 and the average shale content is 0.040. This unit can be considered as the cleanest interval in terms of the shale contents. The lithology of this unit consists of dolomitic limestone, it is a mixture of calcite and dolomite minerals based on the plotted data. This unit is overlaid by dolomitic limestone beds of the Sinjar Formation in the Taq Taq field.

V. DISCUSSION

The Khurmala Formation lithologically comprised dolomitic limestone and dolomite rocks, and these lithologies have a potential to hold and transmit hydrocarbons in reservoir rocks. The calculated porosity in the studied wells is high enough to be considered as a productive reservoir rocks, especially the first (Kh-1), third (Kh-3), and fifth (Kh-5) porosity units as the average corrected total porosity is >0.10 ($>10\%$) similar to the matrix porosity in Upper Qamchuqa and Pilaspi reservoir rocks (Al-Qayim and Othman, 2012; Al-Qayim and Rashid, 2012). However, after mud losing while drilling, a formation test flown sulfurous water at 3840 bpd in Tq-1 and saline water in TT-05 and TT-07 (NOC, 1987, Taq Taq Operation Company, 2006 and 2007). Furthermore, a very limited and minor oil were recorded only throughout the studied field.

High resistivity fluctuations were recorded by the microspherically focused resistivity log (microspherically focused log) in a clean borehole section throughout the studied intervals, Fig. 7. This is interpreted as a fracture zone with high resistivity relevant to cemented fractures and low resistivity to open fractures. Nevertheless, matching between deep and shallow resistivity in the Khurmala Formation associated to a lack of oil is strong arguments supporting the saline water formation hypothesis. Thus, these interval reservoirs are considered as water bearing.

The problematic point for the reservoir evaluation in the Khurmala Formation is lack of hydrocarbon productivity with good reservoir porosity. In addition, the formation is overlaid by Gercus Formation that acted as cap rock for the underlined reservoir rocks. The fluid productivity in this interval can be linked with hydrocarbon migration and entrapment or pore connectivity and permeability distribution.

To explain the fluid migration and hydrocarbon charge into the pore spaces of the Khurmala Formation, we have selected the Pilaspi Formation for comparison in the same wells and field. The Pilaspi Formation is characterized by oil-bearing reservoir rocks in Taq Taq field (Al-Qayim and Othman,

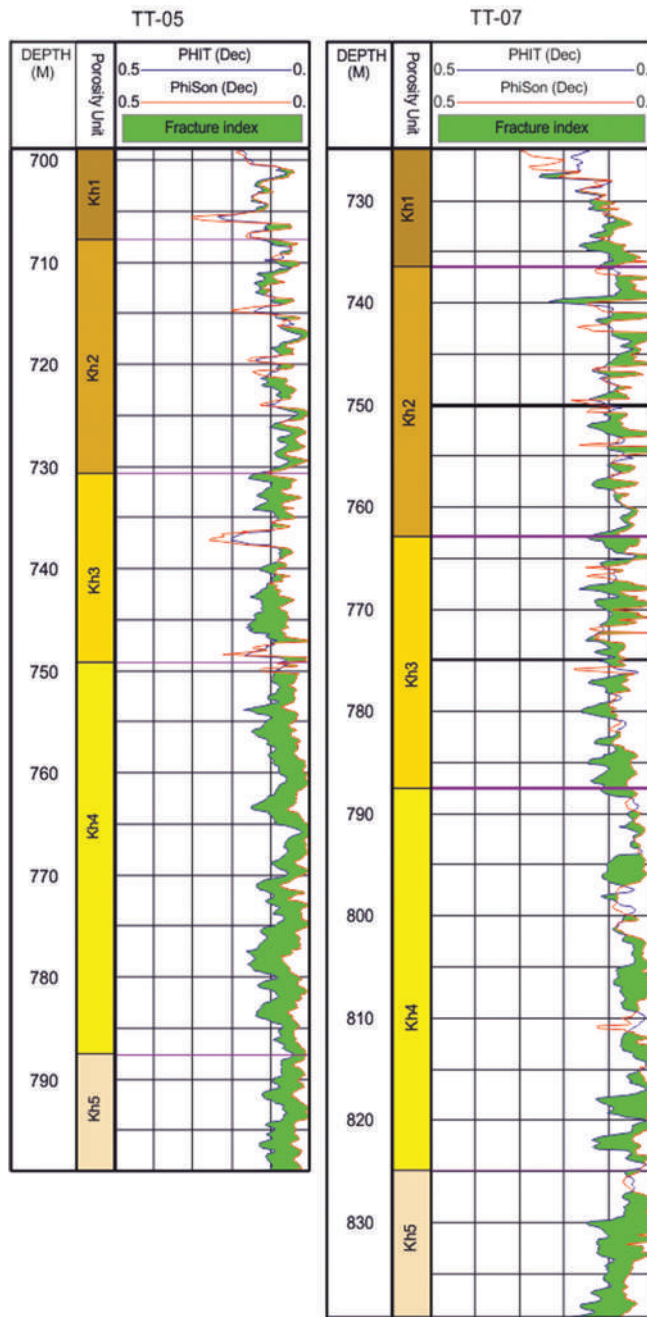


Fig. 9. Fracture index and secondary porosity distributions were obtained from the difference between total porosity (average porosity from the density and neutron log-derived porosity) and sonic log-derived porosity, showing as light green shadow zones.

2012). The hydrocarbon distribution in this reservoir is entrapped by fracture interconnected network, for example, through going fault that already crossed the Khurmala Formation, Fig. 8, that entrapped Pilaspi Formation and left the Khurmala Formation dry in terms of hydrocarbon saturation. The missing of the hydrocarbon in the pore spaces of the Khurmala Formation can be related with the volume of shale content. The formation can be considered as shale rock because of the volume of shale content >10% (0.10) (Kamel and Mabrouk, 2003). Shale contents within dolomitic

limestone and dolomite rocks destroyed the reservoir quality and blocked the pore connectivity and consequently reduced the magnitude of permeability. Besides the clay contents, the origins of the pores are dominantly secondary pore origin and this result can be seen clearly from the different contrast of the magnitude of log-derived porosity from sonic log and density-neutron logs, Fig. 9. The secondary pores commonly are characterized by weak interconnection between pores, isolated distribution and have very low permeability. These factors all together prohibited the migrated oil through fracture pathways to accumulate within the Khurmala Formation in the tertiary petroleum system.

VI. CONCLUSIONS

The main concluded points from the reservoir characterization evaluation and petrophysical investigation from wireline logs, test results, mud logging, and cutting samples of the Khurmala Formation are listed as follows:

- The Khurmala Formation in the Taq Taq oil field lithologically consists of dolomite (upper unit) and dolomitic limestone (lower unit) rocks. Argillaceous clay and fissile shale are intercalated with these carbonate rock units heterogenetically from the top to the bottom of the studied intervals
- The total corrected porosity achieved from the combination of density and neutron logs divided the formation into five respectful porosity units from the top to the bottom including (Kh-1, Kh-2, Kh-3, Kh-4, and Kh-5). The average porosity in the Kh-1, Kh-3, and Kh-5 is equal and >10%
- The calculated shale volumes using Larionov model for Tertiary rocks showed that the shale content in the Khurmala Formation is >10% in the most interval. As result, this formation considered as shale rock in terms of reservoir characterization
- The formation is characterized as water-bearing reservoir based on the flow test result, mud logging result, and resistivity log deflection. However, the Khurmala Formation located in the fracture zone, but the clay contents blocked the pore connectivity and reduced the permeability. Consequently, the migrated hydrocarbon avoided to be accumulated in this interval.

ACKNOWLEDGMENTS

The research data were provided by Taq Taq Operation Company – TTOPCO and Genel Energy. We would like to thank the geology and administrations staffs from the operated companies in Taq Taq field.

REFERENCES

- Adam, A., Swennen, R., Abdulghania, W., AbdImutalib, A., Hariria, M. and Abdulraheem, A., 2018. Reservoir heterogeneity and quality of Khuff carbonates in outcrops of central Saudi Arabia. *Marine and Petroleum Geology*, 89, pp.721-751.
- Al-Qayim, B. and Othman, D., 2012. Reservoir characterization of an intra-

- orogenic carbonates platform: Pila spi formation, taq taq oil field, Kurdistan, Iraq. *Geological Society*, 370, pp.139-168.
- Al-Qayim, B. and Rashid, F., 2012. Reservoir characteristics of the albian upper qamchuqa formation carbonates, taq taq oilfield, Kurdistan, Iraq. *Journal of Petroleum Geology*, 35, pp.317-341.
- Al-Qayim, B.A. and Othman, D.H., 2010. Lithofacies association, dolomitization, and potentiality of the pila spi formation, taq taq oil field, Kurdistan region, NE Iraq. *Iraqi Bulletin of Geology and Mining*, 6(2), pp.95-114.
- Ameen, M.S., 1991. Possible forced folding in the taurus-zagros belt of Northern Iraq. *Geological Magazine*, 128(6), pp.561-584.
- Aqrawi, A.A.M., Goff, J.C., Horbury, A.D. and Sadooni, F.N., 2010. *The Petroleum Geology of Iraq*. Scientific Press, Beaconsfield. p.424.
- Asquith, G. and Krygowski, D., 2004. *Basic Well Log Analysis*. AAPG, Tulsa, Oklahoma. p.244.
- Bhuyan, K. and Passey, Q.R., 1994. *Clay Estimation from Gamma Ray and Neutron-density Porosity Logs*. SPWLA, 35th Annual Logging Symposium, Tulsa.
- Dahlberg, K.E., 1989. *A Practical Model for Analysis of Compensated Neutron Logs in Complex Formations*. SPWLA Annual Logging Symposium, Denver.
- Ellis, D.V. and Singer, J.M., 2007. *Well Logging for Earth Scientists*. Netherlands Springer, Dordrecht.
- Garland, C.R., Abalioglu, I., Akca, L., Cassidy, A., Chiffolleau, Y., Godail, L., Grace, M.A.S., Kader, H.J., Khalek, F., Legarre, H., Nazhat, H.B. and Sallier, B., 2010. Appraisal and development of the Taq Taq field, Kurdistan region, Iraq. *Geological Society, London, Petroleum Geology Conference Series*, 7, pp.801-810.
- Ghafur, A.A. and Hasan, D.A., 2017. Petrophysical properties of the upper qamchuqa carbonate reservoir through well log evaluation in the Khabbaz oilfield. *Journal of Science and Engineering*, 1(1), pp.72-88.
- Hollis, C., 2011. Diagenetic on controls reservoir properties of carbonate successions within the Albian turonian of the Arabian plate. *Petroleum Geoscience*, 17, pp.223-241.
- Hollis, C., Lawrence, D.A., Perière, M.D., Al Darmaki, F., 2017. Controls on porosity preservation within a Jurassic oolitic reservoir complex, UAE. *Marine and Petroleum Geology*, 88, pp.888-906.
- Hussein, D., Collier, R., Lawrence, J., Rashid, F., Glover, P.W.J., Lorinczi, P. and Baban, D.H., 2017. Stratigraphic correlation and paleoenvironmental analysis of the hydrocarbon-bearing early miocene euphrates and jeribe formations in the Zagros folded thrust-belt. *Arabian Journal of Geosciences*, 10, pp.543-554.
- Hussein, D., Lawrence, J., Rashid, F., Glover, P. and Lorinczi, P., 2018. *Developing Pore Size Distribution Models in Heterogeneous Carbonates Using Especially Nuclear Magnetic Resonance*. In: *Engineering in Chalk: Proceedings of the Chalk 2018 Conference*. ICE Publishing, London. pp.529-534.
- Hussein, D.O., 2015. *Reservoir Characterization of Ramp Carbonates: Lessons from the Lower Miocene Euphrates and Jeribe Formations, Kurdistan, N. Iraq* Doctoral Dissertation, University of Leeds.
- Jafarian, A., Fallah-Baghtash, R., Mattern, F. and Heubeck, C., 2017. Reservoir quality along a homoclinal carbonate ramp deposit: The permian upper Dalan formation, South pars field, Persian Gulf Basin. *Marine and Petroleum Geology*, 88, pp.587-604.
- Jassim, S.Z. and Goff, J.C., 2006. *The Geology of Iraq*. Dolin, Prague. p.341.
- Kamel, M.H. and Mabrouk, W.M., 2003. Estimation of shale volume using a combination of the three porosity logs. *Journal of Petroleum Science and Engineering*, 20, pp.145-157.
- Krygowski, D.A., 2003. *Guide to Petrophysical Interpretation*. Wyoming University, Austin Texas USA. p.147.
- Mackertich, D.S. and Samarrai, A.I., 2015. History of hydrocarbon exploration in the Kurdistan region of Iraq. *GeoArabia*, 20(2), pp.181-220.
- Nonmi, R. and Standen, E., 1997. Middle East Evaluation Well Review.
- North Oil Company-Kirkuk (NOC), 1987. *Final Well Report of Exploration Well Number 1 in Taq Taq Oil Field*.
- Rashid, F., Glover, P.W.J., Lorinczi, P., Collier, R. and Lawrence, J., 2015a. Porosity and permeability of tight carbonate reservoir rocks in the North of Iraq. *Journal of Petroleum Science and Engineering*, 133, pp.147-161.
- Rashid, F., Glover, P.W.J., Lorinczi, P., Hussein, D. and Lawrence, J., 2017. Microstructural controls on reservoir quality in tight oil carbonate reservoir rocks. *Journal of Petroleum Science and Engineering*, 156, pp.814-826.
- Rashid, F., Glover, P.W.J., Lorinczi, P., Hussein, D., Collier, C. and Lawrence, J., 2015b. Permeability prediction in tight carbonate rocks using capillary pressure measurements. *Marine and Petroleum Geology*, 68, pp.536-550.
- Rashid, F., Hussein, D., Lawrence, J.A. and Khanaqa, P., 2020. Characterization and impact on reservoir quality of fractures in the cretaceous qamchuqa formation, Zagros folded belt. *Marine and Petroleum Geology*, 113, pp.104-117.
- Rashid, F.N., 2015. *The Kometan Formation: Reservoir Characteristics of Tight Carbonates in the Western Zagros Basin*. Doctoral Dissertation, University of Leeds.
- Rider, M.H. and Kenedy, M., 2011. *The Geological Interpretation of Well Logs*. Rider-French Consulting Ltd., Sutherland. p.280.
- Ryder Scott Company, 2011. *Estimated Unrisked Discovered and Undiscovered Total Petroleum Initially in Place Attributable to Certain Interests in the Shaikan License Block, Kurdistan, Iraq*. Report Prepared for Gulf Keystone Petroleum Ltd., Iraq.
- Schlumberger, 1997. *Log Interpretation/Charts*. Schlumberger Wireline and Testing, Houston, USA.
- Schlumberger, 2012. Definition of porosity: How porosity is measured. *Oil Field Review Autumn*, 24(3), pp.63-64.
- Sherwani, G.H. and Zangana, H.A. 2017. Reservoir characterization of early jurassic formations in selected wells in the duhok governorate, Iraqi Kurdistan region. *Journal of Science and Engineering*, 1(1), pp.11-18.
- Sissakian, V.K., Ibrahim, E.I., Ibrahim, F.A., and Al-Ali, N.M. 2000. *Geological map of Iraq, Scale 1: 1000000, Sheet No. 1*. 3rd ed. State Company of Geological Survey and Mining, Baghdad, Iraq.
- Taq Taq Operation Company, 2006. Final Well Report of Development Well Number 5 in Taq Taq Oil Field.
- Taq Taq Operation Company, 2007. Final Well Report of Development Well Number 7 in Taq Taq Oil Field.
- Van Bellen, R.C., Dunnington, H.V., Wetzel, R. and Morton, D.M., 1959. *Lexique Stratigraphique International: 03 10 Asie (Iraq)*. Paris: Centre National de la Recherche Scientifique Reprinted by Gulfpetro Link, 2005.
- Wiley, R. and Pachett, J.G., 1990. *CNL (Compensated Neutron Log) Neutron Porosity Modeling, a Step Forward*. SPWLA 30th Annual Logging Symposium.
- Zebari, M.M. and Burberry, C.M., 2015. 4-D evolution of anticlines and implications for hydrocarbon exploration within the Zagros fold-thrust belt, Kurdistan region, Iraq. *GeoArabia*, 20, pp.161-188.

Evaluation of Oxidative Stress and some Biochemical Parameters in Normal Pregnant Women

Musher I. Kakey¹, Kamaran K. Abdoulrahman² and Gulbahar R. Uthman²

¹Department of Chemistry, Faculty of Science and Health, Koya University,
Koya KOY45, Kurdistan Region - F.R. Iraq

²Department of Chemistry, College of Science, Salahaddin University,
Erbil, Kurdistan Region - F.R. Iraq

Abstract—Pregnancy is associated with many metabolic changes in normal pregnant woman, this leads to change in physiological, biochemical, and hematological parameters drastically. The test subjects were selected among those attending to Maternity Teaching Hospital in Erbil Governorate between March 2017 and August 2017. Four groups of individuals were included in this study, 230 pregnant women divided into three groups (Group 1 first trimester, Group 2 second trimester, and Group 3 third trimester) and Group 4 contained 90 nonpregnant women as control. Full automatic chemical analyzer (Cobas C311, Germany) was used to determine the biochemical parameters. The EL ×800 Absorbance Microplate Reader from BioTek (USA) instruments is used to measure the activity of superoxide dismutase (SOD), catalase (CAT), and malondialdehyde (MDA) in serum. The results of this study showed a significant increase in serum albumin, glucose, total bilirubin, direct bilirubin, alanine aminotransferase, aspartate aminotransferase, alkaline phosphatase, creatinine, urea, cholesterol, low-density lipoprotein, and MDA in pregnant women as compared to the control group, also show significant decrease in high-density lipoprotein (HDL) level, SOD activity, and CAT activity in pregnant women as compared to nonpregnant women, and nonsignificant difference in uric acid, and HDL.

Index Terms—Pregnancy, Oxidative stress, Liver parameters, Lipid profiles, Kidney function.

1. INTRODUCTION

More than 200 million women become pregnant every year, and in most cases, the outcome of labor is successful. Due to the hormonal status changes during pregnancy, various adaptive mechanisms are initiated due to sex hormones. Among them, change of the energetic metabolism to lipid metabolism is observed (Merabishvili, et al., 2006). Oxidative stress occurs due to an imbalance between the reactive

oxygen species and the antioxidant levels (Miao and Clair, 2009). Oxidants (free radical) are normal products of aerobic metabolism, including superoxide radical, hydroxyl radical, and hydrogen peroxidase. They can be harmful when they produced in excess amounts (Saikumar, et al., 2013). The liver has many important functions, including metabolism, detoxification, and formation of important compounds, including blood clotting factors and albumin (Ali, 2015). The pregnant woman experiences physiological changes to support fetal growth and development. During pregnancy, the serum estrogen and progesterone levels increase progressively and reach a maximum during the third trimester. These sex steroids have effects on metabolic, synthetic, and excretory hepatic functions (Gohel, et al., 2013). During pregnancy, an increase in the levels of estrogens and progesterone will occur. These sex hormones have effects on hepatic metabolism, synthesis, and excretory functions (González, et al., 2000). Pregnant women develop physiological dyslipidemia that can be measured in the laboratory by the lipid indexes; total cholesterol (TC), triglycerides (TG), high-density lipoprotein (HDL), and low-density lipoprotein (LDL) (Merabishvili, et al., 2006). The alterations of serum lipid indexes are associated with the gestational age. Pregnancy is accompanied by significant variations in maternal lipid metabolism (Parchwani, and Patel, 2011). During normal pregnancy, women show an increase in lipid levels, including levels of TG and TC as gestational age progresses (Ogura, et al., 2002). Both TG and TC are taken up by the placenta, metabolized and transported to the fetus in various forms; this shows that both lipids are essential for the development of the fetus. An increase in maternal lipid profile during pregnancy differs with gestational age (Woollett, 2011). It has been observed that the concentration of serum TC, serum TG, HDL cholesterol, and LDL cholesterol in normal pregnant women increased with increasing gestational age (Herrera, 2002). Any increase in the maternal lipid profile in the third trimester is in response to the maternal switch from carbohydrate to fat metabolism which is an alternative pathway for energy generation due to high energy demand. Creatinine and blood urea nitrogen (BUN) are waste products removed from the blood by the kidneys. Creatinine is a breakdown product of creatine phosphate in the muscle.

ARO-The Scientific Journal of Koya University
Vol. VIII, No.1 (2020), Article ID: ARO.10541, 7 pages
DOI: 10.14500/aro.10541

Received 24 June 2019; Accepted 06 February 2020
Regular research paper: Published 20 February 2020

Corresponding author's e-mail: musher.ismael@koyauniversity.org
Copyright © 2020 Musher I. Kakey, Kamaran K. Abdoulrahman and Gulbahar R. Uthman. This is an open access article distributed under the Creative Commons Attribution License.



Serum creatinine is a marker used for renal function assessment. When the kidney function is lost, the level of BUN will be increased, but other factors may affect the BUN level (Kamili, et al., 2013; Patel, et al., 2013).

The aim of the present study is to evaluate the oxidative stress, enzymatic antioxidant activities, and some biochemical parameters in the normal pregnant women at first, second, and third trimesters) as a comparison to nonpregnant women.

II. MATERIALS AND METHODS

A. Samples

The test subjects were selected among those attending to Maternity Teaching Hospital in Erbil Governorate between March 2017 and August 2017. Four groups of individuals were included in this study. Group 1 contained 85 pregnant women in first trimester of pregnancy (1–3 months). Group 2 consisted of 75 pregnant women in second trimester of pregnancy (4–6 months). Group 3 comprised of 70 pregnant women in third trimester of pregnancy (7–9 months) and Group 4 contained 90 nonpregnant women as control group in this study. The blood was drawn into a tube then centrifuged at 5000 RPM and the serum was used to estimation of oxidative stress, lipid profile, liver parameters, and kidney function test. Full automatic chemical analyzer (Cobas C311, Germany) was used to determine the biochemical parameters. Superoxide dismutase (SOD) activity was assayed using (Randox-Ransod kits, USA) (colorimetric method). Catalase (CAT) activity was assayed using (Cayman kits, USA). Serum malondialdehyde (MDA) level was estimated by manual method of thiobarbituric acid reactive substances (Chaudhary, et al., 2003).

B. Statistical Analysis

Data analysis was performed with the GraphPad Prism software. The results for continuous variables are mean+SEM, analysis of variance was used in the assessment of the significance of the difference between group means.

III. RESULTS AND DISCUSSION

This study included 230 pregnant women with age ranged from 23 to 40 years. The mean age was 33 ± 4.5 years with no risk factors and 90 nonpregnant women as control group. The results of the current study are showing in Tables I and II.

The body produces different enzymes, including SOD, CAT, glutathione peroxidase (GSHPX), and glutathione reductase.

Table I and Fig. 1 show a significant increase in concentrations of serum MDA in the test group in comparison with the control group ($P \leq 0.05$). Saikumar, et al. determined a high level of MDA¹⁴ (Saikumar, et al., 2013), which is similar to our result. The increased MDA levels are known to be due to increased generation of reactive oxygen species and increased oxygen demand along with a reduction in activities of enzymes like SOD, GSHPX, and CAT.

Furthermore, the results showed a significant decrease in SOD activity and CAT activity in pregnant women as compared to the control group, as shown in Table I and Figs. 2 and 3, respectively.

The mean levels of biochemical parameters were measured in healthy pregnant women and control group. These data show that the mean level of serum glucose in pregnant women

TABLE I
OXIDATIVE STRESS PARAMETERS IN PREGNANT WOMEN AND CONTROL GROUP

Parameters	Control group	1 trimester	2 trimester	3 trimester
Superoxide dismutase (IU/gHb)	705.0±28.39	545.5±38.59	507.9±43.07	456.8±30.68
Catalase (IU/gHb)	8.378±0.394	7.031±0.254	6.329±0.337	5.756±0.311
Malondialdehyde (nmol/ml)	1.598±0.062	1.834±0.036	2.672±0.098	3.457±0.114

TABLE II
BIOCHEMICAL PARAMETERS IN PREGNANT AND CONTROL GROUP

Parameters	Control	Pregnant group		
		1 st trimester	2 nd trimester	3 rd trimester
Aspartate aminotransferase	19.79±1.400	20.02±0.619	24.71±1.810	27.09±2.117
Alanine aminotransferase	13.25±0.880	20.13±2.036	25.09±2.870	36.07±5.188
Total protein	7.705±0.117	6.938±0.170	6.853±0.333	6.633±0.201
Total bilirubin	0.528±0.021	1.144±0.060	1.666±0.146	1.876±0.215
Albumin	4.766±0.124	4.034±0.119	4.005±0.275	4.078±0.133
Direct bilirubin	0.132±0.008	0.282±0.019	0.424±0.046	0.501±0.046
Alkaline phosphatase	136.8±3.539	191.3±8.800	231.3±14.17	273.0±25.16
Glucose	107.2±4.543	157.9±11.23	171.7±16.17	209.8±13.59
Creatinine	0.597±0.027	0.687±0.036	0.869±0.061	0.905±0.035
Urea	23.78±2.323	27.94±1.868	35.97±3.056	34.82±1.736
Uric acid	3.970±0.144	4.251±0.197	4.743±0.357	4.421±0.192
Total cholesterol	146.6±3.841	201.4±12.21	208.1±15.46	240.8±7.850
Triglycerides	93.29±3.271	205.4±14.19	236.1±29.86	247.3±17.69
High-density lipoprotein	52.63±2.955	47.17±2.077	44.29±2.536	41.67±2.090
Low-density lipoprotein	80.36±2.883	94.33±3.023	94.30±4.775	96.55±3.888

is increased continuously (Table II and Fig. 4). It is in pregnant women significantly higher compared to the control group.

The mean levels of serum TC, TG, and LDL of the test subjects in the pregnant women were higher than those of the control group as shown in Table II and Figs. 5-7, and the mean level of serum HDL in pregnant women in first and second trimester is nonsignificantly decreased as compared to the control group, and the level of HDL showed significantly decreased in the third trimester as compared to the control group, as shown in Table II and Fig. 8. The placenta produces lipid peroxides which are secreted mainly on the maternal side of the placenta and remain in the maternal circulation for some time and increased lipid peroxidation markers are observed during normal pregnancy (Erişir, et al., 2009).

Elevation in TG, TC, and LDL may be due to an increase in hepatic lipase activity and a decrease in lipoprotein lipase activity. Hepatic lipase is responsible for the increased synthesis of TG at the hepatic level, whereas the decreased activity of lipoprotein lipase is responsible for the decreased catabolism at the adipose tissue. The second step of uptake of the chylomicron remnants by the liver is delayed so it leads to accumulation of TGs in plasma (Aziz and Mahboob, 2007). Hormonal variations during pregnancy affect lipid metabolism. The endogenous female sex hormones have a significant effect on serum lipids (Brizzi, et al., 1999). Increased TG plays a part to decrease HDL cholesterol. HDL particles transport cholesterol from peripheral tissues to liver. Impaired transport of cholesterol from peripheral tissues to the target area of utilization may cause the decrease in HDL cholesterol in serum. Hypertriglyceridemia leads to low HDL cholesterol; this may be due mainly to the actions of cholesteryl ester transfer protein (Pirzado, et al., 1999). Hormonal changes during pregnancy, for example, hyperestrogenemia are well documented and contribute to hyperlipidemia (Festus, et al., 2011). Decline in HDL is associated with elevated TC and LDL levels (Welty, 2013). Cholesterol level also increases in pregnancy due to elevated steroid hormone synthesis (Parchwani and Patel, 2011). Therefore, in pregnancy serum TC and LDL cholesterol are elevated. The mean level of serum alanine aminotransferase (ALT) activity was continuously increased during pregnancy (Table II and Fig. 9). It is significantly higher in pregnant women than that of control group ($P < 0.05$). The mean level of serum aspartate aminotransferase (AST) is also increased continuously but not significantly (Table II and Fig. 10). It has been reported that elevation of ALT and AST is associated with pregnancy in different cases such as intrahepatic cholestasis of pregnancy, hyperemesis gravidarum, eclampsia, hepatic infarction, acute fatty liver of pregnancy, and acute viral hepatitis (Westbrook, et al., 2016). An increase in ALT and AST levels was also found during labor, which might be caused by contractions of uterine muscle (Loganathan, et al., 2005). The mean level of serum alkaline phosphatase (ALP) activity was increased continuously during pregnancy (Table II and Fig. 11). It is significantly higher in pregnant women compared to the control group. Total ALP activity in serum almost doubles during normal pregnancy, but much of the increase is attributable to heat-stable placental ALP isoenzymes (Cunningham, 2005).

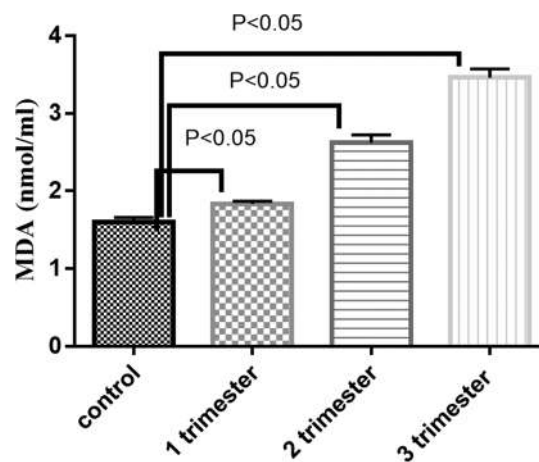


Fig. 1. Malondialdehyde level in pregnant and control group.

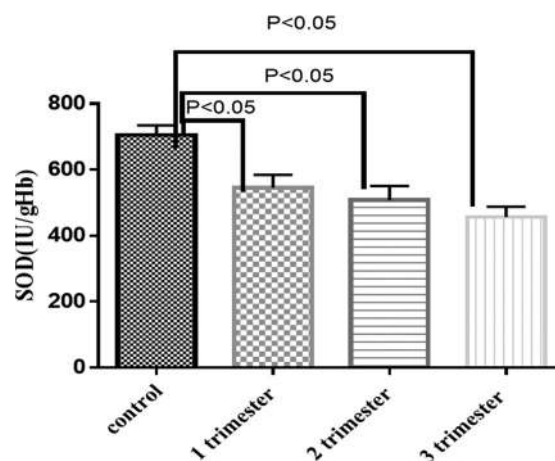


Fig. 2. Superoxide dismutase activity in pregnant and control group.

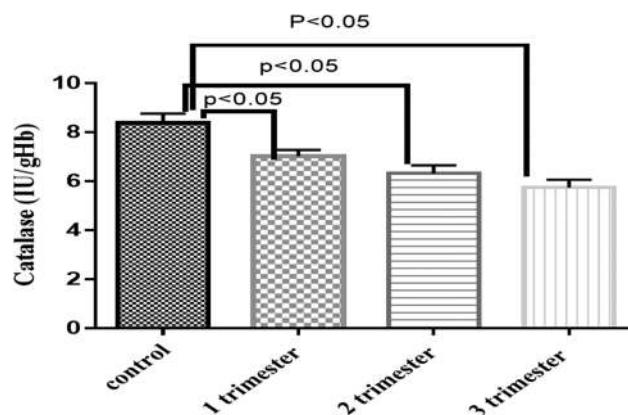


Fig. 3. Catalase activity in pregnant and control group.

Due to the lack of specificity, the measurement of serum ALP activity is a poor test for the diagnosis of cholestasis during the third trimester of pregnancy. There is no significant change in serum total protein concentration. However, serum albumin level was significantly lower in all three trimesters compared to nonpregnant women. These results are in agreement with previous works as in Table II and Figs. 12 and 13 (Festus, et al., 2011). Furthermore, these data show

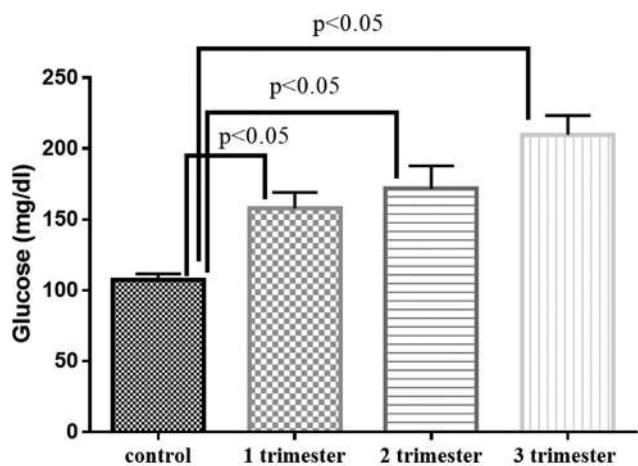


Fig. 4. Glucose level in pregnant and control group.

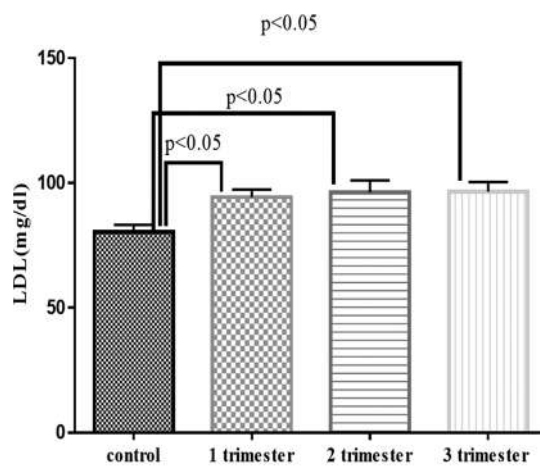


Fig. 7. Low-density lipoprotein level in pregnant and control group.

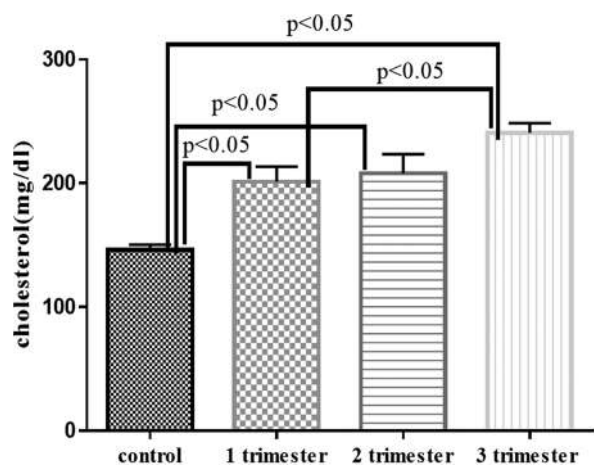


Fig. 5. Cholesterol level in pregnant and control group.

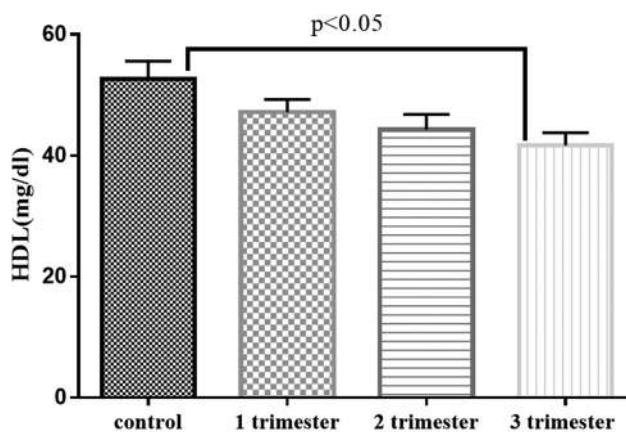


Fig. 8. High-density lipoprotein level in pregnant and control group.

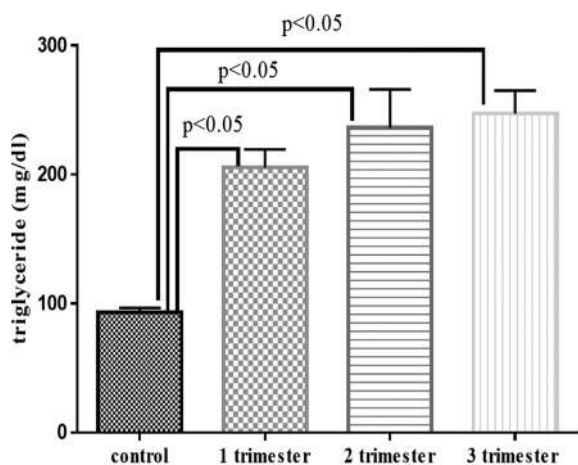


Fig. 6. Triglyceride level in pregnant and control group.

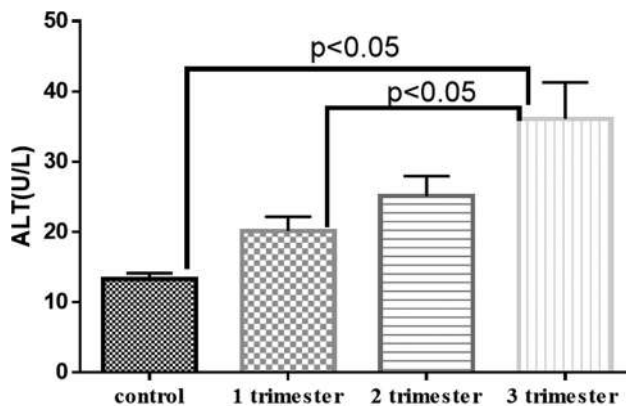


Fig. 9. Alanine aminotransferase level in pregnant and control group.

that the mean levels of total bilirubin and direct bilirubin are significantly elevated in pregnant women compared to the control group (Table II and Figs. 14 and 15). They are also increased continuously during all three trimesters.

Our data are in agreement with those of Duraiswamy, et al., 2016, who reported that the level of bilirubin had increased during pregnancy in the past century; it has been reported that elevation of bilirubin in pregnant women was associated with acute viral hepatitis (Hay, 2008). Duraiswamy, et al., 2016, showed that hyperbilirubinemia is observed in

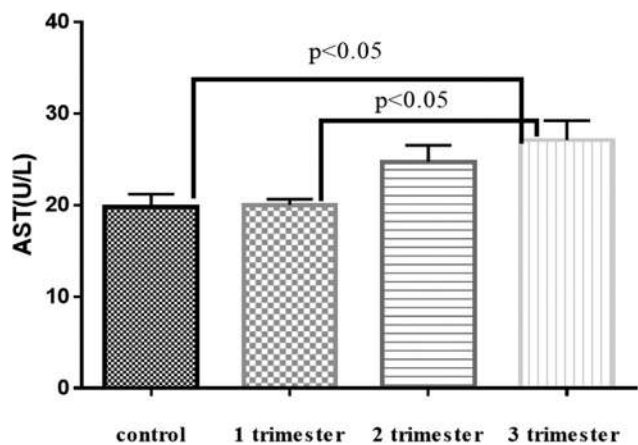


Fig. 10: Aspartate aminotransferase level in pregnant and control group.

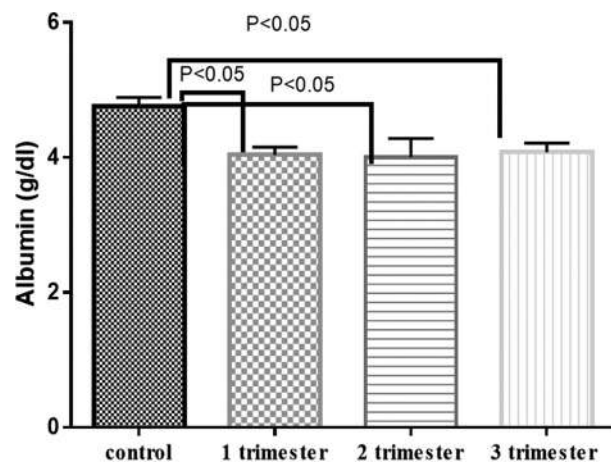


Fig. 13: Albumin level in pregnant and control group.

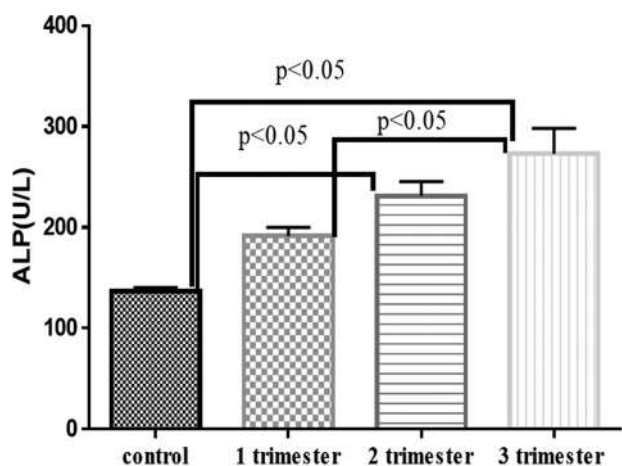


Fig. 11: Alkaline phosphatase level in pregnant and control group.

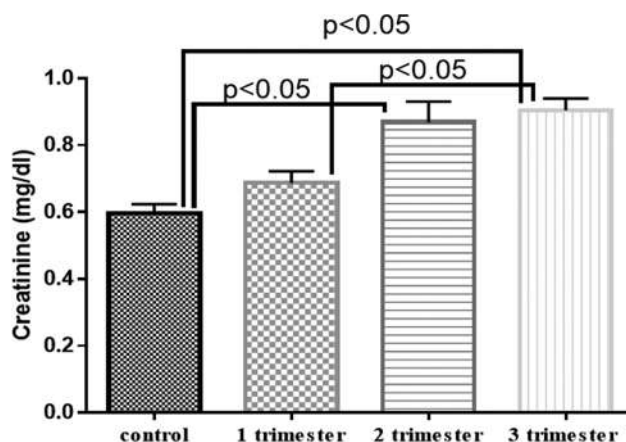


Fig. 14: Creatinine level in pregnant and control group.

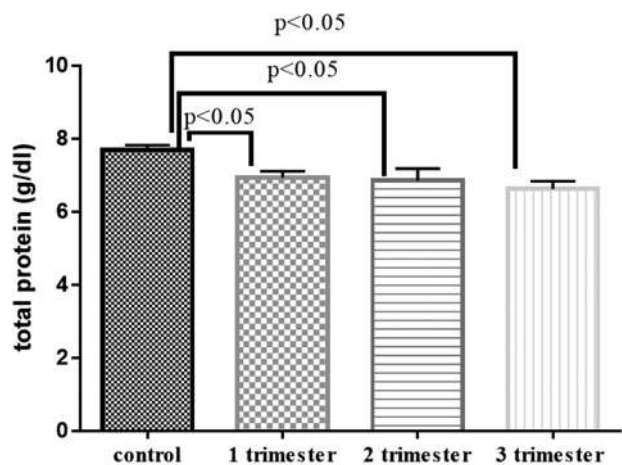


Fig. 12: Total protein level in pregnant and control group.

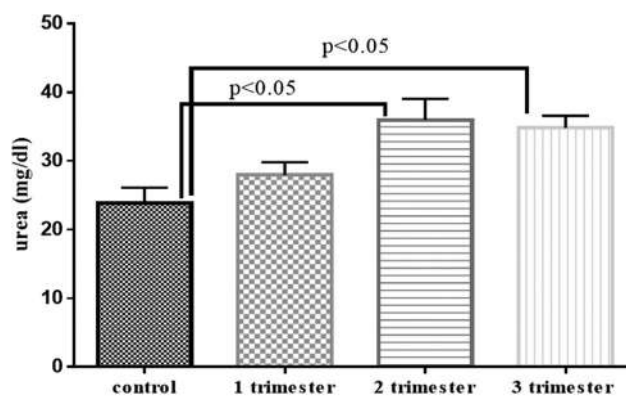


Fig. 15: Urea level in pregnant and control group.

pregnant women who were suffering mostly from gallstone-related disease, pre-eclampsia/eclampsia, and hyperemesis gravidarum.

This study shows that the mean levels of serum creatinine and urea are significantly increased in pregnant women as compared to the control group, whereas the mean level of

uric acid shows nonsignificant increases in pregnant women as compared to the control group (Table II and Figs. 16-18). These data revealed that protein catabolism and high need for energy by pregnant women during the late trimester may affect the catabolism of protein in the body resulting to an increase in urea and creatinine levels.

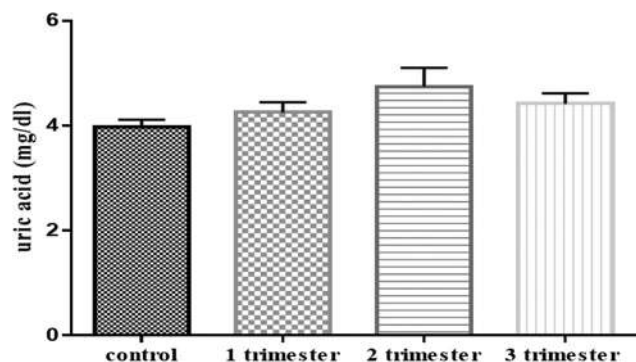


Fig. 16. Uric acid level in pregnant and control group.

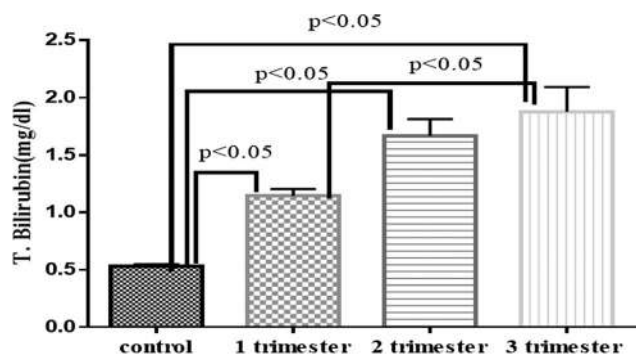


Fig. 17. T. bilirubin level in pregnant and control group.

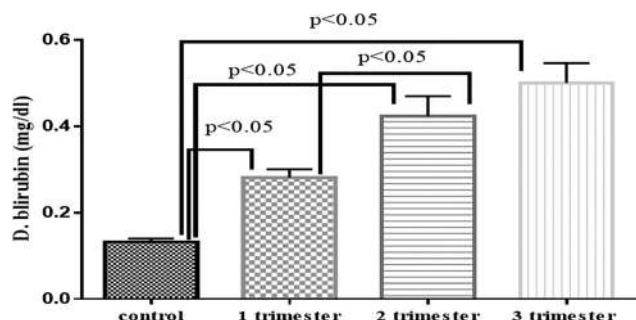


Fig. 18. D. bilirubin level in pregnant and control group.

IV. CONCLUSIONS

As shown in this study, antioxidant enzymes activity (SOD and CAT) decrease and MDA level raised in pregnant women when compared to the control group. Glucose production is increased from the onset of pregnancy to the last trimester as compared to the control group. The results demonstrated that normal pregnancy is associated with raised TG, cholesterol, and LDL, as compared to the control group and a significant decrease in HDL in normal pregnant women as compared to the control group. Elevated levels of serum bilirubin (D. bilirubin and T. bilirubin) and hepatic enzymes ALT, AST, and ALP were seen in pregnant women cases. The results showed a significant increase in serum creatinine and urea and a nonsignificant increase in uric acid level in pregnant women as compared to the control group.

V. ACKNOWLEDGMENTS

The authors would like to thank the Maternity Teaching Hospital in Erbil Governorate for providing the equipment to accomplish this work and also thank all those pregnant women that participate in this work.

REFERENCES

- Ali, D.M. 2015. Effect normal pregnancy and duration on liver enzymes tests. *Global Journal of Medical Research*, 15(1), pp.8-12.
- Aziz, R., and Mahboob, T. 2007. Pre-eclampsia and lipid profile. *Pakistan Journal of Medical Sciences*, 23(5), pp.751.
- Brizzi, P., Tonolo, G., Esposito, F., Puddu, L., Dessole, S., Maioli, M., and Milia, S. 1999. Lipoprotein metabolism during normal pregnancy. *American Journal of Obstetrics and Gynecology*, 181(2), pp.430-434.
- Chaudhary, L., Tandon, O.P., Vaney, N., and Agarwal, N. Lipid peroxidation and antioxidant enzymes in gestational diabetics. *Indian Journal of Physiology and Pharmacology*, 47(4), pp.441-446.
- Cunningham, F.G. 2005. Maternal physiology. *Williams Obstetrics*, 2005, pp.121-150.
- Duraiswamy, S., Sheffield, J.S., McIntire, D., Leveno, K., and Mayo, M.J. 2017. Updated etiology and significance of elevated bilirubin during pregnancy: changes parallel shift in demographics and vaccination status. *Digestive Diseases and Sciences*, 62(2), pp.517-525.
- Erişir, M., Benzer, F., and Kandemir, F.M. 2009. Changes in the rate of lipid peroxidation in plasma and selected blood antioxidants before and during pregnancy in ewes. *Acta Veterinaria Brno*, 78(2), pp.237-242.
- Festus, O.O., Idonije, O.B., Esegibe, M.A., Okhiai, O., Unuabonah, F., and Dike, M. 2011. Comparative study of lipid profile of normal pregnant women in the different trimesters. *Archives of Applied Science Research*, 3(3), pp.528-532.
- Gohel, M.G., Joshi, A.G., Anand, J.S., Makadia, J.S., and Kamariya, C.P. 2016. Evaluation of changes in liver function test in first, second and third trimester of normal pregnancy. *International Journal of Reproduction, Contraception, Obstetrics and Gynecology*, 2(4), pp.616-20.
- González, I.M., Armada, E.R., Díaz, J.R., García, P.D., García, M.M., González, A.G., Fernández, C.B., Iñiguez, A.R., and Rayo, I.L. 2000. Practice guidelines of the spanish society of cardiology for the management of cardiac disease in pregnancy. *Revista Espanola de Cardiologia*, 53(11), pp.1474-95.
- Hay, J.E. 2008. Liver disease in pregnancy. *Hepatology*, 47(3), pp.1067-1076.
- Herrera, E. 2002. Lipid metabolism in pregnancy and its consequences in the fetus and newborn. *Endocrine*, 19(1), 43-55.
- Kamili, A., Bengoumi, M., Oukessou, M., Faye, B., and Lefebvre, H.P. 2013. Assessment of glomerular filtration rate in normally hydrated and dehydrated dromedary camel by plasma exogenous creatinine clearance test. *Emirates Journal of Food and Agriculture*, 25(4), pp.314-319.
- Loganathan, G., George, R., Eapen, C.E., Mathai, M., Jasper, P., Seshadri, L., Shankar, V., Paul, S., Joseph, G., Balasubramanian, K.A., and Chandy, G.M. 2005. Liver function tests in normal pregnancy: A study from Southern India. *Indian Journal of Gastroenterology: Official Journal of the Indian Society of Gastroenterology*, 24(6), pp.268-269.
- Merabishvili, N.V., Kamladze, S.O., and Sulaberidze, G.T. 2006. Peculiarities of lipid metabolism during pregnancy. *Georgian Medical News*, 138, pp.86-89.
- Miao, L., and Clair, D.K. 2009. Regulation of superoxide dismutase genes: Implications in disease. *Free Radical Biology and Medicine*, 47(4), pp.344-56.
- Ogura, K., Miyatake, T., Fukui, O., Nakamura, T., Kameda, T., and Yoshino, G. 2002. Low-density lipoprotein particle diameter in normal pregnancy and preeclampsia. *Journal of Atherosclerosis and Thrombosis*, 9(1), pp.42-7.

- Parchwani, D., and Patel, D. 2011. Status of lipid profile in pregnancy. *National Journal of Medical Research*, 1(1), pp.10-12.
- Patel, S.S., Molnar, M.Z., Tayek, J.A., Ix, J.H., Noori, N., Benner, D., Heymsfield, S., Kopple, J.D., Kovesdy, C.P., and Kalantar-Zadeh, K. 2013. Serum creatinine as a marker of muscle mass in chronic kidney disease: Results of a cross-sectional study and review of literature. *Journal of Cachexia, Sarcopenia and Muscle*, 4(1), pp.19-29.
- Pirzado, Z.A., Sngi, S.A., and Malik, R. 1999. High density lipoprotein cholesterol (HDL) metabolism and its role in ischemic heart disease. *Pakistan Journal of Medical Research*, 38(1), pp.38-41.
- Saikumar, P., Jaya, D., and Devi, M.R. 2013. Oxidative stress in pregnancy. *ISOR Journal of Dental and Medical Sciences*, 3, pp.12-13.
- Welty, F.K. 2013. How do elevated triglycerides and low HDL-cholesterol affect inflammation and atherothrombosis? *Current Cardiology Reports*, 15(9), pp.400.
- Westbrook, R.H., Dusheiko, G., and Williamson, C. 2016. Pregnancy and liver disease. *Journal of Hepatology*, 64(4), pp.933-945.
- Woollett, L.A. 2011. Transport of maternal cholesterol to the fetal circulation. *Placenta*, 1(32), pp.218-221.

Industrial Assessment of the Carbonate Rocks of the Pila Spi Formation at Haibat Sultan Mountain, Iraqi Kurdistan Region

Varoujan K. Sissakian¹, Mohammed J. Hamawandy² and Rahel K. Ibrahim²

¹Department of Natural Resources Engineering and Management, University of Kurdistan Hewler, Erbil, Kurdistan Region - F.R. Iraq

²Department of Civil Engineering, Faculty of Engineering, Koya University, Koya KOY45, Kurdistan Region - F.R. Iraq

Abstract—The Pila Spi Formation is one of the prominent formations forming continuous ridges in Kurdistan Region. The thickness of the formation ranges from 15 to 110 m, consisting of well-bedded limestone, dolomite, dolomitic limestone, and very rare marl beds. The study area is located about 15 km east of Koya town, next to the abandoned tunnel through a deeply cut valley which has exposed 50 m of the formation. However, the uppermost part of the exposed section may belong to one of the Oligocene formations of Kirkuk Group. The study area was selected within the Pila Spi Formation because the rocks of the same formation and along the same ridge, about 45 km west of the study area showed encouraging results for cement industry. The average CaO is about 51%, whereas the average MgO is 1.8%. Therefore, eight samples were collected at constant thickness from the exposed section. The samples were subjected to X-ray fluorescence (XRF) test to indicate the main oxides in the sampled section. The acquired results from the XRF tests showed that the chemical composition of the exposed rocks within the Pila Spi Formation is suitable for cement industry, also for paper and paint but needs some treatment. Accordingly, another eight samples were collected from the same section to increase the density of sampling, totaling to 16 samples.

Index Terms—Cement and paper industries, Industrial assessment, Pila Spi Formation, Quarrying conditions.

I. INTRODUCTION

The Pila Spi Formation (Upper Eocene) forms a long continuous cliff in the Iraqi Kurdistan Region. The formation consists of carbonate rocks; limestone and dolomite (dolostone) with different proportions (Sissakian and Saeed, 2012). Due to extensive facies changes, the percentage of limestone to dolostone is not constant, and it is almost

impossible to indicate a constant ratio for large areas. Moreover, locally, the formation is overlain by one or more of Oligocene rocks of Kirkuk Group. It is worth mentioning that in the majority of the present geological maps, the Oligocene rocks are not presented in those maps. This is because majority of the areas where the Pila Spi Formation is exposed are mapped using aerial photographs in which it is not possible to distinguish the Pila Spi Formation from those of Oligocene age.

A. Aim

The aim of the current work is to conduct an industrial assessment of the carbonate rocks of the Pila Spi Formation at Haibat Sultan Mountain. The assessment was done by indicating the chemical composition of the rocks acquired from the X-ray fluorescence (XRF) test to calculate the weighted average of the oxides and accordingly compare them with the Iraqi and international standards for different industrial uses.

B. Location

The study area is located in Haibat Sultan Mountain located approximately 80 km northeast of Erbil city, between Koisanjak and Dokan towns along the main road (Fig. 1). The sampled section is marked by the following coordinates with an elevation of 923 m (a.s.l.): N 36° 02'41" E 44°45' 52" and N 36°02' 41" E 44°45' 050" with an elevation of 881 m (a.s.l.).

C. Previous Works

Limestone is used in Iraqi Kurdistan Region mainly for cement production. In Iraqi Kurdistan Region, six cement plants have been constructed. Five of them are located in Sulaymaniyah Governorate, whereas only one is located in Erbil Governorate; moreover, three cement plants have been licensed but not constructed yet. Therefore, building a cement plant in Erbil Governorate to cover the requirements of the construction industry is very significant and also in the Duhok Governorate where no any cement plant exists. To locate a cement plant, relevant reserves of limestone should



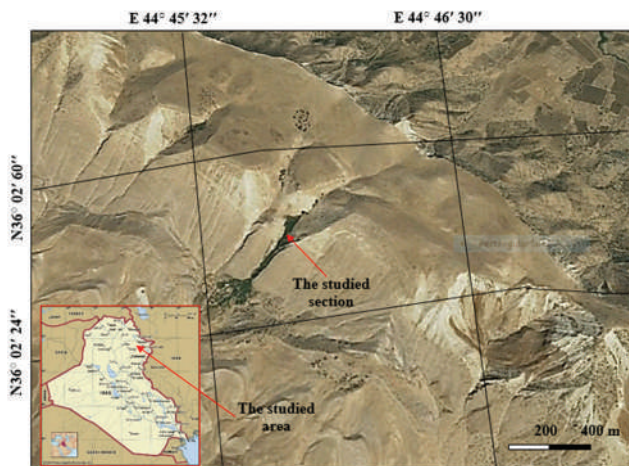


Fig. 1. Satellite image of the study area.

be available with other quarrying conditions besides the presence of clay which is the second main raw material in cement production.

The cement industry in Iraq was very significant subject; therefore, the Iraq Geological Survey (Baghdad) was conducting studies to evaluate the exposed limestone beds everywhere in Iraq since early seventies from the past century. Those studies which dealt with the evaluation of the exposed limestone beds in the Kurdistan Region are briefed hereinafter.

Jaber and Al-Ubaide (1973) evaluated the exposed limestone beds in Kani China area. Al-Rufaie (1976), Al-Rufaie and Muhamad (1976), Al-Murib (1980), and Hafidh et al. (2011) studied and evaluated the exposed limestone beds in the Anah Formation in Qara Chaugh Mountain. They all reported about excellent quality and quantity of limestone for cement industry. Mansour (1976) evaluated the exposed limestone beds in Kirkuk, Erbil, and Sulaymaniya Governorates and concluded about excellent qualities and quantities of limestone which are suitable for cement industry. Mansour (1977) evaluated the exposed limestone beds for the sake of Al-Tamim (Laylan) cement plant and concluded that the nearest exposed suitable rocks for cement industry are in Qara Chaugh and Bazian. Etabi and Ahmed (1979) studied and evaluated the exposed rocks in Tasluja vicinity for the use of Tasluja cement plant and concluded excellent quality and quantity of limestone beds for cement industry. Mansour and Petranek (1980) reported about the occurrences of limestone suitable for cement industry in the whole Iraqi territory. They concluded that the exposed rocks in Bazian and Qara Chaugh vicinities are the only suitable limestone beds for cement industry in the whole Kurdistan Region. Hafidh and Khlaif (2007) evaluated the reserve estimation in category C1 for the limestone of the Sinjar Formation in Bazian vicinity. Hafidh and Abdul Hassan (2008) evaluated the exposed limestone in C1 category in Sartak Bamu vicinity south of Derbendikhan on the behalf of Meran Company. Hafidh et al. (2008a) studied and evaluated the exposed limestone beds in Sartak Bamu and Kani Gal vicinities, south of Derbendikhan. Hafidh et al.

(2008b) studied and evaluated the exposed limestone beds in Agh Jallar vicinity on the behalf of Mawlawi Company and reported about excellent quality and quantity of limestone which is suitable for cement industry. Hafidh et al. (2008c) studied and evaluated the exposed limestone beds west of Sulaymaniyah on the behalf of Washa Company. This deposit was later on studied and Gasin cement plant was constructed. Sissakian et al. (2019) evaluated the carbonate rocks of the Pila Spi Formation in the southwestern limb of Permian anticline and reported about excellent quality and quantity of limestone.

II. GEOLOGICAL SETTING

The study area is located within the southwestern limb of Khalikan anticline, northeast of Erbil city, and east of Koya town along the main persistent ridge which forms the contact between the Low Folded Zone (in the south) and the High Folded Zone (in the north). The main geological aspects are briefly described emphasizing the significant features, which have a direct and/or indirect effect on the current study.

A. Geomorphology

The study area is located; physiographically within the High Mountainous Province (Sissakian and Fouad, 2012). The main geomorphological units are as follows:

- Structural geological units: Among them are the anticlinal ridges, which extend along the anticline. They are developed within the Pila Spi Formation.
- Structural-denudational units: Among them are the flatirons (Fig. 2), which are well developed within the Pila Spi Formation. Other units are the erosional scarps which are developed within the Pila Spi Formation.

B. Tectonic and Structural Geology

The study area is located along the contact between the Low Folded Zone (in the south) and the High Folded Zone (in the north). Both zones are located in the Outer Platform of the Arabian Plate. They also belong to the Zagros Thrust-Fold Belt (Fouad, 2012). The study area occurs within the southwestern limb of Khalikan anticline which is very broad fold giving to the southwestern limb of the anticline a monoclonal form.

C. Stratigraphy

The Pila Spi Formation is widely exposed in the study area. It forms a continuous cliff in the study area forming large flatirons (Figs. 1 and 2). The upper contact of the formation with the overlying Fatha Formation is unconformable. The lithological composition of the formation is almost constant throughout the study area and consists of carbonate rocks. The carbonate rocks are mainly limestone with a presence of dolomitic limestone and dolomite. The thickness of the formation is highly variable, in the study area, it is about 85 m (Sissakian and Fouad, 2014, and Sissakian and Al-Jibury, 2014). However,

in the study area, the Pila Spi Formation is most probably overlain by Oligocene rocks; one of the formations of the Kirkuk Group (Fig. 3).

III. MATERIALS AND METHODS

The following materials were used to perform the current study.

- Geological map at a scale of 1:250,000.
- Satellite images of high resolution.
- Relevant literature, including published papers, books, concerning the usage of the carbonate rocks in industry.
- Samples were collected from the outcrops of the Pila Spi Formation, along a deep cut valley within the main ridge of the formation (Fig. 3).

To perform industrial assessments for the carbonates of the Pila Spi Formation at Haibat Sultan Mountain, eight samples were collected in the first stage and other eight samples in the second stage totaling to 16 rock samples. Samples were prepared and subjected to XRF analyses. After receiving the acquired results from the XRF test, which was carried out in the laboratories of the University of Kurdistan Hewler, the weighted averages for each oxide at each sample were calculated and compared with different standards (Table I) to

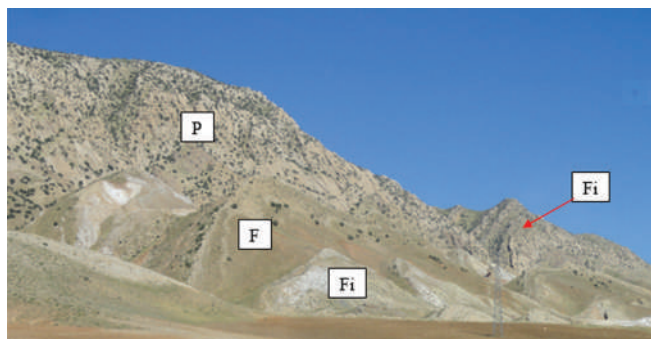


Fig. 2. Flatirons (Fi) within the Pila Spi (P) and Fatha (F) Formations. Note the continuous anticlinal ridge.



Fig. 3. The studied section. The uppermost part (the rusty colored limestone) most probably belongs to one of geological formations of the Kirkuk Group.

indicate the suitability of the studied carbonates for industrial uses.

A. Sample Collection

After selecting the study area at the Haibat Sultan Mountain (Fig. 1) along Koya-Dokan road, the exposed carbonate rocks were sampled in two stages, with different sampling intervals (Table II). The sampling interval was changed with the main change in lithological characters and/or bedding nature. Accordingly, 16 samples were collected starting from the bottom to the top (Fig. 3) of the Pila Spi Formation. The samples were described in the field; the hardness was indicated using geological hammer blows, other characters were described by naked eye.

B. Sample Preparation and Analysis

The collected samples were prepared for XRF test by the following steps:

- The samples were dried in an oven with temperature of 110°C for 1 h.
- The samples were crushed using an electrical samples crusher.
- The crushed samples were ground to powder using mill machine for 5 min.
- From each sample, 12 g were weighed, 0.5 g of steric acid and 0.2 g of methyl cellulose were added to homogenize the powdered sample which was pressed as a pellet.
- Finally, the samples were subjected to XRF test in the laboratories of the University of Kurdistan Hewler.

TABLE I
SPECIFICATIONS OF SOME USAGES OF CARBONATE ROCKS IN DIFFERENT INDUSTRIES (AFTER AL-BASSAM AND AL-KHAFJI, 2011)

Limestone		
Glass industry (%)	Cement industry (%)	Paints (%)
CaCO ₃ >98	MgO<2	CaCO ₃ >99.5
SiO ₂ <2.0	CaO>45	SiO ₂ <1.0
Fe ₂ O ₃ <0.06	SO ₃ <1	Al ₂ O ₃ <0.05
MgO<0.05	Cl 0.5–1.0	Fe ₂ O ₃ <0.05
L.O.I>43	K ₂ O+Na ₂ O 0.05	L.O.I> 43.5
	Fe ₂ O ₃ <0.1 (white cement)	
Steel (%)	Sugar industry (%)	Paper industry (%)
CaCO ₃ 92–95	SiO ₂ <0.66	CaCO ₃ >90
MgCO ₃ 1.3–1.9	Al ₂ O ₃ <0.27	SiO ₂ <1.5
Al ₂ O ₃ 1–2	Fe ₂ O ₃ <0.09	MgO<1.5
CaSO ₄ 0.5–0.8	MgO<4.0	SO ₃ <1
P 0.05–0.09	CaO>55	I.R (in HCL)<4.5
SiO ₂ 1.5–3.5		
Dolomite		
Magnesia (%)	Metallurgy (%)	
MgO>20	MgO 15–20.5	
	CaO 28–35	
	SiO ₂ 1.5–3.5	
	Al ₂ O ₃ 1–3	
	SO ₃ 0.5–1.5	
	Moisture 2–10	

TABLE II
FIELD DESCRIPTION OF THE COLLECTED SAMPLES FROM THE STUDY AREA

Sample no.	Color	Hardness	Thickness (m)		Reaction with HCl acid
			Sample interval	Individual bed	
1.	Grayish-white	Hard	1	0.3–0.5	Reactive
2.	Grayish-white	Hard	2	0.3–0.5	Reactive
3.	Grayish-white	Hard	2	0.3–0.5	Reactive
4.	Yellowish-white	Hard	1	0.2–0.4	Reactive
5.	Grayish-white	Hard	2	0.3–0.5	Highly reactive
6.	White	Hard	2	0.3–0.5	Highly reactive
7.	Grayish-white	Hard	2	0.3–0.5	Highly reactive
8.	Grayish-white	Hard	2	0.3–0.5	Highly reactive
9.	Grayish-white	Hard	2	0.3–0.5	Highly reactive
10.	Grayish-white	Hard	2	0.3–0.5	Highly reactive
11.	Light brown	Very hard	4	0.5–1.5	Highly reactive
12.	Light brown	Very hard	5	0.5–1.5	Highly reactive
13.	Light brown	Very hard	5	1.0–1.5	Highly reactive
14.	Light brown	Very hard	5	1.0–1.5	Highly reactive
15.	Light brown	Very hard	7	1.0–1.5	Highly reactive
16.	Light brown	Very hard	5	1.0–1.5	Highly reactive

TABLE III
CONCENTRATION OF OXIDES IN THE COLLECTED SAMPLES (INDICATED BY XRF TEST)

Sample no.	CaO (%)	MgO (%)	SiO ₂ (%)	Fe ₂ O ₃ (%)	Al ₂ O ₃ (%)	S (%)	L.O.I. (%)
1.	50.10	N.D.	3.03	0.18	N.D.	0.15	46.60
2.	50.23	N.D.	2.93	0.16	N.D.	0.12	46.55
3.	45.5	2.90	3.94	0.38	0.53	0.13	56.60
4.	51.11	1.55	3.60	0.15	N.D.	0.12	44.77
5.	46.50	2.00	2.46	0.13	N.D.	0.13	58.70
6.	50.20	1.01	3.61	0.12	N.D.	0.12	44.78
7.	45.8	2.90	3.30	0.15	N.D.	0.13	57.70
8.	46.22	1.83	3.12	0.11	0.24	0.11	48.30
9.	45.00	2.03	3.17	0.15	0.21	0.15	49.30
10.	51.25	N.D.	3.64	0.14	N.D.	0.15	44.80
11.	51.20	N.D.	2.64	0.16	N.D.	0.17	45.80
12.	51.73	N.D.	1.78	0.12	N.D.	0.13	46.17
13.	49.30	1.84	3.22	0.18	N.D.	0.14	46.30
14.	51.20	1.23	1.76	0.14	N.D.	0.15	48.20
15.	51.21	1.45	1.73	0.11	N.D.	0.13	47.20
16.	51.70	N.D.	1.80	0.13	N.D.	0.14	46.20

N.D.: Not detected

IV. RESULTS

The acquired results from running XRF test on the collected and prepared 16 samples are presented in Table III. The determined percentage of the main oxides which can be used in the industrial assessment of the studied carbonate rocks (Table I) was changed to the weighted averages for each oxide at each sample, the results are presented in Table IV. The weighted average is calculated according to the following equation:

$$\text{Weighted average} = \text{Concentration of each oxide (\%)} \times \text{thickness of each sample (m)}$$

$$\text{Total weighted average} = \frac{\text{Sum of all weighted averages (of each oxide)}}{\text{Total thickness of the samples (m)}}$$

The Na₂O, K₂O, and MnO were also analyzed but all of them were below the detection limits.

V. DISCUSSION

In Iraqi Kurdistan Region, the carbonate rocks are limestone and dolomite. The main use of the limestone beds is only in cement production although enormous amounts of limestone are widely exposed in the region (Sissakian and Saeed, 2012). However, it is very locally used as an aggregate but without any scientific studies as it is the case in the dolomite beds everywhere in the region.

The dolomite, however, is rarely used in its raw state, but it is considered as a useful source in making steel as a refractory lining material, as well as in manufacturing paper, leather, glass, and agricultural dolomite (McGregor, 1963). For glass production, a little amount of dolomitic lime is used to produce durable glass. Dolomite is also used to neutralize soil and high calcium limestone, particularly the one which is 84 parts magnesium carbonate and 100 parts calcium carbonate, having equal powers to neutralize soil (McGregor, 1963). Dolomite can be used as a basic refractory material, especially in the machine tools and steel making industry. Dolomite refractories intensively participate in the steel industry where it is used in open hearth, basic oxygen converters, and other steel refining systems (Moorkah and Abolarin, 2005). However, none of the mentioned industries exist in Iraqi Kurdistan Region although dolomite can be found in all parts of the region with huge thicknesses and amounts (Sissakian and Saeed, 2012).

A. Industrial Assessments

The acquired weighted averages of the analyzed oxides (Table III) were compared with some industrial standards to indicate the suitability of the collected samples which represent the rocks of the Pila Spi Formation east of Koya town (Table V). Accordingly, the acquired results from the XRF test match the specifications of the following industries:

- Cement industry: The weighted averages of the oxides in the collected rock samples match those required for the cement production (Table IV). It is worth to mention that there are



Fig. 4. Claystone beds, (a) (left) Gercus Formation, (b) (Right) Fatha Formation.

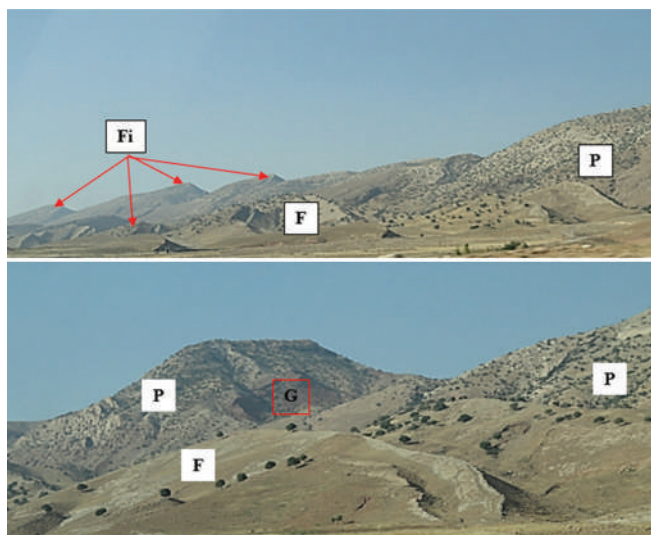


Fig. 5. The Pila Spi Formation (P) in the studied area. Note the absence of overburden, presence of thick claystone beds in the Gercus (G) and Fatha (F) Formations.

huge thicknesses of claystone (the second raw material in cement production) in the study area. These are present above the carbonates of the Pila Spi Formation within the Gercus Formation and below the carbonates present in the Fatha Formation (Fig. 4).

- Paper industry: The weighted averages of the oxides in the collected rock samples match (almost) those required for the paper industry. The infrared radiation (I.R.) concentration is not indicated, but the concentration of the SiO₂ is 2.52% (Table IV), then the I.R. % is <4.5%, which means that it matches the required specification.
- Paint industry: The weighted averages of the oxides in the collected rock samples match (almost) those required for the paint industry although the SiO₂ concentration is 2.52% which is slightly higher than the specified standard (1.0%) (Table IV). This slightly higher concentration will affect on the coarseness and corrosiveness of the paint. However, outdoor paints need such character; accordingly, the exposed rocks can be used for paint industry.
- Sugar and glass industries: The weighted averages of the oxides in the collected rock samples do not match the required specifications (Table IV). However, for each industry, a special treatment may solve the non-matching of the required specifications. For example, in glass industry, adding a pure limestone with high CaO content will solve the problem of non-matching the required specifications. For sugar industry, again adding a pure limestone with high CaO content will solve the problem of non-matching the required specifications. However, the higher Fe₂O₃ will give brownish color for the produced sugar; however, the high SiO₂ will remain an obstacle for sugar productions. The high SiO₂ in the analyzed samples is a problem for all possible industries (Table IV). To get rid of the high SiO₂, special treatment should be performed which is not easy and cause a lot of problems due to its high corrosiveness character.

TABLE IV
CONCENTRATIONS AND WEIGHTED AVERAGES OF THE MAIN OXIDES IN THE EIGHT ANALYZED SAMPLES

Sample no.	Thick. (m)	CaO (%)		MgO (%)		SiO ₂ (%)		Fe ₂ O ₃ (%)		Al ₂ O ₃ (%)		S (%)		L.O.I. (%)	
		Con.	W.A.	Con.	W.A.	Con.	W.A.	Con.	W.A.	Con.	W.A.	Con.	W.A.	Con.	W.A.
1.	2	50.10	100.20	N.D.	N.D.	3.03	6.06	0.18	0.36	N.D.	N.D.	0.15	0.30	46.60	93.20
2.	2	50.23	100.46	N.D.	N.D.	2.93	5.86	0.16	0.32	N.D.	N.D.	0.12	0.24	46.55	93.10
3.	2	45.5	91.00	2.90	5.80	3.94	7.88	0.38	0.76	0.53	1.06	0.13	0.26	56.60	113.20
4.	1	51.11	51.11	1.55	1.55	3.60	3.60	0.15	0.15	N.D.	N.D.	0.12	0.12	44.77	44.77
5.	2	46.50	93.00	2.00	4.00	2.46	4.92	0.13	0.26	N.D.	N.D.	0.13	0.26	48.70	97.40
6.	2	50.20	100.40	1.01	2.02	3.61	7.22	0.12	0.24	N.D.	N.D.	0.12	0.24	44.78	89.56
7.	2	45.8	91.60	2.90	5.80	3.30	6.60	0.15	0.30	N.D.	N.D.	0.13	0.26	47.70	95.40
8.	2	46.22	92.44	1.83	3.66	3.12	6.24	0.11	0.22	0.24	0.48	0.11	0.22	48.30	96.60
9.	2	45.00	90.00	2.03	4.06	3.17	6.34	0.15	0.30	0.21	0.42	0.15	0.30	49.30	98.60
10.	2	51.25	102.50	N.D.	N.D.	3.64	7.28	0.14	0.28	N.D.	N.D.	0.15	0.30	44.80	89.60
11.	4	51.20	204.80	N.D.	N.D.	2.64	10.56	0.16	0.70	N.D.	N.D.	0.17	0.56	45.80	224.00
12.	5	51.73	258.65	N.D.	N.D.	1.78	7.40	0.12	0.60	N.D.	N.D.	0.13	0.65	46.17	230.85
13.	5	49.30	246.50	1.84	9.20	3.22	16.10	0.18	0.90	N.D.	N.D.	0.14	0.70	46.30	231.50
14.	5	51.20	256.00	1.23	6.15	1.76	8.80	0.14	0.70	N.D.	N.D.	0.15	0.75	48.20	241.00
15.	7	51.21	358.47	1.45	10.15	1.73	12.11	0.11	0.77	N.D.	N.D.	0.13	0.91	47.20	330.40
16.	5	51.70	258.50	N.D.	N.D.	1.80	9.00	0.13	0.65	N.D.	N.D.	0.14	0.70	46.20	231.00
Total	50		2495.63		52.39		125.97		7.51		1.96		6.77		2406.18
Average			49.91		1.05		2.52		0.15		0.04		0.14		48.12

N.D.: Not detected

TABLE V
SPECIFICATIONS OF SOME INDUSTRIES AS COMPARED WITH THE RESULTS OF THE CURRENT STUDY

Specifications of industries (%)													
Cement industry		Current study	Paint industry	Current study	Steel industry	Current study	Sugar industry	Current study					
CaO	>45.00	49.91	CaCO ₃	>99.5	96.53	CaCO ₃	92-95	98.03	MgO	<4.00	1.05		
MgO	<2.00	1.05	SiO ₂	<1.00	2.52	MgO	1.3-1.9	1.05	CaO	>55.0	49.91		
Fe ₂ O ₃	<0.10	0.15	Al ₂ O ₃	<0.05	0.05	Al ₂ O ₃	1-2	0.04	Al ₂ O ₃	<0.27	0.04		
SO ₃	<1.00		Fe ₂ O ₃	<0.05	0.15	CaSO ₄	0.5-0.8		Fe ₂ O ₃	<0.09	0.15		
Cl	0.50-1.00		L.O.I.	>43.0	47.18	SiO ₂	1.5-3.5	2.52	SiO ₂	<0.66	2.52		
L.O.I.	>43.00	52.75	CaCO ₃ =CaO+L.O.I. MgCO ₃ =MgO L.O.I.			P ₂ O ₅	0.05-0.09						
Glass industry		Current study	Metallurgy	Current study	Magnesia	Current study	Paper industry	Current study					
CaCO ₃	>98.00	98.03	CaCO ₃	92-95	98.03	MgO	>20	1.05	CaCO ₃	>90	98.03		
SiO ₂	<2.00	2.52	MgO	1.3-1.9	1.05				MgO	<1.5	1.05		
MgO	<0.05	1.05	Al ₂ O ₃	1-3	0.04				SiO ₂	<1.5	2.52		
Fe ₂ O ₃	<0.06	0.15	SiO ₂	1.5-3.5	2.52				SO ₃	<1.0			
L.O.I.	>43.00	48.12	SO ₃	<1					I.R.	4.5			

Legend: ■ Out of the standard, ■ Fit with the standards, ■ Not analyzed or detected, ■ Near to the standard, ■ Suitable, ■ Suitable with treatment, ■ Not suitable, ■ Fairly suitable, IR:Infrared radiation

- Metallurgy and magnesia production: The weighted averages of the oxides in the collected rock samples (Table IV) are very far from the requested specifications. Therefore, the studied rock succession of the Pila Spi Formation cannot be used in metallurgy and magnesia production.

B. Quarrying Conditions

During choosing the studied section, the quarrying conditions (Fig. 5) were considered including dip amount, quarrying faces, transportability, thickness, overburden, inner burden, and availability of other raw materials, especially for cement production. Although the dip amount is about 30°, still considerable thickness can be utilized by quarrying without a need for below surface level quarrying. The large flatirons (Figs. 1,2 and 5) give excellent quarrying faces from three directions. The main Erbil-Sulaymaniyah road passes 2 km south of the studied section. Moreover, the planned (permanently abandoned) tunnel is few hundred meters west of the studied section. The sampled thickness is 50 m; however, the total thickness may reach 65 m. Almost no overburden exists on the limestone beds of the Pila Spi Formation. However, downslope the Fatha Formation is exposed which consists of an alternation of claystone, limestone, and gypsum. All three main components are required in cement production as raw material and/or additive. All the sampled beds showed suitable and almost uniform results in their chemical composition (Table II) which means that there is no inner burden. The well-bedded nature of the limestone beds of the Pila Spi Formation facilitates the quarrying of the rocks by least amount of explosives.

VI. CONCLUSIONS

The exposed rocks in the Pila Spi Formation along the southwestern limb of Khalikan anticline east of Koya town

and along Haibat Sultan Mountain can be used for cement industry. The presence of huge amounts of claystone in both Gercus and Fatha Formations (underlying and overlying the Pila Spi Formation, respectively) encourages construction of a cement plant. All quarrying conditions are suitable besides the presence of huge reserves. Moreover, the limestone beds can be used for paper and paint industries with slight treatments. They can also be used for glass and sugar industries, but a lot of special treatments are needed. However, the studied carbonates cannot be used in magnesia production and other metallurgical uses.

VII. ACKNOWLEDGMENT

The authors would like to express their sincere thanks to the authorities in both University of Kurdistan Hewler and University of Koya for their support to the authors during the performance of the research work which led to the current article. The efforts of Mr. Hassan Omer (University of Kurdistan Hewler) for running the XRF analyses and supplying the chemical composition of the collected rock samples are highly appreciated by the authors. The authors extend their thanks to the esteemed reviewers for their fruitful comments.

REFERENCES

Al-Bassam, K. and Al-Khafaj, A.A., 2011. *Work Procedures of Iraq Geological Survey, Part 13: Mineral Exploration*. Iraq Geological Survey Library Report, No. 2133.

Al-Murib, S., 1980. *Report on Prospecting Works on Limestone for Cement Industry in Southern Qara Chouq Mountain*. Iraq Geological Survey Library Report, No. 1057.

Al-Rufaie, A. and Muhamad, S., 1976. *Report on the Geological Prospecting of Limestone Deposit Suitable for Cement Purpose at Qara Chouq Mountain, Khoshao Locality, Arbil*. Iraq Geological Survey Library Report, No. 1786.

- Al-Rufaie, I., 1976. *Investigation of Limestone Suitable for Cement Industry in Qara Chauq Mountain, Khoshao Area*. Iraq Geological Survey Library Report, No. 1379.
- Etabi, W. and Ahmed, S., 1979. *Final Report on Prospecting Exploration of Tashuja Limestone Deposit Suitable for Portland Cement*. Iraq Geological Survey Library Report, No. 961.
- Fouad, S.F., 2012. *Tectonic Map of Iraq, Scale 1: 1000000*. 3rd ed. Iraq Geological Survey Publications, Baghdad, Iraq.
- Hafidh, S.Q. and Hassan, A.A., 2008. *Exploration of Limestone Suitable for Cement Industry in Categories C1 and B at Sartak South of Derbendikhan*. Iraq Geological Survey Library Report, No. 3125.
- Hafidh, S.Q. and Khlaif, H.O., 2007. *Mineral Exploration and Reserve Estimation in Category C1 of the Carbonate Rocks Suitable for Cement Manufacturing at Tashuja, Sulaimaniyah on the Behalf of Sarchinar Cement Plant*. Iraq Geological Survey Library Report No. 3038.
- Hafidh, S.Q. Ruhman, A., Al-Abaas, F.A., Rasheed, A.Y. and Qanbar, A.S., 2008a. *Preliminary Geological Studies of Limestone Suitable for Cement Industry in Sartak and Kani Kel Vicinity Southeast of Darbandi Khan Southeast of Sulaimaniyah Governorate*. Iraq Geological Survey Library Report, No. 3125.
- Hafidh, S.Q., Al-Jiburi, B.S. and Basheer, W.P., 2011. *Detailed Geological Survey at Scale of 1:5000 in Southern Qara Chauq Mountain, Block/A, for Investigation of Limestone Suitable for Cement Industry in Behalf of Kar Company*. Iraq Geological Survey Library Report, No. 3400.
- Hafidh, S.Q., Salih, H.A. and Abbas, A.K.A., 2008c. *Preliminary Geological Studies on Limestone Suitable for Cement Industry, West of Suliamaniyah on the Behalf of Washa Co*. Iraq Geological Survey Library Report, No. 3127.
- Hafidh, S.Q., Salih, H.A. and Mahmoud, A.A., 2008b. *Preliminary Studies on Limestone Suitable for Cement Industry. Agh Jallar Vicinity on the Behalf of Mawlawi Co*. Iraq Geological Survey Library Report, No. 3128.
- Jaber, F.S. and Al-Ubaidi, H., 1973. *Kani China Recrystalline Limestone*. Iraq Geological Survey Library Report, No. 524.
- Mansour, J. and Petranek, J., 1980. *Major Occurrences and Deposits of Limestone in Iraq*. Iraq Geological Survey Library Report, No. 1073.
- Mansour, J., 1976. *Reconnaissance of the Kirkuk, Erbil, Sulaimaniyah Area on Search for Raw Materials in Connection with Proposed Cement Works*. Iraq Geological Survey Library Report, No. 768.
- Mansour, J., 1977. *Preliminary Examination of the Raw Materials for Al-Tamim Cement Project*. Iraq Geological Survey Library Report No. 840.
- McGregor, D., 1963. *High-Calcium Limestone and Dolomite in Indiana*. 27th ed. Indiana Department of Conservation, State of Indiana, p.1-12.
- Moorkah, H. and Abolarin, M., 2005. Investigation of the properties of locally available dolomite for refractory applications. *Nigerian Journal of Technology*, 24(1), p.79-81.
- Sissakian, V.K. and Al-Jiburi, B.M., 2014. *Stratigraphy of the High Folded Zone. Iraqi Bulletin of Geology and Mining*, 6, p.73-16.
- Sissakian, V.K. and Fouad, S.F., 2012. *Geological Map of Iraq, Scale 1: 1000000*. 4th ed. Iraq Geological Survey Publications, Baghdad, Iraq.
- Sissakian, V.K. and Fouad, S.F., 2014. *Geological Map of Erbil and Mahabad Quadrangles, Scale 1: 250000*. 2nd ed. Iraq Geological Survey Publications, Baghdad, Iraq.
- Sissakian, V.K. and Saeed, Z.B., 2012. Lithological map of Iraq compiled using GIS Techniques. *Iraqi Bulletin of Geology and Mining*, 8(3), p.1-13.
- Sissakian, V.K., Hamoudi, D.A., Omer, H.O. and Niazi, S.A., 2019. Assessment of the carbonate rocks of the Pila Spi formation for cement industry, in Permian mountain, Erbil, Iraqi Kurdistan Region. *UKH Journal of Science and Engineering*, 3(1), pp.1-9.

Potato Peels and Mixed Grasses as Raw Materials for Biofuel Production

Shaaban Z. Omar¹, Ayad H. Hasan¹ and Ivo Lalov²

¹Department of Medical Microbiology, Faculty of Science and Health, Koya University, Daniel Mitterrand Boulevard, Koya KOY45, Kurdistan Region - F.R. Iraq

²Department of Biotechnology, Faculty of Chemical System Engineering, University of Chemical Technology and Metallurgy, 8 Kliment Ohridski Blvd, 1756, Sofia, Bulgaria

Abstract—Biogas and fuel ethanol are renewable energy sources, can be produced from complex organic materials that are decomposed by microorganisms in the anaerobic digestion method. Potato peels (PPs) and mixed *Lolium perenne* and *Dactylis glomerata* grasses were assessed as a potential substrate for biomethanation in a batch method under mesophilic condition (35°C) and ethanol fermentation. The first approach of this work was focused on pre-treatment of PPs using acidic and enzymatic hydrolysis to produce biogas and ethanol fermentation using *Saccharomyces cerevisiae* and *Safbrew S-33*. These experiments proved that enzymatic hydrolysis produced 1.2 g/L of ethanol involved 115 h of fermentation and 665 ml/h of biogas after 451 h of biomethanation, this was more than the outcomes of acidic treatment. The second approach was concentrated on ability of biogas and ethanol production from mixed grasses treated with different acid concentrations that produced 0.16 g/L ethanol over 8 days of fermentation and 500 ml/h of biogas after 13 days of methanation technique. In general, the results pointed out that PPs and combined grasses can be used as potential substrates with raw materials for biogas and ethanol production.

Index Terms—Acid hydrolysis, Biogas, Biomethanation, Enzymatic hydrolysis.

I. INTRODUCTION

Biogases present alternative renewable energy and also decrease the dependence on fossil fuel sources (Aziz, et al., 2019). The conversion of complicated organic compounds to biogas is possible due to the cooperated role of many groups of microorganisms inducing hydrolysis, acidogenesis, acetogenesis, and methanogenesis steps (Mulat, et al., 2018). Bioethanol production from lignocellulosic biomass comprises different steps of pretreatment, hydrolysis, fermentation, and ethanol recovery (Tran, et al., 2019). Pre-treatment is a significant step to modify some structural

components of biomass that inducing glucan and xylan accessibility for additional hydrolysis processes (Thangavelu, et al., 2016). Lignocellulosic biomass is the most plentiful feedstock with seasonal availability of over 220 billion dry metric ton. Such feedstocks can be cultivated in different environments and utilized to produce renewable energy with the great potential to sequester greenhouse gases, mainly CO₂ from the atmosphere (Phuttaro, et al., 2019). One source of lignocellulosic is grasses despite its rigid structure can be counted as a potential feedstock for biogas generation, due to its low water content and served as counter to other crops, and the fact that it can be grown in non-arable areas (Rodriguez, et al., 2017; Wagner, et al., 2018). Therefore, various methods based on the biodegradation and solubilization of lignin and hemicellulose have been developed to support efficient hydrolysis and promote optimal biogas production from grasses (Li, et al., 2012). On the other hand, waste of potato industry could be an economical carbon source for ethanol fermentation industry, this is due to their high contents of starch, cellulose, hemicellulose, lignin, and fermentable sugars to guarantee use as an ethanol feedstock (Izmirliloglu and Demirci, 2012). Potato peels (PPs) can be degraded by subsequential enzymatic hydrolysis and fermentation utilizing *Saccharomyces cerevisiae* to produce ethanol (Liang and McDonald, 2014).

This work aims to investigate renewable biogas and ethanol sources through the biological route of biomethanation process and ethanol fermentation using various biomass wastes (PPs and mixed grass), to analyze and determine the chemical composition of PPs and fresh mixed *Lolium perenne* and *Dactylis glomerata* grasses, and to investigate different strategies of chosen biomass substrate pre-treatment.

II. MATERIALS AND METHODS

A. Activated Sludge (*Methanogenic Consortium*)

The activated sludge used as a standard inoculum in our experiments was supplied from methanogenic reactor for the treatment of water from bioethanol production at the ALMAGEST AD, 2063 Verinsko village Ichtiman municipality, Bulgaria.

ARO-The Scientific Journal of Koya University
Vol. VIII, No.1 (2020), Article ID: ARO.10568, 7 pages
DOI: 10.14500/aro.10568

Received 02 October 2019; Accepted 18 February 2020
Regular research paper: Published 15 March 2020

Corresponding author's e-mail: ayad.hasan@koyauniversity.org

Copyright © 2020 Shaaban Z. Omar, Ayad H. Hasan and Ivo Lalov. This is an open access article distributed under the Creative Commons Attribution License.



B. Substrate Preparation

PPs

Potatoes were obtained from local market and manually peeled. Then, peels were crushed in a blender, to this 120 ml of D.W was added for better homogenization. The liquefied substrate was stored at 4°C (Sanchez and Cardona, 2008).

Grasses

Fresh, perennial ryegrass (*L. perenne*) and cocksfoot (*D. glomerata*) were harvested in the beginning of June 2018 at Studentski grad park, near UCTM University campus in Sofia, fresh grass was first cut to small pieces, then 10 g was weighed to evaluate the dry weight by oven drying at 105°C for 45 min to a constant weight (Sanchez and Cardona, 2008).

Microelements (S3 and S4)

S3: 19.62 mg of $(\text{NH}_4)_2\text{HPO}_4$ dissolved in 100 ml of D.W.

S4: To prepare 100 ml of S4, each of the following salts was dissolved in 100 ml of D.W. $\text{MnSO}_4 \cdot \text{H}_2\text{O}$ (4.29 mg), H_3BO_3 (1.34 mg), NH_4Cl (104.63 mg), $\text{CaCl}_2 \cdot 2\text{H}_2\text{O}$ (63.67 mg), ZnCl_2 (0.57 mg), $\text{CoCl}_2 \cdot 6\text{H}_2\text{O}$ (7.10 mg), KCl (344.14 mg), $\text{CuCl}_2 \cdot 2\text{H}_2\text{O}$ (0.63 mg), $\text{NaMo}_4 \cdot 2\text{H}_2\text{O}$ (0.69 mg), and $\text{MgCl}_2 \cdot 6\text{H}_2\text{O}$ (376.00 mg).

C. Pre-treatment of Substrates

Acid hydrolysis of PPs

Acid hydrolysis of PPs was conducted using two different sources of acidity, which were 0.5 M HCl and 1% H_3PO_4 . HCl hydrolysis was performed by digesting 40 g of PPs with 120 ml of 0.5 M HCl, the mixture was autoclaved (121°C and 1 atm for 15 min). In the case of H_3PO_4 hydrolysis, two various methods were carried out. The first pre-treatment was as follows: 30 g of PPs were digested with 120 ml of 1% H_3PO_4 . The resulted liquid was heated at 100°C in a water bath for 5 h. The second pre-treatment was directed by digesting 30 g of PPs with 120 ml of 1% H_3PO_4 and the mixture was autoclaved.

During sterilization, the carbohydrates from PPs were degraded into fermentable sugars due to the action of acid hydrolysis (0.5 M HCl and 1% H_3PO_4) at high temperature of 121°C and 1 atm for 15 min. After sterilization, the pH was adjusted to 7.0 with 5 M NaOH.

Enzymatic hydrolysis of PPs

Forty grams of PPs were ground with 59 ml of D.W by a homogenizer, and the mixture was heated in a water bath for 1 h at 90°C. The produced substance was treated with either α -amylase (Novozymes) or amyloglucosidase (Novozymes) and Sanferm in two steps, namely, dextrinization and saccharification.

- Dextrinization process: One milliliter of α -amylase (Novozymes) in a process called liquefaction at 90°C and pH 5.8 for 1 h. Samples were taken every 20 min and subjected to glucose analysis using the 3,5-dinitrosalicylic acid method (Miller, 1959).
- Saccharification process: Achieved by cooling down the mixture to 35–40°C, then hydrated with water to the original volume. One milliliter of amyloglucosidase

(Novozymes), 54 ml of D.W., and 1 ml of Sanferm yield enzyme (Novozymes) were added to the mixture and treated at 45°C and pH 4.7 for 2 h.

Acid hydrolysis of mixed grasses

Acid hydrolysis of combined grasses was conducted using 3.5% or 4% HCl and 1% H_2SO_4 . The HCl hydrolysis was achieved by mixing 50 g of fresh grass with 100 ml of D.W., then ground by a homogenizer, 50 ml of either 3.5% or 4% of HCl added, the mixture was autoclaved. H_2SO_4 hydrolysis was carried out by adding 0.5 ml of 1% H_2SO_4 to 50 ml of 3.5% HCl hydrolysate, then the mixture was autoclaved for 45 min at 121°C and 1 atm.

D. Ethanol Fermentation of Pretreated Substrates

Acid hydrolysate (0.5 M HCl) of PPs

Fermentation was carried out by mixing 40 mg of yeast (*Safbrew S-33*) with 2 ml of D.W. The mixture incubated at room temperature for 20–25 min in a 250 ml volume Erlenmeyer flask. Then, 50 ml of acid hydrolysate solution was added to the mixture. The flask was supplemented with tube contains 2 ml of sulfuric acid (H_2SO_4). Fermentation was continued for 5 days, every 24 h, the mass of the flask was measured to find the amount of ethanol g/L production.

Enzymatic hydrolysate of PPs

Hydrolysate solution of enzymatic hydrolysis of PPs was subjected to ethanol fermentation by *S. cerevisiae* in anaerobic condition at room temperature in a 250 ml Erlenmeyer flask. The inoculum was 60 mg of *S. cerevisiae*, 65 ml of enzyme hydrolysis solution, and 2 ml of H_2SO_4 . Fermentation was continued for 4 days, every 24 h, the mass of the flask was measured to find the quantity of ethanol g/L production.

Acid hydrolysate (4% HCl) of mixed grasses

Thirty-five milligrams of *S. cerevisiae* powder were added to 250 ml Erlenmeyer flask that contains 40 ml of 4% HCl hydrolysate combined grasses. The pH adjusted to 7; then, the flask was incubated at room temperature supplemented with 2 ml of H_2SO_4 Erlenmeyer flask tube, the fermentation was continued for 12 days (Arapoglou, et al., 2010).

E. Biomethanation of Pretreated Substrates

Acid hydrolysate of PPs

After the pre-treatment of PPs with 0.5 M HCl, hydrolysate solution was subjected to a batch process methanation at 35°C by adding 20 ml of it pH 7 to 500 ml test bottle that previously filled with 300 ml activated sludge.

Enzymatic hydrolysate of PPs

After the treatment of PPs solution (liquefaction stage) by α -amylase and (saccharification stage) by amyloglucosidase and Sanferm. Yield enzyme was subjected to biomethanation process at 35°C by adding 20 ml of the final product to a test bottle containing 5.4 ml S4, 1 ml S3, and 300 ml activated sludge.

Acid hydrolysate of mixed grasses

After the pre-treatment of mixed grass with 4% HCl, 20 ml of neutralized mixed-grass hydrolysate solution (pH 7) was mixed with 300 ml of activated sludge in a test bottle to

perform methanation in a batch process fermentation under mesophilic temperature 35°C.

Biogas analysis

In this analysis, biogas production rate measurements were performed using a liquid replacement system (Mahmoodi, et al., 2018). The biogas composition was analyzed using the absorptive method (Mahmoodi, et al., 2018). A scaled cylinder is filled with 0.5 M of HCl and is reversibly submerged in a container containing the same liquid. A tube connected to a syringe was inserted into the headspace of the test bottle (which contains the activated sludge plus sample), whereas the other end of the tube was placed in the cylinder. At the connection site between the test bottle and the tube, there is a pin, which will be opened when the tube is located at the right spots at both ends. Then, the produced biogas will flow to the cylinder and replace an equal amount of liquid. The volume of the produced gas (Volume 1 in mL) was determined by measuring the height space in the cylinder. To measure the methane concentration, 5 N NaOH were added to the container to increase the pH (above 9). At this underlying condition, CO₂ and H₂S gas are adsorbed, and the volume of the gas is decreased (Volume 2 in mL). Therefore, the measured volume represents CH₄ content in the biogas mixture. It must be remarked that the variations between the first and the second volume (V1–V2) display the CO₂ content of the biogas because H₂S concentration is entirely negligible in the adsorbed gas.

Analytical methods

The dry weight of PPs and fresh mixed grasses was determined by oven drying at 105°C for 45 min to a constant weight. Biochemical methane potential (BMP) was measured (Chynoweth, et al., 1993). The released reducing sugar was measured by a standard method called dinitrosalicylic (Miller, 1959). Quantitative elemental analysis of PPs and mixed grasses for carbon, nitrogen, and hydrogen was measured by the automated Elemental Analyzer EA 3000 Euro Vector in the Central Research Laboratory – UCTM. The chemical oxygen demand (COD) was determined according to the American Public Health Association, 1995. The protein content was defined (Lowry, et al., 1951).

III. RESULTS AND DISCUSSION

A. Characteristic of Substrates

PPs

PPs composition (Table I) contains 16.84% dry mass weight, 45.5% carbon, 3.16% nitrogen, 6.49% hydrogen, 0.84 mg/ml reducing sugar, and 10.2 gO₂/L COD. According to this data, PPs can be considered as a wealthy medium containing the most nutrients fundamental for microbial growth (Liang, et al., 2014). Furthermore, the richness of this waste with starch can be used as feedstock for ethanol production. However, the low fermentable reducing sugar content makes the fermentation of the raw material not practical. Therefore, initial hydrolysis (acidic or enzymatic) of carbohydrates is necessary (Pathak, et al., 2018).

Mixed grasses

A fresh ryegrass (*L. perenne*) and cocksfoot (*D. glomerata*) have been identified as a promising feedstock candidate for bio-based alternative energy to create biomethane and ethanol. This is due to its high yield of dry mass weight 20.03%. The analysis of blended grasses was as follows: Carbon 43.63%, nitrogen 2.8%, hydrogen 5.83%, and protein 7 mg/ml (Table I). Based on these results, grasses can be identified as a promising feedstock candidate for the anaerobic digestion process to produce biogas and ethanol yield by batch procedure fermentation.

B. Pre-treatment of Substrates

Acid hydrolysis of PPs

Reducing sugar quantity was increased after acid hydrolysis with 0.5 M HCl, the first and second 1% H₃PO₄ treatment by 31.54, 11.47, and 2.45 folds, respectively (Table II). These findings suggest; first, the rate of hydrolysis boosts by increasing acid concentration which can be a consequence of hydrogen ions activity as a catalyst and second, the digesting of PPs by 1% H₃PO₄ at 100°C for 5 h in water bath produces a higher amount of reducing sugars compared with the autoclave method (121°C for 15 min). This is maybe due to the short retention time of the heating solution.

Accordingly, the optimum condition to hydrolyze PPs is utilizing with 0.5 M HCl at 120°C that can liberate high concentration of reducing sugar (26.5 mg/ml). When comparing our results to those of older studies, it must be pointed out that our method led to better values (Arapoglou, et al., 2010). However, even better results are reported by Sheikh, et al. (2016) when adding 0.5% HCl to a dry powder of PPs, then autoclave it at 121°C, for 15 min.

TABLE I
CHEMICAL COMPOSITION OF NATIVE POTATO PEEL AND MIXED GRASSES

Parameters	Potato peels	Mixed grasses
Dry mass weight (%)	16.84	20.03
Nitrogen (%)	3.16	2.8
Carbon (%)	45.5	43.63
Hydrogen (%)	6.49	5.83
Protein content	7.2 mg/ml	7 mg/ml
Reducing sugars	0.84 mg/ml	NA*
COD	10.2 gO ₂ /L	NA

NA*: Not applicable

TABLE II
CHEMICAL COMPOSITION OF HYDROLYSATE POTATO PEELS

Parameters	Hydrolysis by			
	0.5 M HCl	1 st 1% H ₃ PO ₄	2 nd 1% H ₃ PO ₄	Enzymatic
Reducing sugars before fermentation	26.5 mg/ml	9.64 mg/ml	2.06 mg/ml	14.98 mg/ml
COD	35.74 gO ₂ /l	35.74 gO ₂ /l	35.74 gO ₂ /l	32.68 gO ₂ /l
Protein content	2.8 mg/ml	2.94 mg/ml	1.2 mg/ml	3.49 mg/ml
Reducing sugars after fermentation	1.69 mg/ml	NA*	NA*	1.47 mg/ml
BMP	NA*	NA*	NA*	0.5 1CH ₄ /gCOD

NA*: Not applicable, COD: Chemical oxygen demand, BMP: Biochemical methane potential

Enzymatic hydrolysis of PPs

The degrading ability of the following enzymes to digest PPs carbohydrates and to fermentable reducing sugars was tested; Termamyl α -amylase, amyloglucosidase, and Sanferm. The use of Termamyl α -amylase was released 12.45 mg/ml of reducing sugar that has been used as a substrate for amyloglucosidase plus Sanferm yield enzymes, which, in turn, released 14.98 mg/ml of reducing sugar (Table II). These outcomes demonstrate that the saccharification stage alone is an insufficient step for bioethanol production. However, when carbohydrates complex converted into simple monomers, a better production was obtained. Hence, a preparatory dextrinization stage was required. For this reason, the utility of enzyme combination was necessary for compelling hydrolysis of PPs. These results confirm previous findings by Khawla, et al., 2014; Izmirliglu and Demirci, 2012; and Sujeeta, et al., 2018.

Overall, our results confirmed that acid hydrolysis by 0.5 M HCl separates 26.5 mg/ml of fermentable reducing sugar and it has higher 35.74 gO₂/L COD compared to enzymatic hydrolysis, which were 14.98 mg/ml of reducing sugar and 32.68 gO₂/L of COD. These variations of production may due to the way of acid treatment that was carried out under a higher temperature of 120°C and utilizing mild acid concentration. However, enzymatic treatment leads to complete hydrolysis of the starch component and is highly substrate specific (de Souza, et al., 2019).

These results showed that both strategies were successfully recovered reducing sugar from PPs. Financially acid hydrolysis was more beneficial that requires severe conditions such as high temperature (120°C) and low pH (4). However, such conditions support the use of expensive corrosive-resistant equipment. Furthermore, they are restricted by the requirements of a neutralization step before fermentation and the generation of inhibitory by-products such as furfural and 5-hydroxymethylfurfural. Hence, enzymatic hydrolysis is more beneficial due to its low toxicity and low corrosion; no inhibitory is formed and requires less energy and mild environmental conditions (Maurya, et al., 2015).

Acid hydrolysis of mixed grasses

Acid pretreatment is likely to be the preferred choice for fresh grass because of the progressed degradation of xylan, which is the crucial component of hemicellulose. The quantity of reducing sugar increased 2-fold using 4% HCl, if we compare it with 3.5% HCl pre-treatment (Table III) which drive us to conclude that the production of glucose can be increased through increasing the concentration of treated acid. A slight increase in reducing sugar production was observed by adding 1% H₂SO₄ to hydrolysate solution of 3.5% HCl. Our results are broadly in line with other studies (Tanangteerapong, et al., 2017; Valva and Tichagwa, 2013).

C. Bioethanol Production from PPs and Mixed Grasses through Anaerobic Fermentation

Acid hydrolysate of PPs

Acidic hydrolysis produced 26.5 mg/ml reducing sugar. The produced sugar had been subjected to fermentation by

TABLE III
CHARACTERISTIC OF ACID HYDROLYSATE OF COMBINED GRASSES *LOLIUM PERENNE* AND *DACTYLIS GLOMERATA* SPECIES

Parameters	Hydrolysis by		
	3.5% HCl	4% HCl	1% H ₂ SO ₄
Reducing sugars	14.98 mg/ml	28.8 mg/ml	16.92 mg/ml
Protein content	7 mg/ml	6.5 mg/ml	6.1 mg/ml
COD	45.8 gO ₂ /l	45.8 gO ₂ /l	45.8 gO ₂ /l
BMP	0.54 lCH ₄ /gCOD	0.54 lCH ₄ /gCOD	0.54 lCH ₄ /gCOD

COD: Chemical oxygen demand, BMP: Biochemical methane potential

Safbrew S-33, and 1.69 mg/ml of reducing sugar remained and fermentable reducing sugars were 24.81 mg/ml. These results indicate that the yeast efficiently utilized most of the reducing sugar as a nutrient source for fermentation. Fig. 1 shows the investment of ethanol generation (g/L) during PPs hydrolysate fermentation. The maximum ethanol produced was 0.4311 g/L after 98 h fermentation, along these lines leveling off to 98 h with a slight diminish from that point. When comparing our results to the previous studies, it shows lower values than those of Arapoglou, et al., 2010 and Hashem and Darwish, 2010.

The low yields of ethanol are likely due to the presence of microorganism inhibitors such as furfural and 5-hydroxymethylfurfurals within the hydrolysate. This is causing slow xylose and hexose consumption during fermentation. Furthermore, *Safbrew* lacks the mechanism to take up pentose sugars as a substrate in acid hydrolysate, which probably contains a high amount of five-carbon sugar (Robak and Balcerek, 2018).

Enzymatic hydrolysate of PPs

The quantity of reducing sugar after enzymatic hydrolysis of PPs was 14.98 mg/ml. The combination of enzymatic hydrolysates solution was directed to fermentation to assess the ethanol generation. After fermentation, the total amount of reducing sugars was 1.47 mg/ml. From the results, it is clear that *S. cerevisiae* produced high quantities of ethanol on PPs (Fig. 1) that were previously treated with α -amylase, amyloglucosidase, and Sanferm. The highest quantity of ethanol production was achieved after 42 h of fermentation (1.2 g/L).

Results indicate that 19.6 g/L of ethanol was produced after 33 h of fermentation using a combination of Termamyl α -amylase and amyloglucosidase (Khawla, et al., 2014). Higher quantity of ethanol was obtained, which was 30.99 g/L after 48 h of fermentation through enzymatic hydrolysis using a combination of 1 ml α -amylase at 95°C for 3 h and 0.2 ml amyloglucosidase at 30°C for 48 h (Izmirliglu and Demirci, 2012).

This result shows that enzymatic hydrolysis leads to high yield of ethanol generation compared to acidic hydrolysate. It reveals that utilizing *S. cerevisiae* can efficiently ferment both pentose and hexose sugars more than *Safbrew* yeast. The capacity of every microorganism to ferment of reducing sugars, which includes glucose, xylose, arabinose, galactose, and mannose, after hydrolysis of cellulose and hemicellulose are different (Yang, et al., 2014). Our finding on ethanol

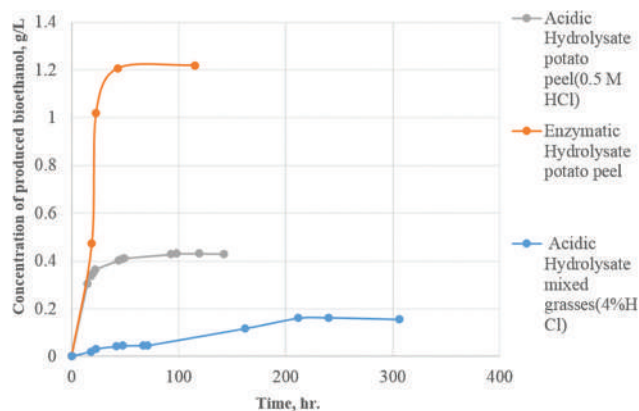


Fig. 1. Kinetics of bioethanol production from hydrolysate potato peels and combined grasses.

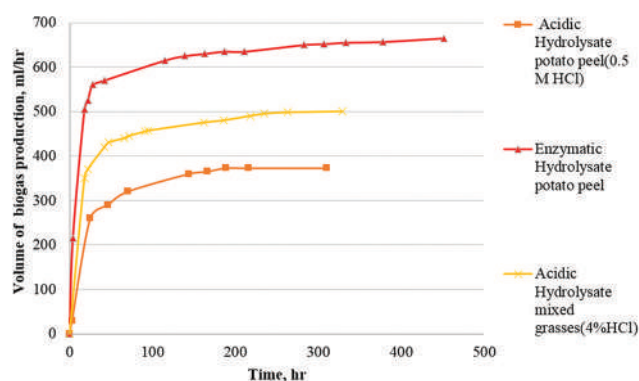


Fig. 2. Batch processes of biogas production from native and pretreated potato peels and mixed grasses.

generation at least provides some critical parameters for ethanol production from PPs which were the enzyme combination, the dose and the residence time of hydrolysis. A high yield of ethanol was obtained after liquefaction, saccharification, and fermentation by *S. cerevisiae*. The method of producing ethanol in this work is promising and shows that PPs of the potato industry treated with a locally produced enzyme, features an appealing feedstock for the bioethanol production. Moreover, bioconversion gives a reasonably priced and secure approach to produce cheap, clean energy and decreases the environmental pollutants caused by PPs.

Acid hydrolysate of mixed grasses

The quantity of reducing sugar was decreased 14.76-fold (from 28.8 mg/ml to 1.95 mg/ml) after fermentation in the presence of *S. cerevisiae*. This suggests that the yeast to grow utilized almost all of the reduced sugar (26.85 mg/ml). In contrast, the production of ethanol was elevated over 8 days of fermentation from 0.05 g/L to 0.16 g/L (Fig. 1). A similar pattern of results with higher values was obtained by Eliana, et al., 2014.

The low level of ethanol production can be returned to many factors, the first is the end product of acid pre-treatment such as acetic acid, furfural, and 5-hydroxymethylfurfural which are yeast growth inhibitors. This problem can be

solved through neutralization and then detoxification of hydrolysates. The second factor can be a result of the inability of *S. cerevisiae* to utilize 5-carbon sugars that include in the mixed grass (Tesfaw and Assefa, 2014).

D. Biogas Production from PPs and Mixed Grasses through Batch Process Methanation

Acid hydrolysate (0.5 M HCl) of PPs

After pre-treatment of PPs with 0.5 M HCl, hydrolysate solution was subjected to a batch process methanation under mesophilic condition 35°C. A rapid degradation rate of organic matter, protein, and carbohydrate with considerable biogas (260 ml/h) was obtained from the 1st day of batch process methanation (Fig. 2). These results suggest a methanogenic phase highly active from the 1st day of anaerobic digestion. After few days, the rate of biogas production steadily increased. The highest average volume of biogas was 373 ml/h after 188 h of methanation process, after that remained constant. This maximum yield of biogas production shows that the highest intake of organic matter was observed on the last day of the methanation process. In comparison with the enzymatic hydrolysate of PPs, low yield of biogas production was obtained from 0.5 M HCl treatment of PPs. The reason can be returned to lack of supplementary microelement, formation of bacterial inhibitor, and production of toxic compounds which, in turn, suppress bacterial growth.

Enzymatic hydrolysate of PPs

The resulted PPs solution from liquefaction and saccharification stages was subjected to biomethanation process at 35°C. The fast degradation rate and intake of organic matter were seen over 24 h of methanation process (Fig. 2) with a considerable amount of biogas investment 215 ml/h, which increased more than 2-fold after 48 h (570 ml/h) of the process.

These results demonstrate two facts; first, the methanogenic phase activates from the 2nd day of anaerobic digestion. Second, the highest quantity of biogas can be acquired after 451 h of methanation process.

Enzymatic hydrolysate of PPs gives higher quantity (2-fold) of biogas production compared to acid hydrolysate, this can be returned to the ability of used enzymes to degrade PPs and make it amenable to bacterial methanogenic fermentation. It is worth mentioning that the presence of microelements in the hydrolysis process has positive effect on enhancing the rate of biogas production, and no inhibitory by-product is formed in enzymatic hydrolysis.

Depending on the obtained data, enzymatic hydrolysis has several benefits compared to acidic hydrolysis. They include works beneath moderate conditions, are biodegradable, enhance yields, decrease energy, water utilization, and the amount of by-products like furfural.

Acid hydrolysate (4% HCl) of mixed grasses

The results of methanization of mixed grasses hydrolysate (4% HCl) of perennial ryegrass (*L. perenne*) and cocksfoot (*D. glomerata*) indicate that the rapid degradation rate of organic matter content was noticed from the 1st day (Fig. 2)

TABLE IV
MEASUREMENT OF BIOGAS COMPOSITION

Substrates	% biogas	% CO ₂	% CH ₄
0.5 M HCl hydrolysis (PPs)	37.3	4	33.3
Enzymatic hydrolysate (PPs)	66.5	2	64.5
4% HCl hydrolysis (mixed grass)	50	2	48

PPs: Potato peels

with a significant quantity of biogas production (350 ml/h). Biogas yields were raised from the 2nd day to the 9th day of batch process methanation. The highest volume over the 13th day of batch process methanation was 500 ml/h. This is consistent with what has been found in the previous studies by Mahnert, et al., 2005 and Ngumah, et al., 2013.

This high yield of biogas may be due to 4% HCl pre-treatment of lignocellulosic combined grasses, and it could hydrolyze most of the hemicellulose into its element sugars. The following values were determined after acid hydrolysis of combined grasses; reducing sugar (28.8 mg/ml), protein content (6.5 mg/ml), COD (45.8 gO₂/L), and BMP (0.54 lCH₄/gCOD). These results confirm that pre-treatment strategies of grasses for biogas manufacturing enhance and boost up the degradation process attaining high biogas yields.

Biogas composition

The two main components of biogas are CH₄ and CO₂, also can include small quantities of nitrogen, hydrogen, hydrogen sulfide, and water vapor (Mahmoodi, et al., 2018).

The ratio of biogas content was produced by the anaerobic digestion process from PPs and combined grasses substrate (Table IV). Methane production was determined after the biogas passed through a cylinder containing 5 N NaOH solution to increase the pH. This alkaline solution adsorbs CO₂ and other gas from the biogas mixture, and the gas volume is decreased. Therefore, the measured volume represents CH₄ content in the biogas mixture. It was noted that the variation between the biogas and methane volume displays the CO₂ content of the biogas because H₂S concentration is entirely negligible in the adsorbed gas. Determination of biogas composition needs to perform to qualify biogas as natural gas which environmentally friendly and safe for health.

IV. CONCLUSION

The main conclusion that can be drawn from this work is that PPs and mixed grasses are valuable substrates for biomethanation, which can be applied in small and big scales.

Importantly, our results proved on the one hand that the enzymatic treatment of PPs produces ethanol and biogas after fermentation much more than the acidic treatment, which was 1.2 g/L ethanol after 42 h of fermentation and 665 ml/h biogas over 451 h of batch process methanation. On the other hand, this work argued that 4% HCl is the best way to hydrolyze blended grass, which released 28.8 mg/ml of reduced sugar, produced 0.16 g/L ethanol over 8 days of fermentation and 500 ml/h of biogas after the 13th day of batch process methanation.

V. ACKNOWLEDGMENT

This research was supported by Erasmus Mundus Marhaba Program. Thanks are due to the Faculty of Chemical System Engineering, Department of Biotechnology, University of Chemical Technology and Metallurgy in Sofia and Bulgaria, where the project was performed. Thanks extend to the Department of Medical Microbiology, Faculty of Science and Health, Koya University.

REFERENCES

- American Public Health Association. 1995. *Standard Methods for the Examination of Water and Wastewater*. American Public Health Association, Washington, DC.
- Arapoglou, D., Varzakas, T., Vlyssides, A. and Israilides, C. 2010. Ethanol production from potato peel waste (PPW). *Waste Management*, 30, pp.1898-1902.
- Aziz, N.I.H., Hanafiah, M.M. and Gheewala, S.H. 2019. A review on life cycle assessment of biogas production: Challenges and future perspectives in Malaysia. *Biomass and Bioenergy*, 122, pp.361-374.
- Chynoweth, D., Turick, C., Owens, J., Jerger, D. and Peck, M. 1993. Biochemical methane potential of biomass and waste feedstocks. *Biomass and Bioenergy*, 5, pp.95-111.
- de Souza, I.A., Orsi, D.C., Gomes, A.J. and Lunardi, C.N. 2019. Enzymatic hydrolysis of starch into sugars is influenced by microgel assembly. *Biotechnology Reports*, 22, p.e00342.
- Eliana, C., Jorge, R., Juan, P. and Luis, R. 2014. Effects of the pretreatment method on enzymatic hydrolysis and ethanol fermentability of the cellulosic fraction from elephant grass. *Fuel*, 118, pp.41-47.
- Hashem, M. and Darwish, S.M. 2010. Production of bioethanol and associated by-products from potato starch residue stream by *Saccharomyces cerevisiae*. *Biomass and Bioenergy*, 34(7), pp.953-959.
- Izmirliglu, G. and Demirci, A. 2012. Ethanol production from waste potato mash by using *Saccharomyces cerevisiae*. *Applied Sciences*, 2, pp.738-753.
- Khawla, B.J., Sameh, M., Imen, G., Donyes, F., Dhouha, G., Raoudha, E.G. and Oumèma, N.E. 2014. Potato peel as feedstock for bioethanol production: A comparison of acidic and enzymatic hydrolysis. *Industrial Crops and Products*, 52, pp.144-149.
- Li, L., Kong, X., Yang, F., Li, D., Yuan, Z. and Sun, Y. 2012. Biogas production potential and kinetics of microwave and conventional thermal pretreatment of grass. *Applied Biochemistry and Biotechnology*, 166, pp.1183-1191.
- Liang, S. and McDonald, A.G. 2014. Chemical and thermal characterization of potato peel waste and its fermentation residue as potential resources for biofuel and bioproducts production. *Journal of Agricultural and Food Chemistry*, 62, pp.8421-8429.
- Liang, S., McDonald, A.G. and Coats, E.R. 2014. Lactic acid production with undefined mixed culture fermentation of potato peel waste. *Waste Management*, 34, pp.2022-2027.
- Lowry, O.H., Rosebrough, N.J., Farr, A.L. and Randall, R.J. 1951. Protein measurement with the Folin phenol reagent. *Journal of Biological Chemistry*, 193, pp.265-275.
- Mahmoodi, P., Farmanbordar, S. and Karimi, K. 2018. *Analytical Methods in Biogas Production*. Springer, Cham, Switzerland, pp.221-238.
- Mahnert, P., Heiermann, M. and Linke, B. 2005. Batch-and semi-continuous biogas production from different grass species. *Agricultural Engineering International: CIGR Journal*, 7, pp.5-10.
- Maurya, D.P., Singla, A. and Negi, S. 2015. An overview of key pretreatment processes for biological conversion of lignocellulosic biomass to bioethanol. *3 Biotech*, 5, pp.597-609.

- Miller, G.L. 1959. Use of dinitrosalicylic acid reagent for determination of reducing sugar. *Analytical Chemistry*, 31, pp.426-428.
- Mulat, D.G., Dibdiakova, J. and Horn, S.J. 2018. Microbial biogas production from hydrolysis lignin: Insight into lignin structural changes. *Biotechnology for Biofuels*, 11, p.61.
- Ngumah, C., Ogbulie, J., Orji, J. and Amadi, E. 2013. Biomethanation of carpet grass (*Axonopus fissifolius*). *Environmental Research, Engineering and Management*, 66(4), pp.34-37.
- Pathak, P.D., Mandavgane, S.A., Puranik, N.M., Jambhulkar, S.J. and Kulkarni, B.D. 2018. Valorization of potato peel: A biorefinery approach. *Critical Reviews in Biotechnology*, 38, pp.218-230.
- Phuttaro, C., Sawatdeenarunat, C., Surendra, K., Boonsawang, P., Chaiprapat, S. and Khanal, S.K. 2019. Anaerobic digestion of hydrothermally-pretreated lignocellulosic biomass: Influence of pretreatment temperatures, inhibitors and soluble organics on methane yield. *Bioresource Technology*, 284, pp.128-138.
- Robak, K. and Balcerek, M. 2018. Review of second generation bioethanol production from residual biomass. *Food Technology and Biotechnology*, 56(2), p.174.
- Rodriguez, C., Alaswad, A., Benyounis, K. and Olabi, A.G. 2017. Pretreatment techniques used in biogas production from grass. *Renewable and Sustainable Energy Reviews*, 68, pp.1193-1204.
- Sanchez, O. and Cardona, C. 2008. Trends in biotechnological production of fuel ethanol from different feedstocks. *Bioresource Technology*, 99, pp.5270-5295.
- Sheikh, R.A., Al-Bar, O.A. and Soliman, Y.M.A. 2016. Biochemical studies on the production of biofuel (bioethanol) from potato peels wastes by *Saccharomyces cerevisiae*: Effects of fermentation periods and nitrogen source concentration. *Biotechnology and Biotechnological Equipment*, 30(3), pp.497-505.
- Sujeeta, K.M., Mehta, S. and Sihag, K. 2018. Optimization of conditions for bioethanol production from potato peel waste. *International Journal Chemical Studies*, 6(1), pp.2021-2024.
- Tanangteerapong, D., Tunjaroensin, T., Trakun-Ung, P. and Kamwilaisak, K. 2017. Production of reducing sugars from hydrolysis of napier grass by acid or alkali. *Chiang Mai University Journal of Natural Sciences*, 16(1), p.32.
- Tesfaw, A. and Assefa, F. 2014. Current trends in bioethanol production by *Saccharomyces cerevisiae*: substrate, inhibitor reduction, growth variables, coculture, and immobilization. *International Scholarly Research Notices*, 2014, 2014, p.532852.
- Thangavelu, S.K., Ahmed, A.S. and Ani, F.N. 2016. Review on bioethanol as alternative fuel for spark ignition engines. *Renewable and Sustainable Energy Reviews*, 56, pp.820-835.
- Tran, T.T.A., Le, T.K.P., Mai, T.P. and Nguyen, D.Q. 2019. Bioethanol production from lignocellulosic biomass. In: *Alcohol Fuels-Current Technologies and Future Prospect*. IntechOpen, London.
- Valva, R.M. and Tichagwa, L. 2013. Low temperature acid hydrolysis of grass-derived lignocellulose for fermentable sugars production. *Cellulose Chemistry and Technology*, 47(7-8), pp.565-572.
- Wagner, A., Lackner, N., Mutschlechner, M., Prem, E., Markt, R. and Illmer, P. 2018. Biological pretreatment strategies for second-generation lignocellulosic resources to enhance biogas production. *Energies*, 11, p.1797.
- Yang, T.C., Kumaran, J., Amartey, S., Maki, M., Li, X., Lu, F. and Qin, W. 2014. Biofuels and bioproducts produced through microbial conversion of biomass. *Bioenergy Research: Advances and Applications*, 2014, pp.71-93.

Design and Performance of Microstrip Diplexers: A Review

Salah I. Yahya^{1,2}, Abbas Rezaei³ and Leila Nouri^{4,5}

¹Department of Software Engineering, Faculty of Engineering, Koya University, Koya KOY45, Kurdistan Region - F.R. Iraq

²Department of Communication and Computer Engineering, Cihan University-Erbil, Kurdistan Region - F.R. Iraq

³Department of Electrical Engineering, Kermanshah University of Technology, Kermanshah, Iran

⁴Institute of Research and Development, Duy Tan University, Da Nang, 550000, Vietnam

⁵Department of Electrical and Electronic Engineering, Duy Tan University, Da Nang 550000, Vietnam

Abstract—The radiofrequency microstrip diplexers are widely demanded nowadays by modern wireless communication systems. Hence, several types of previously reported microstrip diplexers are reviewed and investigated in this work. Microstrip diplexers are three ports devices used for separating desired signals and delivering them through two (or more) different channels. The diplexers are investigated in three categories of dual-channel bandpass-bandpass diplexers, multichannel diplexers, and lowpass-bandpass diplexers. The investigated multi-channel diplexers include a number of four-channel, six-channel, and eight-channel diplexers. Due to the hard design process, the number of reported diplexers with more than four channels is limited. The layout structures and theory design methods of the previously reported diplexers are studied. Moreover, their size and performance are compared while some explanations about their advantages and disadvantages are presented. This comparison includes insertion loss, return loss, fractional bandwidths, isolation, selectivity, and gaps between channels.

Index Terms—Microstrip, Diplexer, Bandpass-bandpass, Lowpass-bandpass, Multichannel.

I. INTRODUCTION

High-performance and compact microstrip devices are strongly demanded by modern telecommunication and wireless networks. These microstrip devices are microstrip filters, couplers, diplexers, multiplexers, power dividers,

and sometimes low-noise amplifiers (Noori and Rezaei, 2017; Shen and Che, 2020; Salehi and Noori, 2014; Chen, et al., 2019; Rezaei and Noori, 2018; Salehi, et al., 2016). A microstrip diplexer is a passive three-port device for frequency-domain multiplexing. It usually consists of two filters which are integrated by a junction circuit (Feng, et al., 2017; Huang, et al., 2016). The signal can be transmitted to the other two ports through a common port connected to the junction circuit (Rezaei, et al., 2019). Each diplexer has two channels working at two frequencies for the specific applications. For examples, the proposed diplexer in Yang, et al., 2014, has been designed for 4G application while the introduced diplexer in Noori and Rezaei, 2017, has been designed for IEEE 802.16 and 802.20 WiMAX technology and wireless applications. When the channels are close together, the diplexer can be employed for frequency division duplex (FDD) scheme (Peng and Chiang, 2015). However, in this case, improving the insertion loss and isolation between channels is hard (Noori and Rezaei, 2017). The diplexers can be formed by two bandpass filters (BPF), which are bandpass-bandpass diplexers (BBDs) (Jun-Mei, et al., 2016; Chinig, et al., 2015; Guan, et al., 2014; Chen, et al., 2015; Xiao, et al., 2015; Rezaei and Noori, 2018; Sasipriya and Aparna, 2018; Rezaei and Noori, 2018). Some of BBDs have two channels (Deng, et al., 2013; Noori and Rezaei, 2017; Rezaei, et al., 2017; Feng, et al., 2014; Chinig, et al., 2015; Salehi, et al., 2016; Chen, et al., 2006; Cheng, et al., 2013; Chinig, 2017; Wang, et al., 2016) named dual-channel diplexers. However, some have more than two channels. The multiplexers have more than three ports and more than two channels (Heng, et al., 2014), but multi-channel diplexers have only three ports with the channel numbers more than two (Liu, et al., 2017; Lee, et al., 2016; Wu, et al., 2013; Lai and Jeng, 2005; Hsu, et al., 2016). Since ultra-wideband has traditional applications in non-cooperative radar, some of diplexers have been designed with wide channels

ARO-The Scientific Journal of Koya University
Vol. VIII, No.1 (2020), Article ID: ARO.10634, 12 pages
DOI:10.14500/aro.10634

Received 12 January 2019; Accepted 12 March 2020

Review paper: Published 15 March 2020

Corresponding author's e-mail: leilanouri@duytan.edu.vn

Copyright © 2020 Salah I. Yahya, Abbas Rezaei, Leila Nouri. This is an open-access article distributed under the Creative Commons Attribution License.



(Deng, et al., 2013). The wideband diplexer can use a very low energy level for short-range and high-bandwidth communications. On the other hand, a number of diplexers have narrow channels (Salehi, et al., 2016). They are suitable for multi-channel long-range RF communication systems (Noori and Rezaei, 2018; Yahya, et al., 2019). The stopband rejection of a high-performance diplexer must be wide with low harmonic level (Yahya, et al., 2019; Bukuru, et al., 2015; Rezaei, et al., 2019). Nevertheless, many designers did not give attention to attenuate the harmonics (Rezaei, et al., 2019; Rezaei, et al., 2019). Other types of diplexers are lowpass-bandpass diplexers (LBDs), which have been formed by a lowpass filter (LPF), BPF, and junction circuit (Rezaei, et al., 2019; Deng and Tsai, 2013; Rayatzadeh and Moloudian, 2019; Heshmati and Roshani, 2018; Capstick, 1999; Hayati, et al., 2019). An important factor related to the diplexer performance is the high selectivity. However, some of the diplexer designers did not improve the selectivity (Rezaei, et al., 2019; Bui, et al., 2017) while the others could design the diplexers with high-frequency selectivity at both channels (Rezaei and Noori, 2018; Lobato-Morales, et al., 2012). A well-designed diplexer must have low loss and high isolation between channels. For example, a microstrip diplexer that reported in Ghafari and Afsahi, 2019, has relatively a good isolation but large measured insertion and return losses at both channels. Furthermore, a diplexer with flat passbands has low time distortion, which is an advantage.

In this work, several kinds of microstrip diplexers are reviewed. The structures and performance of these diplexers are studied to find the best structures with high performance and small size. Moreover, the mathematical methods of analyzing some structures have been reviewed. The Frequency response and overall size of the introduced diplexers are compared in the following categories: Dual-channel BBDs, multichannel bandpass diplexers, and LBDs.

II. DUAL-CHANNEL BBDs

The majority designed diplexers for the wireless communication market are the dual-channel BBDs. Usually, to design this type of diplexer, the designers use two similar BPF but with different overall dimensions. Each filter should create only one passband. Therefore, to design a dual-channel diplexer, we need two single-mode resonators. Several structures have been proposed to design the dual-band bandpass diplexers (Feng, et al., 2017; Huang, et al., 2016; Rezaei, et al., 2019; Yang, et al., 2014; Noori and Rezaei, 2017; Peng and Chiang, 2015; Jun-Mei, et al., 2016; Chinig, et al., 2015; Guan, et al., 2014; Chen, et al., 2015; Xiao, et al., 2015; Rezaei and Noori, 2018; Sasipriya and Aparna, 2018; Rezaei and Noori, 2018; Deng, et al., 2013; Noori and Rezaei, 2017; Rezaei, et al., 2017; Feng, et al., 2014; Chinig, et al., 2015; Salehi, et al., 2016; Chen, et al., 2006; Cheng, et al., 2013; Chinig, 2017; Wang, et al., 2016). To achieve a high performance, different mathematical methods have been used. Some of the layout configurations of diplexers with a summary of their design methods are presented in Table I. In addition to the presented layout, some lumped elements

have been used (Feng, et al., 2017). Due to the symmetric structures, the even/odd modes analysis has been performed (Feng, et al., 2017; Huang, et al., 2016; Yang, et al., 2014; Guan, et al., 2014; Rezaei and Noori, 2018; Sasipriya and Aparna, 2018; Rezaei and Noori, 2018). The even/odd input admittances (Y_{ine} and Y_{ino}) have been calculated to obtain the coupling coefficient k_{12} according to the following formula (Feng, et al., 2017):

$$k_{12} = \frac{\text{Im}[Y_{12}(\omega_o)]}{\frac{\omega_o}{2} \frac{\partial \text{Im}[Y_{11}(\omega_o)]}{\partial \omega}}; Y_{11} = \frac{Y_{ine} + Y_{ino}}{2}, Y_{12} = \frac{Y_{ine} - Y_{ino}}{2} \quad (1)$$

Where ω_o is an angular resonance frequency. As mentioned in Feng, et al., 2017, the coupling factor is strongly affected by the gap between resonators. Accordingly, another way to realize k_{12} is by selecting the gap between the resonators and coupling sections. For analyzing the symmetrical resonators (Huang, et al., 2016; Yang, et al., 2014; Guan, et al., 2014; Liu, et al., 2017), the even and odd modes resonance frequencies f_{even} and f_{odd} are expressed as:

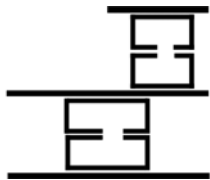
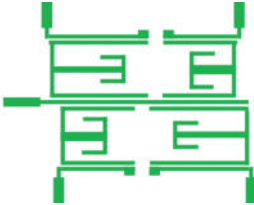
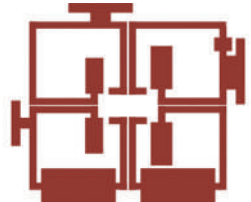
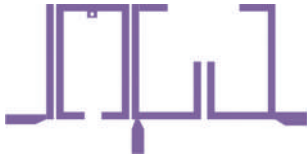
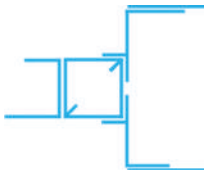
$$f_{odd} = \frac{(2n-1)c}{2L_1\sqrt{\epsilon_{eff}}} \quad \text{and} \quad f_{even} = \frac{nc}{(L_1 + 2L_2)\sqrt{\epsilon_{eff}}} \quad (2)$$

for : $n = 1, 2, 3, \dots$

Where ϵ_{eff} is the effective dielectric constant and c is the speed of light in free space. The physical length of half circuit under odd-mode and even mode excitations are depicted by L_1 and L_2 , respectively. As depicted in Table II, the resonators (Huang, et al., 2016; Yang, et al., 2014) are similar where they are loaded by similar T-shape stubs. On the other hand, they used (2) to calculate the even/odd mode resonance frequencies. However, they have different junction circuits.

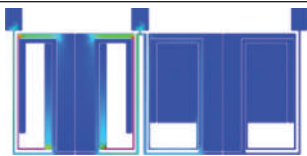
The meandrous lines have been coupled to realize a microstrip diplexer (Rezaei, et al., 2019; Chinig, 2017; Bukuru, et al., 2015), but they are implemented on different substrates. To analyze some resonators, the ABCD matrixes have been calculated (Salehi and Noori, 2014; Noori and Abiri, 2016; Rezaei, et al., 2019; Noori and Rezaei, 2017; Noori and Rezaei, 2017). Using the ABCD matrix (Rezaei, et al., 2019), S_{21} and Z matrix have been calculated. Then for having the lowest insertion loss, the value of S_{21} is obtained. On the other hand, based on the value of Z_{21} , the resonance condition is obtained. Finally, by combining the equations, the values of the physical lengths at a target resonance frequency are obtained. Meanwhile, Noori and Rezaei (2017) calculated the reflection coefficient based on the ABCD matrix to obtain the condition of good isolation. However, due to its special structure, it could not improve the isolation between channels. The transmission matrix (Noori and Rezaei, 2017) is utilized based on an equivalent LC circuit of a basic resonator. It is utilized for calculating the values of the unknown stubs dimensions. As shown in Table I, the simple structure (Jun-Mei, et al., 2016) is analyzed by calculating the external quality factors corresponding to source and load ($Q_{e,o}$ and $Q_{e,N+1}$) using the coupling coefficients ($M_{0,1}$ and $M_{N,N+1}$) as follows:

TABLE I
LAYOUT CONFIGURATION, SUBSTRATE, AND THEORY METHOD OF THE DUAL-CHANNEL BBDS. ϵ_r IS THE SUBSTRATE RELATIVE DIELECTRIC CONSTANT AND h IS THE SUBSTRATE HEIGHT

Refs.	Diplexer structure	Substrate	Theory method
(Feng, et al., 2017)		$\epsilon_r=2.65$ $h=0.508$ mm	1. Calculating the even/odd modes admittances (Y_{ine} and Y_{ino}) 2. Calculating the coupling coefficient
(Huang, et al., 2016)		Rogers RO4003C $\epsilon_r=3.55$ $h=0.508$ mm	Finding the fundamental odd and even modes resonant frequencies
(Rezaei, et al., 2019)		RT_Duroid_5880 $\epsilon_r=2.2$ $h=0.787$ mm	1. Calculating the ABCD matrix 2. Calculating S_{21} and Z matrix from ABCD matrix 3. Calculating the resonance frequency from Z matrix
(Yang, et al., 2014)		$\epsilon_r=3.5$ $h=0.8$ mm	Finding the fundamental odd and even modes resonant frequencies
(Noori and Rezaei, 2017)		RT_Duroid_5880 $\epsilon_r=2.2$ $h=0.787$ mm	1. Calculating the transmission matrix 2. Calculating the reflection coefficient 3. Finding a method to obtain better isolation between two channels
(Jun-Mei, et al., 2016)		$\epsilon_r=2.55$ $h=0.8$ mm	1. Calculating the external quality factors 2. Tuning the space between coupled lines based on quality factors
(Chinig, et al., 2015)		$\epsilon_r=4.4$ $h=1.58$ mm	1. Even and odd modes analysis by calculating the input admittance 2. Calculating the desired frequency ratio of harmonic from the input admittance
(Guan, et al., 2014)		$\epsilon_r=3.5$ $h=0.8$ mm	Calculating the even and odd modes of resonance frequencies
(Chen, et al., 2015)		$\epsilon_r=10.8$ $h=0.653$ mm	Finding the resonance condition based on the equivalent circuit of quarter resonator

(Contd..)

TABLE I
(CONTINUED)

Refs.	Diplexer structure	Substrate	Theory method
(Chen, et al., 2015)		RT_Duroid_5880 $\epsilon_r=2.2$ $h=0.787$ mm	1. Proposing an equivalent LC model of the resonator 2. Even and odd mode analysis using LC circuit
(Sasipriya and Aparna, 2018)		RT_Duroid_5880 $\epsilon_r=2.2$ $h=0.787$ mm	1. Proposing an equivalent LC model of the resonator 2. Even and odd mode analysis using LC circuit

BBDS: Bandpass-bandpass diplexers

TABLE II
PERFORMANCE COMPARISON AMONG DIFFERENT REPORTED BBD

Refs.	IL1, IL2 (dB)	RL1, RL2 (dB)	Size (λ_g^2)	Isolation (dB)	f_{o1}, f_{o2} (GHz)	f_{o2}/f_{o1} (GHz)	FBW1, FBW2 (%)
(Feng, et al., 2017)	1.4, 3.4	15, 20	0.089	45	1.05, 1.87	1.78	6.1, 4
(Huang, et al., 2016)	1, 0.9	Better than 20	0.127	30	2.3, 2.72	1.18	6.1, 5.8
(Rezaei, et al., 2019)	0.36, 0.44	Better than 23.7	0.028	23	2.88, 3.29	1.14	---
(Yang, et al., 2014)	---	---	0.082	30	2.35, 2.59	1.10	6.89, 6.5
(Noori and Rezaei, 2017)	0.6, 0.9	11.3, 12.4	0.076*	13.8	2.6, 6	2.30	---
(Peng and Chiang, 2015)	2.1, 2.1	Better than 20	0.07	20	1.75, 1.85	1.06	5, 5
(Jun-Mei, et al., 2016)	2.2, 2.1	11.9, 12	0.064	30	1.82, 2.41	1.32	2.8, 1.9
(Chinig, et al., 2015)	2.2, 2.2	Better than 16	---	21	1.8, 2.45	1.36	8.7, 6
(Guan, et al., 2014)	1.2, 1.5	---	0.137	35	1.95, 2.14	1.10	3.59, 3.27
(Chen, et al., 2015)	1.83, 1.52	---	0.705	26	1.1, 1.3	1.18	8, 9.2
(Xiao, et al., 2015)	1.43, 1.59	---	0.282	42	2.44, 3.52	1.44	---
(Rezaei and Noori, 2018)	0.14, 0.16	18.5, 20	0.022	34	1.8, 2.4	1.33	11, 7.1
(Rezaei and Noori, 2018)	0.28, 0.29	21.2, 24.3	0.010	30	0.8, 0.9	1.12	3.2, 3.2
(Deng, et al., 2013)	3, 3	Better than 10.3	0.073	37.5	3, 5.8	1.93	80, 5
(Noori and Rezaei, 2017)	0.2, 0.4	15, 16.8	0.09*	19.8	2.36, 4	1.69	---
(Rezaei, et al., 2017)	0.18, 0.39	27.1, 27.6	0.075	20.55	2.4, 2.79	1.15	---
(Feng, et al., 2014)	---	Better than 20	0.32*	30	1.84, 2.41	1.3	6, 6.2
(Chinig, et al., 2015)	2.24, 2.16	Better than 29	0.13*	21	1.8, 2.45	1.36	---
(Salehi, et al., 2016)	1.5, 1.3	Better than 21	0.087*	30	2.3, 2.55	1.10	3.6, 3.4
(Chen, et al., 2006)	2.8, 3.2	16, 17	---	30	1.5, 1.75*	1.16	3.8, 3.3
(Cheng, et al., 2013)	2.86, 3.04	Better than 20	0.688	40	8, 9	1.12	---
(Chinig, 2017)	2.6, 2.4	35, 33	0.079*	24.4	1.7, 2.49	1.46	2.6*, 5.1*
(Wang, et al., 2016)	0.4, 0.3	Better than 13	0.488	70	9.9, 10.02	1.01	0.65*, 0.65*
(Yahya, et al., 2019)	0.85, 0.8	15.7, 24	0.047	21	2.85, 2.72	1.05	---
(Bukuru, et al., 2015)	1.35, 1.31	15, 20	0.05	25	3.65, 5.2	1.42	8.2, 7.69
(Rezaei, et al., 2019)	0.25, 0.26	18.45, 17.47	0.038	24	2.12, 3.94	1.85	---
(Rezaei, et al., 2019)	0.10, 0.16	33, 22	0.054	22	1.6, 2.1	1.31	16.8, 11
(Bui, et al., 2017)	0.4, 0.42	better than 20	0.095	---	1.8, 2.45	2.36	---
(Rezaei and Noori, 2018)	0.21, 0.21	32, 25	0.018	40	1, 1.3	1.3	4.6, 4.6

*: Approximated values. BBDS: Bandpass-bandpass diplexers

$$Q_{e,o} = \frac{1}{FBW M_{0,1}^2} \tag{3}$$

$$Q_{e,N+1} = \frac{1}{FBW M_{N,N+1}^2}$$

Where $M_{i,i+1}$ is the coupling coefficient and fractional bandwidth (FBW) is the FBW. Finally, the space between coupled lines is tuned based on quality factors. The resonator analysis presented by Guan, et al. (2014) and Rezaei, et al. (2017) has been performed by calculating the extra quality factor (Q_e) as defined by the following equation:

$$Q_e = \frac{2f_o}{(\Delta f)_{3dB} 10^{-\frac{-IL}{20}}} \tag{4}$$

Where f_o , IL, and $(\Delta f)_{3dB}$ are resonance frequency in GHz, insertion loss in dB, and -3dB bandwidth, respectively. Proposing an approximated LC circuit is a method to analyze the resonator structure. Fig. 1 presents some resonators with their approximated equivalent LC circuit proposed in Noori and Rezaei, 2017; Rezaei and Noori, 2018; Rezaei and Noori, 2018; Salehi, et al., 2016; Rezaei, et al., 2019. Since the effects of steps in widths and bent are negligible

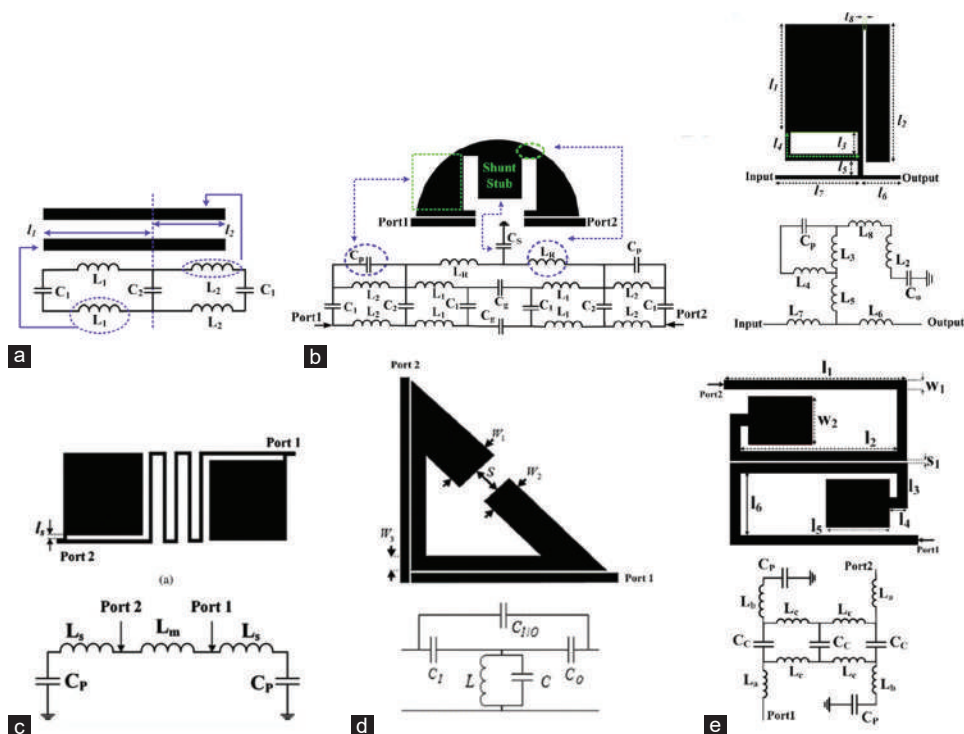


Fig. 1. Layout of some resonators and their equivalent LC circuits reported by: (a) Noori and Rezaei (2017), (b) Rezaei and Noori (2018), (c) Rezaei and Noori (2018), (d) Salehi, et al. (2016), (e) Rezaei, et al. (2019).

at the frequencies lower than 10 GHz, the equivalent lumped elements of these sections are removed. The patch cells are replaced by capacitors, and thin stubs are presented by inductors. As depicted in Fig. 1, the effect of coupling between microstrip lines is replaced by some capacitors. Using these LC circuits, it can be easy to calculate the resonance frequencies, ABCD matrix, input impedance/admittance, and even/odd modes analysis.

A well-designed diplexer must be compact with low loss, sharp roll-off, attenuated harmonics, and high isolation. The simulated and measured frequency responses of dual-channel BBDs in (Huang, et al., 2016; Jun-Mei, et al., 2016; Guan, et al., 2014; Cheng, et al., 2013) are presented in Figs. 2(a)-(d), respectively. As presented in Fig. 2, the parameters S_{21} and S_{31} show the transition between common port (1) and other ports, while the isolation between channels is depicted by S_{23} . However, they could not improve the selectivity while the harmonics did not suppress.

The size and performance of designed dual-band BBDs are compared in Table II. In this table; RL is the return loss, and f_{o1} and f_{o2} are the resonance frequencies of the first and second channels, respectively. As presented in Table II, the lowest insertion losses at both channels are achieved in Rezaei and Noori, 2018, while the best return losses are obtained in Chinig, et al., 2015. The overall sizes of the reported diplexers are presented in λ_g^2 , where λ_g is the guided wavelength calculated at the lower resonance frequencies. The comparison results show that the most compact dual-band BBD is designed in Rezaei and Noori, 2018, with the overall size of $0.01 \lambda_g^2$. Another important factor in the diplexer design is the isolation between channels where the

highest isolation (70 dB) is achieved in Wang, et al., 2016. When the channels are close together, the diplexer can be used for FDD applications. Nevertheless, having a small gap between channels leads to increase in the loss and decrease the isolation. Accordingly, the diplexer with $f_{o2}/f_{o1} \leq 1.1$ has been less designed. As shown in Table II, only the proposed diplexer in Wang, et al., 2016, could reach $f_{o2}/f_{o1} = 1.01$, but it could not improve the common port return loss at both channels. The narrowband and wideband diplexers can be identified from the presented FBWs in Table II. A diplexer with $FBW1 = 2.8\%$ and $FBW2 = 1.9\%$ is designed in Jun-Mei, et al., 2016, where it can be used for long-range RF communication systems. However, having narrow channels increases the group delay that leads to time distortion. On the other hand, a diplexer with 80% first channel FBW is designed in Deng, et al., 2013, which is suitable for ultra-wideband applications.

III. MULTICHANNEL BBDs

Another type of diplexer is multichannel BBDs. Quad-channel diplexers are a type of BBDs which is the most reported one. The quad-channel diplexers have three ports similar to dual-band BBDs, but with four channels. They are suitable for multichannel communication systems. The special applications of dual and multichannel diplexers are related to their resonance frequencies. For example, a diplexer with resonance frequencies at 2.4 GHz and 5.2 GHz is appropriate for wireless local area networks (WLAN) while a diplexer with an operational frequency at 1.8 GHz is suitable for GSM applications (Rezaei and Noori, 2018). The

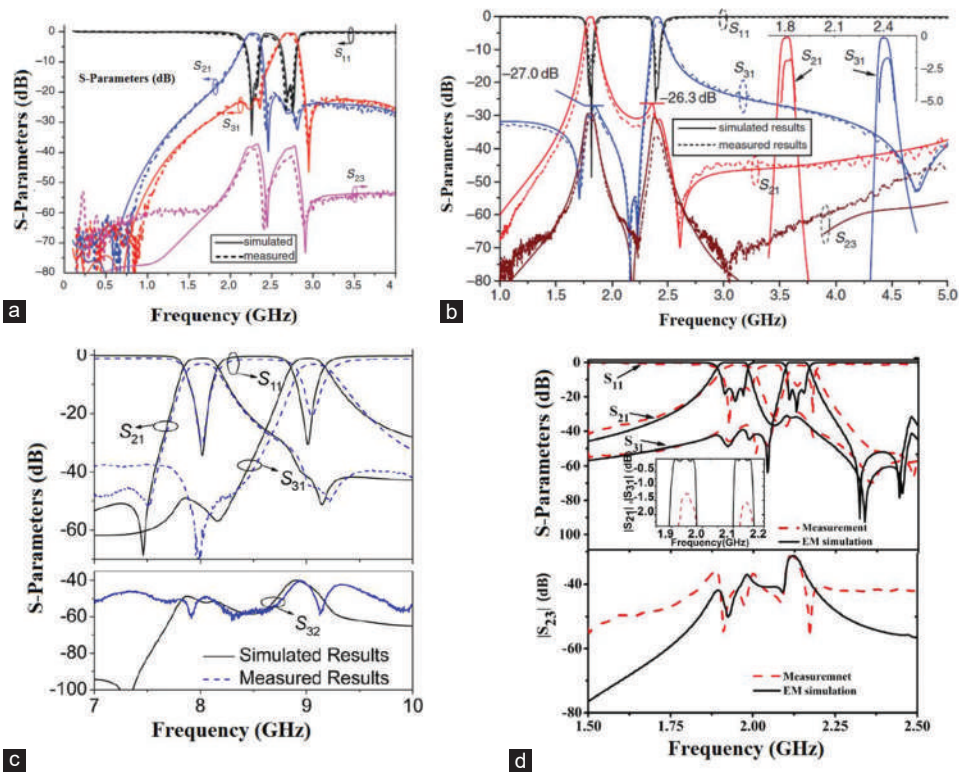


Fig. 2. Simulated and measured frequency responses of dual-channel bandpass-bandpass diplexers. (a) (Huang, et al., 2016), (b) (Jun-Mei, et al., 2016), (c) (Guan, et al., 2014), (d) (Cheng, et al., 2013).

quad-band diplexers are usually composed of two dual-band BPF and a junction circuit. The sizes of this type of diplexer are usually larger than dual-band BBDs. The layout structure, substrate properties, and theory method of the quad-band bandpass diplexers are summarized in Table III.

As illustrated in Table III, the microstrip spiral cells with inductance features have been utilized to design quad-band bandpass diplexers (Heng, et al., 2014; Liu, et al., 2017). They are integrated by murderous microstrip lines. The spiral cells have the advantage of being compact, but the junction circuits (Heng, et al., 2014; Liu, et al., 2017) occupy large implementation areas. When we decrease the gap between spiral cells, they will be coupled to each other. The coupling between them creates some small coupling capacitors. Therefore, the inductor and capacitors can create passbands easily. The quad-band diplexer reported by Heng, et al. (2014) is designed based on proposing an *LC* circuit and finding the coupling coefficients. However, in Liu, et al., 2017, the even and odd modes resonance frequencies have been calculated as functions of ϵ_{eff} and light speed c . This diplexer is designed using BPF. Then, the coupling coefficient from the simulated *S*-parameters is extracted by:

$$M = (f_{o2}^2 - f_{o1}^2) / (f_{o2}^2 + f_{o1}^2) \quad (5)$$

Where f_{o1} and f_{o2} represent the lower and higher resonance frequencies of the proposed filter. To design a microstrip four-channel diplexer in Lee, et al., 2016, the step impedance cells have been used. In this work, the design method is based on the calculation of the resonance frequencies of step

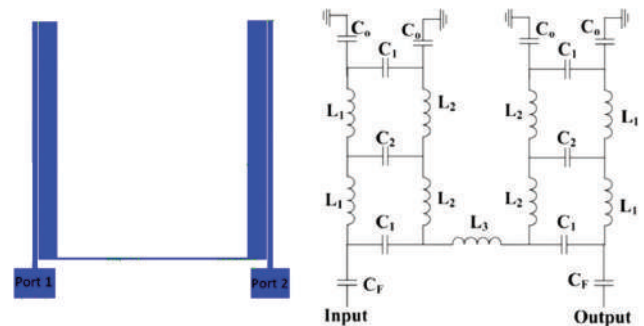
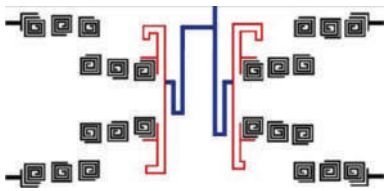
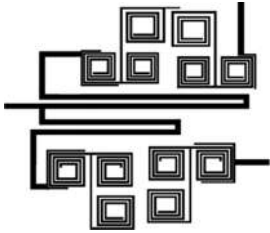
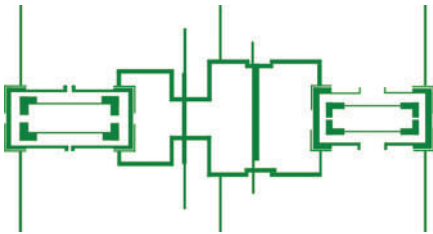
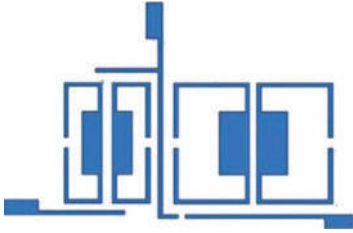
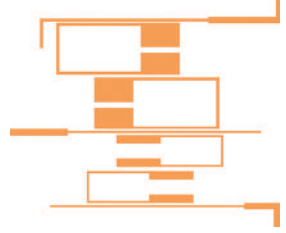
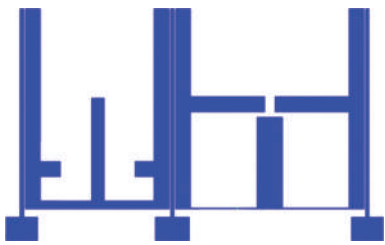


Fig. 3. The basic resonator and its approximated *LC* circuit presented by Noori and Rezaei (2018).

impedance sections without mathematical formulas. Coupled open loops have been integrated on RT/Duroid 5880 substrate with $\epsilon_r = 2.2$ and $h = 0.787$ mm to realize a four-channel diplexer in Wu, et al., 2013. In the loop structures, low impedance sections are utilized. The analysis of this structure is performed based on finding the impedance ratio of the low impedance section. Furthermore, similar to the proposed diplexer in Lee, et al., 2016, the coupling coefficients are obtained from the two resonant modes based on (5) using the full-wave electromagnetic simulator.

Coupled hairpins have been integrated in Hsu, et al., 2016, to obtain a microstrip diplexer with four passbands. This diplexer is designed based on finding the coupling coefficient as functions of the distance between resonators without mathematical formulas. To obtain a four channel diplexer in Noori and Rezaei, 2018, two similar dual-band BPF with

TABLE III
LAYOUT CONFIGURATION, SUBSTRATE TYPE, AND THEORY METHOD OF THE QUAD-BBD

Refs.	Diplexer structure	Substrate	Theory method
(Heng, et al., 2014)		MgO $\epsilon_r=9.8$ $h=0.5$ mm	Proposing an equivalent circuit model for the diplexer
(Liu, et al., 2017)		MgO $\epsilon_r=9.78$ $h=0.5$ mm	<ol style="list-style-type: none"> 1. Calculating of the external quality factors and coupling coefficients of the diplexer 2. Extracting the coupling coefficients from the simulated S-parameters
(Lee, et al., 2016)		RT/Duroid 6010 $\epsilon_r=10.2$ $h=0.635$ mm	Calculating the resonance frequencies of the step impedance sections without mathematical formulas
(Wu, et al., 2013)		RT/Duroid 5880 $\epsilon_r=2.2$ $h=0.787$ mm	Analysis based on finding the impedance ratio of the low impedance section
(Hsu, et al., 2016)		RT/Duroid 6010LM $\epsilon_r=10.2$ $h=0.635$ mm	Calculating the coupling coefficient as functions of the distance between resonators without mathematical formulas
(Noori and Rezaei, 2018)		RT/Duroid 5880 $\epsilon_r=2.2$ $h=0.787$ mm	<ol style="list-style-type: none"> 1. Proposing an Lc model for the basic resonator 2. Calculating the angular resonance frequency from Lc circuit

BBDS: Bandpass-bandpass diplexers

different dimensions have been designed and analyzed. For this purpose, first, an approximated LC model of the basic resonator is presented. Then, the input impedance of the LC circuit is extracted. Finally, an angular resonance frequency is calculated when the input impedance is zero. In this case, the dimensions can be tuned based on a target resonance frequency when the equations show the resonator behavior. The basic resonator and its approximated LC circuit (Noori and Rezaei, 2018) are presented in Fig. 3. As shown in

Fig. 3, the open ends and feed lines are replaced by the capacitors C_o and C_p , respectively.

Similar to the dual-band BBDSs, a high-performance quad-band bandpass diplexer must have low loss, high-frequency selectivity, suppressed harmonics, high isolation, and low group delay. The frequency response of the quad-band bandpass diplexers (Liu, et al., 2017; Lee, et al., 2016; Hsu, et al., 2016; Noori and Rezaei, 2018) is presented in Figs. 4(a)-(d), respectively. Advanced design system full-

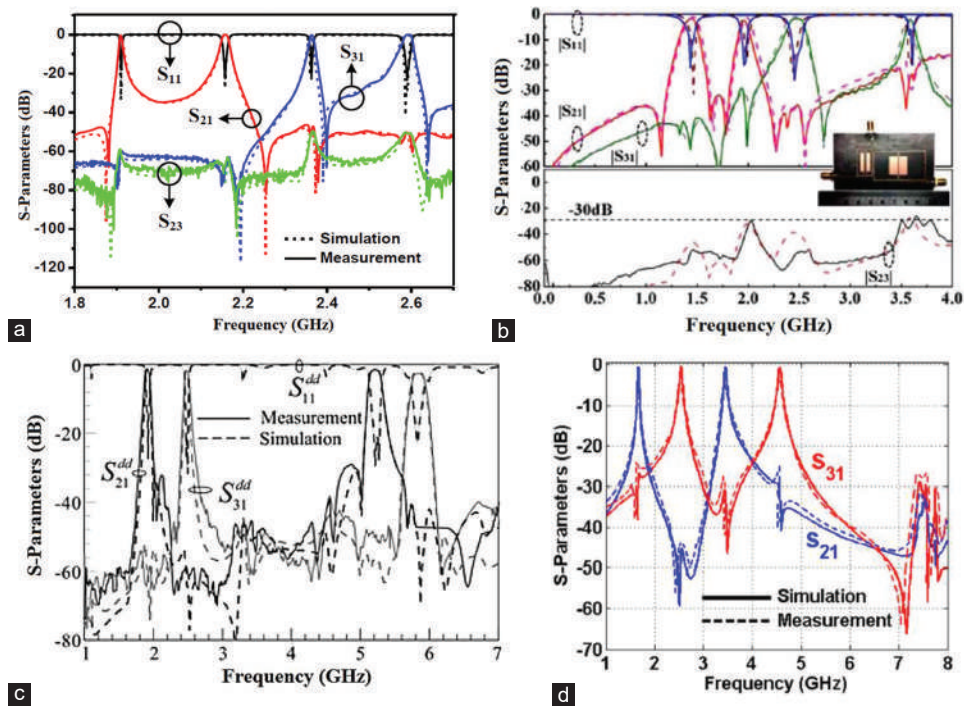


Fig. 4. Simulated and measured frequency response of four-channel diplexers: (a) (Liu, et al., 2017), (b) (Lee, et al., 2016), (c) (Hsu, et al., 2016), and (d) (Noori and Rezaei, 2018).

TABLE IV
PERFORMANCE AND SIZE COMPARISON AMONG DIFFERENT REPORTED QUAD-CHANNEL BBD

Refs.	ILs (dB)	RLs (dB)	Isolation (dB)	$f_{01}, f_{02}, f_{03}, f_{04}$ (GHz)	Size (λ_g^2)	FBWs (%)
(Heng, et al., 2014)	0.4, 0.33, 0.35, 0.45	19, 19, 19, 20	55	2.8, 2.81, 2.82, 2.83	1.17	0.2, 0.2, 0.2, 0.2
(Liu, et al., 2017)	0.24, 0.15, 0.18, 0.28	---	50	1.9, 2.15, 2.3, 2.5	0.037	0.44, 0.65, 0.45, 0.75
(Lee, et al., 2016)	1.38, 1.6, 1.52, 1.8	---	44.8	1.92, 2.45, 5.25, 5.81	0.962	7.8, 6.5, 4, 3.4
(Wu, et al., 2013)	0.8, 1, 0.7, 1.5	---	30	1.5, 2, 2.4, 3.5	0.078	8, 4, 6, 2
(Lai and Jeng, 2005)	---	10, 10, 7.75, 7.75	10	2.52, 4.02, 5.48, 7.13	0.22	---
(Hsu, et al., 2016)	2, 1.5, 2, 2.5	>13 dB	29	0.9, 1.5, 2.4, 3.5	0.042	4.3, 4.6, 3.3, 4
(Noori and Rezaei, 2018)	0.5, 0.38, 0.53, 0.58	20, 21, 25, 22	30	1.67, 2.54, 3.45, 4.57	0.029	1.2, 1.96, 1.15, 1.09
(Rezaei, et al., 2019)	0.59, 0.41, 0.45, 0.73	12.9, 21.6, 16.7, 12.6	23	2.07, 2.37, 3.94, 4.49	0.025	---

*: Approximated values. BBDS: Bandpass-bandpass diplexers

wave EM simulator has been used to simulate the reported diplexers. As depicted in Fig. 4, the selectivity of the proposed diplexer (Liu, et al., 2017) is poor where the other quad-band diplexers (Lee, et al., 2016; Hsu, et al., 2016; Noori and Rezaei, 2018) could improve the frequency selectivity. However, the proposed diplexer (Lee, et al., 2016) has low selectivity at its last channel. On the other hand, any of them could not attenuate the harmonics after the last channel.

The channels with 1% up to 3% FBW are narrowband (Yu and Chang, 1998). However, a narrowband BPF with 0.5% FBW is proposed (Chen, et al., 2015). As shown in Fig. 4d, the reported diplexer by Noori and Rezaei (2018) has very narrow channels with 1.2%, 1.96%, 1.15%, and 1.09% FBWs. The narrow channels of this diplexer give a good resistance against interference. The size and performance of the previously reported quad-channel diplexers are compared. The comparison results are listed in Table IV. The resonance frequency of the quad-channel diplexers at the 1st, 2nd, 3rd, and 4th channels are presented by f_{01}, f_{02}, f_{03} , and f_{04} . As written in Table IV, the lowest insertion losses of quad-band diplexers

are obtained (Liu, et al., 2017) while the best return losses are obtained (Noori and Rezaei, 2018). Getting high isolation between channels, when we have more number of channels is harder. The highest isolation of quad-channel diplexers is 55 dB, which is obtained (Heng, et al., 2014). Meanwhile, the introduced diplexer (Rezaei, et al., 2019) has the minimum overall size of $0.025 \lambda_g^2$ in comparison with the other reported quad-channel diplexers. Among multichannel diplexers, quad-channel diplexers are more designed. However, based on the tri-band unit cell, a six-channel diplexer is proposed in Ghafari and Afsahi, 2019. It operates at 3.4 GHz, 3.7 GHz, 5.6 GHz, 6 GHz, 7 GHz, and 7.6 GHz, which is suitable for wireless and WiMAX applications. Meanwhile, an eight-channel microstrip diplexer with a size of $0.1 \lambda_g^2$ is presented in Tu and Hung, 2014. It is designed using coupled closed loops with different widths. The channels of this diplexer are relatively narrow, with isolation between channels better than 29 dB. High selectivity and attenuated harmonics are the advantages of this work.

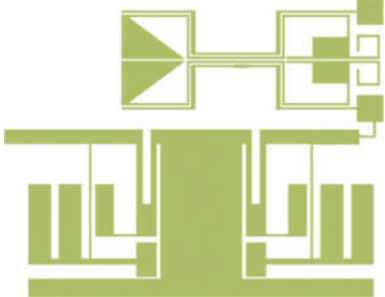
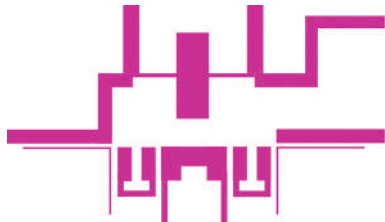
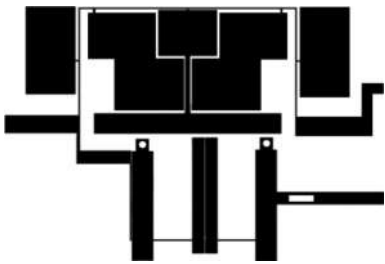
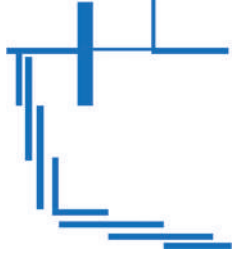
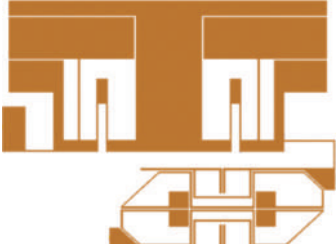
IV. LBDS

The microstrip LBDS are composed of microstrip LPF, BPF, and junction circuit. As mentioned earlier, to achieve a BBD, designing a bandpass resonator was enough. Then, the designed resonator is used to obtain two BPF to use in the diplexer structure.

However, it is necessary to design two bandpass and lowpass resonators to achieve a LBD. The LPF must have high performance with small normalized size. One advantage of a diplexer is its novel structure.

A novel LBD is designed (Rezaei, et al., 2019) for WLAN and WiMAX applications. It is implemented on RT/Duroid 5880 substrate. It includes a novel LPF composed of the patch and thin cells, a BPF, and a small junction circuit. For designing the lowpass section, first, a simple microstrip cell is simulated. Then, it is expanded and simulated step by step so that a very sharp lowpass channel is created. The passband channel of this diplexer is designed based on proposing a basic resonator and its equivalent LC circuit. Then, the even and odd modes of angular resonance

TABLE V
LAYOUT CONFIGURATION, SUBSTRATE TYPE, AND THEORY METHOD OF THE LBDS

Refs.	Diplexer structure	Substrate	Theory method
(Rezaei, et al., 2019)		RT/Duroid 5880 $\epsilon_r=2.2$ $h=0.787$ mm	1. Proposing an Lc model for the basic bandpass resonator 2. Calculating the angular even/odd modes resonance frequencies from Lc circuit
(Deng and Tsai, 2013)		Rogers RO4003C $\epsilon_r=3.55$ $h=1.524$ mm	Calculating of the electric lengths of the shunt open stub and high-impedance transmission line of the LPF
(Heshmati and Roshani, 2018)		RO4003C $\epsilon_r=3.38$ $h=0.813$ mm	Optimization method without mathematical analysis
(Capstick, 1999)		RT/Duroid 5880 $\epsilon_r=2.2$ $h=0.38$ mm	Designing the LPF for 50Ω stub $\lambda/4$ long at the center frequency of the bandpass filter
(Hayati, et al., 2019)		RT/Duroid6002 $\epsilon_r=2.93$ $h=30$ mil	1. Proposing Lc circuits for the LPF and BPF 2. Calculating ABCD matrix of the LPF 3. Finding a method to create a lowpass channel 4. Calculating an angular resonance frequency of the BPF

LBDS: Lowpass-bandpass diplexers, LPF: Lowpass filter, BPF: Bandpass filters

frequencies of the *LC* model are calculated. Furthermore, a method to attenuate the harmonics is performed similarly to the proposed method (Salehi and Noori, 2015). In this method, all resonance frequencies have been calculated, where the resonance frequency is the main and the others are harmonics. To attenuate these harmonics, the undesirable resonance frequencies and main resonance frequency are set equal. Layout configuration, substrate type, and summarized theory method of the previous reported LBDs are presented in Table V. As depicted in Table V, the use of coupled microstrip cells in the lowpass sections is not essential.

However, the engraved patch cells are utilized (Heshmati and Roshani, 2018; Hayati, et al., 2019). The U-shape cells are coupled to create the bandpass channel (Deng and Tsai, 2013), whereas the bandpass channel (Capstick, 1999) is formed by the simple coupled lines. In (Deng and Tsai, 2013), an equivalent circuit model of the proposed LBD is presented. The LPF utilized (Deng and Tsai, 2013) is fifth-order while the electric lengths of the shunt open stub (θ_i) and series high-impedance transmission line (θ_k) are calculated as follows:

$$\theta_i = \tan^{-1}(2\pi f_c C_i Z_i) \text{ for } i = 1,3,5$$

$$\theta_k = \sin^{-1}\left(\frac{2\pi f_c L_k}{Z_k}\right) \text{ for } K = 2,4$$

Where f_c is the cutoff frequency of the LPF, C_i and L_k are the required lumped capacitors and inductors, respectively. The parameters Z_i and Z_k are the characteristic impedances. The proposed LBD (Heshmati and Roshani, 2018) is realized based on an optimization method without mathematical analysis. In Capstick, 1999; first, a lowpass prototype is created with the first capacitor C_1 defined as follows:

$$C_1 = \frac{\tan\left(\frac{\pi f_c}{2f_o}\right)}{2\pi f_c Z}$$

Where f_c , f_o , and Z are the LPF cutoff frequency, the BPF center frequency, and the stub impedance, respectively. Then, the lowpass prototype is transformed into microstrip using the method outlined (Capstick, 1994). After that, a Chebyshev BPF is designed and connected to the LPF. To design the LBD in Hayati, et al., 2019, a perfect mathematical method

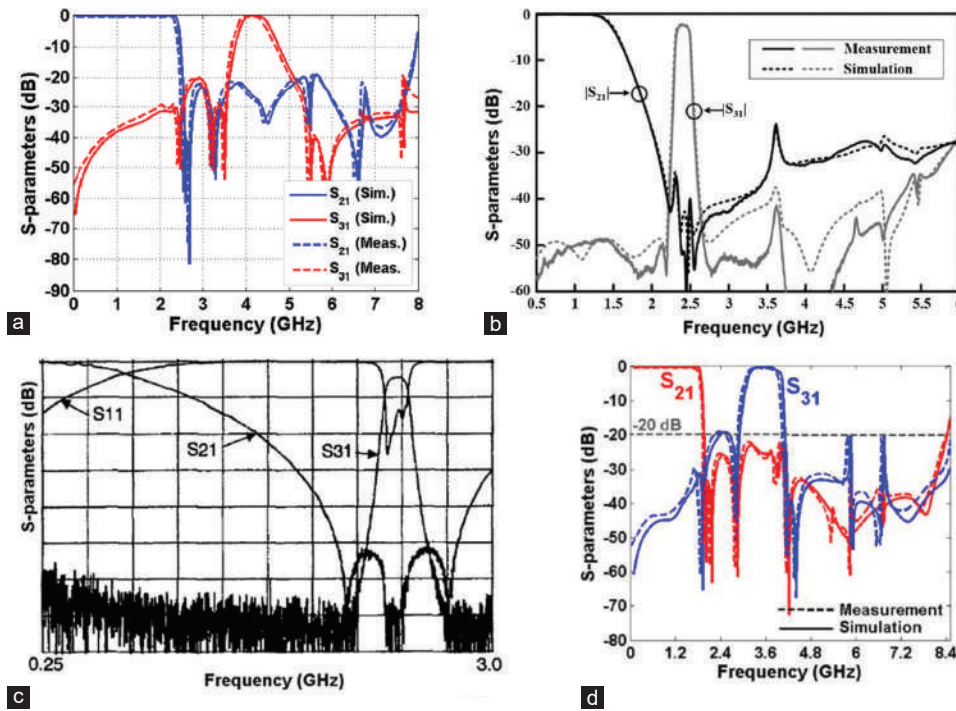


Fig. 5. Simulated and measured frequency responses of four-channel diplexers (a) (Rezaei, et al., 2019), (b) (Deng and Tsai, 2013), (c) (Capstick, 1999), and (d) (Hayati, et al., 2019).

TABLE VI
PERFORMANCE COMPARISON BETWEEN THE LBDs

Refs.	IL1, IL2 (dB)	RL1, RL2 (dB)	Size (λ_g^2)	Isolation (dB)	f_c, f_r (GHz)	f_r/f_c (GHz)
(Rezaei, et al., 2019)	0.15, 0.18	18.2, 41.4	0.036	26	2.4, 4.2	1.75
(Deng and Tsai, 2013)	0.25, 2.42	15, 15	0.49	35	1.5, 2.4	1.6
(Rayatzadeh and Moloudian, 2019)	0.2, 0.8	---	---	30	1, 2.4	2.4
(Heshmati and Roshani, 2018)	0.25, 0.58	15, 30	0.046	35	1, 2.4	2.4
(Capstick, 1999)	1, 4.8	---	---	---	0.6, 2.4	4
(Hayati, et al., 2019)	0.12, 0.10	19.2, 36	0.03	20	1.88, 3.56	1.89

*: Approximated values. LBD: Lowpass-bandpass diplexers

is done to design both lowpass and bandpass sections. The approximated equivalent LC models of both lowpass and bandpass resonators are proposed. Then, using the LC circuits, the ABCD matrix for the LPF and the resonance for the bandpass resonator are calculated and analyzed to find the behavior of the device and better tuning the physical dimensions.

The frequency response of the LBDs is depicted in Figs. 5(a)-(d) (Rezaei, et al., 2019; Deng and Tsai, 2013; Capstick, 1999; Hayati, et al., 2019). As shown in Fig. 5, the designed LBDs (Rezaei, et al., 2019; Hayati, et al., 2019) have the advantage of high selectivity, whereas in (Deng and Tsai, 2013; Capstick, 1999) there are poor roll-off at the lowpass channels.

Moreover, the proposed diplexer (Capstick, 1999) could not attenuate the harmonics. Totally, the best selectivity and suppressed harmonics are obtained (Hayati, et al., 2019). The size and performance of the previous reported LBDs are compared in Table VI. In Table VI, IL and RL are the insertion and return losses where the indexes 1 and 2 are related to the lowpass and bandpass channels, respectively. The lowpass channel cutoff frequency and bandpass channel resonance frequency are shown with f_c and f_p , respectively. As written in Table VI, the best insertion and return losses are achieved (Hayati, et al., 2019) while it occupies the most compact area $0.03\lambda_g^2$. The highest isolation between channels and the smallest gap between channels are obtained (Deng and Tsai, 2013) by victimizing the overall size so that it has the largest size ($0.49\lambda_g^2$).

V. CONCLUSION

Several types of microstrip diplexers are studied in this work. The structures and mathematical design methods of these diplexers are reviewed. The reviewed microstrip diplexers are dual-band BBD, LBDs, and multichannel diplexers. Some of the design methods of these works were based on proposing an equivalent LC circuit. Therefore, we presented and explained some proposed LC models of the resonator layouts. The mathematical equations presented in some works were explained too. The layout configurations of the previously reported works with their used substrates were shown and described. The performance of the reviewed diplexers in terms of losses, isolation, selectivity, harmonics, isolation, and the gap between channels is compared. We believe that this review paper may serve a useful guide for researchers who are interested in microstrip diplexers design.

REFERENCES

- Bui, D.H.N., Vuong, T.P., Allard, B., Verdier, J. and Benech, P., 2017. Compact low-loss microstrip diplexer for RF energy harvesting. *Electronics Letters*, 53(8), pp.552-554.
- Bukuru, D., Song, K. and Xue., 2015. Compact wide-stopband planar diplexer based on rectangular dual spiral resonator. *Microwave and Optical Technology Letters*, 57(1), pp.174-178.
- Capstick, M.H., 1994. Simple fast synthesis method for microstrip lowpass filters. *Electronics Letters*, 30(18), pp.1496-1497.
- Capstick, M.H., 1999. Microstrip lowpass-bandpass diplexer topology. *Electronics Letters*, 35(22), pp.1958-1960.
- Chen, C.F., Huang, T.Y., Chou, C.P. and Wu, R.B., 2006. Microstrip diplexers design with common resonator sections for compact size, but high isolation. *IEEE Transactions on Microwave Theory and Techniques*, 54(5), pp.1945-1952.
- Chen, C.F., Zhou, K.W., Chen, R.Y., Wang, Z.C. and He, Y.H., 2019. Design of a microstrip diplexer-integrated filtering power divider. *IEEE Access*, 7, pp.106514-106520.
- Chen, D., Zhu, L., Bu, H. and Cheng, C.H., 2015. A novel planar diplexer using slot line-loaded microstrip ring resonator. *IEEE Microwave and Wireless Components Letters*, 25(11), pp.706-708.
- Chen, J.X., Zhan, Y., Qin, W., Bao, Z.H. and Xue, Q., 2015. Novel narrow-band balanced Bandpass filter using rectangular dielectric resonator. *IEEE Microwave and Wireless Components Letters*, 25(5), pp.289-291.
- Cheng, F., Lin, X., Song, K., Jiang, Y. and Fan, Y., 2013. Compact diplexer with high isolation using the dual-mode substrate integrated waveguide resonator. *IEEE Microwave and Wireless Components Letters*, 23, pp.459-461.
- Chinig, A., 2017. A novel design of microstrip diplexer using meander-line resonators. *International Journal of Electronic Engineering and Computer Science*, 2(2), pp.5-10.
- Chinig, A., Zbitou, J., Errkik, A., Elabdellaoui, L., Tajmouati, A., Tribak, A., and Latrach, M., 2015. A new microstrip diplexer using coupled stepped impedance resonators. *International Journal of Electronics and Communication Engineering*, 9(1), pp.41-44.
- Chinig, A., Zbitou, J., Errkik, A., Tajmouati, A., Abdellaoui, L.E. and Latrach, M., 2015. Microstrip diplexer using stepped impedance resonators. *Wireless Personal Communications*, 84(4), pp.2537-2548.
- Deng, H.W., Zhao, Y.J., Fu, Y., Ding, J. and Zhou, X.J., 2013. Compact and high isolation microstrip diplexer for broadband and WLAN applications. *Progress in Electromagnetics Research*, 133, pp.555-570.
- Deng, P.H. and Tsai, J.T., 2013. Design of microstrip lowpass-bandpass diplexer. *IEEE Microwave and Wireless Components Letters*, 23(7), pp.332-334.
- Feng, W., Gao, X. and Che, W., 2014. Microstrip diplexer for GSM and WLAN bands using common shorted stubs. *IET Electronics Letters*, 50(20), pp.1486-1488.
- Feng, W., Zhang, Y. and Che, W., 2017. Tunable dual-band filter and diplexer based on folded open loop ring resonators. *IEEE Transactions on Circuits and Systems*, 64(9), pp.1047-1051.
- Ghafari, B. and Afsahi, M., 2019. Design of compact multi-channel diplexer using defected microstrip structure. *Journal of Communication Engineering*, 8(1), pp.138-145.
- Guan, X., Yang, F., Liu, H. and Zhu, L., 2014. Compact and high-isolation diplexer using dual-mode stub-loaded resonators. *IEEE Microwave and Wireless Components Letters*, 24(6), pp.385-387.
- Hayati, M., Rezaei, A. and Noori, L., 2019. Design of a high performance lowpass bandpass diplexer using a novel microstrip structure for GSM and WiMAX applications. *IET Circuits Devices and Systems*, 13(3), pp.361-367.
- Heng, Y., Guo, X., Cao, B., Wei, B., Zhang, X., Zhang, G. and Song, X., 2014. A narrowband superconducting quadruplexer with high isolation. *IEEE Transactions on Applied Superconductivity*, 24(2), pp.21-26.
- Heshmati, H. and Roshani, S., 2018. A miniaturized lowpass bandpass diplexer with high isolation. *AEU International Journal of Electronics and Communications*, 87, pp.87-94.
- Hsu, K.W., Hung, W.C. and Tu, W.H., 2016. Design of four-channel diplexer using distributed coupling technique. *Microwave and Optical Technology Letters*, 58(1), pp.166-170.
- Huang, F., Wang, J., Zhu, L. and Wu, W., 2016. Compact microstrip balun diplexer using stub-loaded dual-mode resonators. *IET Electronic Letters*, 52, pp.1994-1996.

- Jun-Mei, Y., Zhou, H.Y. and Cao, L.Z., 2016. Compact diplexer using microstrip half- and quarter wavelength resonators. *Electronics Letters*, 52(19), pp.1613-1615.
- Lai, M.L. and Jeng, S.K., 2005. A microstrip three-port and four-channel multiplexer for WLAN and UWB coexistence. *IEEE Transaction on Microwave Theory and Technique*, 53(10), pp.3244-3250.
- Lee, C.H., Hsu, C.I.G., Wu, S.X. and Wen, P.H., 2016. Balanced quad-band diplexer with wide common-mode suppression and high differential-mode isolation. *IET Microwaves Antennas and Propagation*, 10(6), pp.599-603.
- Liu, H., Zhu, S., Wen, P., Zhang, X., Sun, L. and Xu, H., 2017. Design of quad-channel high-temperature superconducting diplexer using spiral stub-loaded resonators. *IEEE Transactions on Applied Superconductivity*, 27(4), pp.75-79.
- Lobato-Morales, H., Sun, J.S., Corona-Chavez, A., Itoh, T. and Olvera-Cervantes, J.L., 2012. UWB and WiLAN microstrip diplexer for differential-mode operation. 2012 IEEE/MTT-S International Microwave Symposium Digest.
- Noori, L. and Rezaei, A., 2017. Design of a microstrip diplexer with a novel structure for WiMAX and wireless applications. *AEU-International Journal of Electronics and Communications*, 77, pp.18-22.
- Noori, L. and Rezaei, A., 2017. Design of a microstrip dual-frequency diplexer using microstrip cells analysis and coupled lines components. *International Journal of Microwave and Wireless Technologies*, 9(7), pp.1467-1471.
- Noori, L. and Rezaei, A., 2017. Design of microstrip wide stopband quad-band bandpass filters for multi-service communication systems. *AEU-International Journal of Electronics and Communications*, 81, pp.136-142.
- Noori, L. and Rezaei, A., 2018. Design of a compact narrowband quad-channel diplexer for multi-channel long-range RF communication systems. *Analog Integrated Circuits and Signal Processing*, 94(1), pp.1-8.
- Peng, H. and Chiang, Y., 2015. Microstrip diplexer constructed with new types of dual-mode ring filters. *IEEE Microwave and Wireless Components Letters*, 25(1), pp.7-9.
- Rayatzadeh, S. and Moloudian, G., 2019. Design and fabrication of a miniaturized lowpass-bandpass diplexer with wide tuning range and high isolation, *Journal of Electromagnetic Waves and Applications*, 33, pp.1874-1889.
- Rezaei, A. and Noori, L., 2018. Compact low-loss microstrip diplexer using novel engraved semi-patch cells for GSM and WLAN applications. *AEU-International Journal of Electronics and Communications*, 87, pp.158-163.
- Rezaei, A. and Noori, L., 2018. Miniaturized microstrip diplexer with high performance using a novel structure for wireless L-band applications. *Wireless Networks*, 26, pp.1-8.
- Rezaei, A. and Noori, L., 2018. Novel compact microstrip diplexer for GSM applications. *International Journal of Microwave and Wireless Technologies*, 10(3), pp.313-317.
- Rezaei, A. and Noori, L., 2018. Novel microstrip quadruplexer with wide stopband for WiMAX applications. *Microwave and Optical Technology Letters*, 60(6), pp.1491-1495.
- Rezaei, A., Noori, L. and Jamaluddin, M.H., 2019. Novel microstrip lowpass-bandpass diplexer with low loss and compact size for wireless applications. *AEU-International Journal of Electronics and Communications*, 101, pp.152-159.
- Rezaei, A., Noori, L. and Mohammadi, H., 2017. Design of a novel compact microstrip diplexer with low insertion loss. *Microwave and Optical Technology Letters*, 59(7), pp.1672-1676.
- Rezaei, A., Noori, L. and Mohammadi, H., 2019. Design of a miniaturized microstrip diplexer using coupled lines and spiral structures for wireless and WiMAX applications. *Analog Integrated Circuits and Signal Processing*, 98, pp.409-415.
- Rezaei, A., Noori, L. and Mohammadi, H., 2019. Miniaturized quad-channel microstrip diplexer with low insertion loss and wide stopband for multi-service wireless communication systems. *Wireless Networks*, 25(6), pp.2989-2996.
- Rezaei, A., Yahya, S.I., Noori, L. and Jamaluddin, M.H., 2019. Design and fabrication of a novel compact low-loss microstrip diplexer for WCDMA and WiMAX applications. *Journal of Microwaves Optoelectronics and Electromagnetic Applications*, 18(4), pp.482-491.
- Rezaei, A., Yahya, S.I., Noori, L. and Jamaluddin, M.H., 2019. Design of a novel wideband microstrip diplexer using artificial neural network. *Analog Integrated Circuits and Signal Processing*, 101(1), pp.57-66.
- Salehi, M. and Noori, L., 2015. Miniaturized microstrip Bandpass filters using novel stub loaded resonator. *Applied Computational Electromagnetics Society*, 30(6), pp.692-697.
- Salehi, M. and Noori, L., 2014. Novel 2.4 Ghz branch-line coupler using microstrip cells. *Microwave and Optical Technology Letters*, 56(9), pp.2110-2113.
- Salehi, M.R., Keyvan, S., Abiri, E. and Noori, L., 2016. Compact microstrip diplexer using new design of triangular open loop resonator for 4G wireless communication systems. *AEU International Journal of Electronics and Communications*, 70(7), pp.961-969.
- Salehi, M.R., Noori, L. and Abiri, E., 2016. Prediction of matching condition for a microstrip subsystem using artificial neural network and adaptive neuro-fuzzy inference system. *International Journal of Electronics*, 103(11), pp.1882-1893.
- Sasipriya, S. and Aparna, C.B., 2018. Compact microstrip diplexer using Bandstop filters for GSM applications. *International Journal of Pure and Applied Mathematics*, 119(12), pp.1395-1401.
- Shen, G. and Che, W., 2020. Compact Ku-band LTCC Bandpass filter using folded dual-composite right and left-handed resonators. *Electronics Letters*, 56(1), pp.17-19.
- Tu, W.H. and Hung, W.C., 2014. Microstrip eight-channel diplexer with wide stopband. *IEEE Microwave and Wireless Components Letters*, 24(11), pp.742-744.
- Wang, X., Wei, B., Zheng, T., Cao, B., Jiang, L. and Chen, J., 2016. Design and implementation of a narrow-band superconducting X-band diplexer with high isolation. *Physica C: Superconductivity and its Applications*, 531, pp.9-13.
- Wu, H.W., Huang, S.H. and Chen, Y.F., 2013. Design of new quad-channel diplexer with compact circuit size. *IEEE Microwave and Wireless Components Letters*, 23(5), pp.240-242.
- Xiao, J.K., Zhu, M., Li, Y., Tian, L. and Ma, J.G., 2015. High selective microstrip bandpass filter and diplexer with mixed electromagnetic coupling. *IEEE Microwave and Wireless Components Letters*, 25(12), pp.781-783.
- Yahya, S.I., Rezaei, A., Noori, L. and Jamaluddin, M.H., 2019. Wide Stopband Microstrip Diplexer Using a Novel Configuration for Frequency Division Duplex and GSM-4G Applications. 2019 *International Conference on Engineering, Science, and Industrial Applications*, pp.1-15.
- Yang, F., Guan, X., Zhu, L. and Liu, H., 2014. Compact microstrip diplexer for 4G Wireless communication. *Progress in Electromagnetics Research Symposium Proceedings*, 25, pp.599-602.
- Yu, C.C. and Chang, K., 1998. Novel compact elliptic-function narrow-band Bandpass filters using microstrip open-loop resonators with coupled and crossing lines. *IEEE Transactions on Microwave Theory and Techniques*, 46(7), pp.952-958.

Automatic Recognition of Arabic Poetry Meter from Speech Signal using Long Short-term Memory and Support Vector Machine

Abdulbasit K. Al-Talabani

Department of Software Engineering, Faculty of Engineering, Koya University,

Koya KOY45, Kurdistan Region - F.R. Iraq

Abstract—The recognition of the poetry meter in spoken lines is a natural language processing application that aims to identify a stressed and unstressed syllabic pattern in a line of a poem. State-of-the-art studies include few works on the automatic recognition of Arud meters, all of which are text-based models, and none is voice based. Poetry meter recognition is not easy for an ordinary reader, it is very difficult for the listener and it is usually performed manually by experts. This paper proposes a model to detect the poetry meter from a single spoken line (“Bayt”) of an Arabic poem. Data of 230 samples collected from 10 poems of Arabic poetry, including three meters read by two speakers, are used in this work. The work adopts the extraction of linear prediction cepstrum coefficient and Mel frequency cepstral coefficient (MFCC) features, as a time series input to the proposed long short-term memory (LSTM) classifier, in addition to a global feature set that is computed using some statistics of the features across all of the frames to feed the support vector machine (SVM) classifier. The results show that the SVM model achieves the highest accuracy in the speaker-dependent approach. It improves results by 3%, as compared to the state-of-the-art studies, whereas for the speaker-independent approach, the MFCC feature using LSTM exceeds the other proposed models.

Index Terms—Speech processing, Long short-term memory, Support vector machine, Prosody, Cepstral features.

I. INTRODUCTION

Arabic poetry prosody (APP) (“Arud” عروض in Arabic) is the science that measures classical Arabic rhymed poetry (Stoetzer, 1989). Poetry meters (“Bahr” بحر or “Wazn” وزن in Arabic) are a sequence of diacritics representing a stressed and unstressed syllabic pattern adopted in APP to classify poetries into different classes based on special rules called meters. APP has been adapted to other eastern poetries such as Kurdish, Persian, and Urdu poetries (Kurta and Kara, 2012). A poem’s meter is important for evaluating the

commitment of classical poems to the musical flow. However, unlike understanding a poem’s meaning, detecting a poem’s meter is difficult for the ordinary reader, is much harder for listeners, and is mostly done by experts.

Arud meter recognition (AMR) in Arabic poetry is a much-studied topic. Most of these studies are theoretical and few are practical. The history of theoretical studies in Arud metrics is very old and dates back to the founder of the science, Al-Khalil bin Ahmad Al-Farahidi (AD 718-786) (Arberry, 1965), and addresses the theoretical problems of this science (Morris, 1966). However, few works have been done regarding automatic AMR (AAMR), and none have adopted AAMR using speech signals, but rather they are text-based proposed models. For example, Ismail et al. (2010) developed a prototype, expert system harmony test to provide expert-level solutions for testing harmony correction and to identify the pattern (“Bahr”) of Arabic poetry. In Alnagdawi et al. (2013), the authors implemented a tool to find an Arabic poem meter using context-free grammar. They used trimmed poems (words with “Tashkeel”) to detect the meter in Arabic poetry. Abuata and Al-Omari (2018) introduced an algorithm that can determine the correct meter for a given Arabic poem and are also able to convert the poem into Arud Writing. The algorithm is based on a set of well-defined rules applied only to the first part (“Sadr”) of the poem’s verse. In more advanced work, Yousef et al. (2019) have recognized 16 meters of Arabic poetry and four meters of English from the plain text using recurrent neural network (RNN) with an overall accuracy of 96.38% and 82.31%, respectively.

Another work close to the automatic recognition of Arud meters (AARM) model that is found in the literature is rhyme (“Qafiah” قافية) detection. For instance, Hirjee and Brown (2010) developed a method to score potential rhymes using a probabilistic model based on phoneme frequencies in rap lyrics. However, the work adopted the use of lyric text as an input rather than vocal input. We are not aware of any academic work that takes vocal or audio rendition poetry as an input to the AARM model.

AARM, using audio, aims to analyze the speech signal and uses its features to detect meters from the read poem. This work’s main contribution is to introduce a model to recognize the meters from a voice recording of a spoken line (Bayt) of

ARO-The Scientific Journal of Koya University
Vol. VIII, No.1(2020), Article ID: ARO.10631, 5 pages
DOI: <http://dx.doi.org/10.14500/aro.10631>
Received 03 February 2020; Accepted: 27 March 2020
Regular research paper: Published 14 April 2020

Corresponding author’s e-mail: abdulbasit.faeq@koyauniversity.org
Copyright © 2020 Abdulbasit K. Al-Talabani. This is an open-access article distributed under the Creative Commons Attribution License.



an Arabic poem. The application proposed in this paper will help learners recognize the meters of a poem through reading instead of writing it down. It could be also adapted to help learners to improve their pronunciation of the classical poem in the correct way, as a computer-based assessment of language speaking skills (Araújo, 2010). The poetry meter has also been used as a feature to detect the authorship of unknown poems (Al-Falahi, et al., 2017). Poetry meters could also be used to improve studies that try to find out poets' differences and similarities through analyzing their works using natural language understanding technologies (Zhang and Gao, 2017).

The data used in this work are 230 single poem lines recorded by two male readers of three different meters (Taweel, Kameel, and Baseet), which accounted as the most prevalent meters, and where Taweel is the most used due to its simplicity (Scott, 2010). This work aims to detect the poetry meter, based on the speech prosody characteristics of the recording signal. We proposed to extract the linear prediction cepstrum coefficient (LPCC) and Mel frequency cepstral coefficient (MFCC) cepstral features, where the cepstral coefficients are derived from either LP analysis or a filter bank approach and are almost treated as standard front end features (Rao and Koolagudi, 2013). Cepstral features have achieved a high level of accuracy for speech recorded in a non-noisy environment (Reynolds, 1995) and are used as an essential feature in speaker verification (Sarangi and Saha, 2020). The poetry meter data should have a time series nature because it depends on how the patterns ("Tafa'il" "لـى عافت") come next to each other. The classifier with a time series nature is expected to be more suitable for such an application. In this paper, we adopt the use of long short-term memory (LSTM) (Hochreiter and Schmidhuber, 1997). LSTM is a form of RNN and has been proposed to overcome the problem of vanishing gradient from which RNN suffers. The model changes the standard RNN hidden layer, where each ordinary node in the hidden layer is replaced by a memory cell (Lipton, et al., 2015). In this work, the classifier takes the LPCC and MFCC features and maps each input into a single label or Arud meter. However, we can also deal with the data as a non-time series signal features where the order of the patterns' features is not important, but rather are the global feature of all of the lines of read poetry. Statistics such as mean and standard deviation is used in this work to globalize the features to later feed the support vector machine (SVM) classifier (Vapnik, 1995).

The rest of this paper is organized as follows: In Section II, an entry to the Arabic prosody science (Arud) is presented, followed by the scope of this work in Section III. Section IV presents the methodology needed for this work. Finally, a discussion of the results and a conclusion are reported in Sections V and VI, respectively.

II. ARABIC POETRY PROSODY (APP)

Classical Arabic poems have features common to poems written in some other eastern languages, whereas some features are unique to Arabic poetry. The science was established in the pre-Islamic era and has remained almost unchanged until now (Almuhareb, et al., 2013). The main

two types of Arabic poetry are, rhymed or measured and prose. Al-Khalil bin Ahmad Al-Farahidi is the founder of rhymed, which is called Arud in Arabic. Arud is the science that studies the meter used in classical Arabic and some other eastern languages. Al-Farahidi wrote 15 meters ("seas," Bahr in Arabic) and was followed by another meter written by his student Al-Akhfash giving a total of 16 meters (Yousef, et al., 2019). The measuring unit of meters is called Patterns ("Tafa'il"), in which each contains a certain number of Tafa'il, which the poet follows in every line (Bayt) of the poem. The original main patterns are shown in Table I Abuata and Al-Omari (2018). Classic Arabic poetry ends with the same rhyme (qafiyah), and each meter has its own key which is followed in each line along with the poem. The key consists of a list of patterns that represent the order of the consonant and vowel sounds presented in each Bayt. The pattern could also be represented in terms of scansion (Movement "Harakah" or Stillness "Sukun"). Table II presents the three meters included in this study with their scansion (Yousef, et al., 2019).

III. THE SCOPE OF THE WORK

In this paper, we claim that a poem's meters can be automatically recognized by a spoken line of poetry. In addition, this work will investigate the hypothesis of how a time series representation of the spoken poetry line is different from a non-time series representation. Various meters are supposed to have a different sequence of patterns based on each meter (Figs. 1 and 2). Consequently, whenever the poetry line is read correctly the sequence of features of each speech signal will reflect the sequence of the patterns. This work aims to design a model to map the stream of feature values or a global feature for each poetry line into the correct meter that the poem follows.

IV. METHODOLOGY

As in any pattern recognition process, the feature extraction step is mandatory for discovering the input's most "useful"

TABLE I
THE EIGHT MAIN PATTERNS AND THEIR SCANSIONS (KURTA AND KARA, 2012)

Pattern	Scansion
Fe'ülün	■--
Fâ'ilün	--■-
Müstef'ilün	--■-
Mefâ'ilün	■---
Mef'ülâtü	---■
Fâ'ilâtün	■-■-■-
Mütefâ'ilün	■-■-■-

TABLE II
THE METERS IN THIS WORK AND THEIR SCANSIONS

Meter	Key pattern	Scansion
Al-Taweel	فـولن مفاعيلن فـولن مفاعيلن	o//o// o/o// o/o// o/o//
Al-Kamil	مـتفاعيلن مـتفاعيلن مـتفاعيلن	o//o// o//o// o//o//
Al-Baseet	مـستـعـلـن فـاعـلن مـسـتـعـلـن فـاعـلن	o// o//o/o/ o//o/ o//o/o/

information, related to the pattern needed to be detected or recognized. For speech inputs, and due to the non-stationary characteristics of the speech, features are normally extracted globally or locally. The local feature is computed for each frame for a length of 30 m, where the signal tends to be more stationary (Rutledge, 1995). The global features are the measurements that represent the whole signal that could be computed by applying some statistics to the local feature values in the frames. In this paper, we extracted 12 LPCCs using LP analysis in addition to 12 MFCCs for each frame of 30 m. A total of 24 features represent each frame, and consequently, the time series version of the data will be represented in terms of a number of n samples where each has 24 features for each m_i frame, where $i=1, 2, \dots, n$. One of the problems facing time series applications is the unequal

length of the input samples that occur where the number of frames per samples is different. In this work, we follow sample frame padding for all of the samples to the length of the longest included sample.

There are other time series classifiers such as the well-known hidden Markov model (HMM). However, the traditional Markov model approaches are limited because their states must be drawn from a modestly sized discrete state space S , and the dynamic programming algorithm is used to perform efficient inference with HMMs scales in time $O(|S|^2)$ (Lipton, et al., 2015). The value of each memory cell in LSTM is controlled with input, modulation, forget, and output gates that allow the LSTM network to store values for many time steps by controlling access to the memory cell (Sønderby, et al., 2015). Consequently, in this work, we propose to use the LSTM classifier for the time series based approach. The LSTM model used in this work includes one LSTM layer with 100 hidden units and Adam optimization, in addition to a fully connected layer followed by a softmax layer and the adopted learning rate is 0.001. The whole recognition process is presented in Fig. 3 and the LSTM architecture is presented in Fig. 4.

For the non-time series version of the data, the mean and the standard deviation of every single feature along the frames have been computed and results in 48 features for every single sample. The features feed a three pairwise SVMs and majority voting is adopted to make the final decision.

The dataset used for this work is prepared and includes 230 Bayt chosen from 10 Arabic poems spoken by two subjects. The data include three meters: Taweel, Kameel, and Baseet with 79, 74, and 77 lines (Bayt).

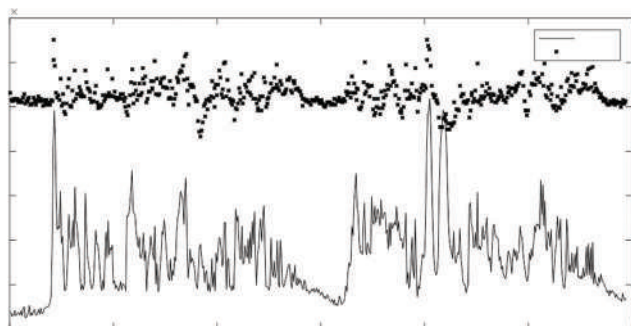


Fig. 1. First and second Mel frequency cepstral coefficient (MFCC) of a sample from the Baset meter. The X-axis represents the number of frames, whereas the Y-axis shows the MFCC value.

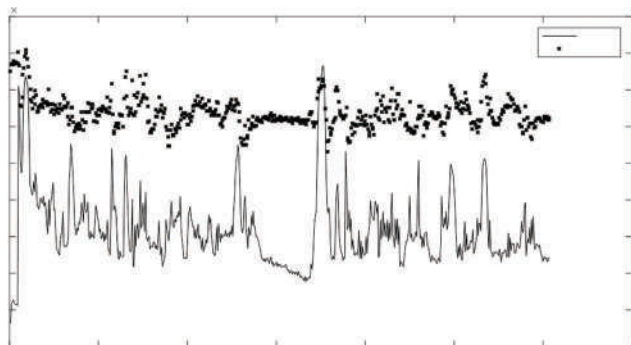


Fig. 2. First and second Mel frequency cepstral coefficient (MFCC) of a sample from the Taweel meter. The X-axis represents the number of frames, whereas the Y-axis shows the MFCC value.

V. RESULTS AND DISCUSSION

The work adopted speaker-dependent (SD) and speaker-independent (SI) approaches to conduct the experiments. In the SD case, 10-fold cross-validation was applied to both time series features, where the LSTM classifier is used, and non-time series features use an SVM classifier. The experiment is applied to each three sets of features, LPCC, MFCC, and in addition to their fusing features. Results show that the MFCC feature achieves better accuracy (0.9957 and 0.9457) than the LPCC feature (0.9939 and 0.9739) using both SVM and LSTM, respectively (Table III). In addition, the fusion features were not able to improve the MFCC accuracy in both models. However, a high diversity

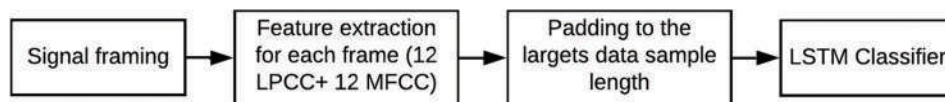


Fig. 3. The adopted algorithm.

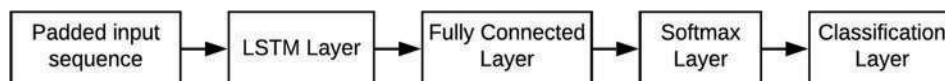


Fig. 4. The adopted long short-term memory architecture.

TABLE III

THE AVERAGE AND STANDARD DEVIATION OF SPEAKER DEPENDENT BASED EXPERIMENTS RESULTS OVER 10 FOLDS, "STD" STANDS FOR THE STANDARD DEVIATION

Classifier	Features	Accuracy mean	Accuracy STD	Precision mean	Precision STD	F score mean	F score STD
LSTM	MFCC	0.9457	0.0728	0.9617	0.0482	0.9506	0.0661
	LPCC	0.8834	0.0665	0.9027	0.0631	0.9129	0.0708
	Both	0.9057	0.0838	0.9117	0.0817	0.909	0.0811
SVM	MFCC	0.9957	0.003	0.9958	0.0031	0.9952	0.002
	LPCC	0.9739	0.006	0.9738	0.0052	0.9738	0.0052
	Both	0.9913	0.005	0.9914	0.0041	0.9914	0.0041

MFCC: Mel frequency cepstral coefficient, LSTM: Long short-term memory, SVM: Support vector machine, LPCC: Linear prediction cepstrum coefficient

TABLE IV

THE RESULTS OF THE SPEAKER INDEPENDENT BASED EXPERIMENTS

Classifier	Features	Accuracy	Precision	F score
LSTM	MFCC	0.8889	0.9167	0.9026
	LPCC	0.5111	0.8181	0.6243
	Both	0.6889	0.7520	0.7191
SVM	MFCC	0.6875	0.6875	0.6875
	LPCC	0.6071	0.6071	0.6071
	Both	0.705	0.705	0.705

MFCC: Mel frequency cepstral coefficient, LSTM: Long short-term memory, SVM: Support vector machine, LPCC: Linear prediction cepstrum coefficient

of accuracies among different folds is observed using LSTM in the time series based approach with a standard deviation of 0.0728, 0.0665, and 0.0838 for MFCC, LPCC, and fusion features, respectively. The standard deviation here is a measurement of how diverse the various fold models fit their data. This might reflect the diversity of the phonemes from one Bayt to another in the same meter, where the order of the consonant and vowels is the same. On the other hand, the non-time series model in the SD experiments using SVM records a standard deviation of 0.003, 0.005, and 0.006 for MFCC, LPCC, and fusion features, respectively, as an indication of the stability of different folds, using global feature representation of the data.

It is obvious that in the SD models, the SVM classifier takes a non-time series signal and outperforms the LSTM classifier applied on the time series inputs. This might be an indication that despite the time series nature of the speech input for poetry meter recognition, the non-time series form and signal global features could represent the input data in a significant way. Such an observation of the significance of using the non-time series version of a time series data has been also recorded in other applications like vehicle controlling data (Wells, et al., 2012). However, this performance is limited to SD experiments and not repeated in the SI experiments.

To validate how various speakers influence the meter recognition, we applied SI-based cross-validation. The data in this work include samples recorded by two speakers, one is used to train the model, whereas the other speaker's data are used for model testing. Here, the number of experiments is equal to one because the test and training sets are fixed to the data belonging to each speaker. Experiments with SI show that the same pattern of MFCC outperforms LPCC, and the incapability of the fusion feature to outperform MFCC is repeated also here (Table IV). The most interesting result here is what MFCC+LSTM achieves, where it significantly outperforms other models (0.8889 of accuracy). Time series

based MFCC features prove their ability to overcome the SI challenge where the properties of the speaker's voice are not involved in training the model.

A comparison to state-of-the-art studies is inconvenient to some extent due to the nature of the input (audio in the current work and text in all state-of-the-art studies), the number of involved meters (varies from 3 to 16), and the characteristics of the speaker's voice that appears in the SI experiments. However, the proposed SD model using MFCC and SVM achieves an accuracy of 0.9957, which outperforms the best achieved accuracy of 0.9638 in the state-of-the-art studies by Yousef et al. (2019).

VI. CONCLUSION

The Arud meter is a stressed and unstressed pattern in a poem. AARM is a natural language processing application that aims to determine the type of meter followed in a poem. The Arud meter is traditionally determined from the text of a poem by experts. However, the musical pattern of the poem can also refer to the meter followed in the poem. The main contribution of this paper is to propose a model that automatically recognizes the Arud meter within Arabic poetry using the speech signal of a spoken line (Bayt) of the poem. To the best of our knowledge, no work has used the human voice as an input to AARM. The paper tests both time series and non-time series representations of both MFCC and LPCC features for AARM speech features. The SI results show that MFCCs outperform LPCCs in all of the conducted experiments. The times series based MFCC feature using LSTM detects useful, meter distinguishing information that is shared among the speakers involved. Despite the time series nature of AARM, global non-time series features achieve the best performance; however, this achievement is limited to the SD experiments.

The main deficiencies of this work are the non-adequate variation in the data in terms of number of speakers, number of classes (meters), and in addition to poems in different languages that adopt the same structure of meters. To improve the generalization of the findings in this work, the current exploited data need to be extended to include more samples, speakers, meters, and languages.

REFERENCES

- Abuata, B. and Al-Omari, A., 2018. A rule-based algorithm for the detection of arud meter in CLASSICAL Arabic poetry. *International Arab Journal of Information Technology*, 15(4), pp. 1-5.

- Al-Falahi, A. Ramdani, M. and Bellafkih, M., 2017, Machine learning for authorship attribution in Arabic poetry. *International Journal of Future Computer and Communication*, 6(2), p. 486.
- Almuhareb, A. Alkharashi, I. Al-Saud, L. and Altuwaijri, H., 2013. Recognition of Classical Arabic Poems. In: *2nd Workshop on Computational Linguistics for Literature*, pp. 9-16.
- Alnagdawi, M., Rashideh, H. and Aburumman, F., 2013. Finding Arabic poem meter using context free grammar. *Journal of Communication and Computer Engineering*, 3(1), pp. 52-59.
- Araújo, L. 2010, Computer-based Assessment (CBA) of Foreign language speaking skills. *JRC Scientific and Technical Reports*, 1, p. 165.
- Arberry, J., 1965. *Arabic Poetry. A Primer for Students*. Cambridge University Press, Cambridge.
- Hirjee, H. and Brown, D., 2010, Using automated rhyme detection to characterize rhyming style in rap music. *Empirical Musicology Review*, 5(4), pp. 121-145.
- Hochreiter, S. and Schmidhuber, J., 1997. Long short-term memory, *Neural computation*, 9(8), pp. 1735-1780.
- Ismail, A., Eladawy, M., Keshk, H. and Saleh, S., 2010. Expert system for testing the harmony of Arabic poetry. *Journal of Engineering Sciences*, 1, pp. 401-411.
- Kurta, A. and Kara, M., 2012. An algorithm for the detection and analysis of Arud meter in Diwan poetry. *Turk Journal of Electrical Engineering and Computer Science*, 20(6), pp. 948-963.
- Lipton, C., Berkowitz, J. and Elkan, C., 2015. *A Critical Review of Recurrent Neural Networks for Sequence Learning*, *arXiv Preprint arXiv: 1506.00019*. Available from: <https://www.arxiv.org/abs/1506.00019>.
- Morris, H., 1966. On the metrics of pre-islamic Arabic poetry. *Quarterly Progress Report of the Research, Laboratory of Electronics*, 83, pp. 113-116.
- Rao, K. and Koolagudi, S., 2013, *Robust Emotion Recognition using Spectral and Prosodic Features*. Springer Science and Business Media. Berlin, Germany, pp. 23-24.
- Reynolds, A., 1995. Speaker identification and verification using Gaussian mixture speaker models. *Speech Communication*, 17(1-2), pp. 91-108. Available from: <https://www.sciencedirect.com/science/article/abs/pii/016763939500009D>.
- Rutledge, J.C., 1995. Fundamentals of speech recognition, by Lawrence Rabiner and Bing-Hwang Juang. *Analysis of Biomedical Engineering*, 23, pp. 526-526.
- Sarang, S.K. and Saha, G., 2020, Improved speech-signal based frequency warping scale for cepstral feature in robust speaker verification system. *Journal of Signal Processing Systems*, 1, 1-14.
- Scott, H. 2010. *Pegs, Cords, and Ghuls: Meter of Classical Arabic Poetry*. Swarthmore College Department of Linguistics. Available from: <https://www.scholarship.tricolib.brynmawr.edu/handle/10066/6864>.
- Sønderby, K., Sønderby, K., Nielsen, H. and Winther, O., 2015. Convolutional LSTM Networks for Subcellular Localization of Proteins. *International Conference on Algorithms for Computational Biology*, Springer, pp. 68-80.
- Stoetzer, W., 1989. *Theory and Practice in Arabic Metrics*. Leiden, Het Oosters Institute.
- Vapnik, V., 1995, *The Nature of Statistical Learning Theory*. Springer-Verlag, New York. Available from: <https://www.springer.com/gp/book/9780387987804>.
- Wells, J.R., Ting, K.M. and Naiwala, C.P., 2012, December. A Non-time Series Approach to Vehicle Related Time Series Problems. Vol. 134. In: *Proceedings of the 10th Australasian Data Mining Conference*, Australian Computer Society, Inc., pp. 61-70.
- Yousef, W.A., Ibrahim, O.M., Madbouly, T.M. and Mahmoud, M.A., 2019. Learning meters of Arabic and English poems with Recurrent Neural Networks: a step forward for language understanding and synthesis, *arXiv preprint arXiv:1905.05700*. Available from: <https://www.arxiv.org/abs/1905.05700>.
- Zhang, L. and Gao, J., 2017, A comparative study to understanding about poetics based on natural language processing. *Open Journal of Modern Linguistics*, 7(5), pp. 229-237.

Moderate Range Static Magnetic Field Promoted Variation of Blood Parameters: An *In vitro* Study

Bestoon T. Mustafa, Sardar P. Yaba and Asaad H. Ismail

Department of Physics, College of Education, Salahaddin University,
Erbil 44001, Kurdistan Region – F.R. Iraq

Abstract—This study was undertaken to investigate the influence of a homogenous and uniform static magnetic field (SMF) on the main blood cell counts *in vitro* experiment. Fresh blood samples were collected from albino rats and exposed to SMF (2.4, 6, 25, 50, 75, and 100 mT) versus 15–60 min. Results showed a significant change of blood counts under the low field effects. A 2.4 mT was a trend of white blood cells (WBCs) count increase non-linearly. However, a 6 mT exposure reduced WBCs with about 39%. Other variations fluctuated within 30%. The 25 mT decreased red blood cells (RBCs), hemoglobin, and hematocrit levels with 13% similarly. The lower exposure field, (2.4 and 6) mT, and effects on RBCs were 6% fluctuation. The 6 mT reduced platelet counts with half in comparison to control blood samples. About 20% increase obtained due to 50 mT exposure during all period. None of 75 and 100 mT exposures dominated blood counts alterations. The quiet magnetic field exposure for a certain time can be interesting to control blood cell count-related diseases.

Index Terms—Aggregation, Blood counts, Hematology, Optical microscopy, Static magnetic field.

I. INTRODUCTION

The effect of static magnetic field (SMF) on biological system has being concerned biomedical researches. The produced magnetic field from magnetic resonance imaging, transmission line, electrical appliance, and other electronic devices provided a tremendous study opportunity to evaluate the cellular effect of magnetic field (Chadwick and Lowesf, 1998; Okano and Ohkubo, 2005; Van Deventer, et al., 2005). Experimental results suggested several cellular disorders. Yet, the results were contradictory rather than declare a clear answer (Mustafa, et al., 2019; Vergallo and Dini, 2018). Main blood cells, white blood cells (WBCs), red blood cells (RBCs), and platelets (PLTs), are body defensive, oxygen support, and hemostasis precursors in animals (Ismail, 2015; Laith, et al., 2020). Several *in vivo* experiments were

conducted to reveal the influence of pulsed and SMF on blood cells. Nevertheless, only a few *in vitro* experiments explained the response of outcomes.

SMF is a time-independent field generated through passing a DC current through a coil (Mustafa, et al., 2020a). SMF can penetrate tissues and thermalize the molecules stabilization (Hashish, et al., 2008). According to the World Health Organization (World Health Organization, 2006), magnetic material found in some organic tissues and hence magnetic field can interact directly with several proteins, ions, and other cellular parts of animals.

RBCs are about 45% of blood content mainly cause blood viscosity manipulation. In addition, disorder in counts and morphology can cause pathological diseases or anima. Wister rats were exposed to SMF *in vivo* experiment (Chater, et al., 2006). A 13-day exposure, 128 mT: 1 h/day, increased hematocrit percentage (HTC%) and hemoglobin (HGB) contents with 7% and 12%, respectively. Milovanovich, et al., 2016, examined 5 days: 1 h/day exposure effect of SMF on mice. The field was applied in two different directions: Up and down. A 128 mT reduced WBCs counts and increased PLTs and HGB contents. Aida, et al., 2014, repeated the same experiment using a homogeneous SMF. Five days exposure rats resulted in an increase of HGB and WBCs counts: 10% and 17%, respectively. The interesting part of the correlated experiments showed an increase of blood WBCs and PLTs.

The influence of long period subchronic uniform SMF studied by Djordjevich, et al., 2012. Male Swiss-Webster mice exposed with 16 mT: 28 days, lymphocytes changed significantly. A magnetic field with as low as 1.4 mT: 28 days continuous exposure decreased PLTs and lymphocytes percentage significantly (Hashish, et al., 2008). Despite to conduct several *in vivo* researches to study the magnetic field effect on blood, there is a significant gap left to determine *in vitro* exposure effect on blood hematology. In this study, we investigated the effect of moderate SMF (2.4, 6, 25, 50, 75, and 100 mT) on rats' blood counts.

II. MATERIALS AND METHODS

A. Housing Animals and Blood Collection

In this experiment, 24 albino rats ages 5 months, weight between 230 ± 20 g, were participated in six selective groups

ARO-The Scientific Journal of Koya University
Vol. VIII, No.1 (2020), Article ID: ARO.10612, 9 pages
DOI:10.14500/aro.10612

Received 20 December 2019; Accepted 18 April 2020
Regular research paper: Published 10 May 2020

Corresponding author's e-mail: bestoon.mustafa@su.edu.krd
Copyright © 2020 Bestoon T. Mustafa, Sardar P. Yaba and
Asaad H. Ismail. This is an open-access article distributed under the
Creative Commons Attribution License.



(A, B, C, D, E, and F). Each group was with four rats kept in a standard plastic cage. The animals were kept in animal house long prior the experiment started date. They were suicide and fresh blood samples were collected. A standard

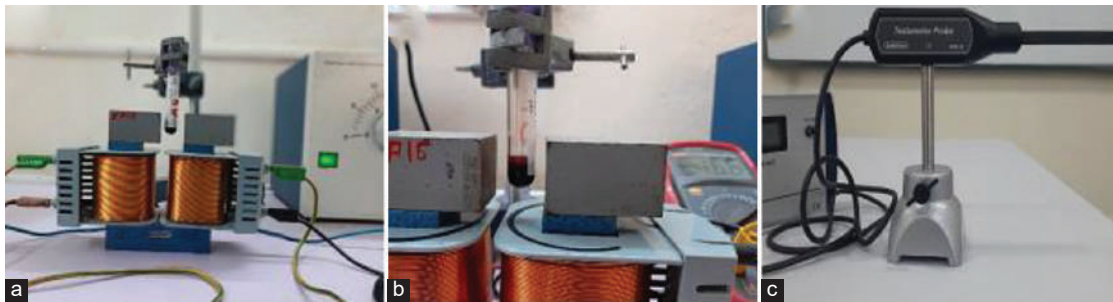


Fig. 1. (a-c) *In vitro* blood exposure system equipped with the digital Teslameter.

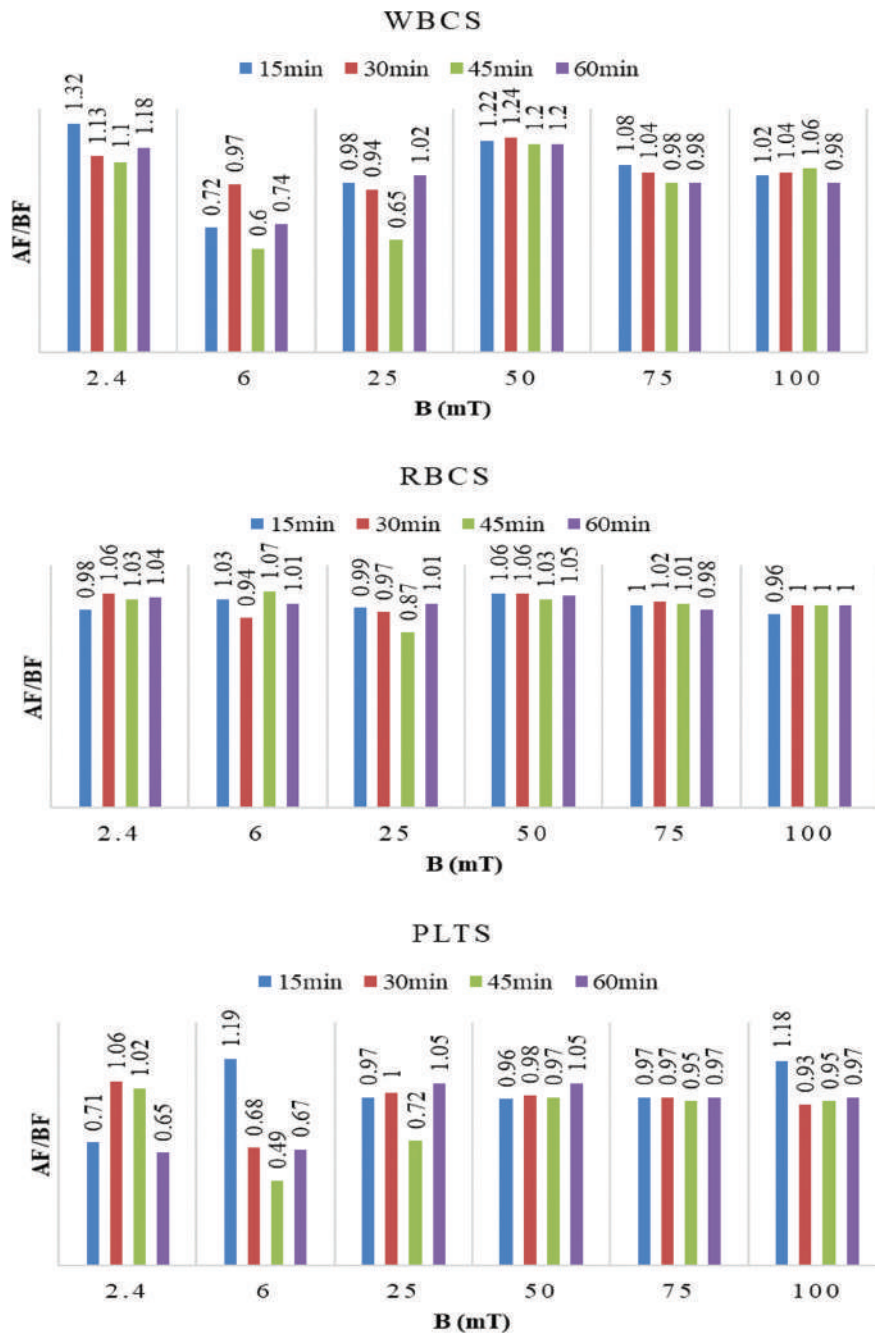


Fig. 2. Blood cells alteration based on exposure time and magnetic field intensity of white blood cells, red blood cells, and platelets. Y-axis represents the ratio between results after exposure to before exposure. A value above “1” represents an increase and below “1” is a decrease compared to control results.

animal house was used in the Biology Department, College of Education, Salahaddin University, Erbil; living atmosphere was 12:12 h light and darkness, photoperiod of 22±2°C, received a standard rat chow and drink (tap water).

A mixture of xylazine and ketamine hydrochloride were prepared and used to anesthetize rats. Blood samples

were withdrawn from cardiac puncture into 6 ml tubes inner wall covered with Ethylenediaminetetraacetic acid anticoagulation. Collected blood from each rat were saved into containers and taken to exposure directly. Each of the groups was prepared for a certain exposure field (2.4, 6, 25, 50, 75, and 100 mT). The exposure time was

TABLE I
BLOOD COUNTS UNDER 2.4 MT STATIC MAGNETIC FIELD VERSUS EXPOSURE PERIOD. A FEW CHANGES ARE SIGNIFICANT ($P<0.05$)

Parameter/period	Exposure time				
	Control	15 min	30 min	45 min	45 min
WBCs ($10^9/l$)	6±0.12	7.9±0.38	6.8±0.19	6.6±0.33	7.1±0.98
LYM ($10^9/l$)	3.4±0.02	3±0.25	3.6±0.15	3.5±0.04	5.8±0.31
LYM%	55.2±1.40	38.8±3.11	52±0.73	52.4±1.11	80.7±3.70
MID ($10^9/l$)	0.7±0.02	1±0.05	0.4±0.09	0.4±0.03	0.6±0.001
MID%	12.3±1.01	13.4±0.16	7±1.00	6.3±0.90	8.5±0.89
GRA ($10^9/l$)	1.9±0.03	3.9±0.02	2.8±0.10	2.7±0.09	0.7±0.00
GRA%	32.5±1.87	47.8±2.11	41±0.94	41.3±1.54	10.8±2.10
RBCs ($10^{12}/l$)	6.69±1.40	6.53±0.74	7.06±0.39	6.88±1.03	6.95±0.52
HGB (g/dl)	11.8±0.49	12.5±2.10	12.9±1.78	12.2±0.88	13.7±2.55
HCT%	32.1±3.21	33.8±3.09	34±1.84	33.1±0.98	39.1±2.46
MCV (fl)	48±3.21	51.8±2.76	48.1±4.01	48±3.29	56.2±2.10
MCH (pg)	17.7±1.02	19.2±3.03	18.2±0.65	17.7±0.93	19.8±1.40
MCHC (g/dl)	36.9±2.09	37.1±3.54	37.9±2.94	36.9±3.65	35.2±2.93
RDWa (fl)	32.3±1.11	36±2.01	32.6±1.43	32.5±1.04	35.6±2.14
RDW%	16.4±2.54	15.7±1.80	16.5±3.01	16.6±2.14	13.9±1.01
PLT ($10^9/l$)	702±23.13	497±19.01	743±30.31	715±21.94	457±25.93
MPV (fl)	6.3±0.91	6.1±0.32	6.3±0.50	6.4±0.98	6.4±0.43
PDWa (fl)	9.3±1.21	9.11.09	9.2±0.94	9.4±1.43	9.5±0.43
PDW%	38±2.13	38.8±1.54	37.5±4.22	38±3.23	39.6±1.84
PCT%	0.44±0.00	0.3±0.01	0.46±0.09	0.45±0.04	0.29±0.08
P-LCR%	5±1.03	4.9±0.94	3.7±0.84	4.6±0.53	6.9±0.31
P-LCC ($10^9/l$)	35±1.50	24±1.01	27±2.09	32±2.43	31±2.04

WBCs: White blood cells, RBCs: Red blood cells, HGB: Hemoglobin, PLT: Platelet

TABLE II
BLOOD COUNTS UNDER 6 MT STATIC MAGNETIC FIELD VERSUS EXPOSURE PERIOD. A FEW CHANGES ARE SIGNIFICANT ($P<0.05$)

Parameter/period	Exposure time				
	Control	15 min	30 min	45 min	45 min
WBCs ($10^9/l$)	8.8±0.38	6.3±0.24	8.5±0.47	5.3±0.14	6.5±0.62
LYM ($10^9/l$)	3.6±0.09	3.3±0.33	4.6±0.19	2.3±0.05	2.6±0.19
LYM%	41.8±0.38	52.2±0.38	53.9±0.52	40.2±0.24	40±0.94
MID ($10^9/l$)	0.5±0.05	0.4±0.02	0.4±0.02	0.25±0.02	0.4±0.03
MID %	6.1±0.14	6.4±0.33	5.2±0.00	7.5.4±0.24	6.1±0.38
GRA ($10^9/l$)	4.7±0.33	2.6±0.14	3.5±0.24	2.9±0.24	3.5±0.24
GRA %	52.1±0.42	41.4±0.42	40.9±0.99	55.4±0.71	53.9±0.52
RBCs ($10^{12}/l$)	6.64±0.16	6.85±0.12	6.26±0.35	7.09±0.28	6.69±0.15
HGB (g/dl)	12.5±0.24	12.2±0.09	12.2±0.09	14.2±0.42	12.9±0.52
HCT (%)	34.4±0.33	33.1±0.33	32.6±0.19	38.1±0.38	35±0.94
MCV (fl)	51.8±0.24	48.4±0.61	52±0.14	52.4±0.28	52.30±0.8
MCH (pg)	18.9±0.14	17.8±0.28	19.4±0.28	20.8±0.71	19.2±0.57
MCHC (g/dl)	36.5±0.24	36.7±0.24	37.4±0.66	35.3±0.61	36.8±1.79
RDWa (fl)	35.5±0.24	32.1±0.19	35.8±0.85	37.1±0.19	36.8±1.09
RDW%	15.5±0.33	16.1±0.33	15.7±0.14	14.5±0.57	16±0.47
PLT ($10^9/l$)	555±2.83	663±10.3	380±4.71	273±10.30	371±00.24
MPV (fl)	6.2±0.24	6.3±0.14	6.1±0.05	7.3±0.47	6.1±0.33
PDWa (fl)	9.3±0.14	9.4±0.19	9±0.24	8.3±0.38	9.2±0.24
PDW%	39.2±0.75	38±0.24	38±0.47	39.2±0.71	39.4±00.75
PCT%	0.34±0.03	0.42±0.04	0.23±0.01	0.42±0.02	0.22±0.03
P-LCR%	5.3±0.14	4.5±0.14	4.7±0.14	4.5±0.09	5±0.24
P-LCC ($10^9/l$)	29±1.41	29±1.04	17±0.47	12±1.47	18±00.47

WBCs: White blood cells, RBCs: Red blood cells, HGB: Hemoglobin, PLT: Platelet

examined versus magnetic field intensity. Controls blood samples were prepared from the same collected blood of each rat. For example, a 6 ml blood collected from each rat divided into 5 tubes, one control and four taken to

exposure with the same magnetic field versus exposure time (15, 20, 45, and 60 min). The same procedure repeated for all rats in each group and then average was taken.

TABLE III
BLOOD COUNTS UNDER 25 Mt STATIC MAGNETIC FIELD VERSUS EXPOSURE PERIOD. A FEW CHANGES ARE SIGNIFICANT ($P<0.05$)

Parameters/period	Exposure time				
	Control	15 min	30 min	45 min	60 min
WBCs ($10^9/l$)	8.6±0.19	8.4±0.66	8.1±0.42	5.6±0.28	8.8±0.17
LYM ($10^9/l$)	5.8±0.52	5.9±0.42	5.8±0.33	3.9±0.38	6.1±0.61
LYM%	66.4±1.60	70.4±2.88	69.8±29.0	69.8±0.90	69±1.65
MID ($10^9/l$)	0.5±0.05	0.8±0.05	0.5±0.09	0.8±0.05	0.6±0.09
MID%	6.8±0.09	9.4±0.38	7±0.71	14.1±1.13	6.7±0.38
GRA ($10^9/l$)	2.3±0.33	1.7±0.19	1.8±0.09	0.9±0.19	2.1±0.52
GRA%	26.8±0.33	20.2±1.32	23.2±0.85	16.1±0.66	24.3±0.52
RBCs ($10^{12}/l$)	6.65±0.25	6.59±0.57	6.48±0.48	5.77±0.30	6.74±0.36
HGB (g/dl)	12.4±0.19	12.3±0.33	12.1±0.66	10.8±0.47	12.5±0.94
HCT%	33.5±0.71	33±0.94	32.4±0.61	29±1.13	33.9±0.71
MCV (fl)	50.4±0.75	50±1.18	50±1.18	50.2±1.08	50.2±1.08
MCH (pg)	18.6±0.19	18.7±0.61	18.7±0.85	18.7±0.42	18.6±0.52
MCHC (g/dl)	36.9±0.90	37.3±0.80	37.4±0.99	37.3±1.13	37.1±0.71
RDWa (fl)	32.9±1.08	33.1±0.42	33.1±1.46	32.8±0.28	33.1±1.32
RDW%	15.4±0.19	15.4±0.52	15.6±0.42	15.4±0.52	15.5±0.42
PLT ($10^9/l$)	615±7.07	599±5.19	614±7.54	445±5.66	647±24.98
MPV (fl)	5.8±0.33	5.7±0.42	5.7±0.47	6.4±0.57	5.8±0.42
PDWa (fl)	8.8±0.33	8.6±0.28	8.7±0.52	9.6±0.80	8.7±0.42
PDW%	38.4±1.27	37.8±1.32	37.7±1.27	39.4±0.38	38±0.75
PCT%	0.35±0.07	0.34±0.04	0.35±0.05	0.28±0.03	0.37±0.06
P-LCR%	3.3±0.33	2.8±0.09	2.7±0.14	4.5±0.09	2.70±0.33
P-LCC ($10^9/l$)	20±1.25	16±0.75	16±0.19	20±1.70	17±0.80

WBCs: White blood cells, RBCs: Red blood cells, HGB: Hemoglobin, PLT: Platelet

TABLE IV
BLOOD COUNTS UNDER 50 Mt OF STATIC MAGNETIC FIELD VERSUS EXPOSURE PERIOD. A FEW CHANGES ARE SIGNIFICANT ($P<0.05$)

Parameters/period	Exposure time				
	Control	15 min	30 min	45 min	60 min
WBCs ($10^9/l$)	5.4±0.38	6.6±0.41	6.7±0.61	6.5±0.37	6.5±0.14
LYM ($10^9/l$)	3.8±0.09	4.7±0.14	4.6±0.37	4.7±0.14	4.7.7±0.35
LYM%	68.4±1.60	70.2±0.85	68.5±0.94	72±0.47	72±0.75
MID ($10^9/l$)	0.3±0.02	0.4±0.05	0.4±0.05	0.4±0.05	0.4.4±0.09
MID%	6.2±0.38	6.4±0.28	6.3±0.57	6.5±0.71	6.5.5±0.38
GRA ($10^9/l$)	1.3±0.14	1.5±0.24	1.7±0.28	1.4±0.42	1.4±0.33
GRA%	25.4±0.28	23.4±0.28	25.2±0.61	21.5±0.52	21.5±0.57
RBCs ($10^{12}/l$)	6.21±0.37	6.59±0.19	6.59±0.33	6.41±0.56	6.41±0.47
HGB (g/dl)	12.6±0.75	13.5±0.24	13.6±0.75	13.2±0.61	13.2±0.94
HCT%	37.1±0.52	38.8±1.32	39±0.24	38.3±0.57	38.3±0.85
MCV (fl)	59.7±0.33	58.8±1.32	59.5±0.94	59.7±0.33	59.7±0.37
MCH (pg)	20.3±0.33	20.6±0.75	20.8±0.75	20.7±0.28	20.7±0.99
MCHC (g/dl)	34±0.61	34.9±0.90	34.9±0.52	34.6±0.47	34.6±0.47
RDWa (fl)	39.5±0.38	39.5±1.18	39.7±0.42	40.4±0.75	40.4±0.27
RDW%	14.4±0.28	14.6±0.66	14.5±0.52	14.8±0.28	14.8±0.42
PLT ($10^9/l$)	497±11.79	478±9.43	489±5.66	484±6.60	484±6.19
MPV (fl)	6.5±0.52	5.8±0.38	5.9±0.28	5.9±0.28	5.9±0.38
PDWa (fl)	9.7±0.33	8.7±0.14	8.8±0.33	8.9±0.42	8.9±0.71
PDW%	41.1±0.42	38.4±0.94	38.2±0.66	38.9±0.90	38.9±0.80
PCT%	0.32±0.01	0.27±0.82	0.29±0.03	0.28±0.05	0.28±0.07
P-LCR%	8.90±0.42	3.70±0.14	4.30±0.38	4.20±0.52	4.2±0.66
P-LCC ($10^9/l$)	44±0.94	27±1.23	21±0.71	20±1.60	20±1.65

WBCs: White blood cells, RBCs: Red blood cells, HGB: Hemoglobin, PLT: Platelet

B. Exposure Method

Solenoid coils were used to generate a highly stable and uniform SMF (Fig. 1). Two coils were connected and the magnetic field was measured between the iron cores using a Teslometer. A magnetic field with intensity up to 115 mT could obtain. The exposure was carried out at room temperature. The

intensity of the field was controlled through the DC current. Time of exposure was examined versus the intensity of exposure. No magnetic field shielding was used. The magnetic field of earth and background was almost zero and neglected. The effect of temperature on blood samples neglected, temperature increase measured during calibration was a 2°

TABLE V
BLOOD COUNTS UNDER 75 MT OF STATIC MAGNETIC FIELD VERSUS EXPOSURE PERIOD. NOT SIGNIFICANT ($P>0.05$)

Parameters/period	Exposure time				
	Control	15 min	30 min	45 min	60 min
WBCs ($10^9/l$)	5.1±0.37	5.5±0.33	5.3±0.14	5±0.12	5±0.26
LYM ($10^9/l$)	3.7±0.14	4.1±0.24	3.9±0.05	3.8±0.24	3.6±0.09
LYM%	71.3±0.80	73.5±1.18	72.2±0.38	73.7±0.14	72.2±0.38
MID ($10^9/l$)	0.2±0.00	0.3±0.02	0.3±0.09	0.2±0.02	0.3±0.09
MID%	5.1±0.28	6±0.24	5.7±0.19	5.3±0.33	5.7±0.19
GRA ($10^9/l$)	1.2±0.09	1.1±0.05	1.1±0.24	1±0.12	1.1±0.24
GRA%	23.6±0.66	20.5±0.24	22.1±0.19	21±0.12	22.1±0.19
RBCs ($10^{12}/l$)	5.78±0.10	5.79±0.10	5.9±0.28	5.86±0.07	5.9±0.28
HGB (g/dl)	12.6±0.19	12.9±0.24	13.1±0.52	12.9±0.57	13.1±0.52
HCT%	36.6±0.66	36.1±0.71	36.8±0.33	36.5±5.12	36.8±0.33
MCV (fl)	63.4±1.70	62.4±0.52	62.4±0.14	62.3±3.12	62.4±0.14
MCH (pg)	21.8±0.66	22.2±0.85	22.1±1.04	22±0.12	22.1±1.04
MCHC (g/dl)	34.4±0.66	35.6±0.66	35.5±0.38	35.3±3.12	35.5±0.38
RDWa (fl)	42.2±0.28	41.1±0.75	41.6±0.47	40.1±1.12	41.6±0.47
RDW%	14.3±0.66	14.2±0.71	14.3±0.33	13.9±0.33	14.3±0.33
PLT ($10^9/l$)	719±14.14	701±3.77	700±5.66	682±8.98	700±5.66
MPV (fl)	6.2±0.52	6.1±0.28	6±0.33	6.1±1.12	6±0.33
PDWa (fl)	9.2±0.52	9±0.61	9±0.28	9±0.12	9±0.28
PDW%	38.3±0.82	37.9±0.75	37.9±0.05	37.8±8.12	37.9±0.05
PCT%	0.45±0.09	0.43±0.08	0.42±0.02	0.41±0.02	0.42±0.02
P-LCR%	4.9±0.24	5±0.28	3.8±0.09	4±0.12	3.8±0.09
P-LCC ($10^9/l$)	35±0.94	35±0.94	26±0.80	26±0.12	26±0.80

WBCs: White blood cells, RBCs: Red blood cells, HGB: Hemoglobin, PLT: Platelet

TABLE VI
BLOOD COUNTS UNDER 100 MT OF STATIC MAGNETIC FIELD VERSUS EXPOSURE PERIOD. NOT SIGNIFICANT ($P>0.05$)

Parameters/period	Exposure time				
	Control	15 min	30 min	45 min	60 min
WBCs ($10^9/l$)	5±0.50	5.1±0.54	5.2±0.12	5.3±0.83	4.9±0.62
LYM ($10^9/l$)	4±0.14	4.3±0.24	4.1±0.14	4.3±0.33	4±0.47
LYM%	79.9±0.28	83.3±0.80	78±1.89	79.9±0.52	79.8±2.2
MID ($10^9/l$)	0.2±0.00	0.5±0.05	0.2±0.00	0.2±0.02	0.2±0.03
MID%	4.3±0.33	9.7±0.33	4.9±0.14	4.3±0.33	4.4±0.28
GRA ($10^9/l$)	0.8±0.09	0.3±0.02	0.9±0.19	0.8±0.09	0.7±0.14
GRA%	15.8±0.33	7±0.42	17.1±0.71	15.8±0.09	15.8±0.3
RBCs ($10^{12}/l$)	6.45±0.45	6.2±0.42	6.48±0.48	6.47±0.25	6.44±0.2
HGB (g/dl)	13.5±0.47	13.3±0.61	14±0.61	14±0.94	13.7±0.8
HCT%	40.4±0.90	38.6±0.05	40±1.13	40±0.94	40.1±0.9
MCV (fl)	62.6±0.80	62.2±0.47	61.7±0.38	61.9±0.05	62.2±0.8
MCH (pg)	20.9±0.75	21.5±0.42	21.5±0.42	21.7±1.08	21.3±0.8
MCHC (g/dl)	33.3±0.99	34.6±0.85	34.9±0.75	35.1±0.90	34.2±0.3
RDWa (fl)	39.90±0.3	39.6±0.66	39.7±0.80	39.3±1.74	40±0.94
RDW%	13.3±0.40	13.2±0.38	13.4±0.52	13.2±0.85	13.4±0.2
PLT ($10^9/l$)	724±14.14	852±5.66	671±10.3	687±13.6	702±9.90
MPV (fl)	6.3±0.38	6.2±0.38	6±0.42	6±0.47	6±0.47
PDWa (fl)	9.3±0.52	9.2±0.33	9±0.42	8.9±0.42	9±0.94
PDW%	39±0.94	39±0.94	38.1±0.44	38.1±0.99	38.6±0.1
PCT%	0.46±0.02	0.53±0.03	0.40±0.02	0.41±0.00	0.42±0.2
P-LCR%	6.2±0.33	5.4±0.28	4.7±0.33	4±0.47	4.2±0.38
P-LCC ($10^9/l$)	44±0.47	46±1.41	31±0.94	27±0.94	29±1.89

WBCs: White blood cells, RBCs: Red blood cells, HGB: Hemoglobin, PLT: Platelet

increase after 1 h operating the exposure set-up. Both control and exposure sample left at the same room and atmosphere.

C. Hematological Analysis

Medonic M-series M32 hematology analyzers (made in Sweden) were used to examine blood counts. It performs the test ultrafast with fully differential parameters. Student's *t*-test was used to extract significance of changes. Microsoft Office 2019 program employed to elicit the rest of data analysis and charts configuration. Percentage of changes calculated in compare to control samples.

III. RESULTS

Tables I-VI represent the blood count changes under the effect of magnetic field (2.4, 6, 25, 50, 75, and 100 mT,

respectively) versus time of exposure (15, 30, 45, and 60 min). Blood count alterations plotted after exposure in ratio to control values (before exposure) are shown in Figs. 2–5. Fig. 2 represents the alteration in main blood parameters. Overall exposure, a 2.4 mT SMF resulted a significant ($P < 0.05$) impact on WBCs and PLTs, yet, insignificantly on RBCs. For instance, a 15 min exposure raised WBCs with 31% and reduced PLTs with 29%. However, this figure has changed at 60 min exposure, whereas WBCs count increased and PLTs count reduced with 18% and 35%, respectively. RBCs fluctuated from 2% to 5% as blood samples exposed from 15 to 60 min.

Blood samples exposed to a 6 mT: 45 min displayed a tremendous reduction of WBCs and PLTs, 40% and 51%, respectively. The 15–60 min of exposure reduced WBCs count from 3% to 40% non-linearly. RBCs count increase

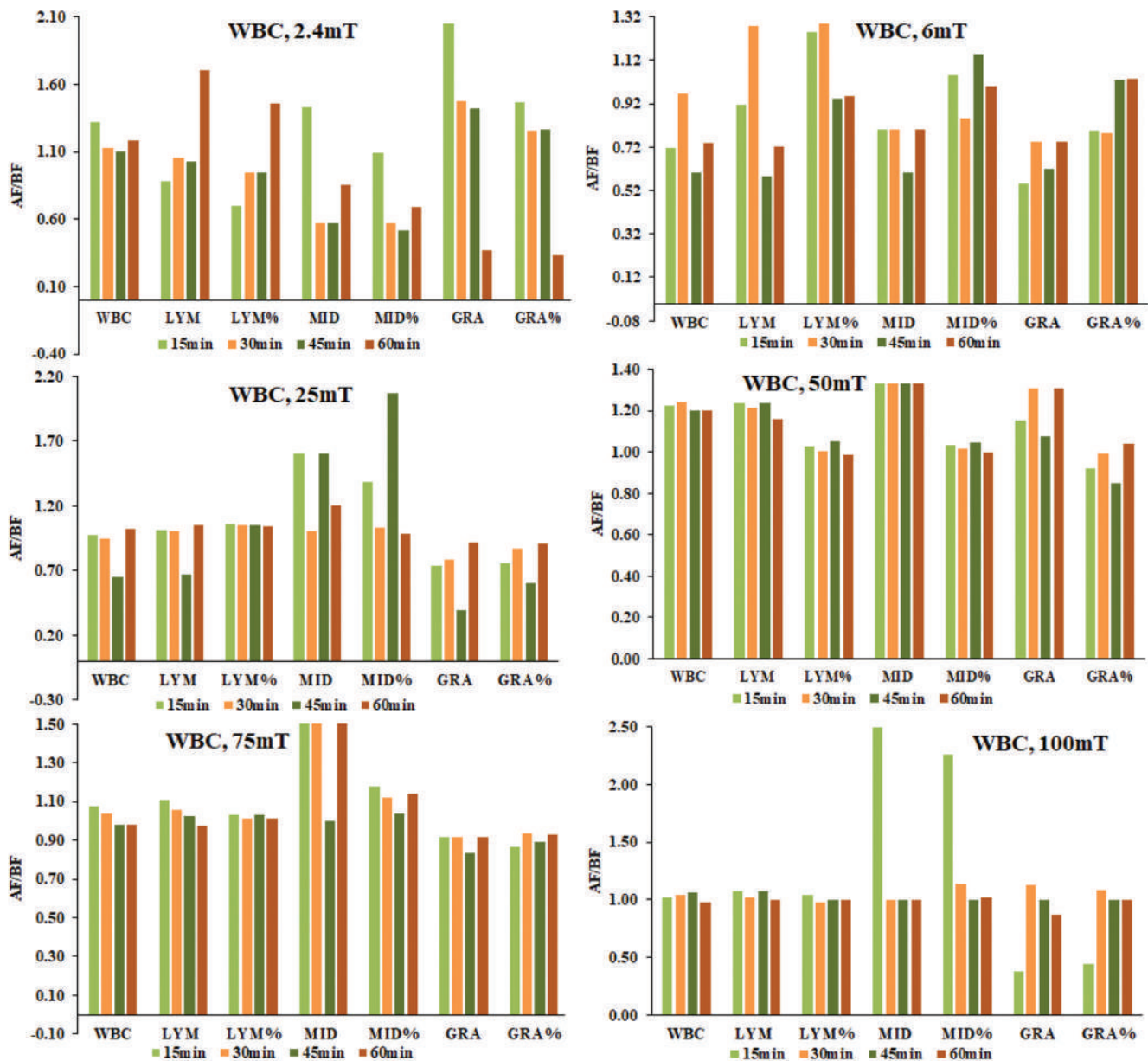


Fig. 3. White blood cell parameters change under the effect of various static magnetic field intensity and exposure duration. Y-axis represents the ratio between results after exposure to before exposure. A value above “1” represents an increase and below “1” is a decrease compared to control results.

fluctuated from 1% to 6%. A remarkable reduces of WBCs, PLTs, and RBCs count obtained with 35%, 28%, and 13%, respectively, under the 25 mT: 45 min. The lower and longer exposure time resulted changes as small as 2%.

The 50 mT of exposure increased WBCs significantly ($P < 005$), about 20% versus exposure period, compare to an insignificant increase in RBCs and PLTs values, RBCs: 3–6% and PLTs: 1–4%. The 75 mT exposure did not enhance blood parameters significantly ($P > 0.05$). The 15 min of exposure increased the WBCs levels with only 7%. Other variations were as small as 1%. The highest exposure field (100 mT) showed a similar response except an enhancement in PLTs level with 17% obtained due to 15 min of exposure. Overall result reveals a non-significant response of WBCs with 75 mT and 100 mT. Concerning RBCs counts, 13% reduction

was the highest obtained at 25 mT, 45 min. Therefore, none of other exposure field/duration is 6% exceeded. In contrast, WBCs level exceeded 39%. PLTs count dropped dramatically as exposure field increased.

There was an increase trend of HGB, HTC content, and lymphocytes (16%, 21%, and 71%) in low exposure field (2.4 mT, 60 min) but not at a higher exposure field. In addition, granulocytes have increased tremendously (doubled: 2.4 mT, 15 min) as well as 63% reduction at 60 min exposure. The HTC percentage caused no alteration at high exposure field. The sharp change was 22% increase at 2.4 mT, 60 min and 13% reduction at 25 mT, 15 min. The exposure field did not produce any impact on platelet distribution width. Nevertheless, 11% increase of RBC distribution width reported at low field exposure, 2.4 mT: 15 min.

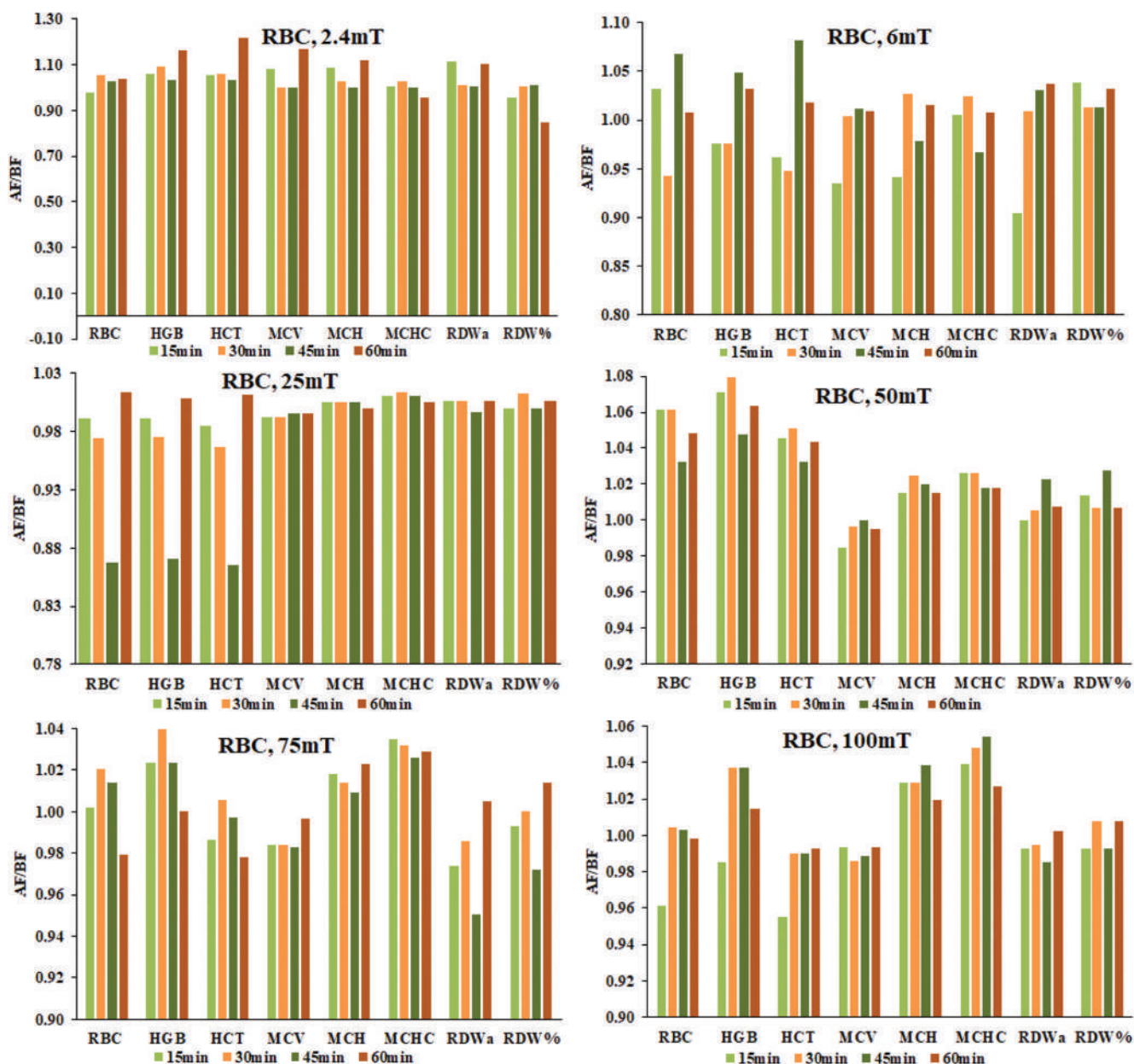


Fig. 4. Red blood cells count variation under the effect of magnetic field intensity versus exposure time. Y-axis represents the ratio between results after exposure to before exposure. A value above “1” represents an increase and below “1” is a decrease compared to control results.

IV. DISCUSSION

Our study revealed that low exposure SMF enhances WBCs and PLTs count significantly ($P < 005$) inconsistent to a less significant increase of RBCs HGB and HTC levels. Similar trend obtained by Chater, et al., 2006, however, their results are inconsistent to a significant RBCs and WBCs variation. HGB counts are RBCs variation correlated. In addition, finding RBCs concentration far from normal can be related to anemia diseases (Blann, 2014). It is believed that changes of RBCs count are mainly aggregation related. A decrease of RBCs aggregation leads to an increase of RBCs count. SMF enhanced aggregation examined by Mustafa, et al., 2020b. According to their investigation, 42.5 mT SMF decreased RBCs count significantly after 30 min exposure *in vitro* experiment, a similar result obtained in our

study at low exposure field. HGB and HTC% enhanced due to 34.8 mT and 15 min.

The previous studies revealed pro-inflammatory changes and reactive oxygen species production under the influence of SMF (Sahebamei, et al., 2007; Zhao, et al., 2011). It shows that HGB is sensitive to SMF. An increase of HGB and HTC levels was summarized as hypoxia-like status (Sihem, et al., 2006). This can be the result of oxygen-binding impairment. RBCs orientation and alignment were demonstrated under magnetic field (Yamagishi, 1990). RBCs orientation increases blood viscosity (Strieth, et al., 2008). Increasing hematological parameters may cause significant cardiovascular risk including vascular reactivity, heart stroke, and blood disorder. The ventricular function is impaired when the HGB level reaches into its 50% reduction. In addition,

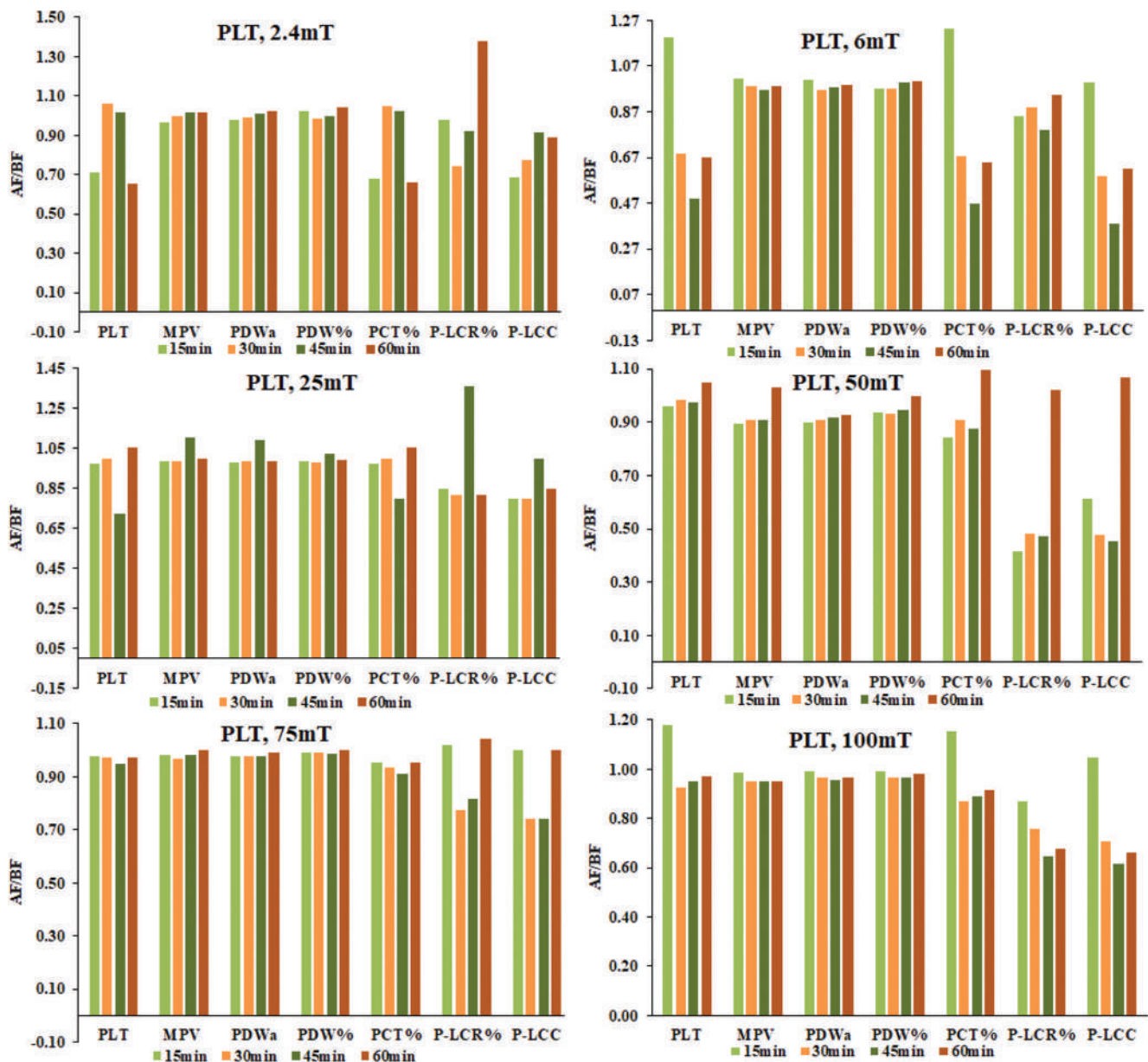


Fig. 5. Blood platelets count variation under the effect of intensity change of magnetic field versus exposure period. Y-axis represents the ratio between results after exposure to before exposure. A value above “1” represents an increase and below “1” is a decrease compared to control results.

the reduction of HGB concentration causes inadequate oxygen support to body tissues, ventricular remodeling, and raising peripheral resistance. These factors contribute the risk of ischemia or its related symptoms (Maulood, 2018).

WBCs (leukocytes) are immunity cells beneficial to fight infections and diseases including AIDS, leukemia, and certain types of blood cancers (AL-Dulaimi, et al., 2018). Leukocyte counts linkage with coronary cardiac diseases was found to produce an independent risk factor. For example, the risk of death related to a 65% increase of leukocyte counts was shown from ischemic heart diseases (Sweetnam, et al., 1997). A small increase of leukocyte counts under the effect of magnetic field contributed an increase of spleen cellularity. In our experiment, granulocyte counts increased significantly under the effect of 2.4, 6, and 25 mT. This result is similar with 16 mT exposure mice where the granulocyte counts raised comparable, regardless to unchanged of RBC counts after 30 days exposure (Djordjevich, et al., 2012). PLTs are a nucleate cellular fragments and essential hemostasis carriers (Italiano, 2007). Disorder in PLTs causes bleeding disorder, which can progress to viral hemorrhagic fevers and can progress to shock and death (Zapata, et al., 2014). With the above discussion, blood cells count variation showed in this study under SMF required extra attention.

V. CONCLUSION

Influence of a homogenous and uniform SMF on the main blood cell counts *in vitro* experiment for the albino investigated. It has concluded that the significant changes of blood cell counts under the low field effects increased non-linearly, and the high exposure SMF did not enhanced blood parameters. WBCs demonstrated the maximal response comparing with the RBC and PLT. RBC indices have not influenced with SMF. The overall change of PLTs was a decrease. From this study, it can be concluded that low static field can interact with WBCs and blood PLTs significantly.

ACKNOWLEDGMENT

The authors give thanks and appreciation to the operational and academic staffs in the blood analysis and medical physics laboratories for their support and facility.

CONFLICTS OF INTEREST

The authors declared that they have no conflicts of interest.

REFERENCES

- Aida, L., Soumaya, G., Myriam, E., Mohsen, S. and Hafedh, A., 2014. Effects of static magnetic field exposure on plasma element levels in rat. *Biological Trace Element Research*, 160, pp.67-72.
- AL-Dulaimi, K., Banks, J., Chandran, V., Tomeo-Reyes, I. and Nguyen, K., 2018. Classification of white blood cell types from microscope images: Techniques and challenges. In: *Microscopy Science: Last Approaches on Educational Programs and Applied Research*. Formatex Research Center, Spain, pp.17-25.
- Blann, A., 2014. Functions and diseases of red and white blood cells. *Nurs Times*, 110, pp.16-18.
- Chadwick, P. and Lowesf, F., 1998. Magnetic fields on british trains. *Annals Occupational Hygiene*, 42, pp.331-335.
- Chater, S., Abdelmelek, H., Pequignot, J.M., Sakly, M. and Ben Rhouma, K., 2006. Effects of sub-acute exposure to static magnetic field on hematologic and biochemical parameters in pregnant rats. *Electromagnetic Biology Medicine*, 25, pp.135-144.
- Djordjevich, D.M., Luka, S.R. De, Milovanovich, I.D., Andjelija, Z., Stefanovic, S., Trbovich, A.M. and Ristic, J.L., 2012. Ecotoxicology and environmental safety hematological parameters' changes in mice subchronically exposed to static magnetic fields of different orientations. *Ecotoxicology Environmental Safety*, 81, pp.8-105.
- Hashish, A.H., El-Missiry, M.A., Abdelkader, H.I. and Abou-Saleh, R.H., 2008. Assessment of biological changes of continuous whole body exposure to static magnetic field and extremely low frequency electromagnetic fields in mice. *Ecotoxicology Environmental Safety*, 71, pp.895-902.
- Ismail, A.H., 2015. Influence of radiation doses on the ratio of blast cells, lymphocytes and neutrophils inside blood samples of leukaemia patients: *In vitro*. *ZANCO Journal of Pure and Applied Sciences*, 27(3), pp.65-74.
- Italiano, J.E., 2007. The structure and production of blood platelets. In: *Platelets in Hematologic and Cardiovascular Disorders*. Cambridge University Press, Cambridge, United Kingdom, pp.1-20.
- Najam, L., AL-Dulamey, Q., and Al-Jawwady, Y., 2020. Effects of low dose gamma ray on some hematological parameters in adult rats. *Iranian Journal of Medical Physics*, 17(3), pp.137-141.
- Maulood, K.A., 2018. Assessment of some hematological, biochemical parameters and cardiac biomarker levels in patients with ischemic heart disease in Erbil city. *Zanco Journal of Pure Applied Sciences*, 30, pp.86-93.
- Milovanovich, I.D., Luka, S.R. De, Djordjevich, D.M., Ili, A.Ž., Popovi, T., Arsi, A., Obradovi, D.D., Opri, D., Risti, J.L. and Trbovich, A.M., 2016. Homogeneous static magnetic field of different orientation induces biological changes in subacutely exposed mice. *Environmental Science and Pollution Research International*, 23, pp.1584-1597.
- Mustafa, B.T., Yab, S.P. and Ismail, A.H., 2020a. Impacts of materials on the intensity of uniform static magnetic fields using a multi Helmholtz coils design. *AIP Conference Proceedings*, 2213(1), pp.020063.
- Mustafa, B.T., Yaba, S.P. and Ismail, A.H., 2019. A review of the effects of magnetic field on main blood cells : *In vivo* and *in vitro* experiments. *ZANCO Journal of Pure and Applied Sciences*, 31(6), pp.40-50.
- Mustafa, B.T., Yaba, S.P. and Ismail, A.H., 2020b. Influence of static magnetic field on red blood cells parameters and platelets using tests of CBC and microscopy images. *Biomedical Physics and Engineering Express*, 6(2), pp.025004.
- Okano, H. and Ohkubo, C., 2005. Effects of neck exposure to 5.5 mT static magnetic field on pharmacologically modulated blood pressure in conscious rabbits. *Bioelectromagnetics*, 26, pp.469-480.
- Sahebjamei, H., Abdolmaleki, P. and Ghanati, F., 2007. Effects of magnetic field on the antioxidant enzyme activities of suspension-cultured tobacco cells. *Bioelectromagnetics*, 28, pp.42-47.
- Sihem, C., Hafedh, A., Mohsen, S., Marc, P.J. and Khmais, B.R., 2006. Effects of sub-acute exposure to magnetic field on blood hematological and biochemical parameters in female rats. *Turkish Journal of Hematology*, 23(4), pp.182-187.
- Strieth, S., Strelczyk, D., Eichhorn, M.E., Dellian, M., Luedemann, S., Griebel, J., Bellemann, M., Berghaus, A. and Brix, G., 2008. Static magnetic fields induce blood flow decrease and platelet adherence in tumor microvessels. *Cancer Biology and Therapy*, 7, pp.632-637.
- Sweetnam, P.M., Thomas, H.F., Yarnell, J.W.G., Baker, I.A. and Elwood, P.C., 1997. Total and differential leukocyte counts as predictors of ischemic

- heart disease: The caerphilly and speedwell studies. *American Journal of Epidemiology*, 145, pp.416-421.
- Van Deventer, T.E., Saunders, R. and Repacholi, M.H., 2005. WHO health risk assessment process for static fields. *Progress in Biophysics and Molecular Biology*, 87, pp.355-363.
- Vergallo, C. and Dini, L., 2018. Comparative analysis of biological effects induced on different cell types by magnetic fields with magnetic flux densities in the range of 1-60 mT and frequencies up to 50 Hz. *Sustainability*, 10(8), pp.2776.
- World Health Organization, 2006. *Static fields, Environmental Health Criteria*. Geneva: World Health Organization.
- Yamagishi, A., 1990. Biological systems in high magnetic field. *Journal of Magnetism and Magnetic Materials*, 90-91, pp.43-46.
- Zapata, J.C., Cox, D. and Salvato, M.S., 2014. The role of platelets in the pathogenesis of viral hemorrhagic fevers. *PLoS Neglected Tropical Diseases*, 8, pp.e2858.
- Zhao, G., Chen, S., Wang, L., Zhao, Y., Wang, J., Wang, X., Zhang, W.W., Wu, R., Wu, L., Wu, Y. and Xu, A., 2011. Cellular ATP content was decreased by a homogeneous 8.5 T static magnetic field exposures Role of reactive oxygen species. *Bioelectromagnetics*, 32, pp.94-101.

On Some Ve-Degree and Harmonic Molecular Topological Properties of Carborundum

Murat Cancan¹, Kerem Yamaç¹, Ziyattin Taş² and Mehmet Şerif Aldemir³

¹Department of Mathematics Education, Van Yüzüncü Yıl University,
Zeve Campus, Tuşba, 65080, Van, Turkey

²Department of Mathematics, Bingöl University,
Faculty of Science and Letters, Bingöl, 12000, Turkey

³Department of Mathematics, Van Yüzüncü Yıl University,
Zeve Campus, Tuşba, 65080, Van, Turkey

Abstract—Carborundum, also known as silicon carbide which containing carbon and silicon, is a semiconductor. Molecular topological properties of physical substances are important tools to investigate the underlying topology of these substances. Ev-degree and ve-degree based on the molecular topological indices have been defined as parallel to their corresponding classical degree based topological indices in chemical graph theory. Classical degree based topological properties of carborundum have been investigated recently. As a continuation of these studies, in this study, we compute novel ve-degree harmonic, ve-degree sum-connectivity, ve-degree geometric-arithmetic, and ve-degree atom-bond connectivity, the first and the fifth harmonic molecular topological indices of two carborundum structures.

Index Terms—Carborundum, Harmonic indices, Ve-degree topological indices.

I. INTRODUCTION

This chemical graph theory study of molecules through topological indices enables to understand and to give information about underlying topology of these molecules. These studies are important part of quantitative structure–property relationship/quantitative structure–activity relationship studies in chemistry. Topological indices are grouped into five categories: Classical degree based topological indices such as Zagreb indices, distance based topological indices such as Wiener index, eccentric connectivity indices, classical degree, and distance based topological indices such as Gutman index, and eigenvalue based topological indices such as Estrada index and matching based topological indices such as Hosoya index. In recent

5 years period, studies of calculating topological indices of molecules have been rising.

Carborundum (silicon carbide), an inorganic compound has a crystal structure like that of diamond and is almost as hard. It is used as an abrasive for cutting, grinding, and polishing, as an antislip additive, and as a refractory. Carborundum is not a natural mineral, but rather is produced in a number of industrial processes. Carborundum has a wide range of industrial uses; in electronic applications including high voltage/high temperature semiconductor and grains bonded together to form extremely hard ceramics, which are used in car brakes and clutches, and plates in bulletproof vests. Stored energy release in neutron irradiated silicon carbide was investigated in (Snead, et al., 2019). 3-D Wire bondless switching cell using flip-chip-bonded silicon carbide power devices were investigated by Seal, Glover and Mantooth (2018). Reddy, Kesavan and Ramnath (2018), mechanical properties of aluminum 6061-silicon carbide, boron carbide metal matrix composite, were investigated. Real-time junction temperature sensing for silicon carbide MOSFET with different gate drive topologies and different operating conditions was studied in (Van der Broeck, et al., 2018). Effect of carbon nanoparticle reinforcement on mechanical and thermal properties of silicon carbide ceramics was studied in (Kaźmierczak-Bałata and Mazur, 2018). Topologically protected interface phonons in two-dimensional nanomaterials: Hexagonal boron nitride and silicon carbide were investigated by Jiang, Wang and Park (2018). Relaxation of residual microstress in reaction bonded silicon carbide was studied in (Wing and Halloran, 2018). Manufacturing isotropic carbon fiber preforms for multilayered silicon carbide composites with a pyrolytic carbon interphase was investigated in (Mei, et al., 2018). Ion irradiation-induced novel microstructural change in silicon carbide nanotubes was studied by Taguchi, Yamamoto and Ohba (2018).

Topological indices of nanostructures have been conducting by many researches recently in chemical graph theory such as (Ediz, 2010), (Ediz, 2011), (Ediz, 2013), (Munir, et al., 2016), (Gao, Asif and Nazeer, 2018), (Anjum and Safdar, 2019), and (Shao, et al., 2019).

ARO-The Scientific Journal of Koya University
Vol. VIII, No.1 (2020), Article ID: ARO.10560, 9 pages
DOI: 10.14500/aro.10560

Received 07 August 2019; Accepted 27 April 2020
Review paper: Published 15 May 2020

Corresponding author's e-mail: mcancan@yyu.edu.tr
Copyright © 2020 Murat Cancan, Kerem Yamaç, Ziyattin Taş,
Mehmet Şerif Aldemir. This is an open-access article distributed
under the Creative Commons Attribution License.



Molecular classical degree based topological properties of silicon carbon structures have been investigated recently in (Imran, et al., 2018). The authors calculated general Randić, Zagreb types indices, geometric arithmetic index, atom-bond connectivity (ABC) index, fourth ABC and fifth geometric arithmetic index of Si_2C_3 -I[p,q] and Si_2C_3 -II[p,q]. As a continuation of this study, generalized first and multiplicative Zagreb indices, the multiplicative version of the ABC index and the generalized multiplicative geometric arithmetic index of Si_2C_3 -I[p,q] and Si_2C_3 -II[p,q] have been investigated in (Kwun, et al., 2018). Reverse Zagreb and reverse hyper-Zagreb Indices for silicon carbide have been computed by Virk, Jhangeer and Rehman (2018).

Harmonic index was defined in (Zhong, 2012). Novel harmonic indices have been defined by Ediz, Farahani and Imran (2017). Novel ev-degree and ve-degree concepts were defined in (Chellali, et al., 2017). Moreover, novel ev-degree and ve-degree topological indices have been defined in (Ediz, 2017; Sahin and Ediz, 2018; Ediz, 2018).

The aim of this study to investigate the first, fifth, sixth harmonic, and ve-degree atom-bond connectivity (ve-ABC), geometric-arithmetic (GA), sum-connectivity, harmonic topological properties of Si_2C_3 -I[p,q] and Si_2C_3 -II[p,q].

II. PRELIMINARIES

In this section, we give some basic and preliminary concepts which we shall use later. A graph $G=(V,E)$ consists of two nonempty sets V and 2-element subsets of V , namely E . The elements of V are called vertices and the elements of E are called edges. For a vertex v , $deg(v)$ show the number of edges that incident to v . The set of all vertices which adjacent to v is called the open neighborhood of v and denoted by $N(v)$. If we add the vertex v to $N(v)$, then we get the closed neighborhood of v , $N[v]$.

And now we give the definitions of ev-degree and ve-degree concepts which were given in Chellali, et al. (2017).

Definition 1 (ve-degree) Let G be a connected simple graph and $v \in V(G)$. The ve-degree of the vertex v , $deg_{ve}(v)$, equals the number of different edges that incident to any vertex from the closed neighborhood of v .

We also can restate the definition 1 as follows: Let G be a connected simple graph and $v \in V(G)$. The ve-degree of the vertex v is the number of different edges between the other vertices with a maximum distance of two from the vertex v .

Definition 2 (ev-degree), let G be a connected graph and $e=uv \in E(G)$. The ev-degree of the edge e , $deg_{ev}(e)$, equals the number of vertices of the union of the closed neighborhoods of u and v .

The authors in (Chellali, et al. 2017) also can give the definition 2 as follows: Let G be a connected graph and $e=uv \in E(G)$. The ev-degree of the edge e , $deg_{ev}(e)=deg_u+deg_v-n_e$, where n_e means the number of triangles in which the edge e lies in.

Definition 3 (ve-ABC index), let G be a connected graph and $e=uv \in E(G)$. The ve-ABC index of the graph G defined as;

$$ABC^{ve}(G) = \sum_{uv \in E(G)} \sqrt{\frac{deg_{ve}u + deg_{ve}v - 2}{deg_{ve}u deg_{ve}v}} \quad (1)$$

Definition 4 (ve-degree GA [ve-GA] index), let G be a connected graph and $v \in V(G)$. Ve-GA index of the graph G defined as;

$$GA^{ve}(G) = \sum_{uv \in E(G)} \frac{2\sqrt{deg_{ve}u deg_{ve}v}}{deg_{ve}u + deg_{ve}v} \quad (2)$$

Definition 5 (ve-degree harmonic (ve-H) index), let G be a connected graph and $uv \in E(G)$. ve-H index of the graph G defined as;

$$H^{ve}(G) = \sum_{uv \in E(G)} \frac{2}{deg_{ve}u + deg_{ve}v} \quad (3)$$

Definition 6 (ve-degree sum-connectivity [ve- χ] index), let G be a connected graph and $uv \in E(G)$. Ve- χ index of the graph G defined as;

$$\chi^{ve}(G) = \sum_{uv \in E(G)} (deg_{ve}u + deg_{ve}v)^{-1/2} \quad (4)$$

Let G be a simple connected graph $G=(V,E)$. Harmonic indices may be defined as;

$$H_{general}(G) = \sum_{uv \in E(G)} \frac{2}{Q_u + Q_v} \quad (5)$$

where Q_u is a unique parameter which is acquired from the vertex $u \in V(G)$.

Definition 9 (First Harmonic Index), the first kind of this Harmonic indices by considering Q_u to be the degree of the vertex u :

$$H_1(G) = \sum_{uv \in E(G)} \frac{2}{d_u + d_v} \quad (6)$$

Definition 10 (Second Harmonic Index), the second kind of this class can be defined by considering Q_u to be the number n_u of vertices of G lying closer to the vertex u than to the vertex v for the edge uv of the graph G :

$$H_2(G) = \sum_{uv \in E(G)} \frac{2}{n_u + n_v} \quad (7)$$

Definition 11 (Third Harmonic Index), the third type of this class can be defined by considering Q_u to be the number m_u of edges of G lying closer to the vertex u than to the vertex v for the edge uv of the graph G :

$$H_3(G) = \sum_{uv \in E(G)} \frac{2}{m_u + m_v} \quad (8)$$

Definition 12 (Fourth Harmonic Index), the fourth type of this class can be defined by considering Q_u to be the eccentricity of the vertex u :

$$H_4(G) = \sum_{uv \in E(G)} \frac{2}{e_u + e_v} \quad (9)$$

Definition 13 (Fifth Harmonic Index), the fifth type of this class can be defined by considering Q_u to be the

$$H_5(G) = \sum_{uv \in E(G)} \frac{2}{S_u + S_v} \quad (10)$$

Definition 14 (Sixth Harmonic Index), and the sixth type of this class can be defined by considering Q_u to be the $M_u = \prod_{v \in N(u)} d_v$

$$H_6(G) = \sum_{uv \in E(G)} \frac{2}{M_u + M_v} \quad (11).$$

III. METHODS

We use combinatorial computing method such as vertex partitioning method, edge partitioning strategy, degree counting strategy, discrete partitioning, and discrete counting strategy to compute our results.

IV. RESULTS

In Imran, et al. (2018), two-dimensional lattices of $Si_2C_3-I[p,q]$ and $Si_2C_3-II[p,q]$ are given in the following Figs. 1 and 2, respectively.

Note that, two rows are being connecting, carbon atom C is brown and silicon atom Si is blue and red lines (edges) connects the upper and lower rows in Fig. 1. $Si_2C_3-I[p,q]$ has $10pq$ vertices and $15pq - 2p - 3q$ edges.

Note that, two rows are connecting and green lines (edges) connect the upper and lower rows in Fig. 2. Furthermore, red lines show the connection between the unit cells in Fig. 2. $Si_2C_3-II[p,q]$ has $10pq$ vertices and $15pq - 2p - 3q$ edges.

From Fig. 1, we give the edge partition of $Si_2C_3-I[p,q]$ with respect to ve-degrees in the following Table I.

From Fig. 2, we give the edge partition of $Si_2C_3-II[p,q]$ with respect to ve-degrees in the following Table II.

And we begin to compute topological indices for $Si_2C_3-I[p,q]$.
Theorem 1

The ve-degree, the first harmonic and the fifth harmonic topological indices of the $Si_2C_3-I[p,q]$ are

$$\begin{aligned} ABC^{ve}(Si_2C_3-I) &= (15pq - 14p - 21q + 20)x\sqrt{\frac{11}{42}} + q - 1 \\ &+ (p + 2q - 4)x\sqrt{\frac{7}{32}} + (2q + 2)x\sqrt{\frac{2}{7}} + (4p + 2q - 7)x\sqrt{\frac{11}{42}} \\ &\bullet (2p + 2q - 5)x\sqrt{\frac{5}{24}} + (2p + 2q - 3)x\sqrt{\frac{2}{7}} + (2p + 4q - 7) \\ &x\sqrt{\frac{5}{24}} + \sqrt{\frac{1}{2}} + \sqrt{\frac{2}{5}} + \sqrt{\frac{8}{25}} + \sqrt{\frac{9}{28}} + \sqrt{\frac{9}{30}} + \sqrt{\frac{13}{56}} \\ GA^{ve}(Si_2C_3-I) &= 15pq - 12p - 17q + 17 \\ &+ (2q + 2)x\frac{\sqrt{35}}{6} + (4p + 2q - 7)x\frac{2\sqrt{42}}{13} + (2q - 2) \\ &x\frac{4\sqrt{3}}{7} + (2p + 2q - 5)x\frac{4\sqrt{10}}{13} + (2p + 2q - 3) \\ &\bullet x\frac{3\sqrt{7}}{8} + (2p + 4q - 7)x\frac{12\sqrt{2}}{17} + \frac{2\sqrt{2}}{3} \\ &+ \frac{2\sqrt{15}}{8} + \frac{4\sqrt{7}}{11} + \frac{2\sqrt{30}}{11} + \frac{4\sqrt{14}}{15} \end{aligned}$$

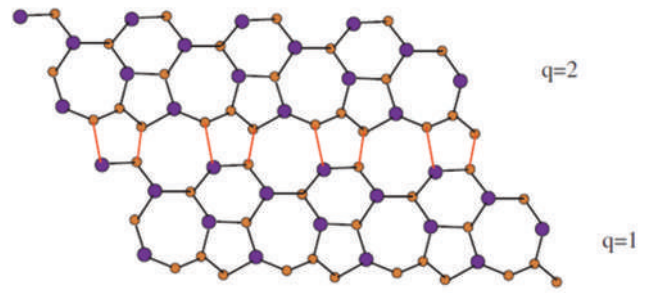


Fig. 1. Two-dimensional structure of $Si_2C_3-I[4,2]$.

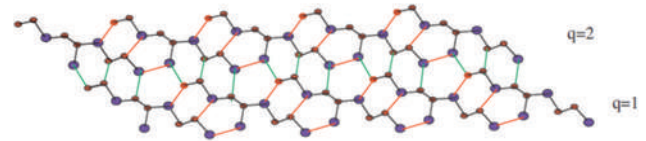


Fig. 2. Two-dimensional structure of $Si_2C_3-II[5,2]$.

TABLE I
VE-DEGREES OF THE END VERTICES OF $Si_2C_3-I[p,q]$

Edge	Ve-degrees of end vertices of edge	Number of edges
(2,1)	(4,2)	1
(3,1)	(5,3)	1
(2,2)	(5,5)	$p+2q$
(3,2)	(5,5)	1
(3,2)	(7,4)	1
(3,2)	(7,5)	$2q+2$
(3,2)	(5,6)	1
(3,2)	(7,6)	$4p+2q-7$
(3,2)	(8,6)	$2q-2$
(3,2)	(8,5)	$2p+2q-5$
(3,3)	(8,7)	1
(3,3)	(8,8)	$p+2q-4$
(3,3)	(9,7)	$2p+2q-3$
(3,3)	(9,8)	$2p+4q-7$
(3,3)	(9,9)	$15pq-14p-21q+20$

TABLE II
VE-DEGREES OF THE END VERTICES OF $Si_2C_3-II[p,q]$

Edge	Ve-degrees of end vertices of edge	Number of edges
(2,1)	(3,2)	2
(3,1)	(7,3)	1
(2,2)	(4,3)	2
(2,2)	(5,4)	2
(2,2)	(5,5)	$2p+2q-4$
(3,2)	(7,5)	$2p+2q$
(3,2)	(7,6)	$2p+2q-2$
(3,2)	(8,6)	$2p+2q-6$
(3,2)	(8,5)	$2p+2q-6$
(3,3)	(8,7)	2
(3,3)	(8,8)	$2p+2q-8$
(3,3)	(7,7)	2
(3,3)	(9,7)	$2p+2q-3$
(3,3)	(9,8)	$2p+2q-5$
(3,3)	(9,9)	$15pq-19p-19q+23$

$$\begin{aligned}
 H^{ve}(Si_2C_3 - I) &= (15pq - 14p - 21q + 20) \\
 &x\frac{1}{9} + (2p + 4q - 7)x\frac{2}{17} + (p + 2q - 4)x\frac{1}{8} \\
 &+ (2p + 2q - 3)x\frac{1}{8} + (4p + 2q - 7)x\frac{2}{13} + (2q - 2) \\
 &\cdot x\frac{1}{7} + (2p + 2q - 5)x\frac{2}{13} + (q + 1)x\frac{1}{3} + (p + 2q + 1) \\
 &x\frac{1}{5} + \frac{2}{11} + \frac{1}{3} + \frac{1}{4} + \frac{2}{11} + \frac{2}{15}
 \end{aligned}$$

$$\begin{aligned}
 \chi^{ve}(Si_2C_3 - I) &= (15pq - 14p - 21q + 20) \\
 &x\frac{1}{3\sqrt{2}} + (2p + 4q - 7)x\frac{1}{\sqrt{17}} + (3p + 4q - 7) \\
 &x\frac{1}{4} + (2p + 2q - 5)x\frac{1}{\sqrt{13}} + (2q - 2)x\frac{1}{\sqrt{14}} \\
 &\cdot + (4p + 2q - 7)x\frac{1}{\sqrt{13}} + (q + 1)x\frac{1}{\sqrt{3}} + (p + 2q + 1) \\
 &x\frac{1}{\sqrt{10}} + \frac{1}{\sqrt{6}} + \frac{1}{2\sqrt{2}} + \frac{2}{\sqrt{11}} + \frac{1}{\sqrt{15}}
 \end{aligned}$$

$$\begin{aligned}
 H_1(Si_2C_3 - I) &= (15pq - 9p - 13q + 9)x\frac{1}{3} + (6p + 8q - 5) \\
 &\cdot x\frac{2}{5} + (p + 2q + 1)x\frac{1}{2}
 \end{aligned}$$

$$\begin{aligned}
 H_5(Si_2C_3 - I) &= (15pq - 14p - 21q + 20) \\
 &x\frac{1}{9} + (2p + 4q - 7)x\frac{2}{17} + (p + 2q - 4)x\frac{1}{8} \\
 &+ (2p + 2q - 3)x\frac{1}{8} + (4p + 2q - 7)x\frac{2}{13} \\
 &\cdot + (2q - 2)x\frac{1}{7} + (2p + 2q - 5)x\frac{2}{13} + (q + 1)x\frac{1}{3} \\
 &+ (p + 2q + 1)x\frac{1}{5} + \frac{2}{11} + \frac{1}{3} + \frac{1}{4} + \frac{2}{11} + \frac{2}{15}
 \end{aligned}$$

Proof of Theorem 1. From Fig. 1, Table I and the definition of ve-ABC index, we can write directly;

$$\begin{aligned}
 ABC^{ve}(Si_2C_3 - I) &= \sum_{uv \in E(Si_2C_3 - I)} \sqrt{\frac{deg_{ve}u + deg_{ve}v - 2}{deg_{ve}u deg_{ve}v}} = \\
 &= 1x\sqrt{\frac{4}{8}} + 1x\sqrt{\frac{6}{15}} + (p + 2q)x\sqrt{\frac{6}{15}} + 1x\sqrt{\frac{8}{25}} + 1x\sqrt{\frac{9}{28}} \\
 &+ (2q + 2)x\sqrt{\frac{10}{35}} + 1x\sqrt{\frac{9}{30}} + (4p + 2q - 7)x\sqrt{\frac{11}{42}} \\
 &+ (2q - 2)x\sqrt{\frac{12}{48}} + (2p + 2q - 5)x\sqrt{\frac{15}{72}} + 1x\sqrt{\frac{13}{56}} \\
 &+ (p + 2q - 4)x\sqrt{\frac{14}{64}} + (2p + 2q - 3)x\sqrt{\frac{14}{63}} + (2p + 4q - 7) \\
 &x\sqrt{\frac{15}{72}} + (15pq - 14p - 21q + 20)x\sqrt{\frac{11}{42}}
 \end{aligned}$$

After simplification we get;

$$\begin{aligned}
 &= (15pq - 14p - 21q + 20)x\sqrt{\frac{11}{42}} \\
 &+ q - 1 + (p + 2q - 4)x\sqrt{\frac{7}{32}} + (2q + 2)x\sqrt{\frac{2}{7}} \\
 &+ (4p + 2q - 7)x\sqrt{\frac{11}{42}} + (2p + 2q - 5)x\sqrt{\frac{5}{24}} \\
 &+ (2p + 2q - 3)x\sqrt{\frac{2}{7}} + (2p + 4q - 7)x \\
 &\sqrt{\frac{5}{24}} + \sqrt{\frac{1}{2}} + \sqrt{\frac{2}{5}} + \sqrt{\frac{8}{25}} + \sqrt{\frac{9}{28}} + \sqrt{\frac{9}{30}} + \sqrt{\frac{13}{56}}
 \end{aligned}$$

Again from Fig. 1, Table I and the definition of ve-GA index, we can write directly;

$$\begin{aligned}
 GA^{ve}(Si_2C_3 - I) &= \sum_{uv \in E(Si_2C_3 - I)} \frac{2\sqrt{deg_{ve}u deg_{ve}v}}{deg_{ve}u + deg_{ve}v} \\
 &= 1x\frac{2\sqrt{8}}{6} + 1x\frac{2\sqrt{15}}{8} + (p + 2q)x\frac{2\sqrt{25}}{10} + 1x\frac{2\sqrt{25}}{10} \\
 &+ 1x\frac{2\sqrt{28}}{11} + (2q + 2)x\frac{2\sqrt{35}}{12} + 1x\frac{2\sqrt{30}}{11} + (4p + 2q - 7) \\
 &x\frac{2\sqrt{42}}{13} + (2q - 2)x\frac{2\sqrt{48}}{14} + (2p + 2q - 5)x\frac{2\sqrt{40}}{13} \\
 &+ 1x\frac{2\sqrt{56}}{15} + (p + 2q - 4)x\frac{2\sqrt{64}}{16} + (2p + 2q - 3)x\frac{2\sqrt{63}}{16} \\
 &+ (2p + 4q - 7)x\frac{2\sqrt{72}}{17} + (15pq - 14p - 21q + 20)x\frac{2\sqrt{81}}{18} \\
 &= 15pq - 14p - 21q + 20 + p + 2q - 4 + p + 2q \\
 &+ (2q + 2)x\frac{\sqrt{35}}{6} + (4p + 2q - 7)x\frac{2\sqrt{42}}{13} + (2q - 2) \\
 &x\frac{4\sqrt{3}}{7} + (2p + 2q - 5)x\frac{4\sqrt{10}}{13} + (2p + 2q - 3)x\frac{3\sqrt{7}}{8} \\
 &+ (2p + 4q - 7)x\frac{12\sqrt{2}}{17} + \frac{2\sqrt{2}}{3} + \frac{2\sqrt{15}}{8} \\
 &+ 1 + \frac{4\sqrt{7}}{11} + \frac{2\sqrt{30}}{11} + \frac{4\sqrt{14}}{15}
 \end{aligned}$$

After simplification, we get it;

$$\begin{aligned}
 &= 15pq - 12p - 17q + 17 + (2q + 2)x\frac{\sqrt{35}}{6} + (4p + 2q - 7) \\
 &x\frac{2\sqrt{42}}{13} + (2q - 2)x\frac{4\sqrt{3}}{7} + (2p + 2q - 5)x\frac{4\sqrt{10}}{13} \\
 &+ (2p + 2q - 3)x\frac{3\sqrt{7}}{8} + (2p + 4q - 7)x\frac{12\sqrt{2}}{17} \\
 &+ \frac{2\sqrt{2}}{3} + \frac{2\sqrt{15}}{8} + \frac{4\sqrt{7}}{11} + \frac{2\sqrt{30}}{11} + \frac{4\sqrt{14}}{15}
 \end{aligned}$$

Now, we prove the ve-H index of $Si_2C_3 - I$. From Fig. 1, Table I and the definition of ve-H index, we can write directly;

$$\begin{aligned}
 H^{ve}(Si_2C_3 - I) &= \sum_{uv \in E(Si_2C_3 - I)} \frac{2}{deg_{ve}u + deg_{ve}v} \\
 &= 1x \frac{2}{6} + 1x \frac{2}{8} + (p+2q)x \frac{2}{10} + 1x \frac{2}{10} + 1x \frac{2}{11} + (2q+2)x \frac{2}{12} \\
 &+ 1x \frac{2}{11} + (4p+2q-7)x \frac{2}{13} + (2q-2)x \frac{2}{14} + (2p+2q-5) \\
 &x \frac{2}{13} + 1x \frac{2}{15} + (p+2q-4)x \frac{2}{16} + (2p+2q-3)x \frac{2}{16} + \left(\frac{2p+}{4q-7} \right) \\
 &x \frac{2}{17} + (15pq-14p-21q+20)x \frac{2}{18} \\
 &= \frac{1}{3} + \frac{1}{4} + (p+2q+1)x \frac{1}{5} + \frac{2}{11} + (q+1)x \frac{1}{3} + \frac{2}{11} \\
 &+ (4p+2q-7)x \frac{2}{13} + (2q-2)x \frac{1}{7} + (2p+2q-5) \\
 &x \frac{2}{13} + \frac{2}{15} + (p+2q-4)x \frac{1}{8} + (2p+2q-3)x \frac{1}{8} \\
 &+ (2p+4q-7)x \frac{2}{17} + (15pq-14p-21q+20)x \frac{1}{9}
 \end{aligned}$$

After some simplifications, we get;

$$\begin{aligned}
 &= (15pq-14p-21q+20)x \frac{1}{9} + (2p+4q-7)x \frac{2}{17} \\
 &+ (p+2q-4)x \frac{1}{8} + (2p+2q-3)x \frac{1}{8} + (4p+2q-7) \\
 &x \frac{2}{13} + (2q-2)x \frac{1}{7} + (2p+2q-5)x \frac{2}{13} + (q+1)x \frac{1}{3} \\
 &+ (p+2q+1)x \frac{1}{5} + \frac{2}{11} + \frac{1}{3} + \frac{1}{4} + \frac{2}{11} + \frac{2}{15}
 \end{aligned}$$

Now, we prove the $ve-\chi$ index of $Si_2 C_3$ -I. From Fig. 1, Table I and the definition of $ve-\chi$ index, we can write directly;

$$\begin{aligned}
 \chi^{ve}(Si_2C_3 - I) &= \sum_{uv \in E(Si_2C_3 - I)} (deg_{ve}u + deg_{ve}v)^{-1/2} \\
 &= 1x \frac{1}{\sqrt{6}} + 1x \frac{1}{\sqrt{8}} + (p+2q)x \frac{1}{\sqrt{10}} + 1x \frac{1}{\sqrt{10}} + 1x \frac{1}{\sqrt{11}} \\
 &+ (2q+2)x \frac{1}{\sqrt{12}} + 1x \frac{1}{\sqrt{11}} + (4p+2q-7)x \frac{1}{\sqrt{13}} \\
 &+ (2q-2)x \frac{1}{\sqrt{14}} + (2p+2q-5)x \frac{1}{\sqrt{13}} + 1x \frac{1}{\sqrt{15}} \\
 &+ (p+2q-4)x \frac{1}{\sqrt{16}} + (2p+2q-3)x \frac{1}{\sqrt{16}} + (2p+4q-7) \\
 &x \frac{1}{\sqrt{17}} + (15pq-14p-21q+20)x \frac{1}{\sqrt{18}} \\
 &= \frac{1}{\sqrt{6}} + \frac{1}{2\sqrt{2}} + (p+2q+1)x \frac{1}{\sqrt{10}} + \frac{2}{\sqrt{11}} + (q+1) \\
 &x \frac{1}{\sqrt{3}} + (4p+2q-7)x \frac{1}{\sqrt{13}} + (2q-2)x \frac{1}{\sqrt{14}} \\
 &+ (2p+2q-5)x \frac{1}{\sqrt{13}} + \frac{1}{\sqrt{15}} + (3p+4q-7)x \frac{1}{4} \\
 &+ (2p+4q-7)x \frac{1}{\sqrt{17}} + (15pq-14p-21q+20)x \frac{1}{3\sqrt{2}}
 \end{aligned}$$

After necessary simplifications, we get;

$$\begin{aligned}
 &= (15pq-14p-21q+20)x \frac{1}{3\sqrt{2}} + (2p+4q-7) \\
 &x \frac{1}{\sqrt{17}} + (3p+4q-7)x \frac{1}{4} + (2p+2q-5)x \frac{1}{\sqrt{13}} \\
 &+ (2q-2)x \frac{1}{\sqrt{14}} + (4p+2q-7)x \frac{1}{\sqrt{13}} + (q+1) \\
 &x \frac{1}{\sqrt{3}} + (p+2q+1)x \frac{1}{\sqrt{10}} + \frac{1}{\sqrt{6}} + \frac{1}{2\sqrt{2}} + \frac{2}{\sqrt{11}} + \frac{1}{\sqrt{15}}
 \end{aligned}$$

Now, we prove the first harmonic index of $Si_2 C_3$ -I. From Fig. 1, Table I and the definition of the first harmonic index, we can write directly;

$$\begin{aligned}
 H_1(Si_2C_3 - I) &= \sum_{uv \in E(Si_2C_3 - I)} \frac{2}{d_u + d_v} \\
 &= 1x \frac{2}{3} + 1x \frac{2}{4} + (p+2q)x \frac{2}{4} + 1x \frac{2}{5} + 1x \frac{2}{5} + (2q+2) \\
 &x \frac{2}{5} + 1x \frac{2}{5} + (4p+2q-7)x \frac{2}{5} + (2q-2)x \frac{2}{5} + \left(\frac{2p+}{2q-5} \right) x \frac{2}{5} \\
 &+ 1x \frac{2}{6} + (p+2q-4)x \frac{2}{6} + (2p+2q-3)x \frac{2}{6} \\
 &+ (2p+4q-7)x \frac{2}{6} + (15pq-14p-21q+20)x \frac{2}{6}
 \end{aligned}$$

After necessary simplifications, we can write that;

$$\begin{aligned}
 &= \frac{2}{3} + \frac{1}{2} + (p+2q)x \frac{1}{2} + \frac{2}{5} + \frac{2}{5} + (2q+2)x \frac{2}{5} + \frac{2}{5} \\
 &+ (4p+2q-7)x \frac{2}{5} + (2q-2)x \frac{2}{5} + (2p+2q-5)x \frac{2}{5} \\
 &+ \frac{1}{3} + (p+2q-4)x \frac{1}{3} + (2p+2q-3)x \frac{1}{3} + \left(\frac{2p+4q}{-7} \right) \\
 &x \frac{1}{3} + (15pq-14p-21q+20)x \frac{1}{3} \\
 &= (15pq-9p-13q+9)x \frac{1}{3} + (6p+8q-5)x \frac{2}{5} + \\
 &+ (p+2q+1)x \frac{1}{2}
 \end{aligned}$$

And now, we prove the fifth harmonic index of $Si_2 C_3$ -I. From Fig. 1, Table I and the definition of the fifth harmonic index, we can write directly;

$$\begin{aligned}
 H_5(Si_2C_3 - I) &= \sum_{uv \in E(Si_2C_3 - I)} \frac{2}{S_u + S_v} \\
 &= 1x \frac{2}{6} + 1x \frac{2}{8} + (p+2q)x \frac{2}{10} + 1x \frac{2}{10} + 1x \frac{2}{11} + (2q+2) \\
 &x \frac{2}{12} + 1x \frac{2}{11} + (4p+2q-7)x \frac{2}{13} + (2q-2)x \frac{2}{14} + \left(\frac{2p}{+2q-5} \right) \\
 &x \frac{2}{13} + 1x \frac{2}{15} + (p+2q-4)x \frac{2}{16} + (2p+2q-3)x \frac{2}{16} \\
 &+ (2p+4q-7)x \frac{2}{17} + (15pq-14p-21q+20)x \frac{2}{18}
 \end{aligned}$$

$$\begin{aligned}
 &= \frac{1}{3} + \frac{1}{4} + (p+2q+1)x\frac{1}{5} + \frac{2}{11} + (q+1)x\frac{1}{3} \\
 &+ \frac{2}{11} + (4p+2q-7)x\frac{2}{13} + (2q-2)x\frac{1}{7} \\
 &+ (2p+2q-5)x\frac{2}{13} + \frac{2}{15} + (p+2q-4)x\frac{1}{8} \\
 &+ (2p+2q-3)x\frac{1}{8} + (2p+4q-7) \\
 &x\frac{2}{17} + (15pq-14p-21q+20)x\frac{1}{9}
 \end{aligned}$$

After necessary simplifications, we can write that;

$$\begin{aligned}
 &= (15pq-14p-21q+20)x\frac{1}{9} \\
 &+ (2p+4q-7)x\frac{2}{17} + (p+2q-4) \\
 &x\frac{1}{8} + (2p+2q-3)x\frac{1}{8} + (4p+2q-7)x\frac{2}{13} \\
 &+ (2q-2)x\frac{1}{7} + (2p+2q-5)x\frac{2}{13} + (q+1)x\frac{1}{3} \\
 &+ (p+2q+1)x\frac{1}{5} + \frac{2}{11} + \frac{1}{3} + \frac{1}{4} + \frac{2}{11} + \frac{2}{15}
 \end{aligned}$$

And now, we begin to compute topological indices for $Si_2C_3-II[p,q]$.

Theorem 2

The ve-degree, the first and the fifth harmonic topological indices of the $Si_2C_3-II[p,q]$ are

$$\begin{aligned}
 ABC^{ve}(Si_2C_3-II) &= (15pq-19p-19q+23) \\
 &x\frac{4}{9} + p+q-3 + (2p+2q-5)x\sqrt{\frac{5}{24}} \\
 &+ (2p+2q-3)x\sqrt{\frac{14}{63}} + (2p+2q-8)x\sqrt{\frac{7}{32}} \\
 &+ (2p+2q-6)x\sqrt{\frac{11}{40}} + (2p+2q-2)x\sqrt{\frac{11}{42}} + \\
 &+ (2p+2q)x\sqrt{\frac{10}{35}} + (2p+2q-4)x\sqrt{\frac{8}{25}} + \sqrt{2} + \sqrt{\frac{8}{21}} \\
 &+ 2x\sqrt{\frac{5}{12}} + \sqrt{\frac{7}{5}} + \sqrt{\frac{13}{14}} + 4x\sqrt{\frac{3}{49}} \\
 GA^{ve}(Si_2C_3-II) &= 15pq-15p-15q+(2p+2q) \\
 &x\frac{2\sqrt{35}}{12} + (2p+2q-2)x\frac{2\sqrt{42}}{13} + (2p+2q-6) \\
 &x\frac{4\sqrt{3}}{7} + (2p+2q-6)x\frac{8\sqrt{10}}{13} + (2p+2q-3) \\
 &x\frac{6\sqrt{7}}{16} + (2p+2q-5)x\frac{12\sqrt{2}}{17} + 13 + \frac{4\sqrt{6}}{5} \\
 &+ \frac{\sqrt{21}}{5} + \frac{8\sqrt{2}}{7} + \frac{8\sqrt{5}}{9} + \frac{16\sqrt{7}}{15}
 \end{aligned}$$

$$\begin{aligned}
 H^{ve}(Si_2C_3-II) &= \frac{4}{5} + \frac{1}{5} + \frac{6}{7} + \frac{4}{9} + (2p+2q-4)x\frac{1}{5} \\
 &+ (p+q)x\frac{1}{3} + (2p+2q-2)x\frac{2}{13} + \binom{2p}{+2q-6}x\frac{1}{7} + \binom{2p}{+2q-6} \\
 &x\frac{2}{13} + \frac{4}{15} + \binom{2p}{+2q-8}x\frac{1}{8} + \binom{2p}{+2q-3}x\frac{1}{8} + \binom{2p}{+2q-5}x\frac{2}{17} \\
 &+ (15pq-19p-19q+23)x\frac{1}{9}
 \end{aligned}$$

$$\begin{aligned}
 \chi^{ve}(Si_2C_3-II) &= \frac{2}{\sqrt{5}} + \frac{1}{\sqrt{10}} + \frac{2}{\sqrt{7}} + \frac{2}{3} + \frac{2}{\sqrt{15}} + \frac{2}{\sqrt{14}} \\
 &+ \binom{2p+2q}{-4}x\frac{1}{\sqrt{10}} + (p+q)x\frac{1}{\sqrt{3}} + \binom{2p+2q}{-2}x\frac{1}{\sqrt{13}} \\
 &+ \binom{2p+}{2q-6}x\frac{1}{\sqrt{14}} + (2p+2q-6)x\frac{1}{\sqrt{13}} + \binom{p+q}{-4}x\frac{1}{2} \\
 &+ \binom{2p+}{2q-3}x\frac{1}{\sqrt{16}} + \binom{2p+}{2q-5}x\frac{2}{\sqrt{17}} + \binom{15pq-19p}{-19q+23}x\frac{1}{3\sqrt{2}}
 \end{aligned}$$

$$\begin{aligned}
 H_1(Si_2C_3-II) &= 5 + p + q + (8p+8q-14)x\frac{2}{5} \\
 &+ (15pq-13p-13q+9)x\frac{1}{3}
 \end{aligned}$$

$$\begin{aligned}
 H_5(GSi_2C_3-II) &= \frac{4}{5} + \frac{1}{5} + \frac{6}{7} + \frac{4}{9} + \binom{2p}{+2q-4}x\frac{1}{5} \\
 &+ (p+q)x\frac{1}{3} + \binom{2p}{+2q-2}x\frac{2}{13} + \binom{2p}{+2q-6}x\frac{1}{7} + \binom{2p}{+2q-6} \\
 &x\frac{2}{13} + \frac{4}{15} + \binom{2p}{+2q-8}x\frac{1}{8} + \binom{2p}{+2q-3}x\frac{1}{8} + \binom{2p}{+2q-5}x\frac{2}{17} \\
 &+ (15pq-19p-19q+23)x\frac{1}{9}
 \end{aligned}$$

Proof of Theorem 2

From Fig. 2, Table II and the definition of ve-ABC index, we can write directly;

$$\begin{aligned}
 ABC^{ve}(Si_2C_3-II) &= \sum_{uv \in E(Si_2C_3-I)} \sqrt{\frac{deg_{ve}u + deg_{ve}v - 2}{deg_{ve}u deg_{ve}v}} \\
 &= 2x\sqrt{\frac{3}{6}} + 1x\sqrt{\frac{8}{21}} + 2x\sqrt{\frac{5}{12}} + 2x\sqrt{\frac{7}{20}} + (2p+2q-4) \\
 &x\sqrt{\frac{8}{25}} + (2p+2q)x\sqrt{\frac{10}{35}} + (2p+2q-2)x\sqrt{\frac{11}{42}} \\
 &+ (2p+2q-6)x\sqrt{\frac{12}{48}} + (2p+2q-6)x\sqrt{\frac{11}{40}} + 2x\sqrt{\frac{13}{56}} \\
 &+ (2p+2q-8)x\sqrt{\frac{14}{64}} + 2x\sqrt{\frac{12}{49}} + \binom{2p}{+2q-3}x\sqrt{\frac{14}{63}} \\
 &+ (2p+2q-5)x\sqrt{\frac{15}{72}} + \binom{15pq-19p}{-19q+23}x\sqrt{\frac{16}{81}}
 \end{aligned}$$

After necessary simplifications we get;

$$\begin{aligned}
 &= (15pq - 19p - 19q + 23)x \frac{4}{9} + p + q - 3 + (2p + 2q - 5) \\
 &x \sqrt{\frac{5}{24}} + (2p + 2q - 3)x \sqrt{\frac{14}{63}} + (2p + 2q - 8)x \sqrt{\frac{7}{32}} \\
 &+ (2p + 2q - 6)x \sqrt{\frac{11}{40}} + (2p + 2q - 2)x \sqrt{\frac{11}{42}} \\
 &+ (2p + 2q)x \sqrt{\frac{10}{35}} + (2p + 2q - 4)x \sqrt{\frac{8}{25}} + \sqrt{2} \\
 &+ \sqrt{\frac{8}{21}} + 2x \sqrt{\frac{5}{12}} + \sqrt{\frac{7}{5}} + \sqrt{\frac{13}{14}} + 4x \sqrt{\frac{3}{49}}
 \end{aligned}$$

And now, we prove the ve-GA index of $Si_2 C_3$ -II. From Fig. 2, Table II and the definition of ve-GA index, we can write directly;

$$\begin{aligned}
 GA^{ve}(Si_2 C_3 - II) &= \sum_{uv \in E(Si_2 C_3 - II)} \frac{2\sqrt{deg_{ve}u deg_{ve}v}}{deg_{ve}u + deg_{ve}v} \\
 &= 15pq - 19p - 19q + 23 + 2 + 2p + 2q - 8 + 2p + 2q - 4 \\
 &+ \frac{4\sqrt{6}}{5} + \frac{\sqrt{21}}{5} + \frac{8\sqrt{2}}{7} + \frac{8\sqrt{5}}{9} + (2p + 2q)x \frac{2\sqrt{35}}{12} + \left(\frac{2p}{+2q-2} \right) \\
 &x \frac{2\sqrt{42}}{13} + (2p + 2q - 6)x \frac{4\sqrt{3}}{7} + (2p + 2q - 6)x \frac{8\sqrt{10}}{13} \\
 &+ \frac{16\sqrt{7}}{15} + (2p + 2q - 3)x \frac{6\sqrt{7}}{16} + (2p + 2q - 5)x \frac{12\sqrt{2}}{17}
 \end{aligned}$$

After necessary simplifications, we can write that;

$$\begin{aligned}
 &= 15pq - 15p - 15q + (2p + 2q)x \frac{2\sqrt{35}}{12} + (2p + 2q - 2) \\
 &x \frac{2\sqrt{42}}{13} + (2p + 2q - 6)x \frac{4\sqrt{3}}{7} + (2p + 2q - 6)x \frac{8\sqrt{10}}{13} \\
 &+ (2p + 2q - 3)x \frac{6\sqrt{7}}{16} + (2p + 2q - 5)x \frac{12\sqrt{2}}{17} \\
 &+ 13 + \frac{4\sqrt{6}}{5} + \frac{\sqrt{21}}{5} + \frac{8\sqrt{2}}{7} + \frac{8\sqrt{5}}{9} + \frac{16\sqrt{7}}{15}
 \end{aligned}$$

And now, we prove the ve-H index of $Si_2 C_3$ -II. From Fig. 2, Table II and the definition of ve-H index, we can write directly;

$$\begin{aligned}
 H^{ve}(Si_2 C_3 - II) &= \sum_{uv \in E(Si_2 C_3 - II)} \frac{2}{deg_{ve}u + deg_{ve}v} \\
 &= 2x \frac{2}{5} + 1x \frac{2}{10} + 2x \frac{2}{7} + 2x \frac{2}{9} + (2p + 2q - 4)x \frac{2}{10} \\
 &+ (2p + 2q)x \frac{2}{12} + (2p + 2q - 2)x \frac{2}{13} + (2p + 2q - 6)x \frac{2}{14} \\
 &+ (2p + 2q - 6)x \frac{2}{13} + 2x \frac{2}{15} + (2p + 2q - 8)x \frac{2}{16} \\
 &+ 2x \frac{2}{14} + (2p + 2q - 3)x \frac{2}{16} + (2p + 2q - 5)x \frac{2}{17} \\
 &+ (15pq - 19p - 19q + 23)x \frac{2}{18}
 \end{aligned}$$

After necessary simplifications, we can write that,

$$\begin{aligned}
 &= \frac{4}{5} + \frac{1}{5} + \frac{6}{7} + \frac{4}{9} + (2p + 2q - 4)x \frac{1}{5} + (p + q)x \frac{1}{3} \\
 &+ (2p + 2q - 2)x \frac{2}{13} + (2p + 2q - 6)x \frac{1}{7} + (2p + 2q - 6) \\
 &x \frac{2}{13} + \frac{4}{15} + (2p + 2q - 8)x \frac{1}{8} + (2p + 2q - 3)x \frac{1}{8} + \left(\frac{2p}{+2q-5} \right) \\
 &x \frac{2}{17} + (15pq - 19p - 19q + 23)x \frac{1}{9}
 \end{aligned}$$

And now, we prove the ve- χ index of $Si_2 C_3$ -II. From Fig. 2, Table II and the definition of ve- χ index, we can write directly;

$$\begin{aligned}
 \chi^{ve}(Si_2 C_3 - II) &= \sum_{uv \in E(GSi_2 C_3 - II)} (deg_{ve}u + deg_{ve}v)^{-1/2} \\
 &= 2x \frac{1}{5} + 1x \frac{1}{10} + 2x \frac{1}{7} + 2x \frac{1}{9} + (2p + 2q - 4)x \frac{1}{10} \\
 &+ (2p + 2q)x \frac{1}{12} + (2p + 2q - 2)x \frac{1}{13} + (2p + 2q - 6) \\
 &x \frac{1}{14} + (2p + 2q - 6)x \frac{1}{13} + 2x \frac{1}{15} + (2p + 2q - 8) \\
 &x \frac{1}{16} + 2x \frac{1}{14} + (2p + 2q - 3)x \frac{1}{16} + (2p + 2q - 5) \\
 &x \frac{1}{17} + (15pq - 19p - 19q + 23)x \frac{1}{18}
 \end{aligned}$$

After some necessary simplifications, we can directly write that;

$$\begin{aligned}
 &= \frac{2}{\sqrt{5}} + \frac{1}{\sqrt{10}} + \frac{2}{\sqrt{7}} + \frac{2}{3} + \frac{2}{\sqrt{15}} + \frac{2}{\sqrt{14}} + (2p + 2q - 4) \\
 &x \frac{1}{\sqrt{10}} + (p + q)x \frac{1}{\sqrt{3}} + (2p + 2q - 2)x \frac{1}{\sqrt{13}} \\
 &+ (2p + 2q - 6)x \frac{1}{\sqrt{14}} + (2p + 2q - 6)x \frac{1}{\sqrt{13}} \\
 &+ (p + q - 4)x \frac{1}{2} + (2p + 2q - 3)x \frac{1}{\sqrt{16}} + (2p + 2q - 5) \\
 &x \frac{2}{\sqrt{17}} + (15pq - 19p - 19q + 23)x \frac{1}{3\sqrt{2}}
 \end{aligned}$$

And now, we prove the first harmonic index of $Si_2 C_3$ -II. From Fig. 2, Table II and the definition of the first harmonic index, we can write directly;

$$\begin{aligned}
 H_1(Si_2 C_3 - II) &= \sum_{uv \in E(Si_2 C_3 - II)} \frac{2}{d_u + d_v} \\
 &= 2x \frac{2}{3} + 1x \frac{2}{4} + 2x \frac{2}{4} + 2x \frac{2}{4} + \left(\frac{2p}{+2q-4} \right) x \frac{2}{4} \\
 &+ (2p + 2q)x \frac{2}{5} + (2p + 2q - 2)x \frac{2}{5} + \left(\frac{2p}{+2q-6} \right) \\
 &x \frac{2}{5} + \left(\frac{2p}{+2q-6} \right) x \frac{2}{5} + 2x \frac{2}{6} + \left(\frac{2p}{+2q-8} \right) x \frac{2}{6} + 2x \frac{2}{6} \\
 &+ \left(\frac{2p}{2q-3} \right) x \frac{2}{6} + \left(\frac{2p}{+2q-5} \right) x \frac{2}{6} + \left(\frac{15pq - 19p}{-19q + 23} \right) x \frac{2}{6}
 \end{aligned}$$

After necessary simplifications, we get;

$$= 5 + p + q + (8p + 8q - 14)x \frac{2}{5} + (15pq - 13p - 13q + 9)x \frac{1}{3}$$

And now, we prove the fifth harmonic index of $Si_2 C_3$ -II. From Fig. 2, Table II and the definition of the fifth harmonic index, we can write directly;

$$\begin{aligned} H_5(GSi_2C_3-II) &= \sum_{uv \in E(GSi_2C_3-II)} \frac{2}{S_u + S_v} \\ &= 2x \frac{2}{5} + 1x \frac{2}{10} + 2x \frac{2}{7} + 2x \frac{2}{9} + (2p + 2q - 4)x \frac{2}{10} \\ &+ (2p + 2q)x \frac{2}{12} + (2p + 2q - 2)x \frac{2}{13} + (2p + 2q - 6) \\ &x \frac{2}{14} + (2p + 2q - 6)x \frac{2}{13} + 2x \frac{2}{15} + (2p + 2q - 8)x \frac{2}{16} + \\ &2x \frac{2}{14} + (2p + 2q - 3)x \frac{2}{16} + (2p + 2q - 5)x \frac{2}{17} \\ &+ (15pq - 19p - 19q + 23)x \frac{2}{18} \end{aligned}$$

After necessary simplifications, we get;

$$\begin{aligned} &= \frac{4}{5} + \frac{1}{5} + \frac{6}{7} + \frac{4}{9} + (2p + 2q - 4)x \frac{1}{5} + (p + q)x \frac{1}{3} \\ &+ (2p + 2q - 2)x \frac{2}{13} + (2p + 2q - 6)x \frac{1}{7} \\ &+ (2p + 2q - 6)x \frac{2}{13} + \frac{4}{15} + (2p + 2q - 8)x \frac{1}{8} \\ &+ (2p + 2q - 3)x \frac{1}{8} + (2p + 2q - 5)x \frac{2}{17} \\ &+ (15pq - 19p - 19q + 23)x \frac{1}{9} \end{aligned}$$

V. CONCLUSIONS

In this study, we calculated the ve -ABC, ve -GA, ve -H, and ve - χ , the first harmonic and the fifth harmonic molecular topological properties of the two silicon carbide structures: $Si_2 C_3$ -I and $Si_2 C_3$ -II. These calculations enable to understand and to give information about the underlying topology of $Si_2 C_3$ -I and $Si_2 C_3$ -II.

Mathematical properties of ev -degree, ve -degree, and novel harmonic topological indices are interesting studies for further studies. It is also interesting to compute ve -degree based topological indices and novel harmonic indices of nanostructures and molecules for further studies.

REFERENCES

Anjum, M.S. and Safdar, M.U., 2019. K Banhatti and K hyper-Banhatti indices of nanotubes. *Engineering and Applied Science Letters*, 2(1), pp.19-37.

Chellali, M., Haynes, T.W., Hedetniemi, S.T. and Lewis, T.M., 2017. On ve -degrees and ev -degrees in graphs. *Discrete Mathematics*, 340(2), pp.31-38.

Ediz, S., 2010. Computing ediz eccentric connectivity index of an infinite class of nanostar dendrimers. *Optoelectronics and Advanced Materials: Rapid Communications*, 4, pp.1847-1848.

Ediz, S., 2011. On the ediz eccentric connectivity index of a graph. *Optoelectronics and Advanced Materials: Rapid Communications*, 5(11), pp.1263-1264.

Ediz, S., 2013. The ediz eccentric connectivity index of one pentagonal carbon nanocones. *Fullerenes, Nanotubes and Carbon Nanostructures*, 21(2), pp. 113-116.

Ediz, S., 2017. A new tool for QSPR researches: Ev -degree randić index. *Celal Bayar Journal of Science*, 13(3), pp.615-618.

Ediz, S., 2017. Predicting some physicochemical properties of octane isomers: A topological approach using ev -degree and ve -degree zagreb indices. *International Journal of Systems Science and Applied Mathematics*, 2(5), pp.87-92.

Ediz, S., 2018. On ve -degree molecular topological properties of silicate and oxygen networks. *International Journal of Computing Science and Mathematics*, 9(1), pp.1-12.

Ediz, S., Farahani, M.R. and Imran, M., 2017. On novel harmonic indices of certain nanotubes. *International Journal of Advanced Biotechnology and Research*, 8(4), pp.87-92.

Gao, W., Asif, M. and Nazeer, W., 2018. The study of honey comb derived network via topological indices. *The Open Journal of Mathematical Analysis*, 2(2), pp.10-26.

Imran, M., Siddiqui, M., Naeem, M. and Iqbal, M., 2018. On topological properties of symmetric chemical structures. *Symmetry*, 10(5), pp.173-182.

Jiang, J.W., Wang, B.S. and Park, H.S., 2018. Topologically protected interface phonons in two-dimensional nanomaterials: Hexagonal boron nitride and silicon carbide. *Nanoscale*, 10(29), pp.13913-13923.

Kaźmierczak-Bałata, A. and Mazur, J., 2018. Effect of carbon nanoparticle reinforcement on mechanical and thermal properties of silicon carbide ceramics. *Ceramics International*, 44(9), pp.10273-10280.

Kwun, Y., Virk, A., Nazeer, W., Rehman, M. and Kang, S., 2018. On the multiplicative degree-based topological indices of silicon-carbon Si_2C_3 -I [p, q] and Si_2C_3 -II [p, q]. *Symmetry*, 10(8), pp.320-336.

Mei, H., Huang, W., Hua, C., Xu, Y. and Cheng, L., 2018. Manufacturing isotropic carbon fibre preforms for multilayered silicon carbide composites with a pyrolytic carbon interphase. *Journal of Manufacturing Processes*, 34, pp.62-69.

Munir, M., Nazeer, W., Nizami, A.R., Rafique, S. and Kang, S.M., 2016. M-polynomials and topological indices of titania nanotubes. *Symmetry*, 8(11), pp.117-125.

Munir, M., Nazeer, W., Rafique, S. and Kang, S.M., 2016. M-polynomial and degree-based topological indices of polyhex nanotubes. *Symmetry*, 8(12), pp.149-156.

Munir, M., Nazeer, W., Rafique, S. and Kang, S.M., 2016. M-polynomial and related topological indices of Nanostar dendrimers. *Symmetry*, 8(9), pp.97-108.

Reddy, P.S., Kesavan, R. and Ramnath, B.V., 2018. Investigation of mechanical properties of aluminium 6061-silicon carbide, boron carbide metal matrix composite. *Silicon*, 10(2), pp.495-502.

Sahin, B. and Ediz, S., 2018. On ev -degree and ve -degree topological indices. *Iranian Journal of Mathematical Chemistry*, 9(4), pp.263-277.

Seal, S., Glover, M.D. and Mantooh, H.A., 2018. 3-d wire bondless switching cell using flip-chip-bonded silicon carbide power devices. *IEEE Transactions on Power Electronics*, 33(10), pp.8553-8564.

Shao, Z., Virk, A.R., Javed, M.S., Rehman, M.A. and Farahani, M.R., 2019. Degree based graph invariants for the molecular graph of Bismuth Tri-Iodide. *Engineering and Applied Science Letters*, 2(1), pp.1-11.

Snead, L.L., Katoh, Y., Koyanagi, T. and Terrani, K., 2019. Stored energy release in neutron irradiated silicon carbide. *Journal of Nuclear Materials*, 514, pp.181-188.

Taguchi, T., Yamamoto, S. and Ohba, H., 2018. Ion irradiation-induced novel microstructural change in silicon carbide nanotubes. *Acta Materialia*, 154, pp.90-99.

Van der Broeck, C.H., Ruppert, L.A., Lorenz, R.D. and De Doncker, R.W., 2018. Methodology for active thermal cycle reduction of power electronic modules. *IEEE Transactions on Power Electronics*, 34(8), pp.8213-8229.

Virk, A.R., Jhangeer, M.N., Rehman, M.A., 2018. Reverse zagreb and reverse hyper-zagreb indices for silicon carbide Si₂C₃-I[r,s] and Si₂C₃-II [r,s].

Engineering and Applied Science Letters, 1(2), pp.37-50.

Wing, B.L. and Halloran, J.W., 2018. Relaxation of residual microstress in reaction bonded silicon carbide. *Ceramics International*, 44(10), pp.11745-11750.

Zhong, L., 2012. The harmonic index for graphs. *Applied Mathematics Letters*, 25, pp.561-566.

Theoretical Study of Diels-Alder Reaction of But-3-en-2-one with Hexa-1,2,4-triene: A Density Functional Theory Study

Rezan J. Hassan^{1,2} and Hassan H. Abdallah¹

¹Department of Chemistry, College of Education, Salahaddin University-Erbil, Erbil 44001, Kurdistan Region - F.R. Iraq

²Department of Chemistry, College of Science, Salahaddin University-Erbil, Erbil 44001, Kurdistan Region - F.R. Iraq

Abstract—The Diels-Alder reaction between but-3-en-2-one with hexa-1,2,4-triene was studied using density functional theory method at B3LYP-D3/6-311++G(d,p) level of theory. The geometries of the transition states were determined. Moreover, calculations of the vibrational frequencies permitted computation of the activation enthalpies and entropies. The computational results show that the cycloadducts from trans conformer have the lower relative energies (−46.48 and −47.50 kcal/mol) as compared to the cis conformer of cycloadducts (−44.45 and −45.87 kcal/mol). The global reactivity indices were analyzed at the ground state of reactants to predict the reactivity of the studied organic molecules in the cycloaddition reactions. The electronic chemical potential of hexa-1,2,4-trien found to be than but-3-en-2-one, which indicates that the net charge transfer will be from hexa-1,2,4-trien toward the electron-deficient but-3-en-2-one reactant.

Index Terms—Cycloaddition, density functional theory calculation, Diels-Alder reaction, mechanism.

I. INTRODUCTION

Synthesis of complex cyclic compounds is necessary for the development of functional materials such as biologically active compounds, so, very recently, computational studies on cycloaddition reactions have been the subject of a number of researches due to their wide applications on synthetic organic compounds (Mohammad-Salim, et al., 2020; Mohammad-Salim and Abdallah,[†] 2019; Salim, Abdallah and Ramasami, 2018a; Salim, Abdallah and Ramasami, 2018b). Among the cycloaddition reactions, the formation of compounds with an unsaturated six-membered ring through the addition of a conjugated diene to a double or triple bond is known as

the Diels-Alder (D-A) reaction. Since the discovery of this reaction, more than 17,000 articles have been published in relation to synthesis, mechanism, and theoretical aspects of the reaction, and about half of these appeared in the 1990–2000 decade (Fringuelli and Taticchi, 2002).

Diels-Alder cycloaddition is one of the most significant and useful tools available in synthetic chemistry (Kal-Koshvandi and Heravi, 2019). This organic reaction is widely used to build six-member rings with a maximum of four stereogenic centers on a regal and stereo-controlled route (Džambaski, et al., 2019; Zhang, et al., 2019). with the potential formation of carbon-carbon, carbon-heteroatom, and heteroatom-heteroatom bonds (Baeza, 2018; Boger and Weinreb, 2012; Siah, Leung and Mok, 1995).

The mechanistic study of the D-A reaction proceeds through concerted mechanism, usually but not necessarily through a synchronous. Experimental results support a concerted mechanism, whereas computational calculations depend on the method used, for example, semi-empirical calculations (for example, AM1 and PM3) predict a stepwise mechanism, whereas density functional theory (DFT) calculations with B3LYP functional and ab-initio calculations using MP2 and coupled-cluster methods favor a concerted mechanism rather than stepwise mechanism (Jursic and Zdravkovski, 1994; Mohammad-Salim and Abdallah, 2019; Pham and Houk, 2014). In the late 80s, experimental and theoretical evidence converged on a synchronous mechanism. In addition, zwitterionic intermediates have been reported for reactions of 1,3-butadienes with strong demand electronics, for example, 1,1-dimethoxy-1,3-butadiene with electronically poor dienophiles (Carey and Sundberg, 2007).

Asymmetrically substituted dienes and dienophiles give a mixture of two regioisomers, and the regioselectivity in the reactions of disubstituted dienes and with a greater degree of substitution depends on the electronic properties and the relative position of the substituents. In this study, the mechanism and regioselectivity of the D-A reaction of hexa-1,2,4-trien and but-3-en-2-one was studied. To the best of our knowledge, the reaction has not been studied neither experimentally nor theoretically. Therefore, the aim of this

ARO-The Scientific Journal of Koya University
Volume. VIII, No.1(2020), Article ID: ARO.10632, 5 pages
DOI: 10.14500/aro.10632

Received 08 February 2020; Accepted: 26 May 2020
Regular research paper: Published 12 June 2020

Corresponding author's, e-mail: hassan.abdallah@su.edu.krd
Copyright © 2020 Rezan J. Hassan and Hassan H. Abdallah. This is an open access article distributed under the Creative Commons Attribution License.



paper is to suggest the mechanism of the studied reaction using DFT method. The mechanism of the reaction is shown in Scheme 1.

II. COMPUTATIONAL METHODS

All calculations in the present work have been done using Gaussian 09 package (Frisch, et al., 2009). DFT method has been proven to be a suitable method for the study of cycloaddition reactions and is achieved in this work as well (Khabashesku, Kudin and Margrave, 2001; Lemal, 2017; Parr and Weitao, 1989). B3LYP functional is used throughout in combination with 6-311++G(d,p) basis set (Ditchfield, Hehre and Pople, 1971; Lee, Yang and Parr, 1988). We also considered the D3 correction to take into account for the role of dispersion energies in the stability of the complexes and intermediates (Grimme, et al., 2010). Frequency calculations were performed to ensure that a transition state has only one negative frequency and a local minimum has no negative frequencies. Intrinsic reaction coordinate computations were carried out to confirm that the reactants and products are connected through the transition states (Fukui, 1970). All energies and thermodynamic parameters reported in this paper were obtained from the frequency calculations at the same level of theory. The CYLview software was used as a graphical interface (Legault, 2009).

The global electrophilicity index (ω) is obtained in terms of the electronic chemical potential (μ) and the chemical hardness (η) using the following simple expression (Parr, Szentpály and Liu, 1999):

$$\omega = \frac{\mu^2}{2\eta} \quad (1)$$

The chemical hardness (η) and the electronic chemical potential (μ) quantities may be approached in terms of the one electron energies of highest occupied molecular orbital (HOMO) and lowest unoccupied molecular orbital (LUMO), ϵ_H and ϵ_L , as (Parr and Pearson, 1983; Parr and Weitao, 1994):

$$\eta \approx \epsilon_L - \epsilon_H \quad (2)$$

$$\mu \approx \frac{\epsilon_H + \epsilon_L}{2} \quad (3)$$

The relative nucleophilicity index (N) obtained based on the energies of HOMO within the scheme of Kohn-Sham (Kohn and Sham, 1965). This quantity can be defined using Equation (4). Where TCE is tetracyanoethylene and is chosen due to its lowest HOMO energy as a reference (Domingo, Chamorro and Pérez, 2008).

$$N = E_{HOMO(Nu)} - E_{HOMO(TCE)} \quad (4)$$

III. RESULTS AND DISCUSSION

The D-A reaction of hexa-1,2,4-trien (R1) with but-3-en-2-one (R2) gives the corresponding products P1a, P1b, P2a, and P2b passing through TS1a, TS1b, TS2a, and TS2b, respectively, as sketched in Scheme 1. Fig. 1 shows the energy profiles of studied reactions. These energy profiles were determined at the B3LYP-D3/6-311++G(d,p)

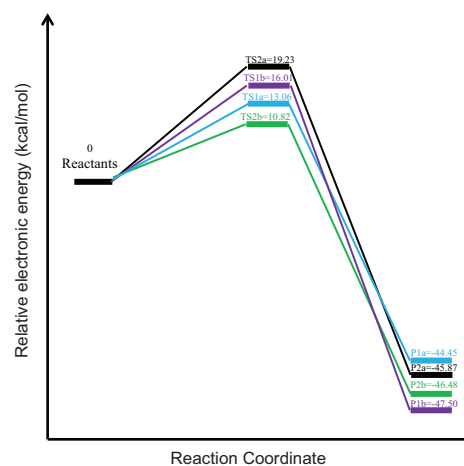


Fig. 1. Energy profile for the [4+2] cycloaddition reaction of hexa-1,2,4-trien (R1) with but-3-en-2-one (R2) using B3LYP-D3/6-311++G(d,p) level of theory. The energies are given relative to reactants (kcal/mol).

level of theory. The reactions occur through a concerted mechanism.

Fig. 1 shows that there is a significant lowering of the activation energy from cis transition state TS2a to trans TS2b, around 9 kcal/mol, and moderate lowering from trans transition state TS1b to cis TS1a, about 3 kcal/mol. It is notable to that the cycloadducts from trans conformer, P1b and P2b, have the lower relative energies as compared to the cis conformer of cycloadducts, P1a and P2a. This indicated that the trans cycloadducts are more stable than the cis cycloadducts.

Four transition states, TS1a, TS2a, TS1b, and TS2b, as sketched in Scheme 1, were obtained from the reaction of R1 with R2. The geometries of these transition states are given in Fig. 2. The studied reactions undergo cycloaddition through highly asynchronous transition states. In all cases, the length of the formed C-C bond with the ketone function is longer than the other formed C-C bond. This is due to the presence of carbonyl group in the dienophile as an electron-withdrawing group. The transition state TS1a has smaller degree of asynchronicity and TS2a has the larger degree of asynchronicity among the other transition states.

The thermodynamic parameters for the reaction of R1 with R2 in the gas phase at 1 atm and 298.15 K with B3LYP-D3/6-311++G(d,p) method are collected in Table I. The activation enthalpies range from 9.85 to 18.11 kcal/mol. It is worth to realize that the activation enthalpies reached the lower value for trans transition state TS2b and highest value cis TS2a, whereas opposite trends were found for TS1a and TS1b this is due to the stereoselectivity in transition states and products. The Gibbs free energies for all products are found to be negative and very close to each other, which indicate that pathways have the same route and no side reactions were found (Kaka, et al., 2019). The enthalpies for products were also found to be negative that indicate that the reactions are possible to occur. The enthalpies for trans products P1b and P2b are lower than the cis products, which refer to the more stability of trans products than cis products.

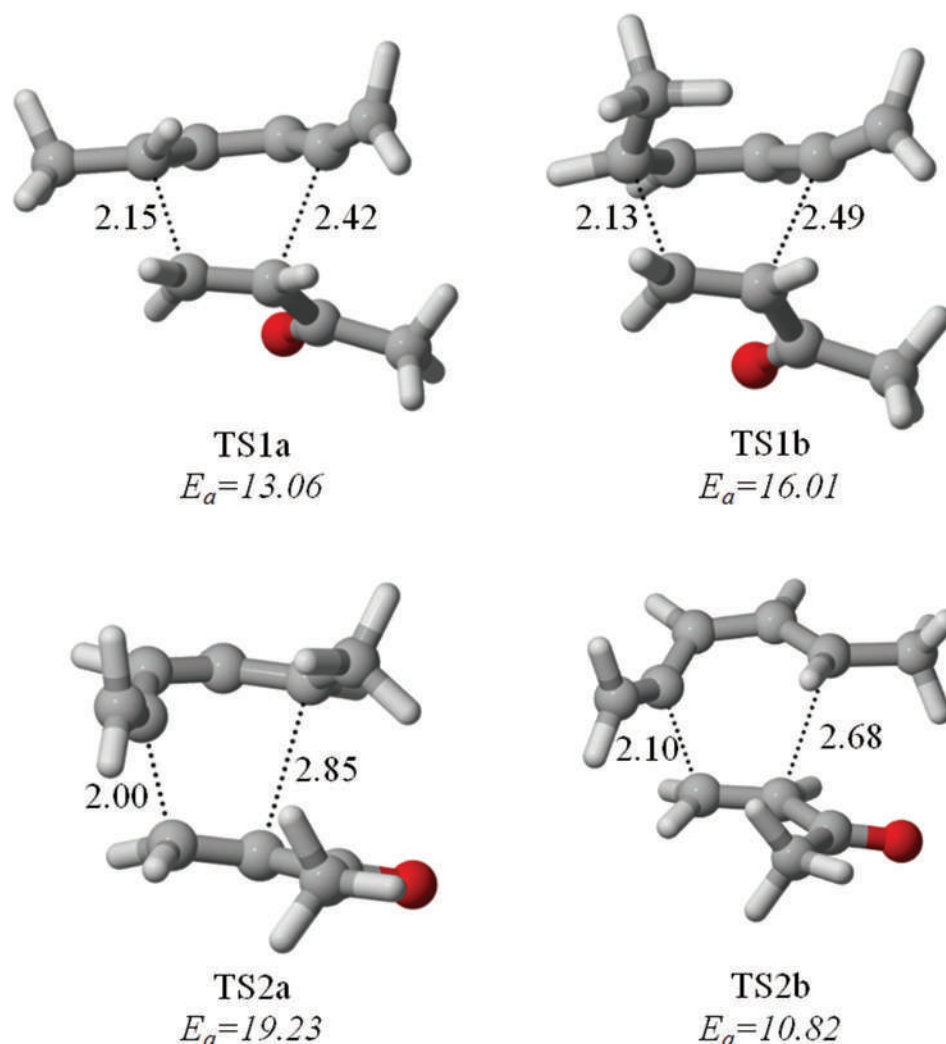


Fig. 2. Optimized geometries of the transition states involved in the [4+2] cycloaddition reactions of hexa-1,2,4-trien (R1) with but-3-en-2-one (R2) using B3LYP-D3/6-311++G(d,p) level of theory. The energy (E_a), in kcal/mol, is given relative to reactants.

TABLE I
THERMODYNAMIC PARAMETERS FOR TRANSITION STATES AND PRODUCTS AT B3LYP-D3/6-311++G(D,P) LEVEL OF THEORY IN (KCAL/MOLE) FOR ΔH AND ΔG AND IN (CAL/MOL.K) FOR ΔS

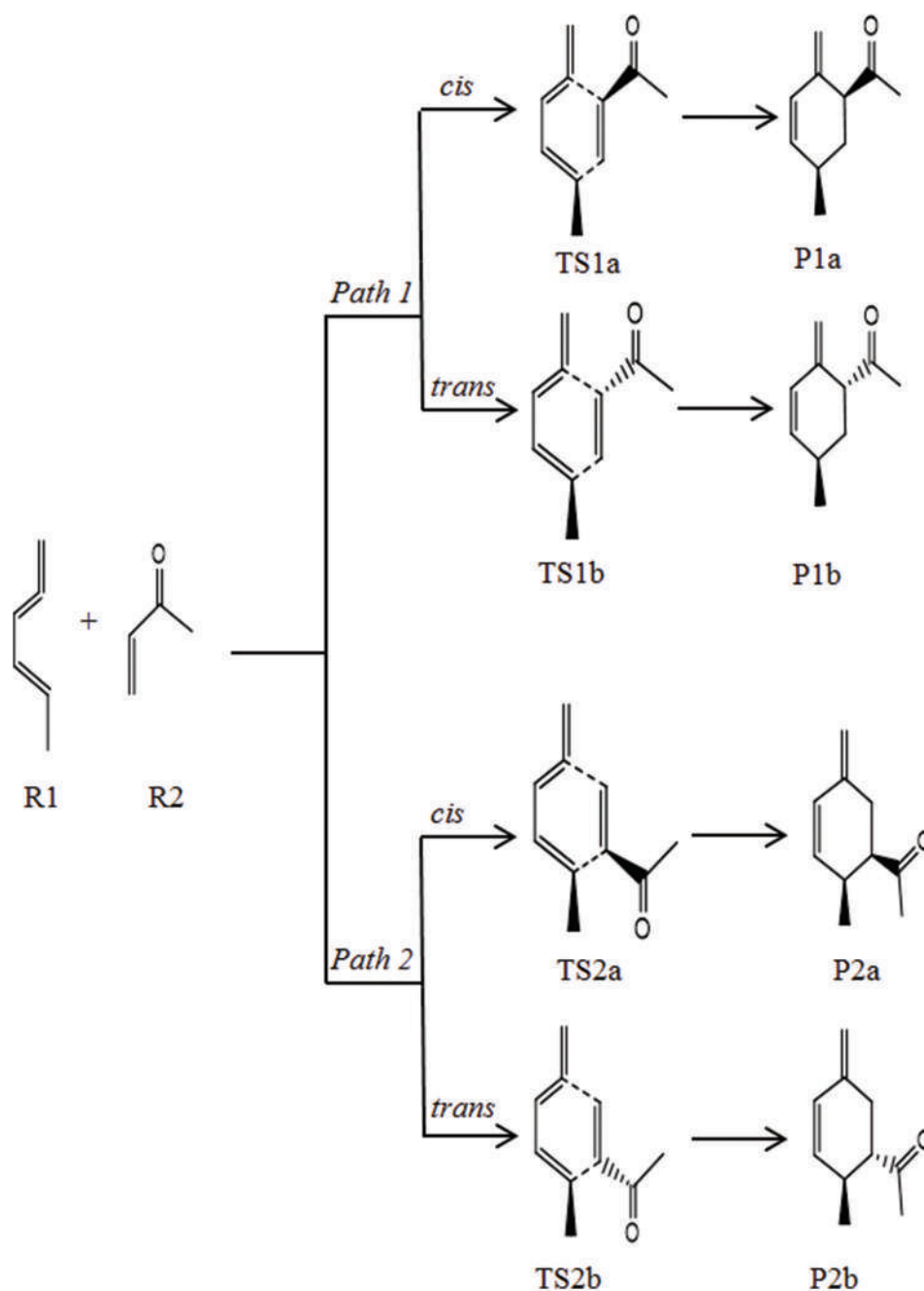
Compound	ΔH	ΔG	ΔS
P1a	-46.19	-29.40	-56.31
P1b	-49.16	-33.09	-53.93
P2a	-47.54	-31.15	-54.96
P2b	-48.20	-32.05	-54.14
TS1a	12.07	27.15	-50.58
TS1b	15.04	30.26	-51.05
TS2a	18.11	33.73	-52.39
TS2b	9.85	24.74	-49.94

From the observed thermodynamic results that the P1b is preferred thermodynamically, whereas P2b is preferred kinetically since it has lower activation energy.

In the D-A reaction, predictions of reactivity and selectivity are normally based on the strength of a single FMO interaction between the diene and the dienophile, dienophiles with conjugating groups are usually good for D-A reactions. Dienes react rapidly with electrophiles because

their HOMOs are relatively high in energy, but simple alkenes have relatively high-energy LUMOs and do not react well with nucleophiles. The most effective modification is to lower the alkene LUMO energy by conjugating the double bond with an electron-withdrawing group such as carbonyl or nitro. This type of D-A reaction, involving an electron-rich diene and an electron-deficient dienophile, is referred to as a D-A reaction with normal electron demand. The HOMO and LUMO energies for all products at B3LYP-D3/6-311++G(d,p) level of theory are listed in Table II. The table shows that cis products have narrower energy gaps than trans products. This indicates that the trans products are more stable than the others. The trans product P1b has wider energy gap than trans product P2b. Such results indicate that the trans product P1b is more stable among trans products. The results from the analysis of molecular orbitals were found to be consistency with the results obtained from the thermodynamic parameters.

The global reactivity indices defined within the conceptual DFT are a powerful tool to study the reactivity in polar cycloaddition reactions (Mohammad-Salim,



Scheme 1. Proposed reaction mechanism paths for the [4+2] cycloaddition reaction of but-3-en-2-one (R2) and hexa-1,2,4-trien (R1).

TABLE II
HOMO ENERGIES, LUMO ENERGIES, AND ENERGY GAP (IN eV UNIT) FOR
REACTANTS AND PRODUCTS AT B3LYP-D3/6-311++G(d,p) LEVEL OF THEORY

Compound	HOMO	LUMO	Energy gap
P1a	-6.41	-1.21	5.19
P1b	-6.44	-0.99	5.45
P2a	-6.36	-1.17	5.20
P2b	-6.37	-1.08	5.29

TABLE III
THE CHEMICAL HARDNESS (η), ELECTRONIC CHEMICAL POTENTIAL (μ), GLOBAL
ELECTROPHILICITY (ω), AND GLOBAL NUCLEOPHILICITY (N) FOR R1 AND R2 IN eV

Compound	η	μ	ω	N
R1	5.16	-3.56	1.23	3.35
R2	5.14	-4.61	2.06	2.31

et al., 2020). The static global properties, namely, chemical hardness (η), global nucleophilicity (N), global electrophilicity (ω), and electronic chemical potential (μ) for all reactants in eV are listed in Table III. The electronic chemical potential of R1 ($\mu=-3.56$) is higher than R2,

which indicates that the net charge transfer will be from R1 towards the electron-deficient R2 reactant. The ω for R1 is 1.23 eV that falls in the range of moderate electrophiles. However, the N for R1 is 3.35 eV, which falls in the range of strong electrophiles within the global nucleophilicity and electrophilicity.

IV. CONCLUSION

DFT method is used to investigate the Diels-Alder reaction between hexa-1,2,4-trien (R1) with but-3-en-2-one (R2) at B3LYP-D3/6-311++G(d,p) level of theory. The concerted mechanism was studied and the geometries of the transition states were determined. The electronic energetic results show that the cycloadducts from trans conformer are more stable than the cis cycloadducts. The global reactivity indices were analyzed at the ground state of reactants to predict the reactivity of the studied organic molecules in the cycloaddition reactions and the results indicate that the net charge transfer will be from hexa-1,2,4-trien toward the electron-deficient but-3-en-2-one reactant.

REFERENCES

- Baeza, A., 2018. *Stereogenic Centers*. Multidisciplinary Digital Publishing Institute, Basel, Switzerland.
- Boger, D.L., and Weinreb, S.M., 2012. *Hetero Diels-Alder Methodology in Organic Synthesis*, Elsevier, Amsterdam, Netherlands.
- Carey, F.A. and Sundberg, R.J., 2007. *Advanced organic chemistry: part A: structure and mechanisms*. Springer Science & Business Media
- Ditchfield, R., Hehre, W.J., and Pople, J.A., 1971. Self-consistent molecular-orbital methods. IX. An extended gaussian-type basis for molecular-orbital studies of organic molecules. *The Journal of Chemical Physics*, 54(2), pp.724-728.
- Domingo, L.R., Chamorro, E., and Pérez, P., 2008. Understanding the reactivity of captodative ethylenes in polar cycloaddition reactions. A theoretical study. *The Journal of Organic Chemistry*, 73(12), pp.4615-4624.
- Džambaski, Z., Tzaras, D.I., Lee, S., Kokotos, C.G., and Bondzic, B.P., 2019. Enantioselective organocatalytic enamine C-H oxidation/diels-alder reaction. *Advanced Synthesis and Catalysis*, 361(8), pp.1792-1797.
- Fringuelli, F., and Taticchi, A., 2002. *The Diels-Alder Reaction: Selected Practical Methods*. Wiley, Hoboken, New Jersey.
- Frisch, M.J., Trucks, G.W., Schlegel, H.B., Scuseria, G.E., Robb, M.A., Cheeseman, J.R., Scalmani, G., Barone, V., Petersson, G.A., Nakatsuji, H., Li, X., Caricato, M., Marenich, A.V., Bloino, J., Janesko, B.G., Gomperts, R., Mennucci, B., Hratchian, H.P., Ortiz, J.V., Izmaylov, A.F., Sonnenberg, J.L., Williams, Ding, F., Lipparini, F., Egidi, F., Goings, J., Peng, B., Petrone, A., Henderson, T., Ranasinghe, D., Zakrzewski, V.G., Gao, J., Rega, N., Zheng, G., Liang, W., Hada, M., Ehara, M., Toyota, K., Fukuda, R., Hasegawa, J., Ishida, M., Nakajima, T., Honda, Y., Kitao, O., Nakai, H., Vreven, T., Throssell, K., Montgomery Jr., J.A., Peralta, J.E., Ogliaro, F., Bearpark, M.J., Heyd, J.J., Brothers, E.N., Kudin, K.N., Staroverov, V.N., Keith, T.A., Kobayashi, R., Normand, J., Raghavachari, K., Rendell, A.P., Burant, J.C., Iyengar, S.S., Tomasi, J., Cossi, M., Millam, J.M., Klene, M., Adamo, C., Cammi, R., Ochterski, J.W., Martin, R.L., Morokuma, K., Farkas, O., Foresman, J.B., and Fox, D.J., 2009, *Gaussian 09 B.01*, Gaussian, Inc., Wallingford, CT.
- Fukui, K., 1970. Formulation of the reaction coordinate. *The Journal of Physical Chemistry*, 74(23), pp.4161-4163.
- Grimme, S., Antony, J., Ehrlich, S., and Krieg, H., 2010. A consistent and accurate ab initio parametrization of density functional dispersion correction (DFT-D) for the 94 elements H-Pu. *The Journal of Chemical Physics*, 132(15), p.154104.
- Jursic, B.S., and Zdravkovski, Z., 1994. Comparison of AM1 and PM3 semiempirical to ab initio methods in the study of Diels-Alder reactions of butadiene and cyclopentadiene with cyanoethylenes. *Journal of Molecular Structure: THEOCHEM*, 309(3), pp.249-257.
- Kaka, K.N., Taher, S.G., Hamad, W.M., and Ibrahim, A.H., 2019. Synthesis of new series of pyrazoline, and study their kinetics and reaction mechanism. *ARO-The Scientific Journal of Koya University*, 7(2), pp.5-13.
- Kal-Koshvandi, A.T., and Heravi, M.M., 2019. Applications of Dainshesky's dienes in the asymmetric synthesis of aza-diels-alder reaction. *The Chemical Record*, 19(2-3), pp.550-600.
- Khabashesku, V.N., Kudin, K.N., and Margrave, J.L., 2001. Density functional theoretical studies of [2+2] cycloaddition of simple transient silenes and germenes to ethylene, formaldehyde, and thioformaldehyde, and vibrational analysis of spectra of reactants and cyclic products. *Russian Chemical Bulletin*, 50(1), pp.20-28.
- Kohn, W., and Sham, L.J., 1965. Self-consistent equations including exchange and correlation effects. *Physical Review*, 140(4A), pp.1133-1138.
- Lee, C., Yang, W., and Parr, R.G., 1988. Development of the colle-salvetti correlation-energy formula into a functional of the electron density. *Physical Review B*, 37(2), pp.785-789.
- Legault, C. 2009, *CYLVIEW 1.0*. Université de Sherbrooke, Sherbrooke.
- Lemal, D.M., 2017. Pathways for concerted [2 + 2] cycloaddition to cumulenes. *The Journal of Organic Chemistry*, 82(24), pp.13012-13019.
- Mohammad, S.H., and Abdallah, H., 2019. Theoretical study for the [2+2] cycloaddition reaction mechanism of ketenes and their derivatives. *Oriental Journal of Chemistry*, 35, pp.1550-1556.
- Mohammad-Salim, H., Hassan, R., Abdallah, H.H., and Oftadeh, M., 2020. The theoretical study on the mechanism of [3+ 2] cycloaddition reactions between α , β -unsaturated selenoaldehyde with nitrene and with nitrile oxide. *Journal of the Mexican Chemical Society*, 64(2), p.20.
- Mohammad-Salim, H.A., Abdallah, H.H., Maiyelvaganan, K.R., Prakash, M., and Hochlaf, M., 2020. Mechanistic study of the [2+2] cycloaddition reaction of cyclohexenone and its derivatives with vinyl acetate. *Theoretical Chemistry Accounts*, 139(2), p.19.
- Mohammad-Salim, H.A., and Abdallah, H.H., 2019. Theoretical study of the [4+2] cycloaddition reaction of trifluoroethylene with five-membered chalcogens heterocyclic compounds. 7(2), p.9.
- Parr, R.G. and Weitao, Y., 1989, *Density-Functional Theory of Atoms and Molecules*. Oxford University Press, Oxford.
- Parr, R.G., and Pearson, R.G., 1983. Absolute hardness: Companion parameter to absolute electronegativity. *Journal of the American Chemical Society*, 105(26), pp.7512-7516.
- Parr, R.G., and Weitao, Y., 1994. *Density-Functional Theory of Atoms and Molecules*. Oxford University Press, Oxford.
- Parr, R.G., Szentpály, L.V., and Liu, S., 1999. Electrophilicity index. *Journal of the American Chemical Society*, 121(9), pp.1922-1924.
- Pham, H.V., and Houk, K.N., 2014. Diels alder reactions of allene with benzene and butadiene: Concerted, stepwise, and ambimodal transition states. *The Journal of Organic Chemistry*, 79(19), pp.8968-8976.
- Salim, H.A.M., Abdallah, H.H., and Ramasami, P., 2018a. Stereoselectivity and regioselectivity of the cycloaddition dimerization of allyl 3-(2-pyridyl) acrylate and allyl 3-(2-pyryl) acrylate: DFT Calculations. *IOP Conference Series: Materials Science and Engineering*, 454, p.012049.
- Salim, H.M., Abdallah, H.H., and Ramasami, P., 2018b. *Mechanism and Thermodynamic Parameters of Paternò-Büchi Reaction of Benzene and Furan: DFT Study*. Conference Paper, pp.415-419.
- Siah, S.Y., Leung, P.H., and Mok, K.F., 1995. Palladium-complex-promoted asymmetric Diels-Alder reaction: Stereoselective synthesis of a new sulfinyl-substituted phosphine ligand containing three carbon, one phosphorus and one sulfur stereogenic centres. *Journal of the Chemical Society, Chemical Communications*, 17, pp.1747-1748.
- Zhang, H., Liu, G., Guan, X., Gao, J., Qin, X., Jiang, G., Sun, D., Zhang, G., and Zhang, S., 2019. Asymmetric synthesis of triaryl-substituted chromans with multiple stereogenic centers by [4+ 2] cycloaddition reaction. *European Journal of Organic Chemistry*, 43, pp.7264-7268.

Chemical and Structural Analysis of Rocks Using X-ray Fluorescence and X-ray Diffraction Techniques

Mohammed M. Sabri

Department of Physics, Faculty of Science and Health, Koya University, Koya KOY45, Kurdistan Region - F.R. Iraq

Abstract—Rock examinations for mining and commercial use are a vital process to save money and time. A variety of methods and approaches have been used to analyze rocks and among them, X-ray fluorescence (XRF), and X-ray diffraction (XRD) techniques proved to be an accurate method. This research was conducted to evaluate the utility and reliability of XRF and XRD to analyze the major and trace elements of rocks as well as their crystalline structures. Results showed that XRF and XRD techniques are fast and reliable, nondestructive and non-invasive analytical tools for mineral analysis, particularly for rocks. For this purpose, the analysis of 28 samples of rocks, which collected from three different places of Kurdistan region-Iraq, is reported. These places are Haybat Sultan (HS) region in Koya city as well as TaqTaq (TA) and Garmuk (GT) district nearby Koya city. Throughout this analysis, 34 major and trace elements were detected in the rocks collected from HS region, whereas forty major and trace elements were detected in the rocks collected from TA district and GT district. In addition, it was found that the structures of these rocks were crystalline in nature. This was proved through the value of diffracted angle and it was found that the majority of these rocks are oxides. The external view (the appearance) of all collected rocks was also discussed and it was found that each rock consists of a variety of minerals which will be the reason that each rock has a specific color.

Index Terms—Minerals, Rocks, X-ray diffraction, X-ray fluorescence.

I. INTRODUCTION

There are a variety of materials available in nature such as rock, soil, oil (some places in the world), and water. Exploring these materials is a matter of interest due to their importance impacts and possible significant applications. Among these materials, rocks with their different types have attracted a special interest by researchers, as the evaluation of the source of the rock is considered as an important task for the purpose

of oil exploration (Mirza et al., 2017; Fatah and Mohialdeen, 2016; Mohialdeen, Hakimi and Al-Beyati, 2015; Tissot and Welte, 1984). In addition, rocks' investigation could be used in the assessment of the source of the rock, such as measuring the level of maturity, the types of organic materials content of the rock as well as to define the paleoenvironmental conditions (Hunt, 1996). Comparing to other regions around the world, Kurdistan region of Iraq is a rich region full of various types of materials such as those mentioned above and especially rocks (Hassan et al., 2015). These regions include, for example, mountains and the regions nearby it. However, limited studies have been conducted in the concern of this matter. It has been demonstrated that to build a clear view of the characteristics of the sediment's source area, the composition of the rocks should be investigated (Roser and Korsch, 1988) and to do so, trace elements are extremely important (Lopez et al., 2005). In fact, there are three types of rocks, which are being formed (and destroyed). Earth's first rocks were igneous rocks. These form from molten rock that has cooled and hardened. Second, sedimentary rocks are formed from the shells and skeletons of microscopic sea creatures. Finally, metamorphic rock forms when rocks are squeezed and heated deep under the earth's crust.

It is important to mention that X-ray fluorescence (XRF) technique has become one of the major instruments in diagnostics (Meenaa et al., 2018; Sarrazin et al., 1998; Vaniman et al., 1998; Vaniman, Bish and Chipera, 1991) due to its ability to analyze the chemistry of the sample (Sanchez et al., 2008; Nayak and Singh, 2007). Besides to XRF (Cornaby et al., 2001), X-ray diffraction (XRD) technique (Wadsworth and Baird, 1989) is also considered to be the most conclusive technique to investigate the phase composition (Mohammed, 2012) of the matter, particularly rocks (Marinangeli et al., 2015; Cornaby et al., 2001; Vaniman et al., 1998; Vaniman, Bish and Chipera, 1991). Each phase (metal or metal oxide) has its own unique diffraction spectrum and therefore, it is possible to distinguish between compounds, as this technique is sensitive to crystal structure rather than to composition (Loubser and Verry, 2008; Sanchez et al., 2008). XRD has its own importance in rocks investigation, as this technique has the ability to identify the structure of rocks in terms of crystallinity or amorphousness. Dealing with the rocks and investigating their chemical and crystalline structures are of

ARO-The Scientific Journal of Koya University
Vol. VIII, No.1 (2020), Article ID: ARO.10643, 9 pages
DOI: 10.14500/aro.10643

Received: 09 March 2020; Accepted: 12 June 2020

Regular research paper: Published 17 June 2020

Corresponding author's e-mail: mohammed.mohammedsabri@koyauniversity.org

Copyright © 2020 Mohammed M. Sabri. This is an open-access article distributed under the Creative Commons Attribution License.



considerable problem that should be taken into consideration due to the impact of rocks' applications in various field such as in industry and particularly in cement industry. Moreover, the existence of metal and/or metal oxide in these rocks is of importance matter due to the possible future applications in a variety of fields such as in electricity. The main aim for conducting this research is to further go inside rocks and analyze their structures, both chemically and structurally.

II. EXPERIMENTAL DETAILS

The experimental process starts with collecting the rock samples from several Kurdistan region of Iraq, then grinding the samples and finally analyzing the rocks using XRF and XRD techniques.

A. Samples (Rocks) Collecting

The rocks that used in this research have been collected from three different places of Kurdistan region of Iraq. Ten of these samples codes of HS1-HS10 were collected from Haybat Sultan (HS) in Koya city and the other ten samples were collected from TaqTaq (TA) codes of TA1-TA10 that located close to Koya city and finally eight samples codes of GT-1-GT8 were collected from Garmuk (GT), which is also related to TA region.

B. Samples (Rocks) Grinding

The bulk of these rocks was then grinded using Mini mill II ball machine of type Malvern Panalytical, Gurgaon (Panalytical India) to obtain a fine powder.

C. Rocks Analysis

In this paper, the collected rocks were chemically and structurally analyzed using both XRF and XRD techniques as discussed in details in below sections.

XRF Technique

The elemental concentration and their emitted energies in KeV for all collected rocks were determined using energy dispersive XRF (EDXRF). All measurements were carried out under vacuum using a Rigaku NEX CG with RX9, Mo, Cu, and Al targets. Chemical elements of high and low concentration were detected within our collected rocks. The EDXRF K^α and K^β lines intensities were measured for all rocks' elements, in which the applied voltage increased in general with the required lines energies. The X-ray measuring time was 200 s for the Al target, whereas was 100 s for the other targets. Furthermore, X-rays from the X-ray tube pass through an optional filter on their way to the rocks sample. The sample placed in the chamber and measured by 20 mm diaphragm in vacuum. The X-rays are then transport from the sample to the detector which is electrically cooled. The signal is then processed by electronics and sent to a computer program, where the chemical compositions and intensity versus energy is measured (Abdullah, Chaqmaqchee and Anwer, 2017; Chaqmaqchee and Baker, 2016). A schematic diagram of the typical EDXRF is shown in Fig. 1.

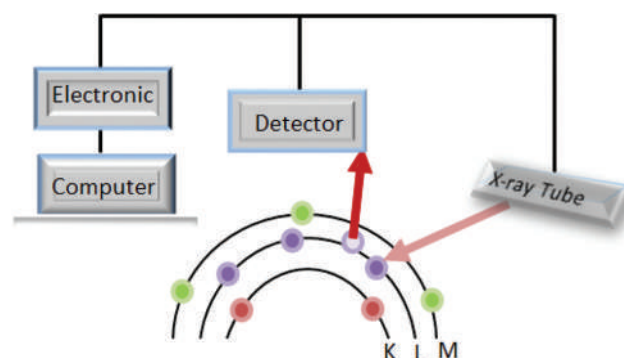


Fig. 1. A schematic of a typical energy dispersive X-ray fluorescence spectrometer.

XRD technique

The crystalline structures of the rocks were analyzed using a high-resolution X-ray powder diffraction technique of type Panalytical Empyrean with CuK^α radiation of the wavelength (λ) of 0.15406 nm. The voltage and the current that used throughout the analysis were 45 kV and 40 mA, respectively (Faraj, Kaka and Omar, 2019; Faraj, Chaqmaqchee and Omar, 2017). The XRD (JCPDS card No. 03-1005) data revealed that all the collected rock samples are crystalline in nature.

III. RESULTS AND DISCUSSION

This section has been divided into three sub-sections of XRF, XRD, and the analysis of rocks appearance.

A. XRF

Rigaku NEX CG XRF spectrometer analyses were used to determine the elements of the collected rocks. When these samples are irradiated with X-rays, the intensity as a function of energy can be calculated over the energy range of 1–20 keV at the same computing conditions. Fig. 2 shows the peaks in the ranges of 1.74, 2.32, 3.69, 4.03, 5.89, 6.4, 14.19, 16.83, and 17.48 keV corresponding to $Si-k^\alpha$, $S-k^\alpha$, $Ca-k^\alpha$, $Ca-k^\beta$, $Mn-k^\alpha$, $Fe-k^\alpha$, $Sr-k^\alpha$, $Nb-k^\alpha$, and $Mo-k^\alpha$ lines. It can be seen from Fig. 2a that the intensity of $Ca-k^\alpha$ for all HS samples has higher intensity (high Ca concentration) compared to other rocks samples of TA and GT (Figs. 2b and c), whereas the intensity of $S-k^\alpha$, $Sr-k^\alpha$, $Mn-k^\alpha$, and $Mo-k^\alpha$ is low or almost negligible. In addition, the intensity of $Fe-k^\alpha$ is high (high Fe concentration) in the rocks labeled HS4, HS5, TA1, TA4, TA5, TA9, TA10, and GT7, as shown in Fig. 2. Rocks are divided into two classes according to whether they contain a greater proportion of iron and magnesium or of potassium, sodium, and calcium. Igneous rocks which contain a high percentage of iron and magnesium (ferromagnesian silicates) tend to possess a dark color and are said to be of basaltic or mafic composition. Because of their iron content, such rocks tend to be both denser and darker in color than those rocks composed mainly of non-ferromagnetic silicates. In contrast, igneous rocks

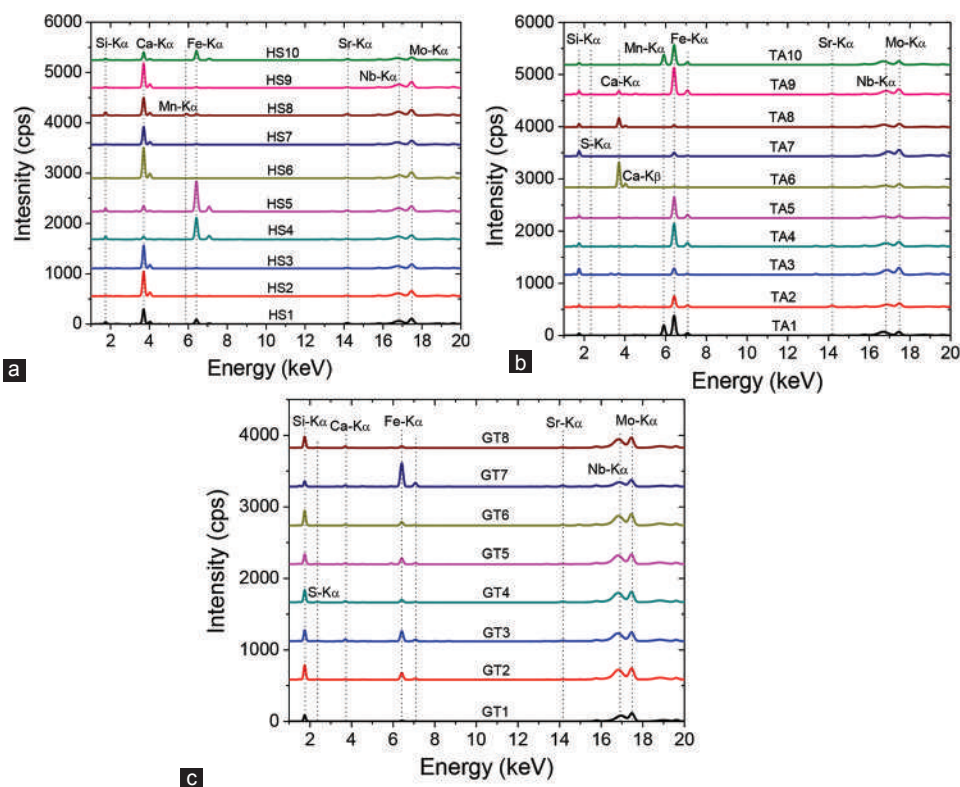


Fig. 2. Intensity versus energy for various rocks of (a) Haybat Sultan, (b) TaqTaq, and (c) Garmuk calculated over the energy range from 1 to 20 keV using X-ray fluorescence with RX9, Mo, Cu, and Al targets.

which contain a greater percentage of potassium, sodium, or calcium (non-ferromagnetic silicates) tend to have a lighter color and are said to be of granitic or felsic composition. Such rocks tend to contain a relatively greater percentage of silica (SiO₂); typically, this is about 70 % by mass. Some minerals are always of the same color, as a consequence of their chemical composition and structure. Their color is a useful aid to identification. Other minerals, such as fluorite, can be different colors due to tiny amounts of chemical impurities, structural flaws, or to their different habits.

Rock types can be classified in terms of chemistry, how the form and environment of formation. Some structures, such as bedding, igneous layering, and gneissic banding, are formed at the same time as the rock itself, but others, such as folding and shearing (stretching of mineral grains), occur later. Many structures exist over a vast range of scale, for example, folding can be seen in microscopic crystal grains as well as across entire cliff faces.

Color is also useful property in rock identification. It can be used to tell apart different varieties of a rock, and it can also provide information on the composition of the rock. In many cases, the color of a rock will be affected by weathering, so a fresh surface should always be exposed.

The ten rock samples collected from HS region have been experienced a geochemical analysis, along with the ten rock samples collected from TA region and the eight rock samples collected from GT region. The raw and processed data are listed in three tables related to the three different places where the rock sample was collected. These tables are

labeled as Table I for HS rock samples, Table II for TA rock samples and finally Table III for GT rock samples.

B. XRD

For the purpose of analyzing the crystalline structure of the rocks, XRD technique was used. This technique has been used to analyze the mineralogical composition of the powder materials as well as the phase analysis of the multiphase mixtures. From the values of *d*-spacing as well as the values of 2θ, it can be confirmed that the possible minerals of the rock samples could be quartz, alumina, hematite, tridymite, illite and kaolinite, and few other minerals, which is in consistent with Mohammed, 2012; Nayak and Singh, 2007. The main peaks of the XRD data of all rocks are related to Ca-oxide and Fe-oxide such as in HS and TA rocks, whereas they related to silica and Fe-oxide in GT rocks. In addition, alumina (Al₂O₃) is also a major trace in all the three rock samples of HS, TA, and GT. These are in consistent with the XRF data. For example, the main peak of HS1 rock (Fig. 3a) at about 29.6286° can be assigned to diffraction of the (220) plane, which could be for iron oxide. In addition, the XRD pattern of TA rocks exhibits a main plane at about 29.1086°, which are corresponding (*hkl*) to the (100) plane, as shown in Fig. 4h. Finally, the XRD spectrum of GT rock shows a peak at about 26.4306°, which corresponding to (111) plane of crystalline phase of silica (quartz), as shown in Fig. 5a. The crystallinity of the collected rock samples from the three different places of HS, TA, and GT are proven in the XRD data, as shown in Figs. 3-5. These figures show the similarity

TABLE I
X-RAY FLUORESCENCE MEASUREMENTS FOR ELEMENTS IN THE HAYBAT SULTAN ROCK SAMPLES AS PERCENTAGES, WHERE THE TOTALS 100%±0.05 STATISTICAL ERRORS

No.	Elements	Haybat Sultan (HS) mass concentration (%)									
		HS1	HS2	HS3	HS4	HS5	HS6	HS7	HS8	HS9	HS10
1	CaO	52.7	80.0	77.3	10.6	20.3	91.1	75.3	56.6	75.3	41.5
2	SiO ₂	24.3	9.74	9.80	53.8	41.8	4.63	11.0	37.0	12.1	30.1
3	Al ₂ O ₃	8.15	3.34	3.60	16.8	14.7	1.54	3.50	2.15	3.38	10.8
4	Fe ₂ O ₃	7.25	0.713	0.649	10.4	14.1	0.334	0.906	0.821	0.699	11.0
5	MgO	3.49	5.75	8.11	3.99	4.72	2.01	8.61	1.63	7.74	2.75
6	K ₂ O	2.51	0.194	0.209	2.68	2.59	0.121	0.238	0.149	0.214	1.85
7	TiO ₂	0.826	0.100	0.118	1.06	1.02	0.0712	0.142	0.0580	0.138	1.10
8	P ₂ O ₅	---	---	---	0.189	0.168	0.0198	---	---	---	0.0968
9	MnO	0.446	0.0266	0.0297	0.193	0.189	0.0214	0.0384	1.44	0.0252	0.329
10	SrO	0.119	0.0323	0.0398	0.0240	0.0401	0.0324	0.0311	0.0551	0.0318	0.0913
11	V ₂ O ₅	0.0522	---	---	0.0261	0.0472	---	---	---	---	0.0242
12	Co ₂ O ₃	0.0229	0.0036	0.0027	0.0331	0.0490	0.0026	0.0054	0.0079	0.0041	0.0521
13	SnO ₂	0.0181	0.0148	0.0124	0.0152	0.0156	0.0204	0.0131	0.0154	0.0200	0.0209
14	Cr ₂ O ₃	0.0168	0.0055	0.0070	0.0239	0.0285	0.0025	0.0095	---	0.0173	0.0146
15	NiO	0.0158	---	---	0.0152	0.0181	---	---	---	0.0081	0.0195
16	ZnO	0.0157	0.0028	0.0031	0.0190	0.0188	0.0025	0.0032	0.0031	0.0098	0.0201
17	CuO	0.0078	0.0042	0.0065	0.0076	0.0134	0.0042	0.0034	0.0038	0.0036	0.0110
18	Rb ₂ O	0.0069	0.0007	0.0007	0.0137	0.0146	---	0.0011	0.0014	0.0009	0.0164
19	PtO ₂	---	---	0.0015	---	---	---	---	---	---	---
20	Y ₂ O ₃	0.0035	---	---	0.0042	0.0044	---	---	0.0021	---	0.0057
21	Ga ₂ O ₃	0.0025	---	---	0.0027	0.0022	---	---	---	---	0.0042
22	PbO	0.0018	0.0011	---	0.0026	0.0032	---	---	0.0016	---	0.0031
23	Ir ₂ O ₃	0.0016	---	---	0.0009	---	---	---	---	---	0.0014
24	As ₂ O ₃	0.0014	0.0004	---	0.0044	0.0066	---	---	0.0003	---	0.0036
25	SO ₃	---	0.0931	0.109	0.0905	0.134	0.0563	0.129	0.0731	0.255	0.0772
26	Ta ₂ O ₅	---	0.0038	0.0037	0.0031	0.0042	---	0.0052	---	0.0033	0.0038
27	BaO	---	---	---	0.0459	0.0398	---	---	---	---	0.0463
28	Cl	---	---	---	0.0109	0.0085	---	---	0.0182	0.0118	---
29	HfO ₂	---	---	---	0.0026	0.0029	---	0.0058	---	---	---
30	ThO ₂	---	---	---	0.0020	0.0026	---	---	---	---	---
31	TeO ₂	---	---	---	0.0013	---	---	---	---	---	---
32	Au ₂ O	---	---	---	0.0012	0.0012	---	---	---	---	---
33	U ₃ O ₈	---	---	---	0.0007	0.0007	---	---	---	---	0.0008
34	Nb ₂ O ₅	---	---	---	---	---	---	---	---	---	0.0059

TABLE II
X-RAY FLUORESCENCE MEASUREMENTS FOR ELEMENTS IN THE TATAQ ROCK SAMPLES AS PERCENTAGES, WHERE THE TOTALS 100%±0.05 STATISTICAL ERRORS

No.	Elements	TaqTaq (TA) mass concentration (%)									
		TA1	TA2	TA3	TA4	TA5	TA6	TA7	TA8	TA9	TA10
1	CaO	9.39	---	4.08	1.96	3.57	90.0	1.35	42.6	12.1	0.197
2	SiO ₂	63.0	24.6	70.5	59.6	29.3	4.79	86.7	49.8	51.9	8.75
3	Al ₂ O ₃	16.2	13.4	13.0	21.9	10.4	1.83	7.36	4.46	18.0	1.27
4	Fe ₂ O ₃	6.62	59.6	2.23	8.89	53.2	1.66	1.61	1.50	10.6	88.2
5	MgO	3.10	1.88	2.62	2.75	2.73	0.883	2.09	1.02	3.90	0.638
6	K ₂ O	0.0997	---	6.94	2.93	0.112	0.188	0.443	0.222	0.267	0.0475
7	TiO ₂	0.670	0.436	0.208	1.23	0.372	0.0800	0.224	0.129	2.30	0.178
8	P ₂ O ₅	0.182	---	---	0.143	---	0.0701	---	---	0.322	0.0551
9	MnO	0.184	---	0.0300	0.0903	---	0.174	0.0286	0.160	0.268	0.436
10	SrO	0.106	---	0.0037	0.0315	---	0.0736	0.0098	0.0280	0.0271	---
11	V ₂ O ₅	0.0154	0.0122	0.0078	0.0420	0.0158	---	0.0073	---	0.0343	0.0455
12	Co ₂ O ₃	0.0224	---	0.0097	0.0350	---	0.0049	0.0094	0.0099	0.0328	---
13	SnO ₂	0.0096	0.0050	0.0134	0.0161	0.0025	0.0241	0.0187	0.0126	0.0136	0.0191
14	Cr ₂ O ₃	---	0.0033	0.0042	0.0191	0.0090	0.0033	0.0136	0.0021	---	0.0036
15	NiO	0.0031	---	0.0053	0.0228	---	---	0.0105	---	0.0047	---
16	ZnO	0.0097	---	0.0035	0.0196	---	0.0061	0.0031	0.0060	0.0157	---
17	CuO	0.0043	---	0.0016	0.0037	---	0.0061	0.0052	0.0031	0.0071	---
18	Rb ₂ O	0.0002	---	0.0161	0.0194	---	0.0016	0.0009	0.0012	0.0012	---

(Contd...)

TABLE II
CONTINUED

No.	Elements	TaqTaq (TA) mass concentration (%)									
		TA1	TA2	TA3	TA4	TA5	TA6	TA7	TA8	TA9	TA10
19	PtO ₂	---	---	---	---	---	---	---	---	---	---
20	Y ₂ O ₃	0.0036	---	0.0039	0.0053	---	0.0016	---	0.0032	0.0032	---
21	Ga ₂ O ₃	0.0019	---	0.0018	0.0032	---	---	0.0009	---	0.0015	---
22	PbO	0.0006	---	0.0007	0.0034	---	0.0021	0.0008	0.0021	0.0011	---
23	Ir ₂ O ₃	0.0007	---	---	0.0014	---	0.0019	---	---	0.0012	---
24	As ₂ O ₃	0.0006	---	0.0004	0.0012	---	0.0012	0.0013	---	0.0008	---
25	SO ₃	0.367	0.0291	0.151	0.0697	0.295	0.214	0.0629	0.0875	0.123	0.0482
26	Ta ₂ O ₅	0.0020	---	0.0024	0.0022	---	0.0037	---	0.0029	0.0040	---
27	BaO	---	0.0080	0.179	0.154	---	---	0.0336	---	0.0205	0.106
28	Cl	0.0066	0.0027	0.0105	0.0109	0.0077	0.0098	0.0152	0.0153	0.0094	0.0077
29	HfO ₂	---	---	0.0022	---	---	---	---	---	0.0014	---
30	ThO ₂	0.0005	---	0.0017	0.0030	---	---	---	---	0.0007	---
31	TeO ₂	---	---	---	---	---	0.0034	0.0012	---	0.0019	---
32	Au ₂ O	0.0006	---	---	0.0007	---	---	---	---	---	---
33	U ₃ O ₈	0.0006	---	---	---	---	---	---	---	---	---
34	Nb ₂ O ₅	---	---	---	0.0056	---	---	---	---	0.0045	---
35	WO ₃	---	---	---	0.0013	---	---	0.0015	---	---	---
36	GeO ₂	---	---	---	0.0011	---	---	---	---	---	---
37	Tl ₂ O ₃	---	---	---	0.0010	---	---	---	---	---	---
38	HgO	---	---	---	0.0005	---	---	---	---	---	---
39	Ag ₂ O	---	---	---	---	---	---	0.0006	---	---	---
40	PdO	---	---	---	---	---	---	---	0.0008	---	---

TABLE III

X-RAY FLUORESCENCE MEASUREMENTS FOR ELEMENTS IN THE GARMUK ROCK SAMPLES AS PERCENTAGES, WHERE THE TOTALS 100%±0.05 STATISTICAL ERRORS

No.	Elements	Garmuk (GT) Mass Concentration (%)							
		GT1	GT2	GT3	GT4	GT5	GT6	GT7	GT8
1	CaO	1.53	1.13	5.58	4.17	2.62	2.36	4.27	5.41
2	SiO ₂	94.5	92.8	85.6	88.8	86.4	93.8	65.1	89.1
3	Al ₂ O ₃	2.40	3.52	4.76	4.72	6.74	2.36	17.9	3.55
4	Fe ₂ O ₃	0.359	1.26	2.14	0.493	1.36	0.658	7.12	0.365
5	MgO	0.762	0.873	1.07	1.24	1.70	0.426	2.35	0.886
6	K ₂ O	0.199	0.199	0.343	0.270	0.570	0.181	1.65	0.197
7	TiO ₂	0.0524	0.0888	0.236	0.155	0.212	0.0620	0.878	0.0641
8	P ₂ O ₅	---	---	---	---	---	---	0.226	---
9	MnO	0.0110	0.0128	0.0549	0.0114	0.249	0.0086	0.155	0.0977
10	SrO	---	0.0035	0.0091	0.0087	0.0057	0.0054	0.0251	0.0083
11	V ₂ O ₅	---	0.0044	0.0057	---	0.0095	0.0033	0.0331	---
12	Co ₂ O ₃	0.0020	0.0083	0.0116	0.0029	0.0093	0.0044	0.0330	0.0031
13	SnO ₂	0.0223	0.0091	0.0097	0.0097	0.0103	0.0098	0.0125	0.0115
14	Cr ₂ O ₃	0.0018	0.0064	0.0034	0.0042	0.0038	0.0034	0.0113	0.0016
15	NiO	---	0.0024	0.0040	0.0019	0.0048	0.0017	0.0068	0.0031
16	ZnO	0.0019	0.0014	0.0080	0.0014	0.0041	0.0011	0.0131	0.0011
17	CuO	0.0018	0.0031	0.0050	0.0015	0.0035	0.0022	0.0020	0.0018
18	Rb ₂ O	---	0.0005	0.0020	0.0004	0.0022	0.0007	0.0066	0.0005
19	PtO ₂	---	---	---	---	---	---	---	---
20	Y ₂ O ₃	---	0.0015	0.0017	---	0.0010	0.0080	0.0044	0.0011
21	Ga ₂ O ₃	---	0.0004	0.0005	---	0.0006	0.0002	0.0034	0.0004
22	PbO	---	0.0006	0.0007	0.0005	0.0007	0.0005	0.0046	0.0025
23	Ir ₂ O ₃	---	---	---	---	---	---	---	---
24	As ₂ O ₃	---	0.0010	---	---	0.0001	0.0003	0.0006	0.0007
25	SO ₃	0.141	0.0502	0.136	0.0480	0.0722	0.0624	0.0532	0.176
26	Ta ₂ O ₅	0.0017	---	0.0016	0.0011	0.0017	0.0008	0.0033	0.0007
27	BaO	---	---	0.0160	0.0268	---	0.0164	0.0603	0.0662
28	Cl	0.0271	0.0144	0.0181	0.0110	0.0206	0.0055	0.0096	0.0261
29	HfO ₂	---	---	0.0012	---	0.0011	0.0008	---	---
30	ThO ₂	---	---	---	---	---	---	0.0028	---

(Contd...)

TABLE III
CONTINUED

No.	Elements	Garmuk (GT) Mass Concentration (%)							
		GT1	GT2	GT3	GT4	GT5	GT6	GT7	GT8
31	TeO ₂	0.0039	0.0013	---	---	---	0.0009	---	0.0010
32	Au ₂ O	---	---	---	---	---	---	---	---
33	U ₃ O ₈	---	---	---	---	---	---	---	---
34	Nb ₂ O ₅	---	---	---	---	---	0.0012	0.0038	---
35	WO ₃	---	---	---	---	---	---	---	---
36	GeO ₂	0.0009	---	0.0005	---	---	---	---	---
37	Tl ₂ O ₃	---	---	---	---	---	---	---	---
38	HgO	---	---	0.0004	---	---	---	---	---
39	Ag ₂ O	---	---	---	---	---	---	---	---
40	PdO	---	---	---	---	---	---	---	---

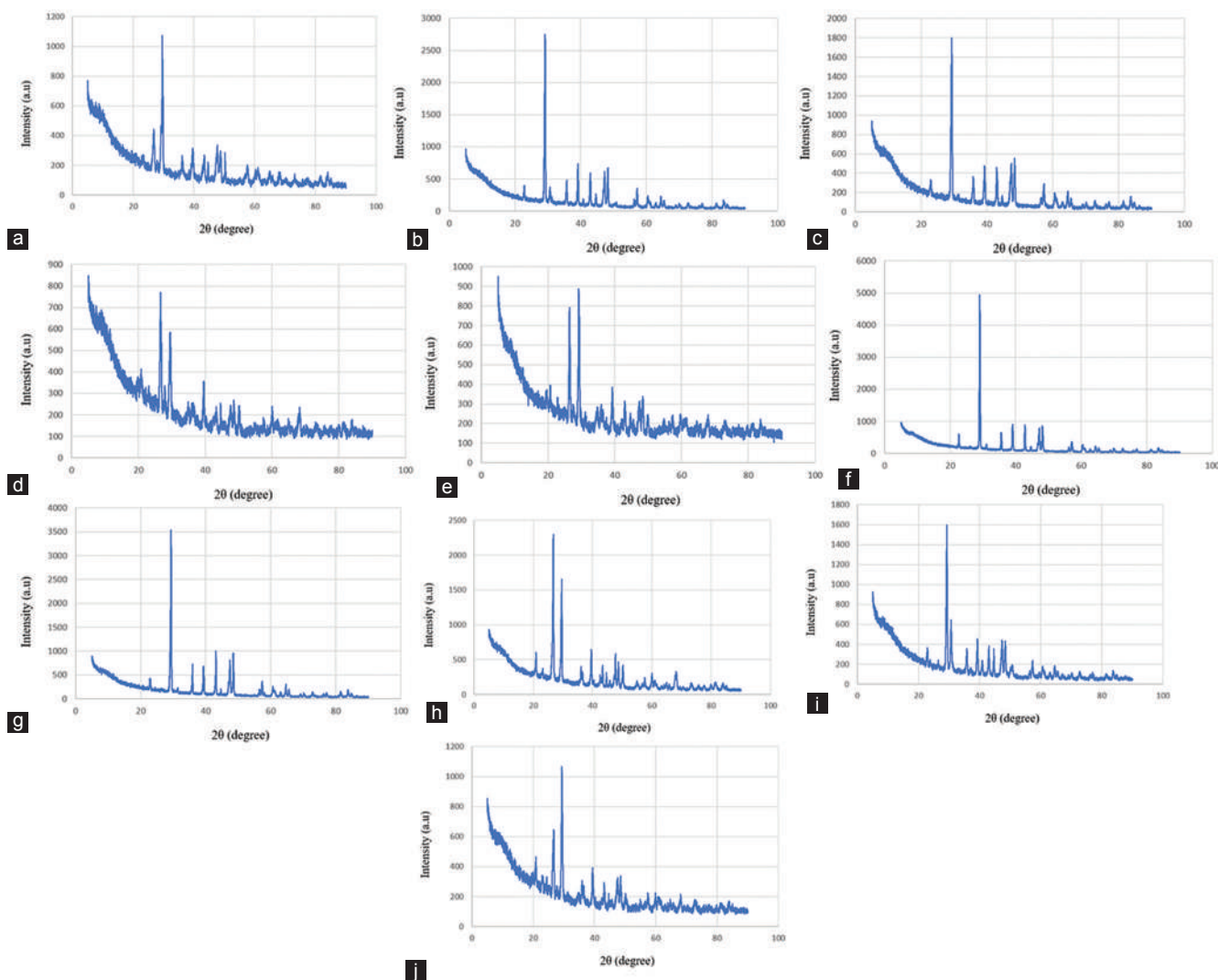


Fig. 3. X-ray diffraction data of the ten different rocks collected from Haybat Sultan place that represented by a-j.

in the XRD data in terms of crystallinity for the majority of the rock samples, although a minor difference can also be seen in these spectra, which could be due the origin place of rocks.

The average crystalline grain size of the powder rock samples was determined using Debye-Scherrer equation (Birks, 1964):

$$D = \frac{0.9}{\beta \cos \theta} \quad (1)$$

where D , λ , β , θ , and 0.9 are the particle size in nm, the wavelength of the X-ray, the full width at half maximum, the peak position, and the Scherrer constant, respectively.

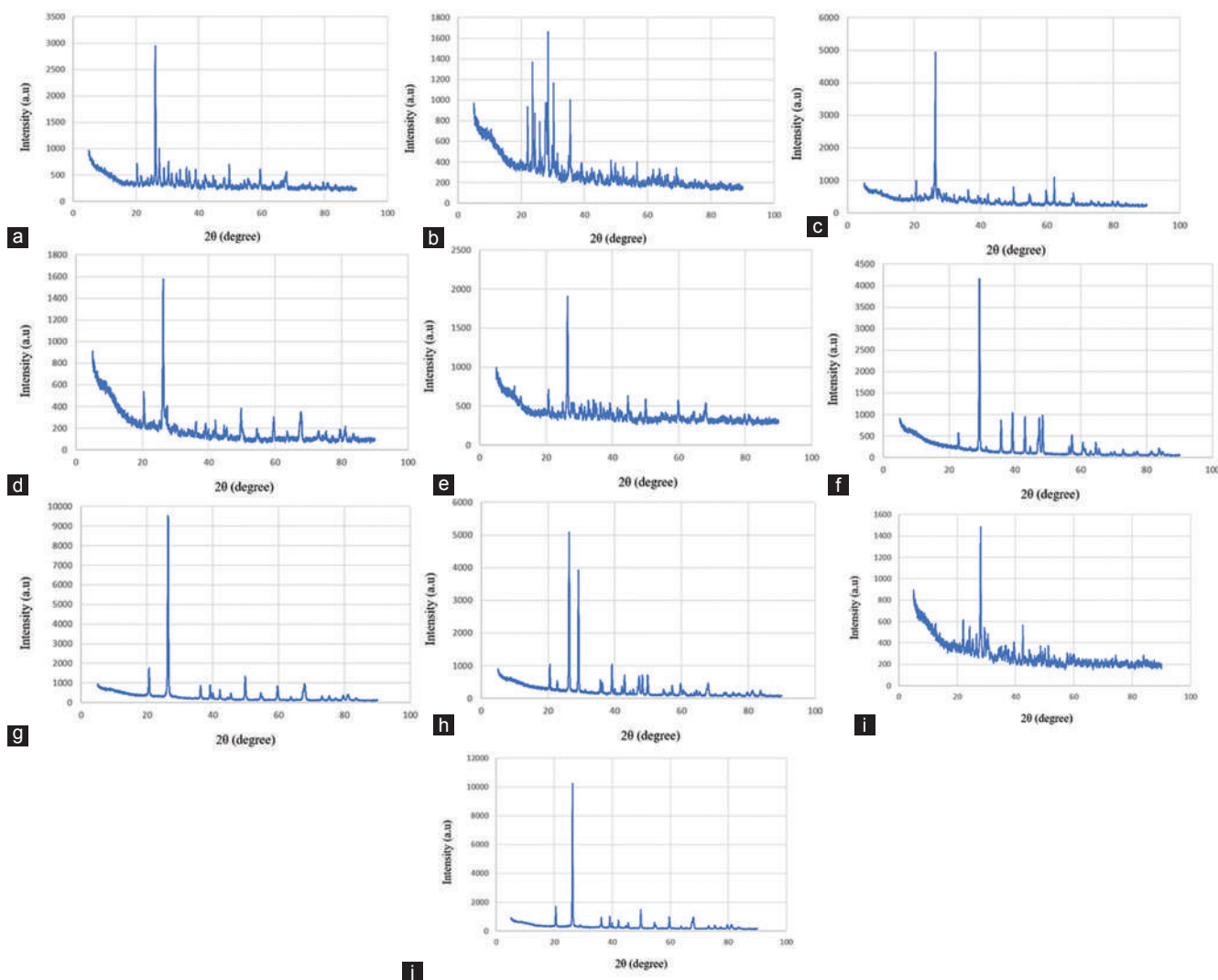


Fig. 4. X-ray diffraction data of the ten different rocks collected from TaqTaq place that represented by a-j.

Using this equation, the crystalline grain size (D) for the collected rocks was found to be as summarized in Table IV:

C. The Rocks Appearance

Rocks on earth can appear with endless array of colors, started from shiny bright and ended with dull dark. The variety of their colors is a result of number of factors. First, the mineral those build up the rocks. Some rock consists only one type of mineral (for example, gold [Au] and silver [Ag]), whereas the majority are consisting of different types of mineral bound together such as ferric oxide (Fe₂O₃) and CaCO₃. Each type of mineral has its chemical composition that determined their unique color. Next factor is the impurities that interact with the minerals and the mineral concentration finally, the atomic bounds within the mineral structure. This factor has observed effect on the absorbed and reflected wavelengths to our eyes, for instance, diamond and graphite are both pure carbon but has different color properties (Mishra, Chhalodia and Tiwari, 2018; Breeding, Magana and Shigley, 2018; Tiwari et al., 2016;

TABLE IV
AVERAGE PARTICLE SIZE FOR THE COLLECTED ROCKS

Rocks code	Average particle size (nm)
HS	1-4
TA	2-5
GT	2-7

Sheng et al., 2011). The appearance of the rock samples shows a variety of colors, as represented in Fig. 6. Overall, samples collected from HS contain high concentration of lime (CaO), which can be responsible of their light color (for example, number 6 of Fig. 6a), whereas the gradient in color refers to different concentration of the other mineral oxides, for instance, iron oxide lends the red color to the sample with consideration of their concentration. To study this effect, HS6 (Fig. 6a) and TA6 (Fig. 6b) can be taken which have the same concentration of CaO whereas the ratio of Fe₂O₃ exceeds by 4 times in TA6 compare to HS6. Besides, the shiny appearance of the rock samples, especially GT samples (Fig. 6c) is due to the high content of silica (SiO₂) relative to the other minerals.

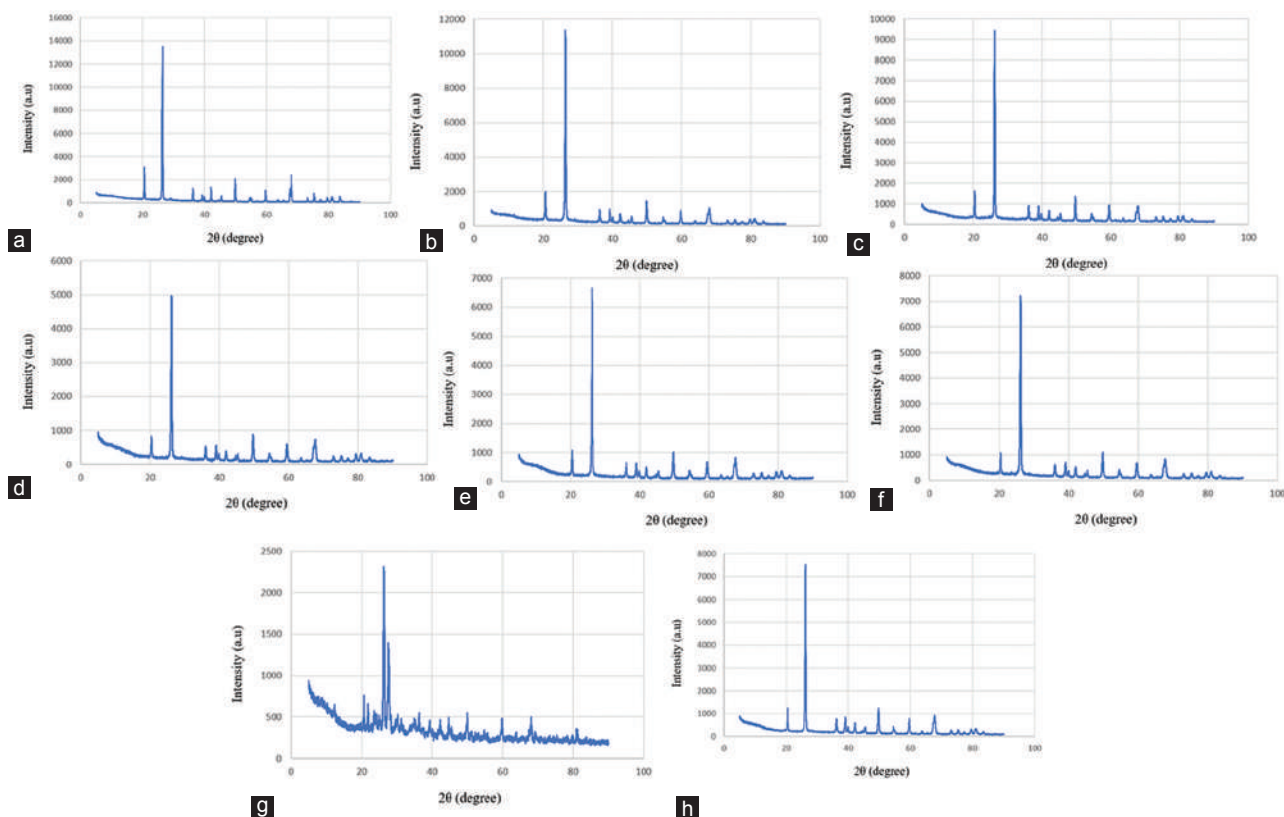


Fig. 5. X-ray diffraction data of the eight different rocks collected from Garmuk place that represented by a-h.



Fig. 6. External view (appearance) of the collected rock samples from (a) Haybat Sultan, (b) TaqTaq, and (c) Garmuk.

IV. CONCLUSION

Twenty-eight samples of different rocks collected from places of Koya city, TA and GT have been analyzed using both XRF and XRD techniques. These two techniques were effective in analyzing the chemical composition and crystalline structure of the collected rocks, as on the one hand, they successfully shown the major and minor minerals in these rocks as well as shown the phases of them, on the other hand. It has been proven from the XRF data that $Ca-K^\alpha$, $Fe-K^\alpha$, and $Si-K^\alpha$ were of high concentrations in HS, TA, and GT rock samples, respectively. Furthermore, the XRD data shown that the nature of all collected rocks from HS, TA, and GT were crystalline. The appearance of the collected rocks, on the other hand, was also discussed and it has been shown that the differences in the view of these rocks were due to the various minerals of different concentration contain in these rocks, which gave each rock a specific color.

ACKNOWLEDGMENT

The author would like to thank Assist. Prof Dr. Faten A Ismael and Dr. Khalid N Sediq for their valuable comments during data analysis.

REFERENCES

Abdullah, B.A., Chaqmaqchee, F.A.I., and Anwer, S.S., 2017. Determination of major and minor elements in kids' milk using XRF technique. *Journal of Chemical, Biological and Physical Sciences*, 7, pp.593-598.

- Birks, L., 1946. Particle size determination from X-ray Line Broadening. *Journal of Applied Physics*, 17, pp.687-692.
- Breeding, C.M., Magana, S.E., and Shigley, J.E., 2018. Natural-color green diamonds: A beautiful conundrum. *Gems and Gemo*, 54, pp.2-27.
- Chaqmaqchee, F.A.I., and Baker, A.G., 2016. Study and characterization of polyaniline at various doping of LiCl wt.% using electrical measurements and XRF analysis. *Journal of Research Updates in Polymer Science*, 4, pp.188-190.
- Cornaby, S., Mena, A.R., Pew, H.K., Moody, P.W., Hughes, T., Stradling, A., Turner, D.C., and Knight, L.V., 2001. An XRD/XRF instrument for the microanalysis of rocks and minerals. *Meas. Sci. Technol*, 12, pp.676-683.
- Faraj, M.G., Chaqmaqchee, F.A.I., and Omar, H.D., 2017. Structural, morphological and electrical properties of Zn doped PbS thin films by chemical spray pyrolysis technique. *JOAM*, 19, pp.421-416.
- Faraj, M.G., Kaka, A.K., and Omar, H.D., 2019. Electrical, optical and structural properties of copper oxide thin films deposited on plastic substrate by spray pyrolysis technique, *ARO*, 7, pp.14-18.
- Fatah, S.S., and Mohialdeen, I.M.J., 2016. Hydrocarbon generation potential and thermal maturity of Middle Jurassic Sargelu Formation in Miran Field, Sulaimani Area, Kurdistan Region, NE Iraq. *Journal of Zankoy Sulaimani*, 2, pp.213-228.
- Hassan, M.M., Jones, B.G., Buckman, S., Al-Jubory, A.I., and Ismail, S.A., 2015. Source area and tectonic provenance of Paleocene-Eocene red bed clastics from the Kurdistan area NE Iraq: Bulk-rock geochemistry. *Journal of African Earth Sciences*, 109, pp.68-86.
- Hunt, J.M., 1996. *Petroleum Geochemistry and Geology*. 2nd ed. W.H. Freeman and Company, New York, p.743.
- Lopez, J.M.G., Bauluz, B., Nieto, C.F. and Oliete, A.Y., 2005. Factors controlling the trace-element distribution in fine-grained rocks: The Albian kaolinite-rich deposits of the Oliete Basin (NE Spain). *Chemical Geology*, 214, pp.1-19.
- Loubser, M., and Verryin, S., 2008. Combining XRF and XRD analyses and sample preparation to solve mineralogical problems. *South African Journal of Geology*, 111, pp.229-238.
- Marinangeli, L., Pompilio, L., Baliva, A., Billotta, S., Bonanno, G., Domeneghetti, M.C., Fioretti, A.M., Menozzi, O., Nestola, F., Piluso, E., Pondrelli, M., Salvia, V.L., Somma, M.C., Tateo, F., Petrinca, P., Giulio, C.D., and Tangari, A.C., 2015. Development of an ultra-miniaturised XRD/XRF instrument for the *in situ* mineralogical and chemical analysis of planetary soils and rocks: Implication for archaeometry. *Rendiconti Lincei. Scienze Fisiche e Naturali*, 26, pp.529-537.
- Meena, B.I., Omar, K.A.K., Khan, A., Chaqmaqchee, F.A.I., and Alsalihi, E., 2018. Characterization and comparison of clay from Iraq and Iran for bricks production. *Clay Research*, 37, pp.8-13.
- Mirza, T.A., Kalaitzidis, S.P., Mohammed, S.H., Rashid, S.G., and Petrou, X., 2017. Geochemistry and genesis of sulphide ore deposits in Sharosh Village, Qandil Series, Kurdistan Region, NE Iraq. *Arabian Journal of Geosciences*, 10, pp.428-446.
- Mishra, R., Chhalodia, A.K., and Tiwari, S.K., 2018. Recent progress in nanodiamonds: Synthesis, properties and their potential applications. *Ver. Funct. Nano*, 2, pp.1-23.
- Mohammed, T.A.M., 2012. Composition and phase mineral variation of Portland cement in Mass Factory Sulaimani Kurdistan Region NE- Iraq. *International Journal of Basic and Applied Sciences*, 12, pp.109-118.
- Mohialdeen, I.M.J., Hakimi, M.H., and Al-Beyati, F.M., 2015. Biomarker characteristics of certain crude oils and the oil-source rock correlation for the Kurdistan oilfields, Northern Iraq. *Arab J Geosci*, 8, pp.507-523.
- Nayak, P.S., and Singh, B.K., 2007. Instrumental characterization of clay by XRF, XRD and FTIR. *Bulletin of Materials Science*, 30, pp.235-238.
- Roser, B.P., and Korsch, R.J. 1988. Provenance signatures of sandstone-mudstone suites determined using discriminant function analysis of major-element data. *Chemical Geology*, 67, pp.119-139.
- Sanchez, J.S., Romani, J.R.V., Mosquera, D.F., and Alves, C.A., 2008. Study of origin and composition of coatings in a monument built with granitic rocks, by SEM, XRD, XRF and DTA-TGA. *X-Ray Spectrom*, 37, pp.346-354.
- Sarrazin, P., Blake, D., Bish, D., Vaniman, D., and Collins, S., 1998. A miniature XRD/XRF instrument for *in-situ* characterization of Martian soils and rocks. *Journal of Physique. IV France*, 8, pp.465-470.
- Sheng, X.L., Yan, Q.B., Ye, F., Zheng, Q.R., Su, G., 2011. T-carbon: A novel carbon allotrope. *Physical Review Letters*, 106, pp.155703-5.
- Tissot, B.P., and Welte, D.H., 1984. *Petroleum Formation and Occurrence*. 2nd Springer-Verlag, Berlin, Heidelberg, New York, p.699.
- Tiwari, S.K., Kumar, V., Huczko, A., Oraon, R., De Adhikari, A., and Nayak, G.C., 2016. Magical allotropes of carbon: Prospects and applications. *Critical Reviews in Solid State and Materials Sciences*, 41, pp.257-317.
- Vaniman, D., Bish, D. and Chipera, S., 1991. *In-situ* planetary surface analyses: The potential of X-ray diffraction with simultaneous X-ray fluorescence. *Lunar and Planetary Science Conference*, 22, pp.1429-1430.
- Vaniman, D., Blake, D., Bish, D., Collins, S., Sarrazin, P., Elliot, T., and Chipera, S., 1998. Landed XRD/XRF analyses of prime target in the search for past or present Martian life. *Journal of Geophysical Research*, 103, pp.31477-31489.
- Wadsworth, W.B., and Baird, A.K., 1989. Modal analysis of granitic rocks by X-RAY diffraction. *Canadian Minerologist*, 27, pp.323-341.

Effect of Modeling Techniques on the Simulation: Calculating the Stress Concentration Factors in Square Hollow Section T-Joints as a Case Study

Serwan S. M. Talabani¹, Ahmad T. Azeez¹, Silvio D. Barros^{2,3}, Basim M. Fadhil¹ and Hewa H. Omer⁴

¹Department of Manufacturing and Industrial Engineering, Faculty of Engineering, Koya University, Koya KOY45, Kurdistan Region - F.R. Iraq

²Federal Center of Technological Education in Rio de Janeiro – CEFET/RJ, Rio de Janeiro, Brazil

³GeM Institute, UMR 6183 CNRS, CESI, Saint-Nazaire, France

⁴Department of Chemical Engineering, Faculty of Engineering, Soran University, Kurdistan Region - F.R. Iraq

Abstract—The capability of the simulation software motivates the engineers to analyze the stress in complex welded joints where ordinary mathematical expression may lack. However, unfortunately, the simulations were interpreted mechanically without considering the simulation parameters deeply. For this reason, this research aims to study the effect of simulation parameters on the stress concentration factor of square hollow sections structures using ANSYS workbench. In this context, two main meshing techniques (face split vs. slicing) and various behavior of materials (linear vs. nonlinear) having been considered. The outputs of the investigations revealed the superiority of the materials nonlinearity over linear behavior in terms of results acceptability comparing to their corresponding real-life ones. For instance, the supercritical fluid of nonlinear plastic material estimated to be 14 which was closest to the 12 obtained experimentally by Mashiri et al. In addition to that, face split technique outperformed the slicing in terms of result accuracy and solving time. Solving the face split model elapsed 254 s only which is dramatically less than the minimum time (1605 s) of sliced models. This is because any slicing process will lead to the formation of the contact elements at interfaces and uncomfortable meshing which may in turn adversely effect on the simulation efficiency.

Index Terms—ANSYS Workbench, Face split, Modeling of materials, Stress concentration factor, Welding toe.

I. INTRODUCTION

In modern life, due to the great development in the field of the computers, the engineers rely to a large extent on simulating

virtual physics in a circumstance comparative to their real-life conditions. Accordingly, simulation is a crucial instrument to obtain immediate results of the models operating under different working conditions. This contributes to shortening the design session and also enables the engineers to review, manipulate, and improve their designs continuously at low levels of cost (Sinha, et al., 2000) For this reason, different simulation programs were innovated to cover the specific scientific requirements of different engineering disciplines. For example, ANSYS which is a multiphasic package developed by ANSYS Inc., USA, and has been widely used by engineers due to the enjoyed capability and has different products such as Axiomatic Product Development Lifecycle and WORKBENCH.

On the other hand, welding is an effective method for assembling parts together, especially in construction applications such as bridges, towers, and offshore platforms. Such structures, considering their purpose of the building may be vulnerable to *in situ* loading/unloading cycles originated from traffic loads, winds, or sea waves, leading to fatigue damage (Saini, Karmakar and Chaudhuri, 2016). The dynamic load may initiate crack at welded joints which may propagate resulting in the collapse of the structures eventually. The abnormal increment of the stresses at welded beads related to the discontinuity at the joints is the main source of crack initiation (Zhao, et al., 2001). Thus, considering the supercritical fluids (SCFs) in the detailed design is a top concern. According to the recommendations for fatigue design in welded joints, the SCFs, which are the ratio of the hot spot stress (σ_{hs}) to the nominal stress, can be calculated either practically or numerically as these are the only applicable methods to determine the σ_{hs} . Unlike, the nominal stress is covered by simple beam theory (Hobbacher, 2008).

ARO-The Scientific Journal of Koya University
Volume VIII, No.1 (2020), Article ID: ARO.10585, 7 pages
DOI: 10.14500/aro.10585

Received: 03 November 2019; Accepted: 23 June 2020

Regular research paper: Published: 28 June 2020

Corresponding author's email: serwan.talabani@koyauniversity.org

Copyright © 2020 Serwan S. M. Talabani, Ahmad T. Azeez, Silvio de Barros, Basim M. Fadhil, Hewa H. Omer. This is an open-access article distributed under the Creative Commons Attribution License.



Calculating SCFs numerically require qualitative meshing such as fine meshes around the weld toe to improve data capture and coarser elements elsewhere to reduce the cost of computations (Zhao, et al., 2001). Consequently, the researchers analyzed the welding joints under different considerations of meshing such as size, type (solid or shell), and shape (hexagonal or tetrahedral) and different conclusions have been made (Zhao, et al., 2001), (Hobbacher, 2008), and (Neimi, Fricke and Maddos, 2004). For instance, it is estimated that solid elements prevailed over shell elements in terms of accuracy unless the shell elements manipulated (Rizzo and Codda, 2010). Subsequently, a set of rules to mesh the model with large shell elements have been developed by Chattopadhyay (Chattopadhyay, et al., 2011) and the new formula enabled the calculation of the SCFs effectively. In the same context, numerous researches refined the elements around the welding toe without any refereeing to the effect of the meshing technique on the performance of the simulation in terms of time or the results accuracy. In many cases, the literature did not explain the technique used in mapping the models and the researchers concentrated on discussion their works from a pure mechanical point of view such as Tong (Tong, et al., 2016), Chiew (Chiew, et al., 2000), and (Chiew, et al., 1999) without any attention to the modeling part.

It is obvious from the literature that the effect of the meshing techniques on the simulation performance is by far still obscure and needs to be demonstrated. In accordance, this paper aims to study two meshing techniques (slicing and face split) provided by ANSYS workbench in mapping the elements in square hollow section (SHS) welded tubes and investigate their effects on the simulation performance. In addition, the effect of the material was also included to cover this subject from its different aspects. The paper will also verify the result of the SCFs by considering the real life behavior of the welded structures cited in the literatures.

II. METHODOLOGY

A. Calculating Stress Concentration Factors (SCFs)

SCF is a multiplication factor of the stress around discontinuous regions, defects, crack, etc., and welding joints are not excluded. Dividing the σ_{hs} by the nominal stress will determine SCFs at welding toes which depend on different dimensionless parameters. Unfortunately, the available analytical methods are incapable of calculating the σ_{hs} on the surface of the tubes, hence, the engineers depend on the practical and/or numerical method to determine the structural stress (Saini, Karmakar and Chaudhuri, 2016), (Zhao, et al., 2001), and (Hobbacher, 2008). The numerical method depends on extrapolation the stresses at particular points from the weld edge linearly for circular tubes or quadratically for SHS [2]. The distances of the extrapolation points in the SHS with their minimum limits are given in Table I, as recommended by Zhao et al. (Zhao, et al., 2001). Experimentally, it is feasible to estimate the strains pointed at specific distances using a special type of chips known as strain gauge. For this reason, strain concentration factor will

be determined first then it will be converted to SCF using the following formulas:

$$SCF=1.1 SCNF \text{ for rectangular hollow sections (RHSs)}$$

$$SCF=1.2 SCNF \text{ for circular hollow sections (CHSs)}$$

Furthermore, it is important to notice that rising of the stress in the extrapolation region has a negatively concaved scheme, as shown in Fig. 1.

B. Finite Element Method

Finite element is an active method for solving differential equations and analyzing complex systems in engineering and physics where the ordinary analytical methods are incapable of solving the problems. The method consists of discretizing the virtual prototype into definite parts with a specific number of nodes based on the shape of the element. Each individual part has a stiffness matrix which will be assembled to the global stiffness matrix following a particular algorithm. An example of such matrix may be found in Equation 1.

$$\{F\}=[K]\{d\} \quad 1$$

$\{F\}$: Global nodal force matrix

$[K]$: Global stiffness matrix

$\{d\}$: Global nodal unknown displacement matrix

The size of the previous matrices depends on the total number of unknown degrees of freedom (DOF) of the nodes in the model which, in turn, depends on the number of nodes. Investigating the PCS files provided by ANSYS revealed the fact that the total number of DOF is 3 times the number of nodes recalling that three-dimensional (3D) solid being used in meshing. Off course, this is not a general trend to be globalized fundamentally, actually, the aforementioned trend of DOFs depends on the types of the elements used in

TABLE I
BOUNDARY CONDITION OF THE EXTRAPOLATION REGION [3]

Distance from welding toe	Chord	Brace	Minimum limits
Lr,min	$0.4t_0^a$	$0.4t_1^b$	4 mm
Lr,max	$Lr,min+t_0$	$Lr,min+t_1$	$Lr,min+0.6t_1$

a and b are the thickness of the chord and brace, respectively

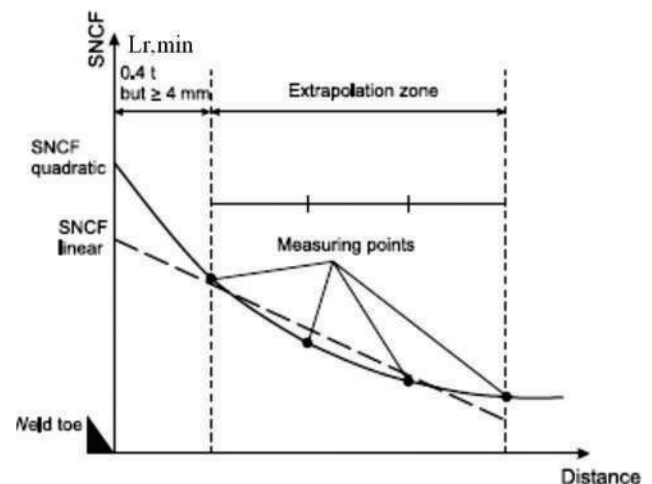


Fig.1. Extrapolation methods (Zhao, et al., 2001).

meshing and might be restricted to the models used in this research, see the upcoming sections for details. Accordingly, simulating 3D models reflect adversely on the elapsed time (which is the time required by the software to solve the matrices and obtain the results) due to DOFs factor explained previously. In the same context, it is sensible to say that any meshing refinement leads to increment in the running time of the simulation since the matrices size enlarge in combination with the number of DOF (Bhashyam, 2002).

On the other hand, slicing off the models to control the partitioning process will lead to the formation of the contact elements at the interface. Such contact pairs need a specific algorithm that controls the interaction of the physics at interfaces in a manner similar to their real-life behavior. Consequently, various formulations are available such as pure Penalty and Augmented Lagrange which have the following form (Contact Formulation Theory, 2016) and (Stupkiewicz, 2003).

$$\text{Pure Penalty } f_n = k_n \times \text{penetration} \quad (2)$$

$$\text{Augmented Lagrange } f_n = k_n \times \text{penetration} + \lambda \quad (3)$$

f_n : Finite contact force

k_n : Contact stiffness matrix

λ : Lagrange multiplier vector defined on the contact surface.

It is thought that the presence of contact pairs in the models consumes time since the software has to deal with forces transfer between the nodes at interfaces according to the contact formulas.

III. MODELING AND SIMULATION

A. Modeling of Materials

Materials modeling means selecting the most consistent mathematical expressions in the simulation that keeps the response of the materials to the various working conditions in a context to the physical evidence (Haupt, 1993) otherwise the simulation will be useless. Accordingly, different behaviors were used to investigate the effect of the materials modeling on the SCFs and the elapsed time. The three known models, linear, bilinear, and multilinear, were tested. The

modulus of elasticity and Poisson’s ratio for steel were taken as 205 GPa and 0.3, respectively. The curves of different materials behavior are shown in Fig. 2. (Liu and Day, 2009). The tangent modulus was calculated manually from the multilinear data and estimated to be 868 MPa.

B. Meshing Control and Boundary Condition

The intact meshing of the objects to the specific map may be obstructed by the complexity of the models unless advanced techniques utilized. Two of the advanced methods to control the meshing in ANSYS workbench are face split and slicing. Face split, as the name suggests, depends on splitting the faces without cutting off the object through the thickness; hence, no contact will be formed at the splitting interfaces. Slicing, on the other hand, relies on partitioning the model into smaller parts.

Despite that, slicing provides the users the facility of controlling meshing process, especially in complex geometry, but the process is not free of risks. Models being sliced have a new physical state at interfaces due to the formation of contact elements which in turn may result in convergence problem especially when nonlinear materials having been adapted in the simulations (Barrett, 2014). However, the elements around the weld toe were sized to 1 × 1 mm and approximately 20 mm width faraway, the welding profile has been concaved with 6 mm diameter to oversize the weld bead as recommended by Mashiri [18], Fig. 3a.

Regarding boundary condition, a 2 kN in-plane lateral force was applied on the top surface of the brace of dimensions 50 × 50 × 3 mm, whereas the 100 × 100 × 3 mm chord constrained from its two side faces, Fig. 3b. The length of each of the chord and the brace was 6 times their widths (Tong, et al., 2016). The previous specific dimensions of the tubes were selected to verify the resulted SCFs with its corresponding practical value obtained by Mashiri (Mashiri, et al., 2007). Unfortunately, slicing produced uncomfortable meshing as can be seen in Fig. 3c and d. Such meshing may have detrimental effects on the simulation efficiency. The nodes in uncomfortable meshing may be brought into intimated contact using node merging option available in ANSYS workbench 16.1 release. Each node merging process contributes to reducing the total degree of freedom of the model which,

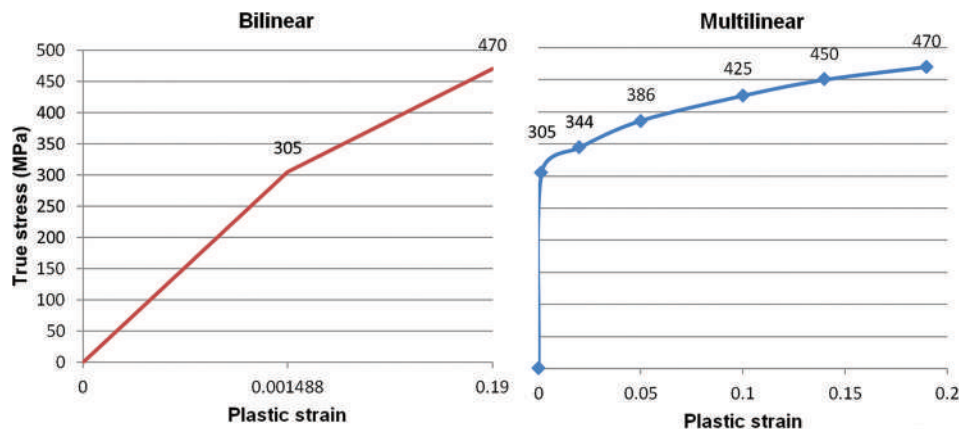


Fig. 2. Models of materials (the experimental data cited from Liu and Day, 2009).

in turn, affects the simulation process. Accordingly, four models were tested in order to evaluate the performance of the simulation considering meshing robustness, each with a specific degree of freedom resulted from merging the nodes (model 1-model 4, table II). The technique of meshing itself (face split vs. slicing) will be criterion to complete the evaluation of the simulation efficiency. Not to mention that hexagonal elements with dimension 1×1 mm around the weld toe and 1×20 mm elsewhere being used to mesh the models as explained previously.

IV. RESULTS AND DISCUSSION

A. Materials Modeling

The hot spot stress estimated by extrapolating the maximum principal stresses quadratically within the limits 4 and 7 mm from the weld toe according to the welding design criteria recommended to select the boundary of the extrapolation region required to calculate the σ_{hs} , as indicated in Table I. The method of extrapolation was developed in the 1970s to calculate the σ_{hs} raised on the surface of the welded structures due to uneven levels of deformations in brace and chord and to distinguish it from notch stress which is a local stress originated from the notch of the weld toe (Saini, Karmakar and Chaudhuri, 2016) and (Zhao, et al., 2001). The value of the extrapolation region should also be 3 mm away from the corner where the maximum stress occurred to avoid the singularity as advised by Wingerde (Wingerde, 1992), Fig. 4a. The third point could be selected arbitrarily

between them (Mashiri, et al., 2002) and it was selected at a distance of approximately 6 mm away from the weld edge.

SCFs were calculated in different models through quadratic extrapolation using Microsoft® Excel sheet. The value of σ_{hs} could be simply estimated by substituting x with zero in the trend line equation indicated in Fig. 4b. The σ_{hs} then divided by the nominal stress (16.4 MPa) calculated manually in the chord using simple beam theory.

Moreover, the effect of different materials behavior on the SCFs and elapsed time is shown in Fig. 5. Modeling the material multilinearly best fitted the real-life behavior as expected because the calculated SCF 14 was closest to the practical value 12 estimated by Mashiri (Mashiri, et al., 2007). Unfortunately, it is not possible to obtain the same SCF as in the referred work because the authors did not provide any stress-strain data that could be used in here. The SCFs in both linear and bilinear modeling diverged from the practical value and exceeded 17, as shown in Fig. 5.

Regarding the elapsed time, a variant trend was observed as the running time increased dramatically from 254 s to more than 3500 s, as shown in Fig. 5, due to the increment of the total iterations in preconditioned conjugate gradient from 1453 to more than 2000 in linear and nonlinear (bilinear and multilinear) models, respectively. However, this is not always the case, because if multiple cores of CPU are used (parallel processing), the nonlinearity will increase the time required to solve one iteration rather than the number of iterations itself (Koslpski, 2017). The elapsed time may vary from one machine to another based on the capability of the system, but the obtained trend plotted in Fig. 5. is expected to remain the same.

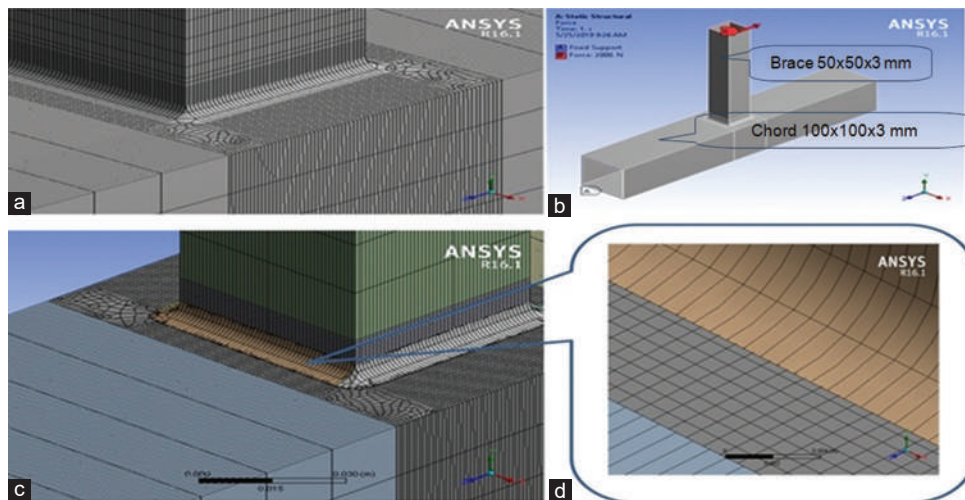


Fig. 3. Meshing techniques and boundary conditions. a. Face split b. Boundary condition c. Sliced technique d. Uncomfortable meshing.

TABLE II
EFFECT OF MESHING TECHNIQUES ON THE RUNNING TIME

Criteria	Face split	Sliced models			
		Model 1	Model 2	Model 3	Model 4
Elapsed time (s)	254	2792	2773	2750	1605
Number of nodes	25,0671	199,064	198,865	198,764	198,727
Degree of freedoms	752,013	597,192	596,595	596,292	596,181
Non-zeros in upper triangular part of global stiffness matrix	752,013	40,559,457	40,514,532	40,488,627	40,476,282

B. Effect of Meshing Techniques

The recommended meshing map for calculating SCFs in welded joints can be controlled using advanced technique such as face split or slicing. Slicing, as explained previously, will result in interface at the cutoff planes and sometimes uncomfortable meshing at contact boundary of the parts that may have detrimental effects on the simulation performance. Consequently, four models, each one with a specific number of nodes produced due to slicing, were investigated and compared to one-part object in which the meshing process was controlled through face splitting.

To reduce the running time and avoid the convergence problems related to the contact nonlinearities of the sliced models, the material behavior was modeled linearly and compared to their corresponding linearly deformed material in face split models. The SCFs, for instance, even could not be evaluated in sliced models since the stress in the extrapolation region concaved positively in contrast to the

standard trend, as can be seen comparing Fig. 6. with Fig. 1. This leads to σ_{hs} of magnitude 399 MPa at weld toe which is lower than 475 MPa determined at a distance 4 mm from welding edge and of course such result is unacceptable.

Fortunately, the stress in the linear model meshed using face split concaved up in agreement to the standard style and the SCF was calculated to be 17, as discussed in the previous section. The reason may be due to the differences in the meshing style through the thickness (as shown in Fig. 7) despite their similarity on the surface as ANSYS meshed the sliced model piece wisely whereas the face split as one part.

On the other hand, uncomfortable meshing produced in the sliced models adversely affected the elapsed time as the number of nodes increased. Subsequently, merging nodes (a technique that brings the nodes into intimate contact at interfaces) plays a key role in reducing the number of nodes hence improves the performance of simulation in terms of running time (Bhashyam, 2002).

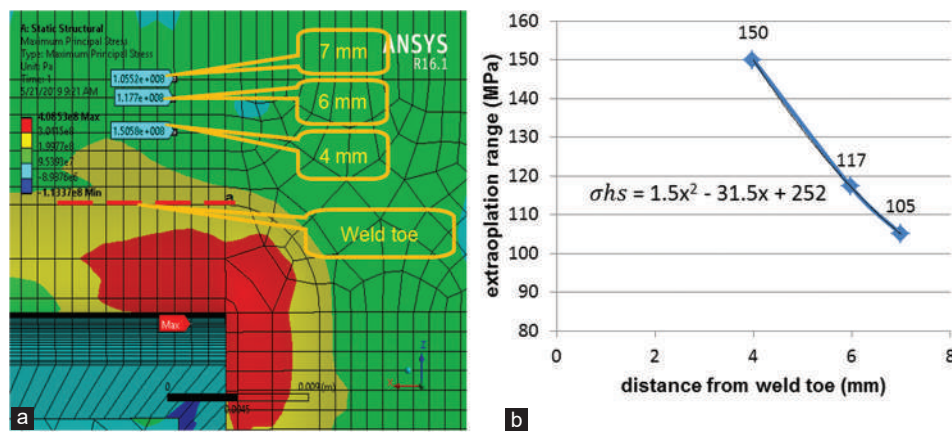


Fig. 4. Calculating the hot spot stress a. Maximum principal stress on the chord surface at the location of maximum square b. The result of the extrapolation.

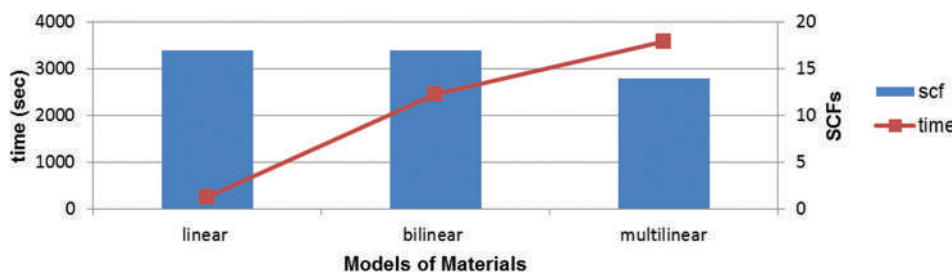


Fig. 5. Effect of materials behavior on the supercritical fluid and elapsed time.

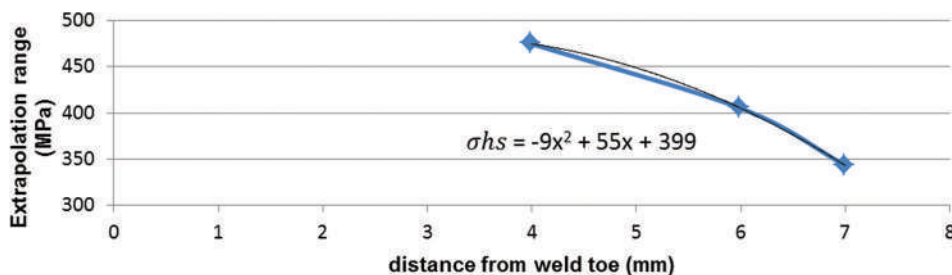


Fig. 6. Convex extrapolation region in the sliced model of linear material.

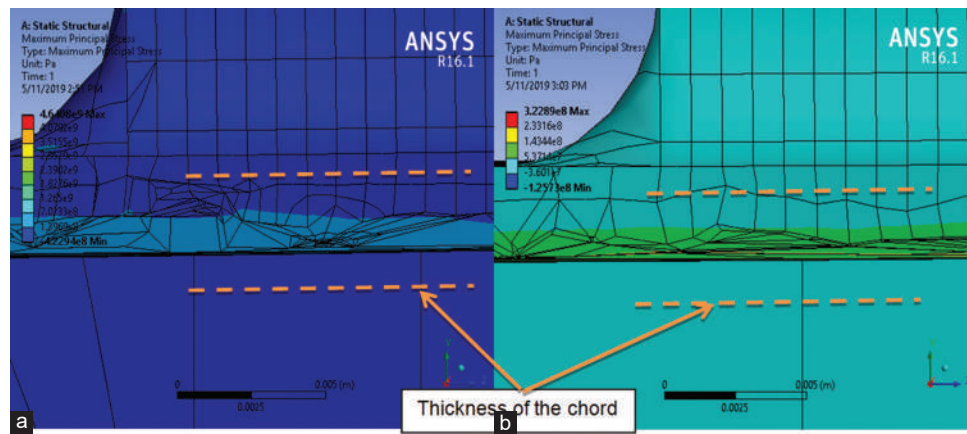


Fig. 7. The differences in the meshing through the thickness. a. Sliced model, b. Face split model.

The elapsed time reduced by a parallel reduction in the number of nodes from 2792 s to 1605 s as the number of nodes decreased from 199,064 to 198,727 in models 1 and 4, respectively, by merging nodes to produce comfortable meshing. The obtained results agreed to the mathematical expressions provided by Equation 1. The lower the number of nodes, the lower the degree of freedom related to the models hence lower non-zeros numbers that ANSYS has to solve, Table II. Unfortunately, additional reduction in the number of the nodes was not possible since any further nodes merging would produce highly deformed elements that did not converge during solving probably due to poor meshing quality.

However, comparison with face split may change the aforementioned discussion. Despite of that face split model contains 250,671 nodes, the elapsed time was only 254 s compared to more than 1600 s for sliced models due to the presence of the contact elements in the later. In sliced models, ANSYS has to solve additional equations related to contact stiffness matrix. For example, the face split contains 752,013 non-zeros in the global stiffness matrix compared to more than 40 million factors in other models. The additional non-zeros factors may be originated from the contact stiffness matrix and decrement of such non-zeros coefficients through reduction of the degree of freedoms in the sliced models by merging nodes also support such an explanation, Table II.

It is clear from the previous discussion that face split outperformed slicing technique due to inaccurate-high cost for the later. However, slicing is still an efficient tool of meshing if the disadvantages of the process avoided. For instance, considering the contact problems and the robustness of the meshing at the interface are the main criteria to be considered.

V. CONCLUSION

The paper investigated the effect of different parameters such as materials behavior and meshing techniques on the results of simulations using ANSYS software. The previous discussions led to important conclusions regarding the simulation process and software behavior that can be summarized as follows:

- 1) Simulation the material nonlinearly though its time-consuming process but best verified the resulted SCF as compared to the real-life value.
- 2) Face split unless the problematic factors have been avoided outperformed the slicing technique in terms of results accuracy and running time.
- 3) Presences of contact elements in the sliced models adversely affected the simulation efficiency and dramatically increase elapsed time as the number of degree of freedom increased.

VI. FUTURE WORK

The paper investigated the effect of various parameters on the simulation results in welded joints using ANSYS WORKBENCH. However, the output of the work disclosed completely new gaps to be covered in extended works. For example, comparing the obtained results from another software rather than ANSYS with that cited in this paper. However, the authors recommend comparing under the same working conditions as element size, type, and number, the model design and dimensions, and the material data to guarantee a pure attribution of the results on the software type. On the other hand, estimating the residual stress in welded joints is another factored to be considered in the future.

REFERENCES

- Barrett, P. 2014. *Stress Analysis Convergence Tips for Dummies*. Available from: <https://www.caeai.com/blog/stress-analysis-convergence-tips-dummies>. [Last accessed on 2019 May 24].
- Bhashyam, G.R. (2002) *ANSYS Mechanical A Powerful Nonlinear Simulation Tool*. ANSYS, Inc., Canonsburg, Pennsylvania.
- Chattopadhyay, A., Glinka, G., El-Zein, M. and Qian, J. 2011. Stress analysis and fatigue of welded structures. *Welding in the World*, 55(0708), pp.1-21.
- Chiew, S.P., Soh, C.K., Members, A.S.C. and Wu, N.W. 1999. Experimental and numerical stress analysis XT-joint. *Journal of Structural Engineering*, 125, pp.1239-1248.
- Chiew, S.P., Soh, C.K., Members, A.S.C. and Wu, N.W. 2000. Experimental and numerical SCF studies of multiplanar tubular XX-joint. *Journal of Structural Engineering*, 126, pp.1331-1338.

- Contact Formulation Theory. 2019. Available from: https://www.sharcnet.ca/Software/Ansys/16.2.3/en-us/help/wb_sim/ds_contact_theory.html#ds_form_pure_aug. [Last accessed on 2019 May 26].
- Haupt, P. 1993. On the mathematical modeling of material behavior in continuum mechanics. *Acta Mechanica*, 100, pp.129-154.
- Hobbacher, A. 2008. *Recommendations for Fatigue Design of Welded Joints and Components*. International Institute of Welding, Paris.
- Koslpski, J. 2017. *Speeding up Your Analysis Part 1*. Available from: <https://www.caeai.com/blog/speeding-your-analysis-%E2%80%93-part-1>. [Last accessed on 2019 May 21].
- Liu, Y.C. and Day, M.L. 2009. Concept modeling of tapered thin-walled tubes. *Journal of Zhejiang University Science A*, 10(1), pp.44-53.
- Mashiri, F.R., Zhao, X.L., Grundy, P. and Tong, L. 2002. Fatigue design of welded very thin-walled SHS to-plate joints under in-plane bending. *Thin Walled Structures*, 40, pp.125-151.
- Mashiri, F.R., Zhao, X.L., Hirt, M.A. and Nussbaumer, A. 2007. Size effect of welded thin walled tubular joints. *International Journal of Structural Stability and Dynamics*, 7(1), pp.101-127.
- Neimi, E., Fricke, W. and Maddos, S. 2004. *Structural Stress Approach to Fatigue Analysis of Welded Components Designer's Guide*. International Institute of Welding, Springer, Singapore.
- Rizzo, C.M. and Codda, M. 2010. Application of the structural stress approach to a welded joint with complex geometry. *Welding International*, 24(5), pp.390-400.
- Saini, D.S., Karmakar, D. and Chaudhuri, S. 2016. A review of stress concentration factors in tubular and non-tubular joints for design of offshore installations. *Journal of Ocean Engineering and Science*, 1, pp.186-202.
- Sinha, R., Liang, V.C., Paredis, C. and Khosla, P. 2000. Modeling and simulation methods for design of engineering systems. *The ASME Journal of Computing and Information Science in Engineering*, 1(1), pp.84-91.
- Stupkiewicz, S. 2003. Augmented Lagrangian Formulation and Sensitivity Analysis of Contact Problems. *VII International Conference on Computational Plasticity*, Barcelona.
- Tong, L., Xu, G., Yan, D. and Zhao, X.L. 2016. Fatigue tests and design of diamond bird-beak SHS T-joints under axial loading in brace. *Journal of Construction Steel Research*, 118, 49-59.
- Wingerde, A.M. 1992. The fatigue behavior of T and X-joint made of square hollow sections. *Heron*, 37(2), pp.3-182.
- Zhao, X.L., Herion, S., Packer, J.A., Puhtli, R.S., Sedlacek, G., Wardenier, J., Weynand, K., Wingerde, A.M. and Yeomans, N.F. 2001. *Design Guide For Circular and Rectangular Hollow Section Welded Joints Under Fatigue Loading*. TÜV-Verlag GmbH, Germany.

High Security and Capacity of Image Steganography for Hiding Human Speech Based on Spatial and Cepstral Domains

Yazen A. Khaleel

Department of Software Engineering, Faculty of Engineering, Koya University,
Danielle Mitterrand Boulevard, Koya KOY45, Kurdistan Region – F.R. Iraq

Abstract—A new technique of hiding a speech signal clip inside a digital color image is proposed in this paper to improve steganography security and loading capacity. The suggested technique of image steganography is achieved using both spatial and cepstral domains, where the Mel-frequency cepstral coefficients (MFCCs) are adopted, as very efficient features of the speech signal. The presented technique in this paper contributes to improving the image steganography features through two approaches. First is to support the hiding capacity by the usage of the extracted MFCCs features and pitches extracted from the speech signal and embed them inside the cover color image rather than directly hiding the whole samples of the digitized speech signal. Second is to improve the data security by hiding the secret data (MFCCs features) anywhere in the host image rather than directly using the least significant bits substitution of the cover image. At the recovering side, the proposed approach recovers these hidden features and using them to reconstruct the speech waveform again by inverting the steps of MFCCs extraction to recover an approximated vocal tract response and combine it with recovered pitch based excitation signal. The results show a peak signal to noise ratio of 52.4 dB of the stego-image, which reflect a very good quality and a reduction ratio of embedded data to about (6%–25%). In addition, the results show a speech reconstruction degree of about 94.24% correlation with the original speech signal.

Index Terms—Image steganography, Mel-frequency cepstral coefficients, Speech reconstruction.

I. INTRODUCTION

Steganography is the science of hiding covert information in a cover public media without attracting attention. Modern steganography methods use the characteristics of digital media using them as carriers (covers) to hold secret information. Covers can be different types including text, speech/audio, image, and video. Thus, the sender embeds

secret data in a digital cover file using a key to generate a stego-file, in which that an observer cannot feel the existence of the hidden message (Cox, et al., 2008).

The name of the steganography method depends on the type of cover media file used for hiding the secret data (such as image steganography, audio steganography, and video steganography) (Saroj, and Dewangan, 2018).

Many state of art algorithms have been suffering from the capacity storage area of the host image, low security, and robustness. This paper proposes a new technique in image steganography type, in which a secret speech signal is to be hidden inside a digital color image as a cover media. The most two common challenges that facing any steganography techniques are: How can increase the capacity of the host cover image to embed as much as possible secret data and in the same time, and how the unauthorized persons cannot distinguish the presence of hidden message.

This work contributes to develop in these both two challenges mentioned above. As it does not depend on directly hiding all the speech signal samples inside the digital image, it rather extracts some important features from the speech signal and embeds them inside the digital image.

On the authorized person side that receives the stego-image, the algorithm will extract the confidential information (features) from the transmitted stego-image. Then, these returned features will be used to reconstruct the speech clip again by reversing the steps of getting these features and then merging the result with an excitation frequency (Pitch) to get back the speech clip again. These features are called Mel-frequency cepstral coefficients (MFCCs). The usage of MFCCs features as data to be hidden rather than all the samples of the speech signal themselves. This means decreasing the amount of the data to be embedded. The reduction ratio depends on the time width of the frames chosen during the MFCCs extraction process (will be discussed later). The method of hiding the extracting MFCCs features inside the cover digital image will exploit the all bits in the three digital color image components (Red, Green, and Blue) rather than using only the least significant bits (LSBs) or the bits in the image edges as traditionally done

ARO-The Scientific Journal of Koya University
Volume VIII, No.1 (2020), Article ID: ARO.10670, 12 pages
DOI: 10.14500/aro.10670

Received: 28 April 2020; Accepted: 22 June 2020

Regular research paper: Published: 28 June 2020

Corresponding author's email: yazen.adnan@koyauniversity.org

Copyright © 2020 Yazen A. Khaleel. This is an open-access article distributed under the Creative Commons Attribution License.



in most image steganography approaches. This technique will increase the hiding capacity of the cover image.

Many articles consider the image steganography to hide the human speech signal as the secret information. Saroj and Dewangan (2018) presented a method to hide the audio secret data in image with multilevel protection using LSB techniques. Their technique implements hybrid audio steganography which hides the audio information by encrypting in multiple levels and embed into the variable LSB's of the selected samples based on polynomial expression as a function of audio and image cover file. Sharma (2015) proposed a method works by hiding sequence of speech signal elements in an image by varying the y dimension of the image while keeping x and z dimension of the image as constant. The value of the x dimension is changed by some interval for storing next speech signal elements. For the varied value of x dimension, y dimension is varied across the same interval as above whereas z dimension is constant here the next sequence of speech signal elements is saved.

Nipanikar, Deepthi and Kulkarni (2017) proposed a method for image steganography using sparse representation, and an algorithm named particle swarm optimization (PSO) algorithm for effective selection of the pixels for embedding the secret audio signal in the image. PSO-based pixel selection procedure uses a fitness function that depends on the cost function. Cost function calculates the edge, entropy, and intensity of the pixel for evaluating fitness.

In this work a new method for speech hiding and reconstruction is developed, based on the model of speech production. Section II briefly reviews the speech model parameters, cepstral analysis, and MFCCs that need to be extracted from the speech signal. Section III considers the methodology of the proposed approach. Results, evaluation of the steganography and speech reconstruction is presented in Section IV and a conclusion comes in Section V.

II. CEPSTRAL ANALYSIS AND MFCCS

The excitation vocal signal which is generated by the human vocal cords is filtered by the shape of the vocal tract that includes the fauces, tongue, and teeth. This shape specifies what sound comes out. If it can determine the shape accurately, this could give an accurate representation of the phoneme being generated. The form of the vocal tract appears within the envelope of the speech power spectrum. Fig. 1 and equation (1) represent the human voice speech model $s(n)$.

$$s(n) = e(n) * v(n) \tag{1}$$

Where $e(n)$ is the glottal excitation signal represents the signal which is produced by the vocal cords. It is periodic pulses with a relatively high frequency in its spectrum $E(k)$. The $v(n)$ represents as the impulse response of the vocal tract which has low frequency spectrum $V(k)$ compared with the excitation signal frequency. The shape of the vocal tract is unique for every human that gives the

person his/her voiceprint. It is referred to as the filter with a relatively smooth frequency response $V(k)$ that specifies what sound comes out and the person voiceprint. Then, the speech features should be extracted from $V(k)$ rather than $E(k)$. Therefore, two components of $S(k)$ are combined (convolution) together and should be separated into two components $E(k)$ and $V(k)$. The Fourier transform of $s(n)$ gives $S(k)$, as shown in equation (2) below:

$$S(k) = E(k) \cdot V(k) \tag{2}$$

If the components were combined in the convolution, no clear results would be got after using a filter as these two components in the frequency domain (spectrum) are multiplied (nonlinearly combined).

Now, it is necessary to transform the *Spectrum* into a new domain called "Cepstrum" or new frequency domain called "Quefrequency domain" that represents a transformation on speech signal with two important properties:

- 1) The two signal components will be separated.
- 2) The components will be linearly combined (summation of components).

By taking the logarithm of the absolute part of the spectrum, the real cepstrum domain is generated that achieves the above two properties. Equation (3) and Fig. 2 abbreviate the computation of the real cepstrum.

$$\begin{aligned} C_s(\omega) &= \log |S(k)| \\ &= \log |E(k) \cdot V(k)| \\ &= \log E(k) + \log V(k) \\ &= C_e(k) + C_v(k) \end{aligned} \tag{3}$$

The purpose of real cepstrum is to resolve the two convolved parts of the speech $e(n)$ and $v(n)$, into two additive components as in equation (4):

$$c_s(n) = c_e(n) + c_v(n) \tag{4}$$

Using a low time lifter (lifter is equivalent to filter in frequency domain) to select the vocal tract component $C_v(k)$ and eliminate the excitation one $C_e(k)$.

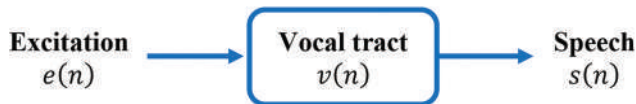


Fig. 1. Basic speech model.

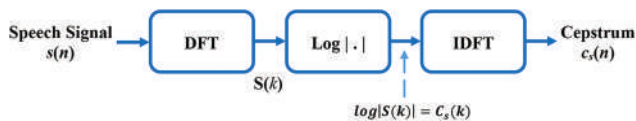


Fig. 2. Computation of the real cepstrum.

For this reason, the MFCCs are selected as good features that reflect the speech in which these features come from cepstral analysis. The job of MFCCs is to accurately represent the envelope of the speech spectrum (Huang, Acero and Hon, 2001). The motivating idea of using MFCCs is to reduce information about the vocal tract (smoothed spectrum) into a little number of coefficients.

MFCCs are features widely used in speech recognition, speaker identification, and verification. MFCCs are understood to represent the filter (vocal tract). They were presented by Davis and Mermelstein (1980).

This following introduces the MFCCs extraction steps, as shown in Fig. 3:

1. Dividing the signal into series of short overlapped time segments (frames) with width 20–40 ms.
2. Windowing each individual frame (Typically Hamming window).
3. Computing the Fast Fourier Transform for each frame and its power spectrum (periodogram).
4. Applying the Mel-frequency filter bank to the power spectra, sum the energy in each filter.
5. Taking the logarithm of all filter-bank energies.
6. Taking the discrete cosine transform (DCT) of the log filter-bank energies.

The Mel filter bank has a triangular band-pass frequency response, as shown in Fig. 4. The spacing and the bandwidth are determined by a constant Mel frequency interval. The number of Mel spectrum coefficients is 12–40, as shown in Fig. 4. The filter bank comes as vectors. Each vector is mostly zeros, but it is non-zero for a particular section of the spectrum. To calculate filter-bank energies, each filter bank is multiplied with the power spectrum, and then sum of the coefficients is numbers that show how much energy was in each filter bank. The Mel-frequency scale is a linear frequency spacing below 1000 Hz and a logarithmic spacing above 1000 Hz. Equation (5) represents the transfer function from linear to Mel frequency scale. Mel filter banks perform the sum of energy that exists in various frequency regions. The first filter is very narrow and gives a sign of how much energy exists close to 0 Hertz. As the frequencies go higher, the filters become wider because it becomes less attentive about variations (Chakroborty, Roy and Saha, 2007).

$$F(\text{Mel scaled}) = \lceil 2595 \log(1 + f(\text{Hz}) / 700) \rceil \quad (5)$$

Once the filter-bank energies is calculated, the logarithm of them is taken. Human hearing also motivates this. The

human does not hear loudness on a linear scale. In general, to double the perceived volume of a sound it must put 8 times as energy amount into it. This means that large variations in energy might not sound all that different if the sound is loud, to start with. This operation makes the extracted features match more closely what humans actually hear.

The last step is converting the log Mel spectrum coefficients back to time domain using the DCT. DCT decorrelates the features, taking the DCT of the log filter-bank energies to get the cepstral coefficients. According to the application and the accuracy required, any desired number of coefficients can be kept and neglecting the others. For example, in case of speech or speaker recognition, only 12 (2nd–13th) of the DCT coefficients are kept as they are enough for this application. In the current research, 26 coefficients per frame will be taken. A short notation can summarize the steps as in equation (6):

$$c_v = \text{DCT}(\log[\text{Mel}(\text{PSD})]) \quad (6)$$

Where c_v is the cepstral coefficients (MFCCs) associated with the vocal tract part of speech model, Mel means the Mel-Filter bank, and power spectral density (PSD) is the PSD of the speech signal (magnitude spectrum).

III. METHODOLOGY

In general, the proposed technique consists of two main parts. The first one is the analyzing a voice in terms of its pitch (fundamental frequency) and spectral envelope and then extracting the MFCCs features. These extracted features are embedded inside the cover digital color image. The second part is the recovering the hidden data (MFCCs features and the pitches) and then reconstructing (synthesizing) the speech clip.

The proposed technique is implemented using MATLAB R2019a. A speech clip of about 10 s long will be used as an example case through the following steps of the methodology:

A. Preprocessing on the Speech Signal

The first step is the enrollment of the human voice utterance. Some preprocessing steps are required and carried out such as converting the audio file to WAV format, one channel, and sampled with a sampling frequency (f_s). For example, if the speech clip is with 10 s as assumed above and sampled with 48 kHz sampling rate then the total number of samples (N) is 480,000.

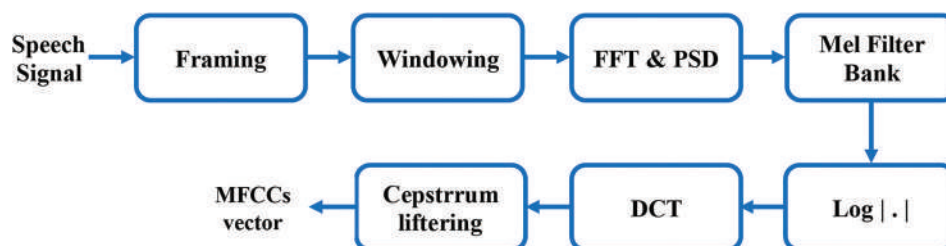


Fig. 3. Main successive steps of extracting the Mel-frequency cepstral coefficients.

B. Features Extraction

The frame width (fw) and the overlap length (ol) between the adjacent frames determine the number of frames, in which the speech signal could be segmented into. The fw is typically taken between 20 and 40 ms (30 ms is standard) which means 1440 samples per frame, and the default ol is taken $\frac{2}{3}fw$ (20 ms). The number of the segmented frames (F) can be calculated as following in equation (7):

$$F = T / (fw - ol) \tag{7}$$

For tradition values of $fw = 0.03$ s then $ol = 0.02$ s, the number of created frames will be as in equation (8):

$$F = 100T \tag{8}$$

Where T is the total time of the speech clip in seconds. Here, we can notice that the sampling rate fs does not affect the number of the obtained segmented frames.

For the selected example above, there are 1000 frames. The extraction steps of the MFCCs are applied to each frame. Then, 26 MFCCs will be returned per frame as explained in Section II. This leads that the total extracted features will be as 1000×26 matrix (26,000 features). Before the encoding step, the MFCCs features are rounded into two digits after the decimal point to simplify the quantization step. Equation (9) shows how to calculate the number of the extracted MFCCs features.

$$MFCCs = 100T M_F \tag{9}$$

Where MFCCs is total number of the Mel frequency coefficients features and M_F is the number of the coefficients per frame. A single pitch frequency (fundamental frequency represented by a series of pulses) for each time segment (frame) of the speech is also computed by the Short-Term Fourier Transform. It is included as an extra component to the features vector.

C. Encoding of the Pitch and MFCCs Features

For normal human speech of about 55 dB loudness, it is found that the dynamic range of the extracted MFCCs is

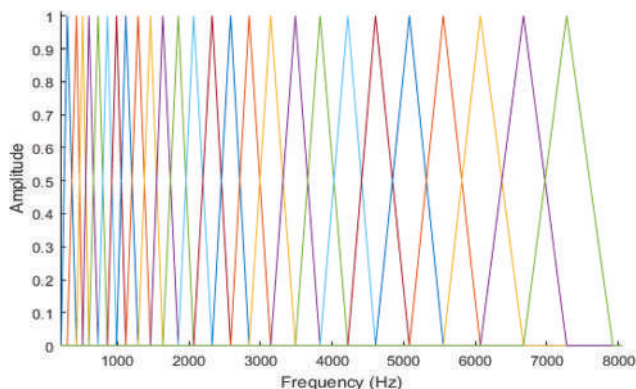


Fig. 4. Mel frequency filter-bank (Oliveira, Cerqueira and Filho, 2018).

real values usually no more than 10. This range is found by testing many speech utterances for many persons and with different time lengths. A specific lookup table (LUT) is created to encode the all-possible values of the features using 10-binary digits analog to digital conversion process with 1024 quantization levels and a resolution equal to 0.01. This means the minimum value takes the code (0000000000) and the maximum value has a code of full ones (1111111111). Table I shows a part of the LUT. By this LUT, all MFCCs features could be converted into digital form during the embedding step inside the digital cover media.

A single pitch frequency is inferred to each time frame of the speech signal. Because of the pitch frequency may take values up to about 4 kHz (human voice frequency band), then using 12 bits word in binary system to represent the pitch values.

D. Cover Color Image Preparations

A digital color image is selected to be the cover media. First, the color image is decomposed into its three components (Red, Green, and Blue), each pixel is represented by three decimal values ranged (0–255) and then the decimal numbers are converted into 8-bit binary representation. Traditional image steganography methods attempt to hide their messages directly in areas of the LSBs of the spatial domain where human visual system does not perceive. On the other hand, various image stego-analysis schemes have been developed to detect the presence of any secret messages in the LSBs area of the cover image, and then it might be easy to discover the embedded data by estimation different scenarios.

Therefore, the current research will hide the secret speech message represented by its features (MFCCs and pitches) within the higher significant bits (HSBs) and using the LSBs only to indicate the necessary information required to recover where the embedded messages. Actually, hiding

TABLE I
THE LOOKUP TABLE OF MFCCs CODING

Sequence	MFCCs	Code (using 10 Binary Digits)
1	0	0100101100
2	0	0100101100
3	0	0100101100
4	0	0100101100
5	0	0100101100
6	0	0100101100
7	0.19	0100111111
8	0.58	0101100110
9	-0.05	0100100111
10	-0.12	0100100000
11	0.56	0101100100
12	2.71	1000111011
⋮	⋮	⋮
25999	0.12	0100111000
26000	0.19	0100111111

MFCCs: Mel-frequency cepstral coefficients

the secrete data within the HSBs will not increase the capacity of the cover image, but it improves the security of the steganography process. The information hidden in the LSBs is meaningless and useless if it falls into the hands of unauthorized persons. Only the target person has the key of how to use this information inserted in the LSBs to cover up the secret data from the HSBs.

Before the hiding process, a virtual spatial framing of the cover image should be done. Each of the three components of the cover digital image is divided into equally square

frames (10×10 pixels' sub images). After that, each frame is reshaped to be 1×100 vector. Each decimal pixel value in the frame is converted to its 8-bit binary representation. Then, a new digital array form is created with dimensions 8×100 that can be named binary frame panel (BFP), as shown in Fig. 5.

E. Secrete Data Hiding

The hiding process used in this research made modifications to the method presented by Abdulraman,

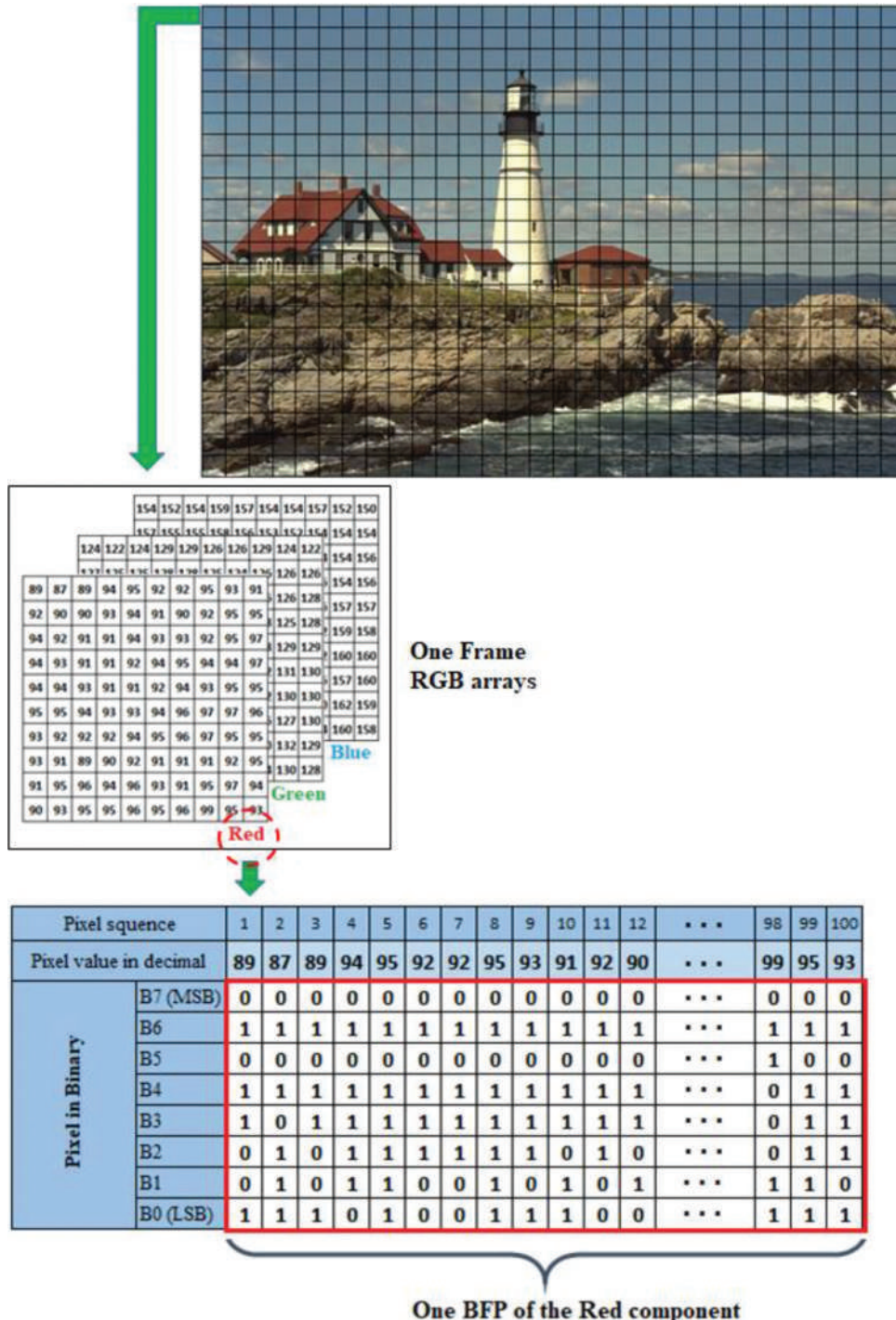


Fig. 5. Cover color image preparations and binary frame panel creation.

et al. (2019). These modifications help to increase the hiding capacity and reducing the number of unused bits. The hiding steps begin in the red array component of the color image by taking the first MFCC feature (10-bit word) and make searching inside the first BFP rows. The searching starts from the 1st row of the BFP up to the 7th row and leaving the 8th row (LSBs row) for indication. The searching tries to find any match between the ten-bit of the first MFCC feature and any 10-bit combination in this row. If the searching process does not find the similar word in first 10 bits, it will continue the searching by shifting one bit to the right to compare with a next 10-bit combination and so on until the end of the whole BFP. For the result of searching, there are two possibilities, either can find an exact similar 10-bit combination or cannot find any match in that BFP.

The LSB row (last row) of each BFP is virtually divided into nine indication segments. Each one consists of 11 bits that means 99 bits are used for the indication and leaving the last bit unused. Each segment is dedicated to indicate information about one MFCC feature where the exact match is found. This leads to ability of hiding at most

nine successive MFCCs features per BFP. In case an exact matching is found, then logic 1 is assigned to first bit of the first segment, this bit is named the matching bit. The next three bits represent the row number (in binary), where the exact similar 10-bit combination is located. The last seven bits are used to record the column number (in binary) in the BFP where the exact 10-bit combination starts from. Fig. 6a shows the matching case.

If no exact word is found, then logic 0 is assigned to the matching bit of the first indication segment. Fig. 6c shows all the nine indication segments per one BFP. Now, the 10-bit MFCC themselves are directly copied into the rest ten locations of the segment. These steps are repeated for all other MFCCs feature and so on. Fig. 6b shows the no matching case. This procedure continues to hide at most nine successive MFCCs features per BFP. At the end of hiding 26 MFCCs (features of 1-time frame of the speech signal) using three BFPs, nine features in both 1st and 2nd BFPs, respectively, and the rest eight features in the 3rd BFP. The last 12 bits of the third BFP remains and it is dedicated to insert the pitch frequency binary value of that time frame represented by 12-bits binary number. The same steps are carried out to hide

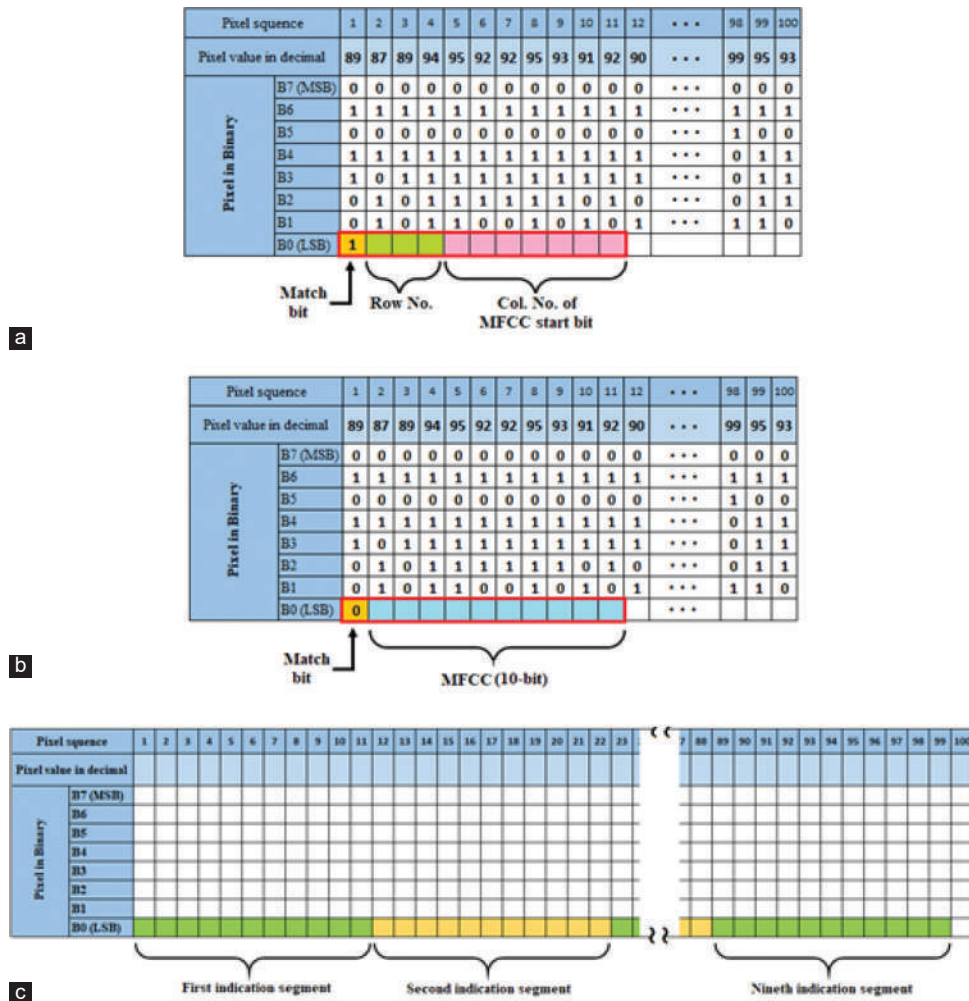


Fig. 6. The indication segment details (a) in case of full matching is found (b) in case of no matching is found (c) indication segments per binary frame panel.

all the extracted features using the three image arrays. Last information has to be embedded which is the speech signal time period in seconds (T) that is represented by 12-bit that helps in the recovery side to know the number of embedded MFCCs. The proposed method suggests inserting this data in the last 12 bits of LSB row in the last BFP of the blue array. Fig. 6 shows the indication segment details. Fig. 7 shows the over view of the proposed methodology.

It is worth noting the following points:

- In one row, it can hide more than one feature word, and on the other hand, it may not be possible to find any match within it. In one row, there are 91 possibilities of 10-bit combinations and then 637 possibilities per BFP.

- The same 10-bit combination in a BFP can be reused for hiding more than one feature word.
- Preserve the sequence of the MFCCs features during the embedding process is essential.
- The selected cover image should be able to accommodate all MFCCs features and the pitches. Each three BFPs can provide indication for 1-time frame features (26 MFCCs + 1 Pitch). For the suggested example above, there are 1000 segmented time frames that need 3000 virtual BFPs in the cover image. Because of using a color image (three arrays), then 1000 BFPs are required per a component array. The square image frame has 100-pixel resolution N_p (10×10), then it needs a cover color image with a pixel's resolution no $< 100,000$. In general, the color image resolution can be determined by the suggested formula in equation (10):

$$RES_{req} \geq \frac{3TN_p}{3(fw-ol)} \quad (10)$$

Where, RES_{req} is the minimum required resolution of the cover image (number of pixels in an image = height pixels X width pixels), T is the duration of the speech signal (s), N_p is the number of pixels per square image frame, fw is the time frame width (s), and ol is the overlap length (s) between adjacent time frames.

The users usually deal with the utterance period (T) in seconds and the cover color image resolution, then, using the tradition values such as $N_p = 100$, $fw = 0.03$ s, and $ol = 0.02$ s, then the minimum required resolution is $TRES_{req} \geq 10,000 T$ and the maximum speech duration T_{max} can be hidden in a specific color image with resolution (RES) can be calculated as:

$$T_{max} \leq \frac{RES}{10000} \quad (11)$$

Increasing the image resolution with about 10% could be suggested and encouraged to enhance and ensure the accommodation capacity. Here in MFCCs based proposed technique, both the minimum required resolution and T_{max} do not depend on the sampling frequency.

For direct speech samples embedding technique, (direct_based) the minimum required resolution (RES_{req}) to hide a specific speech signal with duration time t can be calculated as in equation (12).

$$RES_{req} \geq \frac{10 \times T \times F_s}{3} \quad (12)$$

Or the maximum duration (T_{max}) of a speech clip can be embedded in a specific color image as in equation (13).

$$T_{max} \leq \frac{3RES}{10F_s} \quad (13)$$

In the direct_based technique, both the minimum required resolution and T_{max} depend on the sampling frequency value.

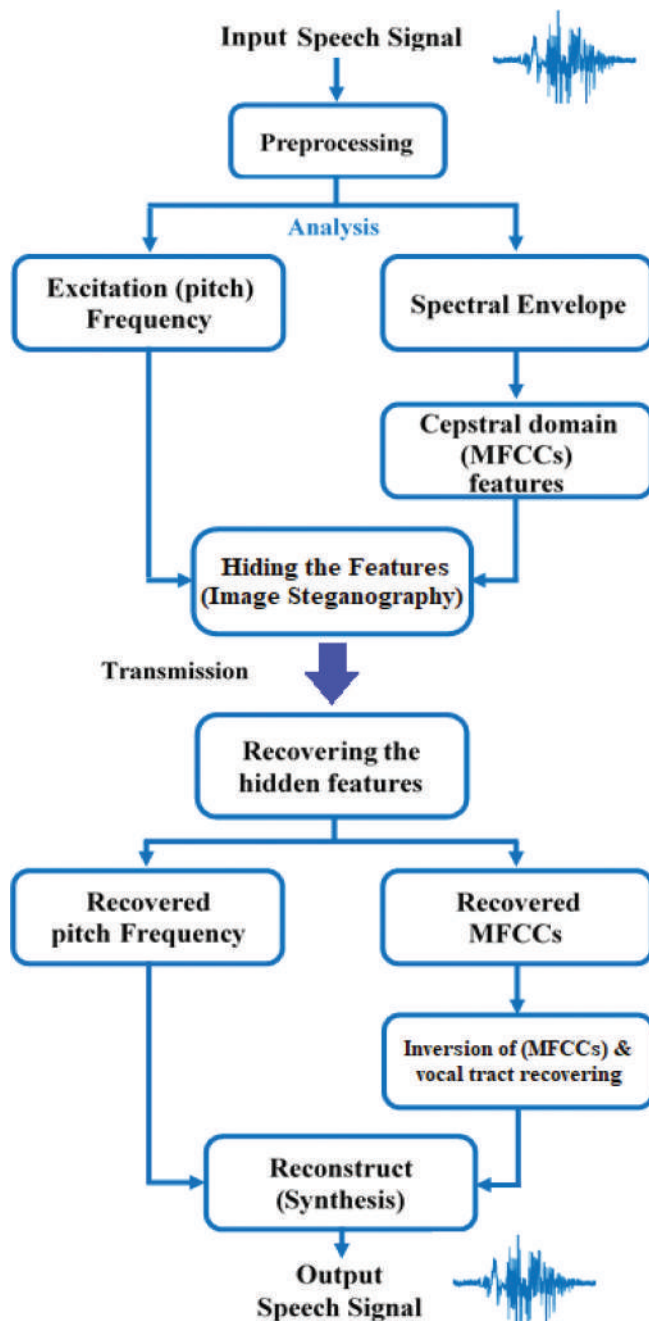


Fig. 7. Over view of the proposed methodology.

Concerning to the *accommodation bit capacity*, in the tradition direct_based steganography, when all the samples of the speech signal are required to be embedded directly behind the cover media. At least, if each sample is digitized by 10-bit and using sampling frequency fs , this leads the total number of bits ($Nbit$) in the digitized speech ($Nbit$) is as in equation (14):

$$Nbit = 10T fs \quad (14)$$

Where 10 means ten bits per sample. For example, If fs is taken as 48 kHz, then $Nbit = 480000 T$.

For the introduced method, $Nbit$ can be calculated through equation (15):

$$Nbit = [100T \times MCF \times 11] + [100T \times 12] \quad (15)$$

Where, MCF is the number of the Mel Coefficients per time Frame, $100T$ is the total number of the segmented time frames as in equation (8), 11 means the $Nbits$ required per MFCC, and 12 is the $Nbits$ to represent the pitch value of each frame.

The suggested value of MCF is 26, and then equation (15) will be as in equation (16):

$$Nbit \cong 30000T \quad (16)$$

By a rational comparison between the $Nbit$ in these two cases above, the required $Nbits$ to represent the speech clip is reduced to about 6–7%. In other words, the accommodation capacity of the cover image could be increased by about 16 times.

For the assumed example of 10 s utterance duration which is sampled by fs (48 kHz). This means 4,800,000 bits have to be embedded inside the cover image if a tradition steganography is achieved. By the proposed method, 300,000 bits are required to represent this 10 s speech. By simple rational comparison, it is clear that the reduction ratio of the required bits is about 6.25%. In other words, if a color cover image can hide 10 s speech signal (as maximum capacity), then by the proposed method, 160 s can be embedded in the same image size.

F. Recovering of the Secrete Data

In the receiver side, the authorized person should have the technique how to deal with information inserted in the LSBs rows in the BFPs of the received stego-image. In the recovering side, the technique implements, the same steps of image decomposition into its three components (RGB), virtual division into (10×10) frames, and creating the (8×100) BFPs. The recovering stage starts by checking all the indication segments in the rows of the BFPs sequentially one by one. Each segment provides the enough information to recover a specified feature.

If the matching bit of the segment is logic 1 (exact matching existing), then the next three bits gives the number of the row in the HSBs of the BFP that under process. The rest seven bits means the column number in BFP that the required 10-bit combination starts from.

Now, the 10-bit combination location is discovered and its contents copied into the MFCCs recovery matrix. If the matching bit of the segment is logic 0 (no exact matching was found), then the next 10 bits represent the feature word itself directly. They are also directly copied into the recovery matrix. These steps are sequentially implemented for the successive BFPs to keep the order of the MFCCs. Last 12 bits of the third BFP represent the pitch frequency value associated to the recovered MFCCs features. The previous steps in the recovering stage are repeated for the whole BFPs sequentially to recover all the embedded features (MFCCs and their associated pitch frequencies). At the end of the recovering process, all recovered MFCCs features are stored in a specific matrix called (MFCCs recovery matrix). This matrix is a set of MFCCs column vectors; each column vector represents the features of 1-time frame. All recovered pitch frequencies are kept in another vector called (recovery pitch vector). The MFCCs and their related pitches are converted back to the decimal values. The conversion of the MFCCs is done using the same specific LUT in Table I that has to be provided to the recovering side.

G. Magnitude Spectrum Recovering

The recovered MFCCs features are used to re-build the vocal tract filter. This is achieved by reversing the MFCCs back to a smoothed magnitude spectrum using an IDCT and anti-Log (exponential) operation. The required excitation signal is generated from the series of the recovered pitch pulses. This enables the location of the spectral peaks (main formants) in the speech model to be determined. The amplitudes of the peaks were determined from the smoothed spectral.

As shown in Fig. 3, the process by which the MFCCs features are extracted from a speech signal has a number of invertible steps. It is possible to make certain approximations to the information that has been discarded to allow an inverse to be calculated (as the phase c/cs is lost).

The first stage of inverting the MFCCs vector into a magnitude spectral representation needs a logarithmic filter-bank vector. An inverse DCT to be computed as in equation (17):

$$\log C_v(k) = \sum_{n=0}^{K-1} c_v(n) \cos \left[\frac{(2k+1)n\pi}{2K} \right] \quad (17)$$

Where K is the number of the Mel filter-bank channels (in this work, is 26).

Equation (17) gives a smoothed of the logarithmic filter-bank vector. The log operation can be reversed, by the using of the exponential operation, and gets the Mel-filter-bank vector. Again, by a short notation, the recovering of the vocal tract frequency response can be in the reverse direction of equation (6) and as in equation (18) below:

$$\widehat{PSD} = Mel^{-1} [10^{IDCT(c_v)}] \quad (18)$$

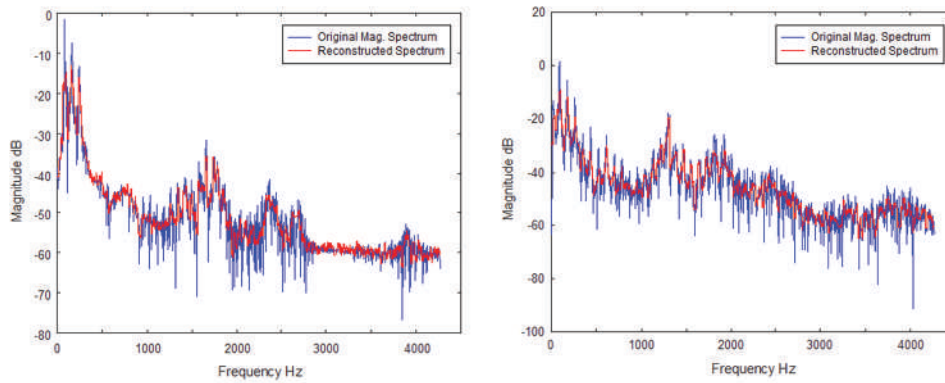


Fig. 8. Two randomly selected recovered magnitude spectrum versus original one.



Fig. 9. The steps of vocal tract recovering.

Where \widehat{PSD} refers to the recovered PSD (estimated magnitude spectrum).

Fig. 8 shows two random recovered magnitude spectrums in red line versus original one in blue line.

The area under the triangular filters is used in the Mel-filter-bank analysis increases at the upper frequencies. The effect of this is to impose a high frequency deviation on the resulting Mel-filter-bank channels which make distortion in the generated magnitude spectrum. This deviation can be canceled in the frequency domain by scaling the Mel-filter-bank outputs, by the area of the corresponding triangular Mel-filter.

H. Vocal Tract Recovering

The vocal tract filter coefficients can be computed using Wiener-Khinchine theorem (Kleijn and Paliwal, 1995) that relates the autocorrelation coefficients to the PSD using IFF. The excitation signal is easily reconstructed using a series of the recovered pitch pulses. A suitable value for gain can be added from the log energy element of the feature vector. The steps of vocal tract recovering are shown in Fig. 9.

I. Speech Reconstruction

The recovered vocal tract and the pitch-based excitation signal are merged to reconstruct the speech signal using equation (1). The over view of speech reconstruction is shown in Fig. 10.

IV. RESULTS AND EVALUATION

The evaluation of the proposed method has two lines. The first one is to evaluate the process of hiding the secret information represented by human speech clip and its impact on the host image quality. This includes the extent

of awareness of the unauthorized person of the possibility of data hidden or not. The results show the relationship of the image size with the length of the hidden speech clip and the amount of the hidden data. The second line deals with the reconstructed voice quality using the recovered features detected in the received stego-image.

As mentioned before, the direct embedding of the speech samples is a tradition method of steganography (direct_based). In this case, each sample should be converted to digital form so the size of the digitized speech clip depends on the time length T and on the digitization characteristics (sampling rate f_s and N_{bits} per sample). The minimum required resolution of the host image should follow the threshold value mentioned in equation (12) to hide a specific length of speech. In the same time, the maximum length of the speech has to satisfy equation (13) in case of using a specific cover image that has a limited hiding capacity.

Testing the image quality after the steganography is done by both eyes vision tests and by measuring the value of the peak signal to noise ratio (PSNR). The signal in this case is the original host image, and the noise is the bits introduced through the embedding steps. PSNR is an approximation to human perception of image quality. First, the PSNR is measured for the direct_based method. A color host image with 0.62 Mb resolution (720×900) is chosen to hide a speech clip. According to equation (13), the maximum loading of this image is about 16 s speech signal duration if the sampling frequency equal 12 kHz.

To test other standard sampling frequency values (24 kHz and 48 kHz), another larger image is required. Therefore, a color image with 2.3 MB resolution (1080×2240) is selected. Fig. 11a shows the PSNR for different partial and full loadings of speech duration time (25%, 50%, 75%, and 100%). As clear from the figure, the sampling frequency in direct embedding method has a great effect on the selected cover image size and on the time length of the speech that to be inserted in the host image. Doubling the sampling rate leads necessarily to reduce the speech time to the half or duplicating the image size. However, the most noticeable thing in Fig. 11a is for one ratio of speech loading, the PSNR values are almost equal regardless to the sampling frequency.

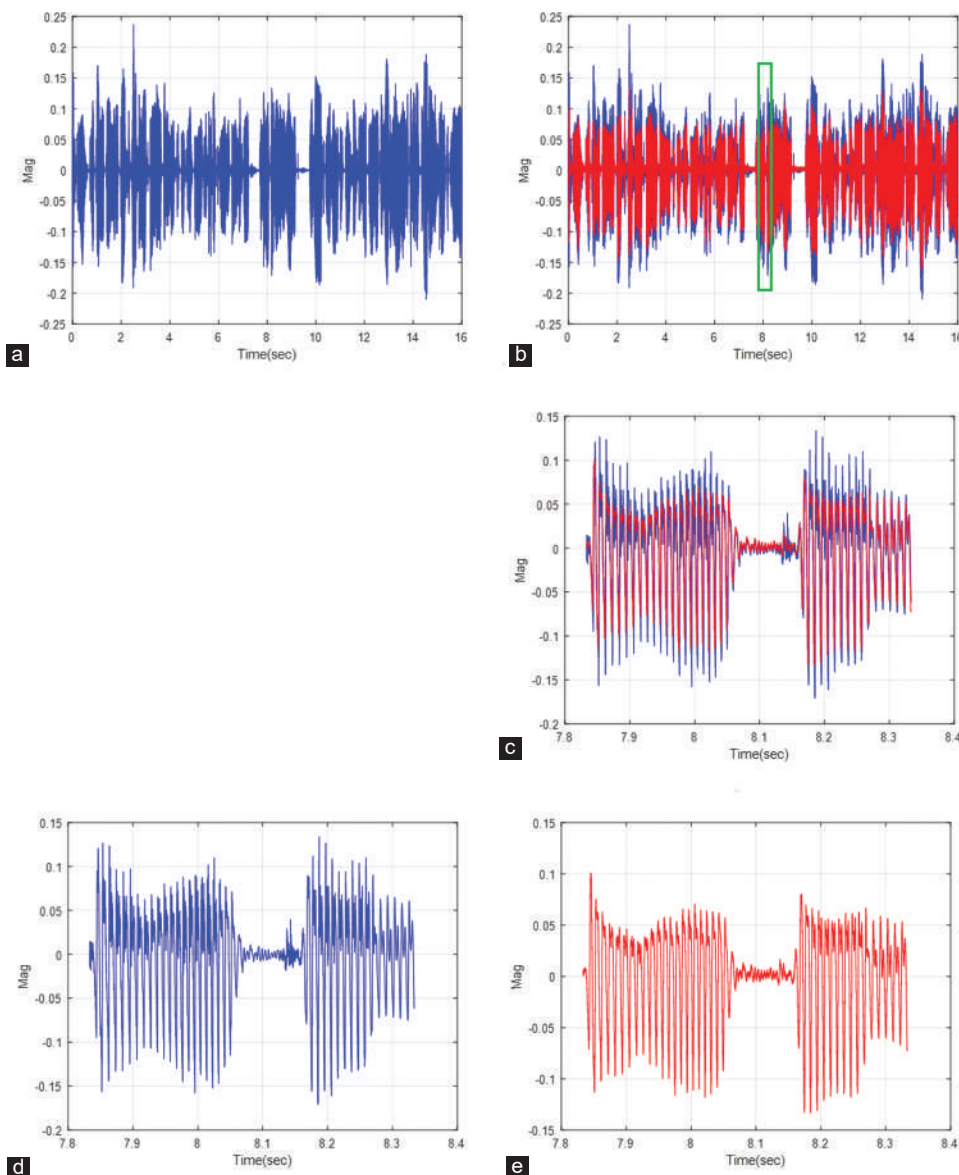


Fig. 10. Over view of speech reconstruction. (a) The original speech signal, (b) both original speech signal (blue line) and the recovered speech signal (red line), (c) zoom in for both original signal (blue line) and the recovered signal (red line), (d) zoom in for original speech signal, (e) zoom in for recovered signal.



Fig. 11. (a) Peak signal to noise ratio (PSNR) for the direct based method of hiding. The legend includes the sampling frequency, max speech duration, and host color image resolution in Mb, respectively. (b) PSNR for the Mel-frequency cepstral coefficients based on proposed method of hiding for three standard values of sampling frequency.

Concerning to the evaluation for the proposed method of hiding the secret data using the MFCCs features (MFCCs_based) rather than all clip samples. The same color host

image is chosen again that has size 2.3 Mb (720 × 900). For this case and according to equation (11), a speech of about 64 s can be full loading this image, that is, 4 times more than if the direct way to hide the samples is used. Fig. 11b shows the PSNR for different partial and full loading (25%, 50%, 75%, and 100%) using three normally used sampling rates (12 kHz, 24 kHz, and 48 kHz). The same observation appears in which the PSNR values for one speech-loading ratio are almost equal regardless to the used sampling rate.

Fig. 12 shows the original host image and the stego-image of full capacity speech loading using the proposed technique (MFCCs_based). It is clear that no major vision effects are appearing in the stego-image compared with original one.

Relating to the *Nbits* represents the all secret data that are used in the hiding process. *Nbits* has effects on the stego-

image quality. Table II and Fig. 13 show the difference in the *Nbits* for both techniques of the data hiding, the direct_based

TABLE II
NBITS USED IN BOTH DIRECT AND MFCCs TECHNIQUES

Speech time duration (s)	Nbits (Mb) (Direct_Based)			Nbits (Mb) (MFCCs_Based)
	fs 12 kHz	fs 24 kHz	fs 48 kHz	Any fs
10 s	1.2	2.4	4.8	0.3
20 s	2.4	4.8	9.6	0.6
30 s	3.6	7.2	14.4	0.9
40 s	4.8	9.6	19.2	1.2
50 s	6	12	24	1.5
60 s	7.2	14.4	28.8	1.8
70 s	8.4	16.8	33.6	2.1

MFCCs: Mel-frequency cepstral coefficients, Nbits: Number of bits

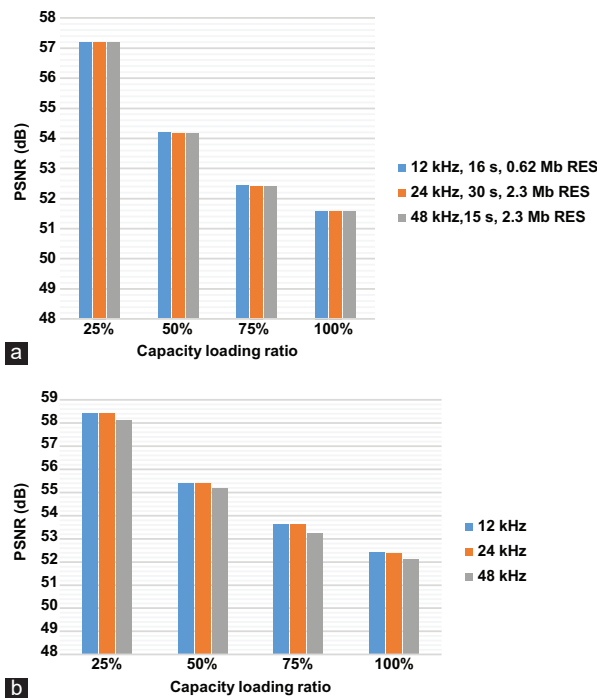


Fig. 12. (a) Original host color loading image. (b) Stego-image after full capacity speech signal loading.

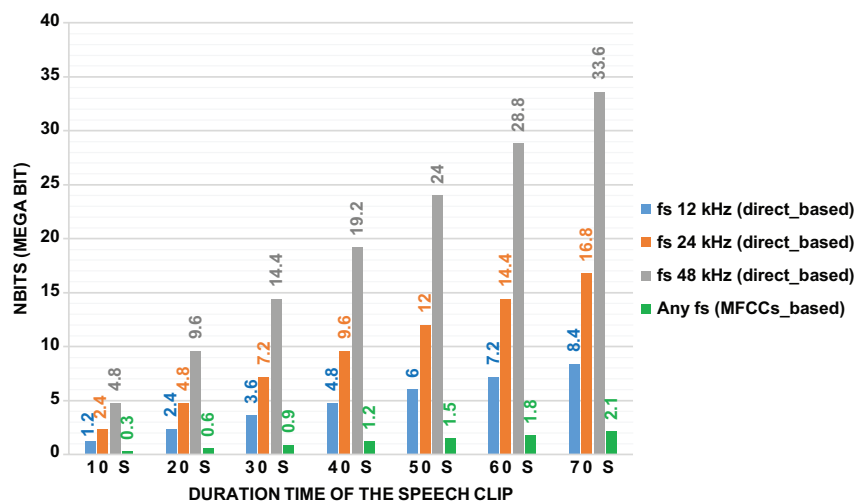


Fig. 13. Number of bits with respect to the speech duration time for different sampling rates.

hiding of all samples, and the MFCCs_based hiding. The results shown in Table II are got using equations (14) and (16). In the direct hiding technique, the *Nbits* very related to both of the value of the sampling frequency and on the speech duration time, whereas the proposed MFCCs_based hiding depends only on the duration and the sampling rate has no effect on the *Nbits* used in the hiding process. The *Nbits* also affect on the time required of the hiding and recovering processes.

The reduction ratio in *Nbits* using the proposed MFCCs_based is within (6.25%–25%).

The second line of the evaluation for the proposed technique is the rating of the quality for the reconstructed speech compared with the original one. Listening tests show that clear and very acceptable speech signals were produced. Fig. 8 shows both the recovered magnitude spectrum and that computed from the original speech signal for two random selected time frames. The magnitude spectrum estimated directly from the original frames is shown as the blue line whereas the magnitude spectrum got from the recovered MFCCs and pitches vectors is shown as the red line. The figures also show that the envelope of the magnitude spectrum has been reasonably well conserved. Some problems may appear where the magnitude spectrum gives formants merging into a single peak.

The comparison is also done by measuring the correlation coefficient between the original speech signal and the reconstructed one. Fig. 14 shows the correlation coefficients versus different number of extracted MFCCs from the speech signal to be embedded inside the cover image. The high number of the MFCCs leads to higher *Nbits* and then needing bigger image size or less speech time duration besides increasing the time required for the process. The selected number of MFCCs equation (26) is the best choice that corresponds to the requirements of the process in terms of the amount of data, the accuracy of the results (gives a correlation coefficient 94.24%), and the time required for the execution of the steps.

Table III presents a comparison between the proposed MFCCs based technique with some other existing models.

TABLE III
COMPARISON BETWEEN THE PROPOSED MFCCs BASED TECHNIQUE WITH SOME OTHER EXISTING MODELS

Method	Used domain	Host media	Secrete data	PSNR (dB)
(Nipanikar, Deepthi and Kulkarni, 2017)	DWT	Digital Gray Image	Speech signal	47.6
(Saroj and Dewangan, 2018)	Spatial and DCT	Digital Color Image	Audio signal	-
(Sharma, 2015) 28	Spatial	Digital Color Image	Speech signal	-
(Abdulraman, et al., 2019)	Spatial	Digital Gray Image	Text	51.9
(Jamel, 2019)	DWT	Digital Gray Image	Digital Gray Image	36.84
(Navas, Thampy and Sasikumar, 2008)	Integer WT	Digital Gray Image	Patient's records	44
(Al-Qershi and Khoo, 2011)	DWT	Digital Gray Image	Patient's records	41.25
Proposed MFCCs based technique	Spatial and Cepstral	Digital Color Image	Speech signal	52.41

MFCCs: Mel-frequency cepstral coefficients, PSNR: Peak signal to noise ratio

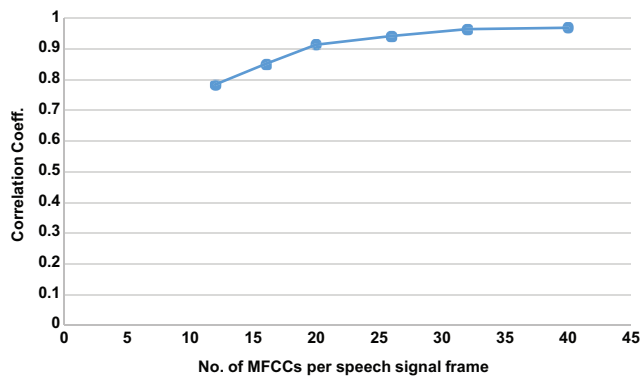


Fig. 14. The correlation coefficient with respect to the number of extracted Mel-frequency cepstral coefficients per speech frame.

V. CONCLUSION

This work presented a proposed technique of human speech signal hiding in a color cover digital image. The proposed technique introduces solutions for some challenges facing the steganography process, such as increasing the security of sending the secrete data, reducing the amount of the hidden data, and increasing the capacity of the host image. The presented method depends on sending the MFCCs features plus additional information relating the excitation signal and speech duration that should be inserted with the features. The speech reconstruction is possible from a stream of the recovered features using a model of speech production. Sending the speech features rather than the whole samples of the speech signal is the main reason to reduce the amount of the embedded data and can increase the security as well. The method used to hide the confidential data depends on including it in the host image at the higher significant levels and not as in the traditional methods do at the least significant levels. The most noticeable conclusion here that in the MFCCs_based steganography, the value of the sampling rate f_s used in the speech digitization has no effect on the loading percentage inside the host image. Another conclusion, that for a specific speech-loading ratio, the PSNR is invariant with the change of the sampling frequency used. The possible MFCCs can be extracted from a speech signal which can be between 12 and 40. Therefore, it is concluded that 26 MFCCs is an optimal choice that considers both the low data amount and acceptable speech reconstruction degree with about 94.24%

correlated with the original speech. If high number of MFCCs is used, better-quality speech reconstruction is possible from the MFCCs despite the missing of phase information in MFCCs_based steganography but with more hidden data, lower PSNR, and longer time of processing. The amount of the hidden data depends only on the duration time of the speech signal not on the sampling rate as in the direct method.

REFERENCES

- Abdulraman, L.S., Hma-Salah, S.R., Maghidid, H.S. and Sabir, A.T., 2019. A robust way of steganography by using blocks of an image in spatial domain. *Innovaciencia*, 7(1), pp.1-7.
- Al-Qershi, O.M. and Khoo, B.E., 2011. High capacity data hiding schemes for medical images based on difference expansion. *Journal of Systems and Software*, 84(1), pp.105-112.
- Chakroborty, S., Roy, A. and Saha, G., 2007. Improved closed set text independent speaker identification by combining mfcc with evidence from flipped filter banks. *International Journal of Signal Processing*, 4(2), pp.114-122.
- Cox, I.J., Miller, M.L., Bloom, J.A., Fridrich, J. and Kalker, T., 2008. *Digital Watermarking and Steganography*. 2nd ed. Morgan Kaufmann Publishers, USA.
- Davis, S. and Mermelstein, P., 1980. Comparison of Parametric Representations for Monosyllable Word Recognition in Continuously Spoken Sentences, 28(4), pp. 357-366.
- Huang, X., Acero, A. and Hon, H.W., 2001. *Spoken Language Processing*. Prentice Hall, Inc., USA.
- Jamel, E.M., 2019. Secure image steganography using biorthogonal wavelet transform. *Journal of Engineering and Applied Sciences*, 14, pp.9396-9404.
- Kleijn, W.B. and Paliwal, K.K., 1995. *Speech Coding and Synthesis*. Elsevier Science Inc., New York, United States.
- Navas, K., Thampy, S.A., Sasikumar, M. 2008. EPR hiding in medical images for telemedicine. *International Journal of Biomedical Science*, 2(1), pp.292-295.
- Nipanikar, S.I., Deepthi, V.H. and Kulkarni, N., 2017. A sparse representation based image steganography using particle swarm optimization and wavelet transform. *Alexandria Engineering Journal*, 57, 2343-2356.
- Oliveira, M.L.L., Cerqueira, J.J.F. and Filho, E.F.S., 2018. *Simulation of an Artificial Hearing Module for an Assistive Robot*. Intelligent Systems Conference, London, UK.
- Saroj, N. and Dewangan, S.K., 2018. An implementation of hiding audio secure data in images using steganography. *Journal of Emerging Technologies and Innovative Research*, 5(9), 20-25.
- Sharma, D., 2015. Steganography of Speech Signal into an Image. *Second International Conference on Recent Advances in Engineering and Computational Sciences*, USA.

Long-wavelength GaInNAs/GaAs Vertical-cavity Surface-emitting Laser for Communication Applications

Faten A. Chaqmaqchee

Department of Physics, Faculty of Science and Health, Koya University, University Park,
Danielle Mitterrand Boulevard, Koya KOY45, Kurdistan Region – F.R. Iraq

Abstract—This paper presents a comprehensive study of optical and electrical properties of vertical-cavity surface-emitting lasers (VCSELs) for long wavelength communication applications. The device consists of GaInNAs/GaAs multi-quantum wells (QWs) that are enclosed between standard top and bottom epitaxially grown on AlGaAs/GaAs distributed Bragg reflectors. The impact of driven currents and injecting optical powers through QWs layers on the output light emission is addressed. Room temperature spectra measurements are performed at various applied currents using 980 nm pump laser and maximum intensity amplitude at around 21 dB was achieved.

Index Terms—Vertical-cavity surface-emitting lasers, GaInNAs/GaAs, Light-current-voltage characterization, Optical pumping, Electrical pumping.

I. INTRODUCTION

Dilute nitride III-V alloys are becoming increasingly important for optoelectronic devices applications, such as lasers, modulators, photodetectors, and optical amplifiers for the 1.3 μm window of optical fiber communication systems. One potentially important material for such applications is the quaternary alloy GaInNAs (Kondow, et al., 1996; Buyanova, et al., 2001; Chaqmaqchee, et al., 2011) or the quinary alloy GaInNAsSb (Korpijärvi, et al., 2015; Chaqmaqchee, et al., 2020). GaInNAs may be grown pseudomorphically on GaAs, allowing the use of high-quality Al(Ga)As/GaAs distributed Bragg reflectors (DBRs) (Chaqmaqchee and Balkan, 2014), with potential cost advantages over InP-based approaches due to their electronic structure can maintain stronger carrier confinement even at high temperatures (Hetterich, et al., 2000). Whereas there is no transport problem for the electrons in the n -type bottom DBR, there is a serious problem for the holes in the p -type

DBR due to larger effective mass, resulting in high series resistance in the VCSEL structures. Such a high resistance causes a major self-heating effect and reduces the flow through the DBR. Therefore, p -type compositional graded AlGaAs/GaAs DBR is designed for a peak reflectivity at 1.3 μm to overcome the poor hole conduction through the p -type DBR layer.

Dilute nitride structures have already found applications in several devices, such as high-performance laser diodes among which are cavity surface emitting lasers vertical-cavity surface-emitting lasers (VCSELs) emitting in the 1.3 μm window. VCSEL (Chaqmaqchee, 2019; Haghighi, et al., 2018) is driven above lasing threshold and shows some very interesting advantages over edge-emitting lasers and in plane SOAs (Poza, et al., 2008). The vertical cavity geometry for such devices yields high coupling efficiency to optical fiber which is useful for achieving a low noise figure. It also allows for on chip testing techniques, single wavelength amplification, and two-dimensional array fabrication, hence lowering the power consumption and manufacturing cost. The narrower bandwidth of the vertical cavity structures makes the devices also good for filtering applications (Piprek, et al., 2001; Karim, et al., 2000).

The device is based on GaInNAs/GaAs material for operation in the 1.3 μm wavelength range and has increased functionality using undoped DBRs. This coupled with direct injection into the active region is expected to yield improvements in the gain and bandwidth. The design of VCSEL devices is based on the transfer matrix method for multilayer structures (Yeh, 1991;

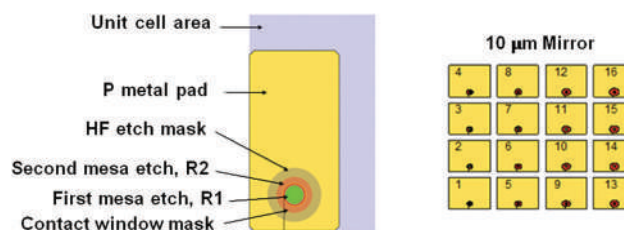


Fig. 1: Fabrication processes for vertical-cavity surface-emitting lasers (VCSELs) device including mask etch step, contact window mask and Ti/Pt/Au metallization with pad size of 120 μm \times 200 μm , and pad-to-pad metal separation 50 μm as in the right side. One set of 16 VCSEL devices with 10 μm mirrors diameters as in the left side.

ARO-The Scientific Journal of Koya University
Volume VIII, No.1 (2020), Article ID: ARO.10627, 5 pages
DOI: 10.14500/aro.10627

Received 29 January 2020; Accepted 27 June 2020

Regular research paper: Published: 30 June 2020

Corresponding author's e-mail: faten.chaqmaqchee@koyauniversity.org

Copyright © 2020 Faten A. Chaqmaqchee. This is an open access article distributed under the Creative Commons Attribution License.



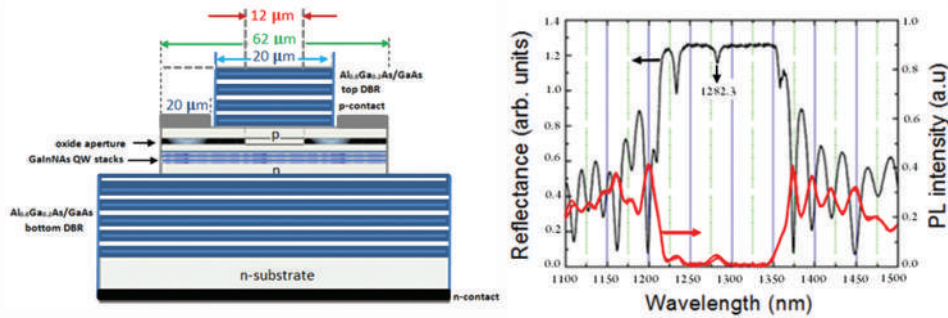


Fig. 2: The structure of the GaInNAs vertical-cavity surface-emitting laser coded G0428 with their PL intensity and reflectivity measurements at 300 K.

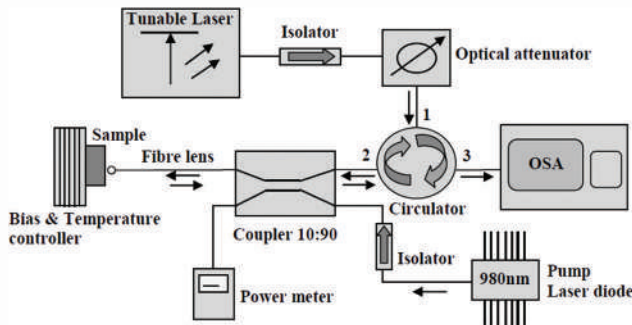


Fig. 3. Schematic of the vertical-cavity surface-emitting laser experimental setup used for optical pumping of top emitting device characterization under continuous-wave operation.

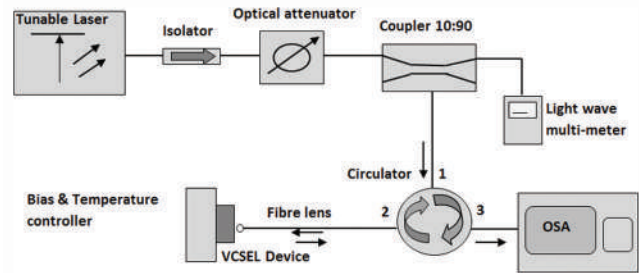


Fig. 4. The experiment setup of vertical-cavity surface-emitting laser for operation in the reflection mode through electrical pumping.

Shen, et al., 2019), and the optical field distribution within the structure, where the determination of the position of quantum wells is crucial. The operation of the devices is based on the injecting of the carriers (e-h) in their active region by the application of longitudinal electric fields. The emission light is always coming from the cathode region. However, the emitting region might be changed depending on the polarity of applied voltages (Wah and Balkan, 2004).

In this study, we have tested and demonstrated the operation of VCSEL devices based on dilute nitrides and to operate in the 1.3 μm communication windows for metro and access networks applications. Output light-current-voltage (L-I-V) at different temperatures and spectra measurements at various applied currents was achieved. In addition, peak intensities of the VCSEL, input signal, and the combined VCSEL plus input signal at a fixed bias current of 12 mA and various input signal powers from 1 to 4 mW were studied.

II. MATERIALS AND METHODS

The fabrication procedure for VCSELs required a number of lithography steps, including etch steps to facilitate wafer bonding structure. In the first mesa mask, the planned radii are 10 μm and 15 μm . In the second mesa mask, the planned radii are from 20 μm to 36 μm with step 1 μm . The total number of photolithography steps for all the devices could be reduced by combining the SiO_2 or Si_3N_4 hard mask etch steps, including the contact window definition. Finally, a multilayer metallization system of titanium-platinum-gold (Ti/Pt/Au) was used. Titanium is used to promote adhesion between substrates

and sputtered gold films, which can diffuse up to the gold surface after annealing and then degrade the wire bondability (Harman, 1997). The proposed pad size is 120 $\mu\text{m} \times 200 \mu\text{m}$, where pad to pad metal separation is around 50 μm . As depicted in Fig. 1, there are nine different sets of 16 devices, each set has a fixed mirror diameter (first mesa etch) of 10 μm and 15 μm , with etching of the confinement layer which was fabricated and each set has marked the above device. The radius of the second, electron confinement mesa (mesa 2) is different for each device within the set; therefore, the radius (R) and the diameter (D) of mesa 2 can be calculated by $R=20 \mu\text{m}+\{\text{Device Number}\}$ and $D=2 \times R$ respectively.

Fig. 2 shows the GaInNAs/GaAs VCSEL structure including three elements. The bottom DBR mirror constitutes 24 pairs $\text{Al}_{0.98}\text{Ga}_{0.02}\text{As}/\text{GaAs}$ resulting in over 99.9% reflectivity. The top DBR mirror consists of 21 pairs of undoped $\text{Al}_{0.8}\text{Ga}_{0.2}\text{As}/\text{GaAs}$ quarter wavelength thick layers to provide >99% reflectivity for the optical microcavity and gain region. The choice of 0.8 and 0.98 Al content in the DBRs was to allow 0.98 Al for the oxidation layer. The gain region is made of nine QWs that are distributed equally in three stacks of 7 nm thick $\text{Ga}_{0.65}\text{In}_{0.35}\text{N}_{0.02}\text{As}_{0.98}$ QWs separated by 20 nm thick GaAs. The QWs were positioned at the antinodes of the field to provide resonant periodic gain and to maximize available gain. High gain and wider bandwidth can be achieved simultaneously by reducing the top mirror reflectivity of the device (Bjorlin, et al., 2001; Chaqmaqchee, et al., 2012). The photoluminescence PL intensity matches the cavity of reflectivity measurements at wavelength of 1282.3 nm, as shown in the right side of Fig. 2.

In general, VCSELs can be optically pumped or electrically driven. Optical pumping is usually seen as a

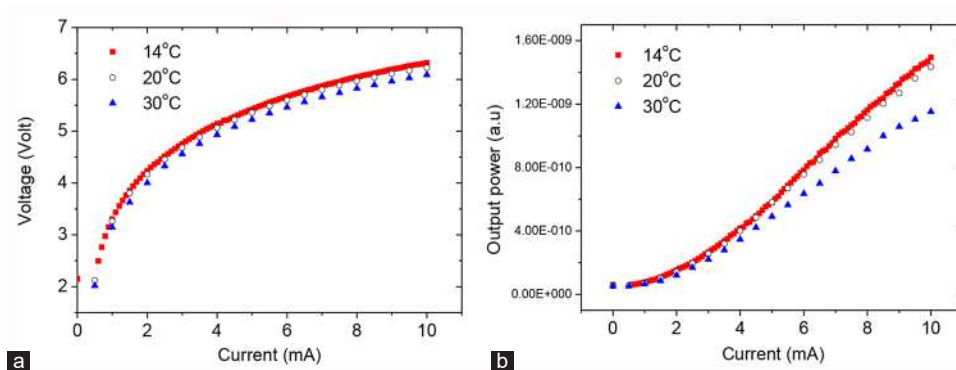


Fig. 5: Comparison of the three vertical-cavity surface-emitting laser temperatures for aperture diameter of 10 μm (a) voltage-current (V I), and (b) light-voltage (LI) characteristics under CW operation.

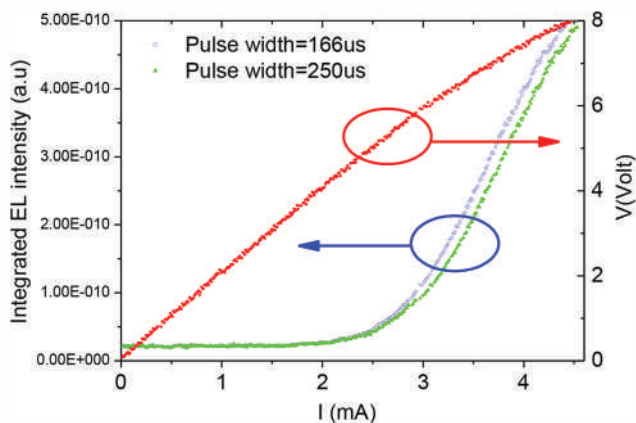


Fig. 6: Light-voltage-current characteristics of vertical-cavity surface-emitting laser under pulsed operation with aperture diameter of 15 μm and the second mesa etch diameter of 70 μm at $T=14^\circ\text{C}$.

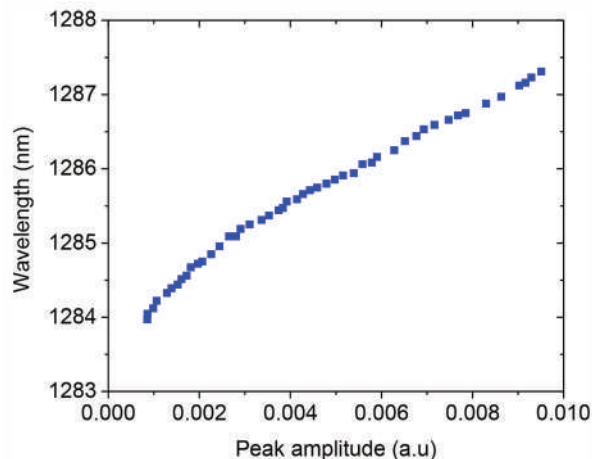


Fig. 8: Wavelength as a function of peak amplitude at room temperature.

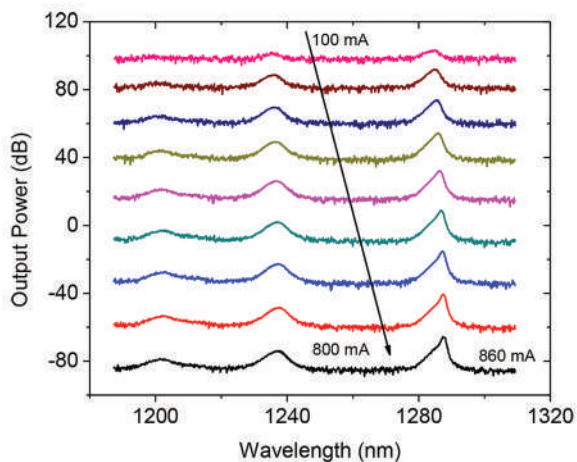


Fig. 7: The spectra of the vertical-cavity surface-emitting laser samples as a function of different applied currents between 100 and 860 mA at room temperature.

preliminary to electrical injection. The characterization of amplifiers was measured under continuous-wave (CW) pumping using the fiber-based system sketched in Fig. 3. The NI PXI-1033 tunable laser diode is used as an input signal source. The tunable laser wavelengths are varied from 1265 to 1345 nm, whereas the output power is varied

from 1 to 6 mW. The laser output power is controlled by the means of an optical variable attenuator. A single-mode fiber patch cord is used to connect one end of the isolator, and the other end is connected through an FC/APC adaptor to the port of an optical coupler, where the output power from the 90% coupler was about 85 mW to reach lasing threshold, whereas 10% split from the output power was measured on the power meter. A 980 nm fiber pigtailed single-mode diode laser (1999 PLM 980 nm pump module) is used for VCSEL excitation through a 980 nm isolator and an optical coupler. The output power from the laser is about 810 mW and is reduced to <250 mW at the sample due to the losses through fibers. The laser signal passes through an isolator to prevent reflections and instabilities. The long focus fiber (with radius of 8 μm) is brought very close to the surface of the sample. The device under test is perfectly mounted on the temperature controlled heat sink fixed in a simple two-axis gimbal mount. The circulator is used as a special fiber-optic component to separate the amplified signal from the input signal and pump light. The circulator usually has three ports. The first port is connected to the optical attenuator and the second one is connected to the coupler and the last one is connected to the optical spectrum analyzer, which measures the optical power as a function of wavelength or frequency. In this case, the light

intensity is exhibited as a function of wavelength over a fixed wavelength range (Chaqmaqchee, 2014).

Investigation of amplification performance was realized using an optical fiber system, as depicted in Fig. 4. A single-mode long-focus fiber with a diameter of $16 \pm 1 \mu\text{m}$ was coupled to port 2 of the circulator using an FC/APC adapter, and the other end was positioned close to the GaInNAs VCSEL structure. A 1300 nm tunable laser is used as signal source with power not $>1 \text{ mW}$ to inject the signals from the top mirrors using the long focus fiber. An ILX Lightwave laser diode controller was used as the current and temperature controller. The device is also pumped by an electrical bias under either CW or pulsed mode operation. The sample is mounted on the heat sink that is connected directly to the temperature controller for controlling the device temperature.

III. RESULTS AND DISCUSSION

Fig. 5 illustrates the temperature dependence of output L-I-V characteristics of the device with the VCSEL emitting at a wavelength of $1.3 \mu\text{m}$ for an aperture diameter of $10 \mu\text{m}$ and the second mesa etch diameter is $60 \mu\text{m}$. The device shows CW operation up to 30°C heat sink temperature. The emission occurred at bias current as low as 2 mA and no threshold current was observed and thus the device emitted spontaneously. Series resistance was high ranging from 50Ω to 150Ω and this might be due to the thin p-doped layer. As a result, no CW lasing was observed at room temperature.

Furthermore, the L-I-V characteristics of the VCSEL at temperature of 18°C have been measured under pulsed conditions using a pulse generator, as shown in Fig. 6. The pulse widths of $W_{\text{puls}} = 166$ and $250 \mu\text{s}$ are applied along the

device of $70 \mu\text{m}$ diameter, but no emissions were detected using the light wave multimeter.

Fig. 7 illustrates the spectra of VCSEL sample at various applied currents with the 980 nm pump laser and at a temperature of 15°C . Fundamental mode shifts with increasing current from 100 to 800 mA, and the maximum intensity amplitude at around 21 dB at peak wavelength of 1287.5 nm is recorded. Fig. 8 shows wavelength as a function of amplitude intensity and confirms the plot of Fig. 7, where the maximum intensity at peak wavelength of 1287.3 nm is observed.

Fig. 9 shows the peak intensities of the VCSEL, input signal, and the combined VCSEL plus input signal at a fixed bias current of 12 mA and various input signal powers from 1 to 4 mW. The tuned wavelength laser was varied from 1292 nm to 1312 nm. The peak intensities of the VCSEL have high amplitude at a wavelength of 1304 nm due to the cavity resonance. The peak intensities of the input signal were also recorded. Finally, the combined VCSEL plus input signal at various bias currents and input signal powers have been measured. Because the most change in device response occurs at the resonance wavelength, the gain evolution at the resonance wavelength as the input power is increased has been measured. However, no amplification was observed with injected power of 1, 2, 3, and 4 mW, first due to this, VCSEL was very promising and designed for electrically driven vertical cavity semiconductor optical amplifier and might be required a nano or few milliwatts of injected optical power to obtain high gain (Lisesivdin, et al., 2014). In addition, a significant problem can be encountered with electrically pumped GaInNAs VCSEL is the free carrier absorption in p-type DBRs that vary with wavelength (Harris, 2002).

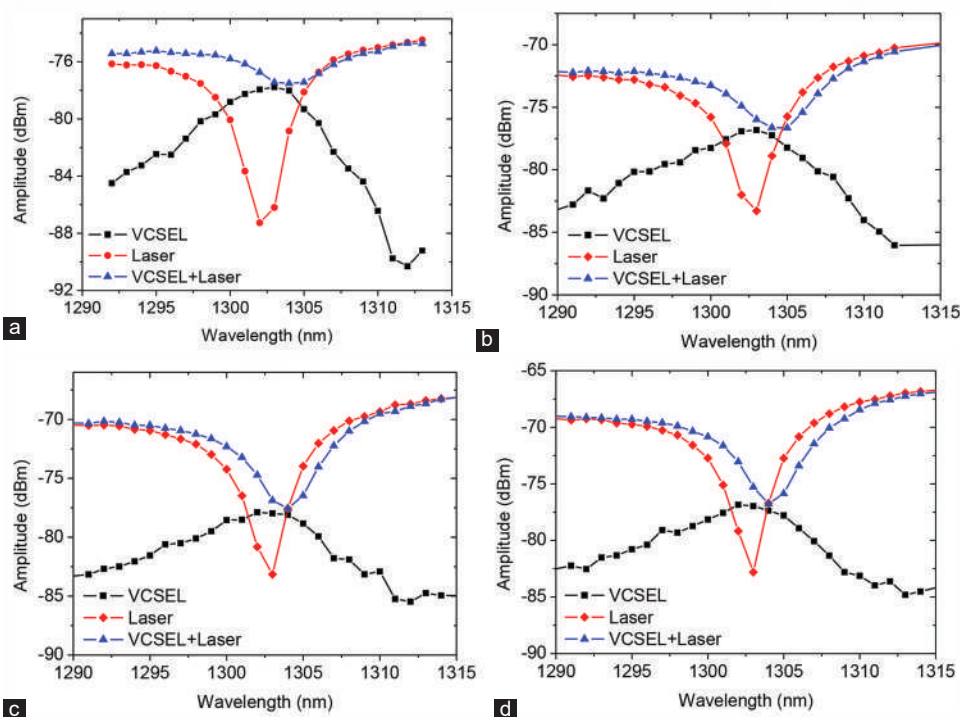


Fig. 9. Peak intensities of input signal, vertical-cavity surface-emitting laser (VCSEL), and the combined VCSEL and input signal were measured under fixed bias current of 12 mA and input powers: (a) 1 mW, (b) 2 mW, (c) 3 mW, and (d) 4 mW and at $T = 14^\circ\text{C}$.

IV. CONCLUSION

In this paper, we have tested GaInNAs/GaAs VCSEL devices in the 1.3 μm communication windows. Optical and electrical characterizations at various applied currents and temperatures were achieved, respectively. In addition, the combine of VCSEL and input signal at fixed bias current and different input powers was studied. The highest peak intensity at around 21 dB for VCSEL in reflection mode is obtained using 980 nm pump laser. Thus, in an optically pumped VCSEL, further progress should be performed using high power to enhance the recombination process in the quantum wells, while using low injecting optical power to obtain high gain in an electrically driven dilute nitride VCSELs. Future improvements in performance can be achieved by further adapting the well-established 1300 nm VCSEL technology.

ACKNOWLEDGMENT

This work was funded by the Ministry of Higher Education and Scientific Research in Baghdad-Iraq. FC highly appreciates the support of University of Essex in Colchester-UK through this research. FC also acknowledges Koya University, Faculty of Science and Health, Department of Physics for allowing this study.

REFERENCES

- Bjorlin, E.S., Riou, B., Abraham, P., Piprek, J., Chiu, Y.J., Black, K.A., Keating, A. and Bowers, J.E., 2001. Long wavelength vertical cavity semiconductor optical amplifiers. *IEEE Journal of Quantum Electronics*, 37(2), pp.274-281.
- Buyanova, I.A., Chen, W.M. and Monemar, B., 2001. Electronic properties of Ga(In)NAs alloys. *MRS Internet Journal Research Nitride Semiconductor*, 6(2), pp.1-19.
- Chaqmaqchee, F.A., 2014. Optically and electrically pumped of Ga_{0.65}In_{0.35}N_{0.02}As_{0.98}/GaAs vertical-cavity surface-emitting lasers (VCSELs). *The Arabian Journal for Science and Engineering*, 39(7), pp.5785-5790.
- Chaqmaqchee, F.A.I. and Balkan, N., 2012. Gain studies of 1.3- μm dilute nitride HELLIH-VCISO for optical communications. *Nanoscale Research Letters*, 7(526), pp.1-4.
- Chaqmaqchee, F.A.I. and Balkan, N., 2014. Ga_{0.35}In_{0.65}N_{0.02}As_{0.08}/GaAs bidirectional light-emitting and light-absorbing heterojunction operating at 1.3 μm . *Nanoscale Research Letters*, 9(37), pp.1-5.
- Chaqmaqchee, F.A.I., 2019. Performance characteristics of conventional vertical cavity surface emitting lasers VCSELs at 1300 nm. *ZANKO Journal of Pure and Applied Sciences*, 31(2), pp.14-18.
- Chaqmaqchee, F.A.I., Mazzucato, S., Oduncuoglu, M., Balkan, N., Sun, Y., Gunes, M., Hugues, M. and Hopkinson, M., 2011. GaInNAs-based HELLISH-vertical cavity semiconductor optical amplifier for 1.3 μm operation. *Journal Nanoscale Research Letters*, 6(104), pp.1-7.
- Chaqmaqchee, F.A.I., Mazzucato, S., Sun, Y., Balkan, N., Tiras, E., Hugues, M. and Hopkinson, M., 2012. Electrical characterisation of p-doped distributed Bragg reflectors in electrically pumped GaInNAs VCISOs for 1.3 μm operation. *Journal Materials Science and Engineering B*, 177(10), pp.739-743.
- Chaqmaqchee, F.A.I., Salh, S.A.A. and Sabri, M.F.M., 2020. Optical analysis of 1300 nm GaInNAsSb/GaAs vertical cavity semiconductor optical amplifier. *ZANKO Journal of Pure and Applied Sciences*, 32(2), pp.87-92.
- Haghighi, N., Rosales, R., Larisch, G., Marcin, G., Frasunkiewicz, L., Czeszanowski, T. and Lott, J.A., 2018. Simplicity VCSELs. *Proceedings of SPIE*, 10552, pp.1-9.
- Harman, G.G., 1997. *Wire Bonding in Microelectronics: Material, Processes, Reliability and Yield*. McGraw-Hill, New York. Available from: <https://www.bookdepository.com/Wire-Bonding-Microelectronics-Materials-Processes-Reliability-Yield-George-Harman/9780070326194>. [Last accessed on 2019 Dec 10].
- Harris, J.S.Jr., 2002. GaInNAs long-wavelength lasers: Progress and challenges. *Semiconductor Science and Technology*, 17(8), pp.880.
- Hetterich, M., Dawson, M.D., Egorov, A., Bernklau, D. and Riechert, H., 2000. Electronic states and band alignment in GaInNAs/GaAs quantum-well structures with low nitrogen content. *Applied Physics Letters*, 76(8), pp.1030.
- Karim, A., Bjorlin, S., Piprek, J. and Bowers, J.E., 2000. Long-wavelength vertical-cavity lasers and amplifiers. *IEEE Journal of Selected Topics in Quantum Electronics*, 6(6), pp.1244-1253.
- Kondow, M., Uomi, K., Niwa, A., Kitatani, T., Watahiki, S. and Yazawa, Y., 1996. GaInNAs: A novel material for long-wavelength-range laser diodes with excellent high-temperature performance. *Japanese Journal of Applied Physics*, 35(2B), pp.1273.
- Korpijärvi, V., Kantola, E.L., Leinonen, T., Isoaho R. and Guina, M., 2015. Monolithic GaInNAsSb/GaAs VECSEL operating at 1550 nm. *IEEE Journal of Selected Topics in Quantum Electronics*, 21(6), pp.480-484.
- Lisesivdin, S.B., Khan, N.A., Mazzucato, S., Balkan, N., Adams, M.J., Korpijärvi, V.M., Guina, M., Mezosi, G. and Sorel, M., 2014. Optical gain in 1.3- μm electrically driven dilute nitride VCISOs. *Nanoscale Research Letters*, 9(22), pp.1-5.
- Piprek, J., Bjorlin, E.S. and Bowers, J.E., 2001. Optical gain-bandwidth product of vertical cavity laser amplifiers. *Electronics Letters*, 37(5), pp.298-299.
- Pozo, J., Vogiatzis, N., Ansell, O., Hearda, P.J., Rorison, J.M., Tuomistoc, P., Kontinen, J., Saarinen, M., Peng, C., Viheriälä, J., Leinonen, T. and Pessa, M., 2008. Fabrication and characterization of GaInNAs/GaAs semiconductor optical amplifiers. *Proceedings of SPIE*, 6997, pp.1-9.
- Shen, C.C., Hsu, T.C., Yeh, Y.W., Kang, C.Y., Lu, Y.T., Lin, H.W., Tseng, H.Y., Chen, Y.T., Chen, C.Y., Lin, C.C., Wu, C.H., Lee, P.T., Sheng, Y., Chiu, C.H. and Kuo, H.C., 2019. Design, modeling, and fabrication of high-speed VCSEL with data rate up to 50 Gb/s. *Nanoscale Research Letters*, 14(276), pp.1-6.
- Wah, J.Y. and Balkan, N., 2004. Low field operation of hot electron light emitting devices: Quasi-flat-band model. *IEE Proceedings Optoelectronics*, 151(6), pp.482-285.
- Yeh, P., 1991. *Optical Waves and Layered Media*. John Wiley and Sons, New York. Available from: <https://www.wiley.com/en-us/optical+waves+in+layered+media-p-9780471731924>. [Last accessed on 2019 Dec 10].

Energy Optimization Using a Pump Scheduling Tool in Water Distribution Systems

Karwan A. Muhammed^{1,2}, Raziye Farmani³

¹Department of Water Resource, College of Engineering,
University of Sulaimani, Sulaymaniyah, Kurdistan Region – F.R. Iraq

²Department of Civil Engineering, College of Engineering, Komar
University of Science and Technology, Sulaymaniyah, Kurdistan Region – F.R. Iraq

³Centre for Water Systems, College of Engineering, Mathematics and Physical Sciences,
University of Exeter, Exeter, EX4 4QF, U.K

Abstract—Water distribution management system is a costly practice and with the growth of population, the needs for creating more cost-effective solutions are vital. This paper presents a tool for optimization of pump operation in water systems. The pump scheduling tool (PST) is a fully dynamic tool that can handle four different types of fixed speed pump schedule representations (on and off, time control, time-length control, and simple control [water levels in tanks]). The PST has been developed using Visual Basic programming language and has a linkage between the EPANET hydraulic solver with the GANetXL optimization algorithm. It has a user-friendly interface which allows the simulation of water systems based on (1) a hydraulic model (EPANET) input file, (2) an interactive interface which can be modified by the user, and (3) a pump operation schedule generated by the optimization algorithm. It also has the interface of dynamic results which automatically visualizes generated solutions. The capabilities of the PST have been demonstrated by application to two real case studies, Anytown water distribution system (WDS) and Richmond WDS as a real one in the United Kingdom. The results show that PST is able to generate high-quality practical solutions.

Index Terms—Optimization, Pump scheduling, Water distribution systems.

I. INTRODUCTION

Large amounts of energy are consumed in the water sector to satisfy increasing demands and regulatory requirements. The main consumption of energy is associated with pumping large amounts of water from sources to distribution systems (Mala-Jetmarova, Sultanova and Savic, 2018; León-Celi, et al., 2016; Ghaddar, Naoum-Sawaya and Kishimoto, 2015; and

Makaremi, Haghghi and Ghafouri, 2017). The environmental footprint associated with these large energy demands also remains a challenge. Therefore, an efficient pump operation to save energy and reduce environmental impact (e.g., carbon emissions) in water supply systems has become a common concern for water utilities. Optimum pump scheduling has been found to be an efficient method to optimize pump energy consumption (Kougias and Theodossiou, 2013 and Giacomello, Kapelan and Nicolini, 2013), which can lead to significant saving in energy without any infrastructure changes to the components of water supply system. Pump scheduling problems are large-scale, non-linear, and highly complex computational optimization problems (Ghaddar, Naoum-Sawaya and Kishimoto, 2015; Choi and Kim, 2019; Amirabdollahian and Mokhtari, 2015; Skworcow, et al., 2014; Tsai, et al., 2008; Behandish and Wu, 2014; and Abdallah and Kapelan, 2017), due to the large number of decision variables and constraints, and several conflicting objectives that need to be considered (Blinco, et al., 2016). The size of solution space exponentially grows with the number of decision variables (Nowak, et al., 2018) and proportionally changes with the number of pumps and the length of simulation period. The number of possible solutions for a problem with P pumps during a 24 h simulation period snapshot is equal to $2^{(P*24)}$. The most widely considered objective function in different approaches is to minimize total operational costs (Kougias and Theodossiou, 2013; Blinco, et al., 2016; Farmani, et al., 2007; Jung, et al., 2014; Menke, et al., 2016; Vieira, et al., 2019; Kurian, et al., 2018; and Odan, Ribeiro Reis and Kapelan, 2015), whereas in some approaches, the problem is formulated as a two-objective optimization problem (Wang, Chang and Chen, 2019; Fayzul, Pasha and Lansey, 2014; and Housh and Salomons, 2018), considering the total number of pump switches as a second objective.

Another important aspect of pump scheduling problems is the representation of a candidate schedule. A specific representation effectively defines how an optimization algorithm handles the problem (López-Ibáñez, Prasad and Paechter, 2011), and how a set of decision variables

ARO-The Scientific Journal of Koya University
Volume VIII, No.1(2020), Article ID: ARO.10635, 12 pages
DOI: 10.14500/ARO.10635

Received: 14 February 2020; Accepted: 30 June 2020

Regular research paper: Published: 30 June 2020

Corresponding author's email: karwan.muhammed@univsul.edu.iq

Copyright © 2020 Karwan A. Muhammed, Raziye Farmani. This is an open-access article distributed under the Creative Commons Attribution License.



is selected for a pump scheduling problem. Usually, the representation of pump control decision variables can be introduced in two different ways: (1) The implicit way which uses the hydraulic conditions of system components to define the operation of pumps such as simple control rules based on tank water trigger levels (Behandish and Wu, 2014 and van Zyl, Savić and Walters, 2004) or simple control rules with time base (Marchi, Simpson and Lambert, 2016), pump speeds (Hashemi, Tabesh and Ataekia, 2014 and Zhang and Zhuan, 2018), and pump flow (Bene and Hos, 2012) and (2) the explicit way in which the status of pumps is specified explicitly based on time. The three most common types of explicit pump scheduling are as follows: (1) Duration of pump operation (López-Ibáñez, Prasad and Paechter, 2008); (2) on/off pump status during pre-defined equal time intervals (Costa, de Athayde Prata and Ramos, 2015; Naoum-Sawaya, et al., 2015, Siew, Tanyimboh and Seyoum, 2016; and Mala-Jetmarova, Barton and Bagirov, 2015); and (3) start/end run times of the pumps (Bagirov, et al., 2013). Alternative representations of pump scheduling may enhance optimization algorithms and are likely to have an impact on the quality of solutions (López-Ibáñez, 2009). A number of decision support tools have recently been developed, each with a particular schedule type, for optimizing the pump operation of water distribution systems (WDSs) including the Pollution Emission Pump Station Optimization tool (Sadatiyan and Miller, 2019); water distribution cost-emission nexus (Stokes, Simpson and Maier, 2014); Darwin Scheduler (Alighalehbakhani, et al., 2015); and Markov decision processes (Fracasso, Barnes and Costa, 2013).

In all above-mentioned approaches, the tools and models have been developed for specific application purposes and posed as either a single or multiobjective (MO) optimization problem. This paper presents a new powerful model-driven decision support tool called the pump scheduling tool (PST). The PST is a dynamic tool that can handle both implicit and explicit fixed speed pump scheduling types, considering four different pump scheduling formulation options (on and off, time control, time-length control, and simple control [water levels in tanks]) to generate optimum pump operation schedules for water systems. The tool has a dynamic user friendly interface used for simulation of water systems based on: (1) A hydraulic model input file, (2) an interactive interface which can be modified by the user, and (3) a pump scheduling generated by an optimization algorithm. This allows testing different operation options and identifying schedules that are most cost effective. The PST has been developed as an Excel add-in with a user-friendly interface and is an extension of the linkage between the EPANET hydraulic solver and the GANetXL (Savić, Bicik and Morley, 2013) optimization algorithm. The user-friendly interface allows easy parameter setting for a desired pump scheduling type. The GANetXL optimization tool provides the optimization engine for the PST. The problem has been posed as the minimization of energy cost while satisfying a set of hydraulic constraints. The optimization problem can be set as a MO optimization or single objective optimization to obtain an optimum pump schedule. The structure,

feature, and methodology used for the PST development are presented below followed by the application of the tool to two case studies and finally the key findings and future research direction in the conclusions.

II. DEVELOPMENT OF PST

To develop an efficient decision support tool (DST) in a generic framework which is applicable and flexible for a range of WDS operation problems, a number of crucial prior considerations should be taken into account. The important prior considerations involved in the PST development are pump scheduling problem requirements, hydraulic simulation model, and optimization method.

A. Pump Scheduling Problem

Pump scheduling can be defined as the method of choosing which of the available pumps in a WDS are to be utilized and operated during specific times of the day. The main objective is to find the best pump schedule that minimizes total operation costs while satisfying the system performance requirements such as supplying water to the customers at desired pressure, allowing for emergency water level in tanks and full recovery of tank levels by the end of the simulation period.

Pump operation costs include the cost of energy consumed by pumps and pump maintenance costs resulting from the workload forced on pumps. The energy consumption charge is considered as the main objective in most optimization models of pump operation (Mala-Jetmarova, Sultanova and Savic, 2017). On the other hand, maintenance costs, including the costs of repairing and replacing damaged pumps, are measured using a surrogate objective (Mala-Jetmarova, Sultanova and Savic, 2017), such as the number of pump switches. A pump switch is defined as changing the status of a pump in a time step from off to on or vice versa. Frequent pump switching causes wear and tear on pumps, which subsequently increases maintenance costs (López-Ibáñez, Prasad and Paechter, 2008).

B. Simulation Model and Optimization Algorithm

It is important to select an appropriate hydraulic simulation model for a real water distribution application (Stokes, Simpson and Maier, 2015). Due to the availability of EPANET simulation models for most real WDS (De Corte and Sörensen, 2013), and the ease of integrating EPANET with optimization algorithms, EPANET 2.0 (Marchi, Simpson and Lambert, 2016 and Rossman, 1999) is considered as a hydraulic solver in the PST development. Advantages of using such a simulation approach are its ability to implicitly handling the equations of conservation of mass and energy and hydraulic constraints that define the flow phenomena as well as having a graphical user interface to visualize the results of simulations. An extended period simulation (EPS) model is conducted to hydraulically simulate the pumping operation of WDS and evaluate the effects of changing water usage overtime.

Due to the large number of possible solutions in a WDS operation problem as well as the non-linearity of the system, changes made at one component of the system may influence the performance at another. This requires an optimization method that can handle such problems. Heuristic optimization methods, especially genetic algorithms (GAs), are particularly suited for use (Matott, Tolson and Asadzadeh, 2012) and have proved to be effective in the management of WDS problems (Tsoukalas, et al., 2016) specifically those with highly nonlinear combinatorial search spaces, multiple local optima, and many constraints (e.g., pump scheduling problem) (van Zyl, Savić and Walters, 2004 and Walski, Chase and Savic, 2003). GANetXL has been used as the optimization tool in this work.

III. PROBLEM FORMULATION IN PST

The problem is posed as optimum pump scheduling which aims to minimize total energy cost of pumping in water systems. The PST can handle four different pump scheduling representations in a single framework to generate optimum pump operation schedules. The tool has a dynamic user-friendly interface which makes it easy to be used for different types of pump scheduling problems. In addition to automatic optimization task, the integrated model has specific submodels to perform only hydraulic simulation of current schedule of a given problem or manual modification of existing schedule. The formulations of decision variables, objective functions, and constraints in the tool are explained in the following subsections.

A. Decision Variables

The PST handles the pump configuration decision variables using the two most popular pump status representations: Explicit representation based on time control, time-length control, and on/off at each time step and implicit representation based on simple control (water levels in tanks). The formulations of these four schedule types used in the PST are detailed in the following sections.

Time control

For time control, the number of pumps operating in each time step is defined as a decision variable and formulated as follows:

$$TCS = \begin{bmatrix} t_j & t_{(j+1)} & t_{(j+2)} & \cdot & \cdot & \cdot & t_{(j+M-1)} \\ NAP & NAP & NAP & \cdot & \cdot & \cdot & NAP \end{bmatrix}, 0 \leq NAP \leq N$$

where, TCS is the time control schedule matrix, NAP is the possible number of combinations of active pumps in each time step, N, M, and t are the number of pumps, simulation period, and time step value, respectively.

Time-length control

A pump schedule can also be explicitly defined by specifying the time during which each pump is on or off. From an operation perspective, explicit pump scheduling based on time-length is considered as a more practical schedule than other schedule representation approaches (Bagirov, et al., 2013). In this schedule representation, the length of time (TL) in which pumps are on and the time

when a pump switches on (ST) are considered as decision variables. To simplify the formulation and reduce the solution search space, usually, the maximum number of pump actions is specified beforehand (López-Ibáñez, Prasad and Paechter, 2008). The maximum number of actions allowed per pump during a scheduling period is assumed to be two, since frequent pump switching also causes wear and tear on pumps which subsequently increases maintenance costs [(López-Ibáñez, Prasad and Paechter, 2008). Time-length control schedule matrix is used to define the decision variables.

$$TLCS = \begin{bmatrix} S_{P_i}^{(OPr1_i, OPr2_i)} \\ \vdots \\ S_{P_{(i+1)}}^{(OPr1_{(i+1)}, OPr2_{(i+1)})} \\ \vdots \\ \vdots \\ S_{P_{(i+N-1)}}^{(OPr1_{(i+N-1)}, OPr2_{(i+N-1)})} \end{bmatrix}$$

where, S_{P_i} is the schedule of i_{th} pump, and $OPr1_i$ and $OPr2_i$ are the first and second operation periods of i_{th} pump during a 24 h simulation period. Since the number of pumping actions is two, there are only two operation periods. OPr is an array for storing decision variables, including time when a pump switches on (ST) and the length of time it stays on (TL) (i.e., $OPr1=[ST1, TL1]$).

On and off

The configuration of the pump is defined by binary coded chromosomes. The binary notation is used to represent the on/off status of a particular pump in a specific time interval (1: pump is on and 0: pump is off). A decision variable matrix is introduced to store the pump status binary values during the simulation period.

$$DVM = \begin{bmatrix} & t_j & t_{(j+1)} & \cdot & \cdot & t_{(j+M-1)} \\ S_{P_i}^i & 0/1 & 0/1 & \cdot & \cdot & 0/1 \\ S_{P_{(i-1)}}^{P_{(i-1)}} & 0/1 & 0/1 & \cdot & \cdot & 0/1 \\ \cdot & \cdot & \cdot & \cdot & \cdot & \cdot \\ \cdot & \cdot & \cdot & \cdot & \cdot & \cdot \\ S_{P_{(i+N-1)}}^{P_{(i+N-1)}} & 0/1 & 0/1 & \cdot & \cdot & 0/1 \end{bmatrix}$$

where, $S_{P_i}^i$ is the schedule of i_{th} pump, i is the pump index ($i=1,2,3,\dots,N$), (N is the total number of pumps involved in the optimization), t_j is the j_{th} time step, and j is the time index ($j=1,2,3 \dots M$).

Simple control

In this case, the pump operation variables are defined in terms of tank level controls. Each pumping action is linked with a pair of pre-determined water levels (lower and upper trigger levels, as shown in Fig. 1) such that when water falls or reaches the predefined levels, the pumps are switched on

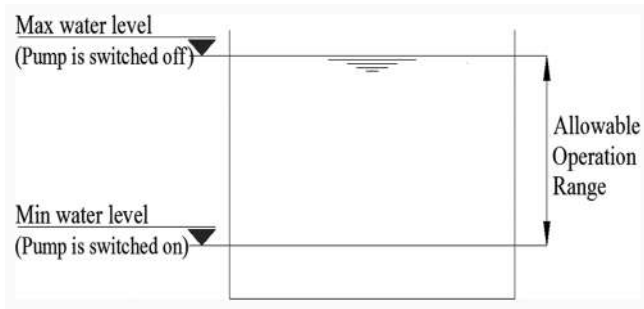


Fig. 1. Trigger levels for a tank.

or off, respectively. This can be done using a subset of simple control rules for trigger levels of the tank and the maximum and minimum water level values are determined by the water level of the full tank and emergency storage requirements. The water levels in the tanks at the start of operation are considered as decision variables that vary between maximum and minimum water levels in each tank.

B. Objective Function

The optimization model integrated in the PST is posed as a cost optimization model for the pump scheduling problem which aims to minimize the total cost of supplying water, while maintaining a set of system boundaries and constraints. The total energy cost and the number of pump switches (as a surrogate measure for maintenance costs) are considered as two main objectives in the optimization procedure. Such formulation represents a better way of assessing the trade-offs between the energy costs and the maintenance costs caused by an excessive number of pump switches (Walski, Chase and Savic, 2003). The mathematical formulation of the objective functions is given in Equations 1 and 2.

$$\text{Minimise}(TE) = \sum_{i=1}^N \sum_{t=1}^M S_{i,t} \times E_{i,t} \times P_{i,t} \quad (1)$$

$$\text{Minimise}(TNPS) = \sum_{i=1}^N \left(\sum_{t=1}^M P S_{i,t} \right) \quad (2)$$

where, TE is the total energy cost of the pumps during the operation period M (e.g., 24 h), E and P are the consumed energy (kWh) and the unit energy cost of the pump operation in time-step t, S is the status of the pump i, and N is the total number of pumps in the system. TNPS is the total number of pumps switches. PS is the pump switch indicator value for the configuration of each pump between 2 time steps, which is 1 if the pump is active in the current time step (t) and was not active in the previous time step (t-1), or vice versa.

The tool can be used to solve the problem either as a two objective optimization, considering proposed objective functions in Equations 1 and 2 or as a single objective optimization, in which case a decision can be made whether to consider the number of pump switches as a constraint added to the penalty function or not.

C. Constraints

To generate a feasible schedule, a number of system constraints have to be satisfied. In general, the constraints can be divided into hydraulic constraints (system constraints) and operational performance constraints. In the simulation model, the hydraulic simulator, EPANET, implicitly handles hydraulic constraints. For those cases which the hydraulic equations that model flow and energy balance in a network cannot solve (e.g., due to ill conditioned equation systems), a specific error or a warning message (e.g., pumps cannot deliver enough flow or head, and system has negative pressures) is generated by EPANET. The number of those messages is considered as a hydraulic constraint to eliminate those solutions which contain such errors and satisfy a successful hydraulic run.

The two important operational constraints are, water should be supplied to customers with adequate pressure head and the water levels in each tank at the end of simulation period must be higher than or equal to the water levels of that tank at the start of the simulation period (Equations 4 and 5).

$$P_{\text{Min},i} \leq P_{i,t} \leq P_{\text{Max},i} \quad (4)$$

$$FTWL_{j(t=M)} \geq ITWL_{j(t=0)} \quad (5)$$

where, $P_{\text{Min},i}$ and $P_{\text{Max},i}$ are the minimum and maximum acceptable pressures for junction i, $P_{i,t}$ is the pressure of junction i at time t, i is the junction index (i=1, 2,3,..., n), and t is the time index (t=1,2,3,..., M). $FTWL_{j(t=M)}$ and $ITWL_{j(t=0)}$ are the final and initial tank water levels of jth tank. The sum of the number of EPANET errors/warning messages and total nodal pressure and tanks water levels violations are considered as a penalty in the optimization model.

IV. PST

The PST is a model-based DST and is available for users (PST, 2019). It is a dynamic tool that can handle four different pump scheduling formulation types, including on and off, time control, time-length control, and simple control (tank water levels), to generate an optimum pump operation schedule for water systems. For a selected schedule type, the PST has the capability to integrate a MO evolutionary optimization package (GANetXL) with an external hydraulic solver (EPAENT) (Rossman, 1999) to obtain an optimum schedule. The PST has been built on a single framework as an Excel add-in, (Fig. 2A) that has a user-friendly interface which allows the user to easily formulate the optimization problem based on their desired schedule type. In addition, the PST interface enables the user to use the tool as standalone for simulation of a WDS model based on a hydraulic model's input file and in the interactive mode by changing pump status on the interface.

To achieve the optimum pump schedule with considerations outlined in Section 2, the PST framework is developed as an Excel add-in (Fig. 2A). The framework contains a

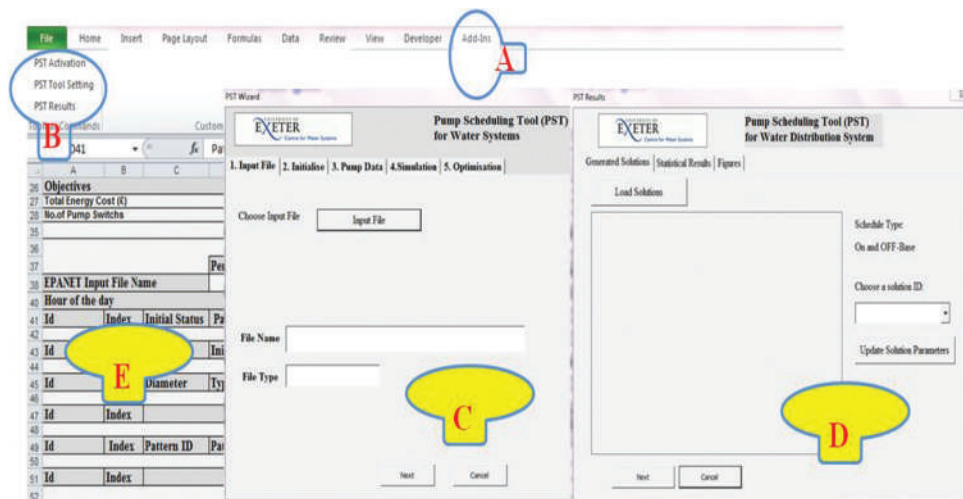


Fig. 2. The main components of the pump scheduling tool framework.

number of components, including a toolbar (Fig. 2B), a PST Configuration Wizard (Fig. 2C), PST result setting (Fig. 2D), and the interface spreadsheet of simulation model (Fig. 2E). The task of each component is described in the following sections.

A. Toolbar

The toolbar contains three control buttons including PST Activation, PST Tool Setting (Configuration Wizard), and PST results (Fig. 2B). The PST Configuration Wizard (Fig. 2C) is required to set all the parameters outlines above. After configuration of all the parameters and completion of an optimization run, the PST results (Fig. 2D) interface allows representation of the generated solutions and their corresponding parameters.

B. PST Configuration Wizard

The configuration wizard is an interactive interface which directs the user through the necessary steps and options to give user-defined simulation and optimization parameters required for any pump scheduling optimization problem executed within the PST. To configure a problem setting, the wizard has five main tabs: (1) Input file, (2) initialization, (3) Pump Data, (4) simulation, and (5) optimization.

Input file

By clicking on the “Input file” control button in the Input File tab (Fig. 2C), a search application window allows the user to easily browse for and choose an input file, and automatically imports it into the tool. An EPANET model in INP file format is required. Once the hydraulic model’s (EPANET’s) input file is plugged into the tool, the interface is automatically updated to simulate the model for further analysis. A warning message is issued by the PST when a non-EPANET input file type is chosen and hence the user is given an opportunity to choose another file.

Initialization

To perform the simulation and optimization model, the PST has two main worksheets (“Simulation Sheet” and

“Read Input File Sheet”) as Excel spreadsheet models. The “Simulation Sheet” is the main simulation interface sheet and dedicated to the hydraulic simulation model outputs. The “Read Input File” sheet is designed to store most of the features of a WDS modeled by EPANET, which can be plugged into the tool as an EPANET input file. By initializing the model using the “Press to Initialize” control button (Fig. 3A), the system component parameters (e.g., number of pumps, tanks, valves, nodes, etc.) are retrieved from the external input file and populated in the “Read Input File Sheet.” In addition, the tool has the ability to obtain other important parameters of the EPANET model and save them in the sheet, such as pattern (e.g., pump status and energy tariff pattern), time options (e.g., simulation duration time and simulation start time), and simple control rules.

A summary of statistical data plus an existing pump schedule type in the input file is presented in the initialization tab (Fig. 3A). For any new WDS model plugged to the tool, the worksheets are automatically updated: The previous data are removed, the hydraulic parameters of the new model components are retrieved and populated into the worksheets.

Pump data

In the Pump Data interface tab, three user-defined options (Fig. 3B) are available for system operators: Simulation (conducting only a hydraulic simulation run), modification and simulation (modifying the existing pump schedule using the interactive interface), and optimization (generating optimal schedule). The tool directs the user to perform the first two options in the interface sheet. A user-defined schedule type dropdown list in the Pump Data tab, shown in Fig. 3B-3, allows the user to choose a desired schedule from among four proposed alternative schedule types. A user-controlled “Add pump” button with corresponding dynamic dropdown list (Fig. 3B-3) allows the user to select desired pumps to be included in the optimization routine. The dropdown list is updated for any input file with related parameters such as pump ID, pump patterns, and control index. Once a pump ID is selected and the “Add pump” control button is clicked, the related parameters are added to

the decision variable list in the simulation sheet. The number of decision variables is then automatically determined by the tool based on the number of pumps considered in the optimization process. Based on the selected pump schedule type, an appropriate range of each decision variable is set by PST and linked with the optimization part of the PST.

Simulation

The user can run the hydraulic model simulation for any EPANET input file in the simulation tab (Fig. 3B-1) using the “Run Simulation” control button. In addition, the interface sheet (Fig. 3B-2) allows the user to conduct trial and error simulations for user-defined manual schedule scenarios in the interactive interface.

Optimization

The optimization tab of the PST configuration wizard (Fig. 4) is dedicated for configuring optimization parameters. The PST has direct links with GANetXL that provides the optimization engine for the pump scheduling problem. The GA tab (Fig. 4A) allows the user to set GA parameters (e.g., optimization type, algorithm type, population size, etc.), and the configuration data are dynamically saved into

the GANetXL configuration setting worksheet. The PST framework allows the user to pose a problem either as single or MO optimization. Cell range locations, ranges, and number of the decision variables can be automatically updated in the optimization parameters tab (Fig. 4B) for the selected schedule type and pumps in the optimization routine. The tool gives opportunity to select objective functions to be included in the optimization routine. The PST uses the setting defined in the optimization tabs (GA and optimization parameters). The constraints are also automatically evaluated during the optimization process. Since allowable nodal pressure ranges and considerations are case specific, the PST enables the user to decide inclusion of the pressure constraint (Fig. 4B). If this is considered, the user is required to set the minimum and maximum limits for nodal pressure. Based on the selected scheduling type, the tool sets the corresponding decision variables and evaluates the objective functions and constraints.

C. PST Results Interface

The PST results tab (shown in Fig. 5) is a visualization interface to display detailed information (e.g., decision

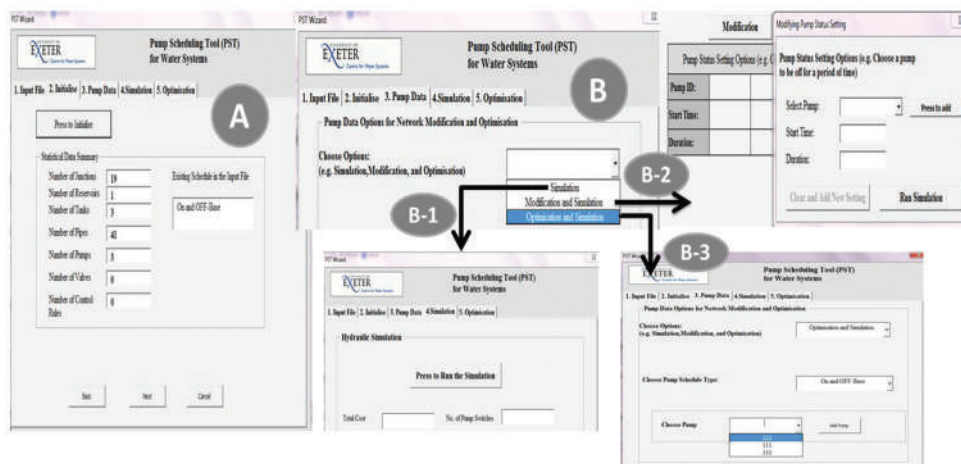


Fig. 3. The pump scheduling tool configuration wizard.

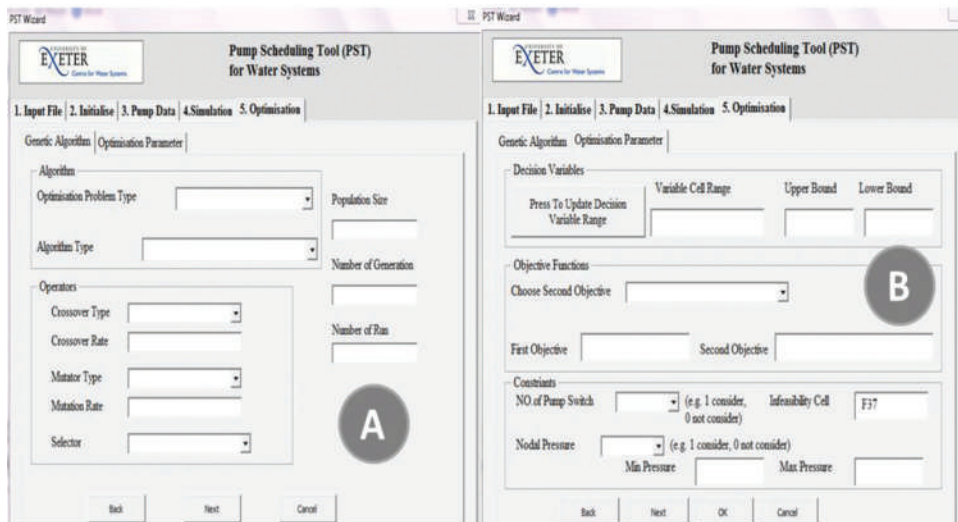


Fig. 4. The pump scheduling tool optimization tabs.

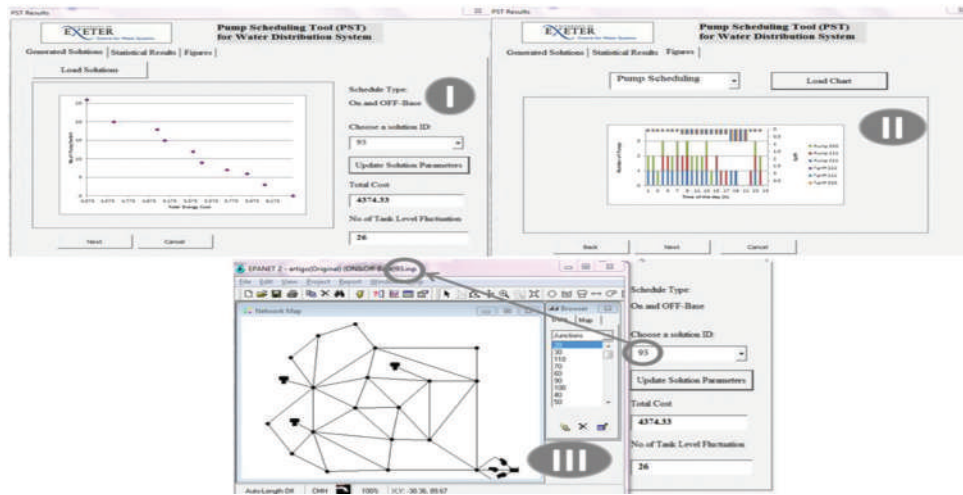


Fig. 5. The pump scheduling tool results interface.

variables, objective functions, and schedule) about the generated solutions. PST results can be invoked in the PST toolbar (Fig. 2B). The generated solutions in the result sheet can be easily displayed in a two-dimensional plot, just by clicking on the “load Solution” button.

The user can also interact with the generated solution parameters by choosing an individual solution ID (Fig. 5I) and clicking on the “Update Solution Parameters” button, which consequently loads the solution into the interface to demonstrate the change in decision variables, objective functions, and all the relevant information will be updated for that solution automatically. The solution will also be saved as an input file format in the current folder of the tool and automatically visualized in the EPANET interface (Fig. 5III).

The tool also facilitates the visual presentation of results (Fig. 5II) (e.g., water levels in the tanks over the operation period). When a solution is selected, the corresponding figures are automatically generated. The rich visualization and the analysis environment of the results representation by the PST helps the decision maker to analyze and assess the characteristics of solutions (e.g., through a Pareto-optimal front of solutions in the MO pump scheduling problem) and make informed decisions.

D. Simulation Interface Spreadsheet Model

The “Simulation Sheet” is a dynamic simulation interface sheet. This sheet is a second worksheet of the PST used to automatically make a link between the hydraulic model and the optimization model; and describe the fundamental parameters of the models. Presenting unknown intermediate parameters in the sheet would give the opportunity for users to explicitly monitor or investigate the model simulation results and optimization process. Each part of the sheet is dedicated to a specific analysis problem; designated cells for such analysis are dynamically sized for any EPANET input file. A general Dynamic Matrix (DM) is introduced in the sheet to manipulate those in-between variables for any given input file. The horizontal dimension (R) of the DM is equal to length of the EPS (e.g., 24 h), and the vertical dimension (C)

is equal to the number of elements (e.g., number of pumps). The extent of the sheet size tends to be system specific, varying from system to system, depending on the number of components available in the system. For example, assuming an input file has three pumps and two tanks, then the size of the DM for pumps is 3 by 24 and for the tanks is 2 by 24. Once the model is initialized, the process of directly loading statistical information of WDS elements from the input file sheet into the simulation sheet automatically updates the DMs as the format below.

$$DM = \begin{bmatrix} dm_{(1,1)} & dm_{(1,2)} & dm_{(1,3)} & \cdot & dm_{(1,R)} \\ dm_{(2,1)} & dm_{(2,2)} & dm_{(2,3)} & \cdot & dm_{(2,R)} \\ \cdot & \cdot & \cdot & \cdot & \cdot \\ \cdot & \cdot & \cdot & \cdot & \cdot \\ dm_{(C,1)} & dm_{(C,2)} & dm_{(C,3)} & \cdot & dm_{(C,R)} \end{bmatrix}_{(C \times R)}$$

V. APPLICATION OF PST TO CASE STUDIES

A. Problem Description

To demonstrate the capabilities of the PST, it has been applied to two most widely used WDS pump scheduling optimization problems. Anytown WDS is a well-known benchmark which was originally created by Walski, et al. (1987), and the modified version, so called Anytown (Modified) or AT(M) network, has been frequently used (Costa, de Athayde Prata and Ramos, 2015 and Rao and Alvarruiz, 2007) The second case is Richmond WDS which is a real one in the United Kingdom. The Richmond WDS was initially studied by van Zyl, Savić and Walters (2004) and later by Giacomello, Kapelan and Nicolini (2013). A full problem description can be found in van Zyl, Savić and Walters (2004). The EPANET input files for both networks are available from University of Exeter’s Benchmark Library (CWS, 2018). EPANET network layout representations of

both networks are shown in Fig. 6. Table I summarizes the general properties of both case study networks.

The main objective of both problems is to minimize the running costs of pumps while maintaining an acceptable level of service to customers. Both optimization problems are subject to some performance and physical limitations: (1) The water levels in the tanks should be between the minimum and maximum permitted levels throughout a simulation period of 24 h, (2) at the end of the simulation period, the water levels in the tanks should be higher than the water levels at the start of the operation, and (3) minimum pressure requirement should be satisfied at all demand nodes. To ensure the search space is explored adequately, the optimization algorithm is

run for 25,000 and 50,000 fitness function evaluations for Anytown and Richmond WDS, respectively.

VI. RESULTS AND DISCUSSION

The PST successfully managed to produce a Pareto front containing a set of feasible solutions for different pump schedule types for each network. Figs. 7 and 8 demonstrate the results produced by the PST, presenting four sets of Pareto fronts of non-dominated solutions generated based on four pump scheduling approaches for Anytown and Richmond WDS, respectively. The results correspond to only a single run of the optimization model, and all the solutions along the Pareto front curves are fully feasible, with no violation of any constraint during the simulation period. As can be observed in Fig. 8, utilization of various schedule strategies produces different sets of solutions. It can be also seen that the achieved solutions using time-length control and on and off schedules are better than the other solutions obtained using time control and simple control (tank water levels) approaches. This shows that various way of handlings and formulations of decision variables in a problem by an optimization algorithm can affect quality of the solution. The

TABLE I
PROPERTIES OF CASE STUDY NETWORKS

Network properties	Anytown	Richmond
Number of reservoirs	1	1
Number of storage tanks	3	6
Number of pumps	3	7
Number of energy tariff patterns	1	7
Time horizon (h)	24	24
Search space size	$2^{(3 \times 24)} \approx 4.73 \times 10^{21}$	$2^{(7 \times 24)} \approx 3.74 \times 10^{50}$

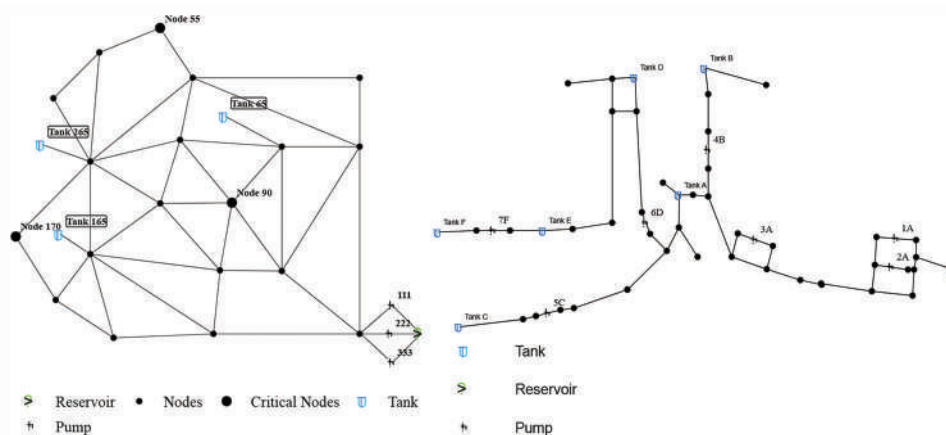


Fig. 6. Schematic representation of (1) Anytown and (2) Richmond networks.

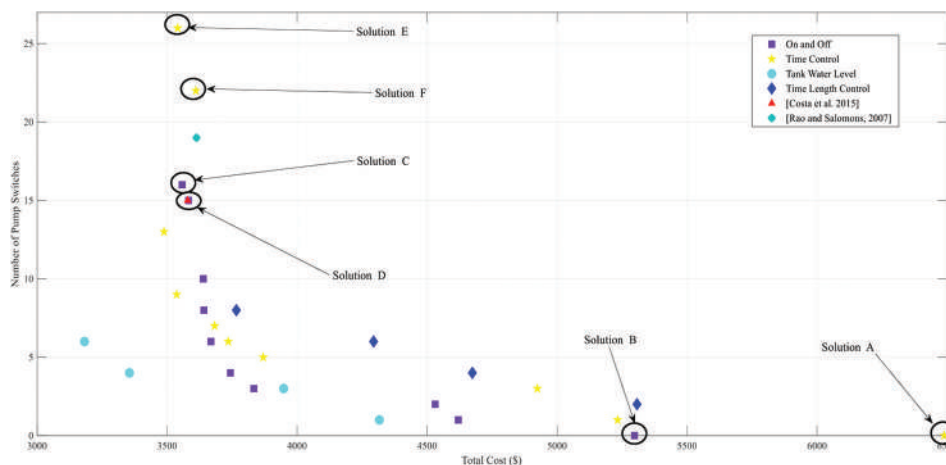


Fig. 7. Pareto fronts of the Anytown water distribution systems problem.

result for the Anytown problem shows that the on and off-based approach has advantages over the other approaches. As can be shown in Fig. 7, Solutions A and B have the same (zero) number of pump switches, whereas Solution B on the on and off curve is much cheaper than Solution A on the time control curve. These demonstrate the usefulness of the PST in solving pump scheduling problems by considering different types of control strategies and helping the decision-maker to make quantitative comparison between them.

To assess the robustness of the tool, the results are compared with those reported in the literature, as shown in Table II. The best presented solution for Anytown network by Rao and Salomons (2007) had a cost of \$3612.84 and 19 pump switches. This was later improved by Costa, de

Athayde Prata and Ramos (2015) with a reduced cost of \$3578.66 and fewer pump switches (i.e., 15). Solution C in Fig. 7 has a cost of \$3557.70 and 16 pump switches, which is 1.52% lower cost than the solution presented by Rao and Salomons (2007) and 0.59% less than the solution reported by Costa, de Athayde Prata and Ramos (2015). The number of pump switches for Solution D (Fig. 7) is 15 which is less than and equal to the number of pump switches presented by Rao and Salomons (2007) and Costa, de Athayde Prata and Ramos (2015), respectively. This solution has a cost of \$3582.16. Solution E on time control curve, Fig. 7, is also 1.07%, and 2% cheaper than the solutions reported by Rao and Salomons (2007) and Costa, de Athayde Prata and Ramos (2015), respectively.

Finally, Figs. 9 and 10 are automatically produced by the PST for Solutions C, D, E, and F in Fig. 7. These figures show the variation of water levels in the three tanks and the corresponding number of pumps operating during the course of the day in the Anytown network for each solution. Both figures show that water level in all tanks fluctuate between minimum and maximum acceptable levels throughout the

TABLE II
LIST OF SOLUTIONS

Solution	Total cost (\$)	No. of pump switch
C	3557.70	16
D	3582.16	15
Rao and Salomons	3612.84	19
Costa, et al.	3578.66	15

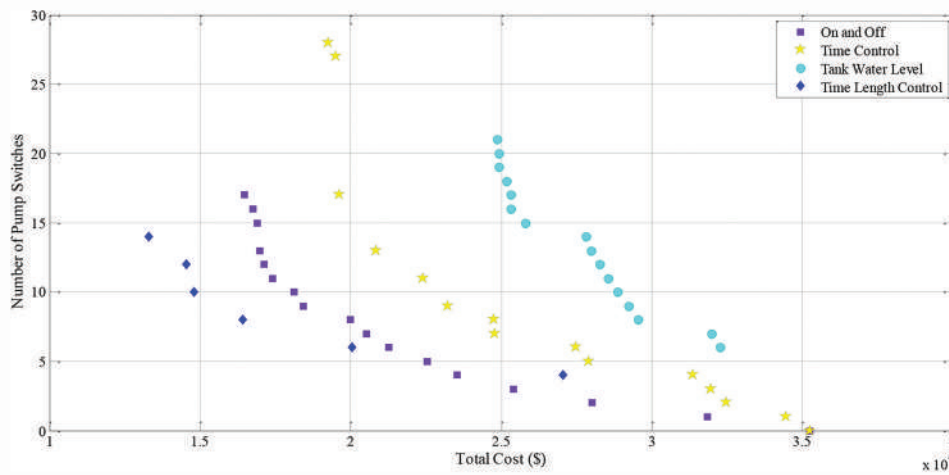


Fig. 8. Pareto fronts of the Richmond water distribution systems problem.

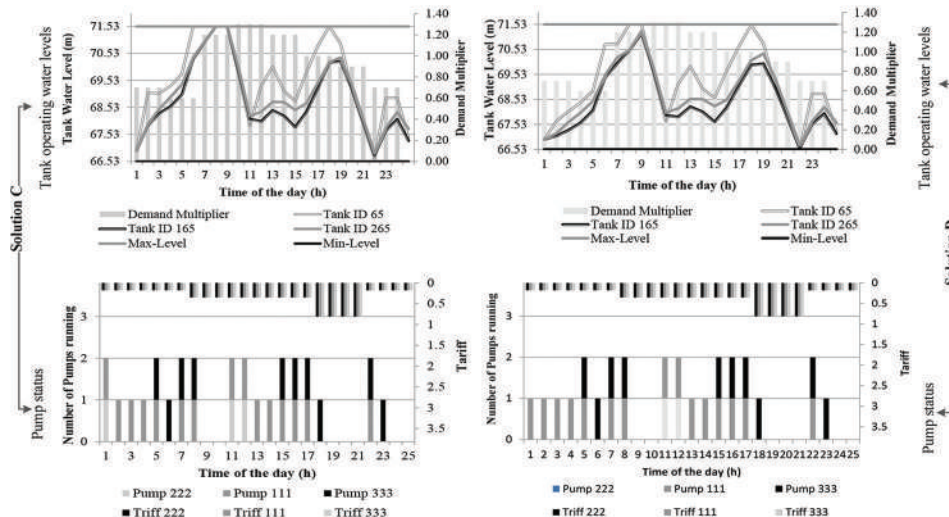


Fig. 9. Tank water levels and pump status for Solutions C and D for Anytown water distribution systems.

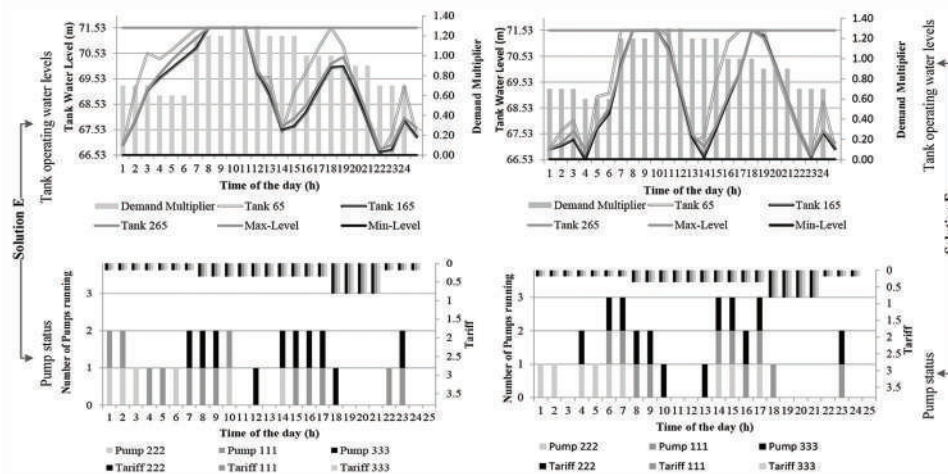


Fig. 10. Tank water levels and pump status for Solutions E and F for Anytown water distribution systems.

day, indicating short water residence times within the tanks which cause less water quality degradation. Turning off the pumps and supplying water from the tanks during peak water demand period (e.g., during early morning and late afternoon), as well as shifting heavy pumping load and filling up the tanks during cheaper energy periods (e.g., after mid-night) can also be observed in both Figs. 9 and 10. The results demonstrate the ability of the tool to effectively generate high-quality practical solutions for WDS pump scheduling problems using various schedule techniques in a single optimization run.

VII. CONCLUSION

The operating cost of pumps in a WDS represents a substantial part of the total expenditure incurred in the operation of WDS. A dynamic DSS tool, the PST developed in a very sophisticated Excel spreadsheet-based model, is presented in this paper that supports four alternative pump scheduling schemes (on and off, time control, time-length control, and simple control [Tank water levels]) for WDS. It has the capability to generate and present pump scheduling solutions for a given problem. The tool includes linkage between an optimization algorithm with the EPS model to evaluate the impact of various pumps scheduling on the system performance over the operation period and calculate the objective function values. The easy-to-use interface of the tool offers simulation of WDS model based on: (1) A hydraulic model input file, (2) an interactive interface which can be modified by the user, and (3) pump operation generated by the optimization algorithm. The “result interface” of the PST also allows decision-makers to easily access detailed parameters of the generated solutions.

The PST application to two different water distribution networks shows a powerful decision support tool which requires no changes to the tool/interface as the tool automatically updates all the information based on the EPANET input file. Furthermore, the dynamic nature of the tool allows four different types of pump scheduling approaches in a single framework with no changes to the tool

or interface. The generated results show that the tool is also able to deliver high-quality practical solutions for a given pump scheduling problem in comparison to the solutions reported in the literature. Future possible extension of this work could be considering variable speed pumps in the optimization of pump scheduling problems.

ACKNOWLEDGMENTS

This work forms part a collaborative research project between the UK and Chile, funded by the UK Government’s prosperity fund. The PST description and its availability can be found in this link (<http://emps.exeter.ac.uk/engineering/research/cws/resources/pst/>). The GANetXL can also found in here (<http://emps.exeter.ac.uk/engineering/research/cws/resources/ganetxl/>).

CONFLICTS OF INTEREST

The authors declare no conflicts of interest.

REFERENCES

Abdallah, M., and Kapelan, Z., 2017. Iterative extended lexicographic goal programming method for fast and optimal pump scheduling in water distribution networks. *Journal of Water Resources Planning and Management*, 143(11), p.04017066.

Alighalehbabakhani, F., Miller, C., Abkenar, S., Fracasso, P., Jin, S., and McElmurry, S., 2015. Comparative evaluation of three distinct energy optimization tools applied to real water network (Monroe). *Sustainable Computing: Informatics and Systems*, 8, pp.29-35.

Amirabdollahian, M., and Mokhtari, M., 2015. Optimal Design of pumped water distribution networks with storage under uncertain hydraulic constraints. *Water Resources Management*, 29(8), pp.2637-2653.

Bagirov, A.M., Barton, A.F., Mala-Jetmarova, H., Al Nuaimat, A., Ahmed, S.T., Sultanova, N., and Yearwood, J., 2013. An algorithm for minimization of pumping costs in water distribution systems using a novel approach to pump scheduling. *Mathematical and Computer Modelling*, 57(3-4), pp.873-886.

Behandish, M., and Wu, Z., 2014. Concurrent pump scheduling and storage level optimization using meta-models and evolutionary algorithms. *Procedia Engineering*, 70, pp.103-112.

- Bene, J.G., and Hos, C.J., 2012. Finding least-cost pump schedules for reservoir filling with a variable speed pump. *Journal of Water Resources Planning and Management*, 138(6), pp.682-686.
- Blinco, L., Simpson, A., Lambert, M., and Marchi, A., 2016. Comparison of pumping regimes for water distribution systems to minimize cost and greenhouse gases. *Journal of Water Resources Planning and Management*, 142, p.04016010.
- Choi, Y.H., and Kim, J.H., 2019. Self-adaptive models for water distribution system design using single-/multi-objective optimization approaches. *Water*, 11(6), p.1293.
- Costa, L., de Athayde Prata, B., Ramos, H., and de Castro, M., 2015. A branch-and-bound algorithm for optimal pump scheduling in water distribution networks. *Water Resources Management*, 30(3), pp.1037-1052.
- CWS, 2018. Richmond Network Benchmark at Centre for Water Systems. Available from: <http://www.emps.exeter.ac.uk/engineering/research/cws/resources/benchmarks/operation/richmond.php>. [Last accessed on 2018 Jul 07].
- De Corte, A., and Sörensen, K., 2013. Optimisation of gravity-fed water distribution network design: A critical review. *European Journal of Operational Research*, 228(1), pp.1-10.
- Farmani, R., Ingeduld, P., Savic, D., Walters, G., Svitak, Z., and Berka, J., 2007. Real-time modelling of a major water supply system. *Water Management*, 160(2), pp.103-108.
- Fayzul, M., Pasha, K., and Lansey, K., 2014. Strategies to develop warm solutions for real-time pump scheduling for water distribution systems. *Water Resources Management*, 28(12), pp.3975-3987.
- Fracasso, P., Barnes, F., and Costa, A., 2013. Energy cost optimization in water distribution systems using markov decision processes. In: *International Green Computing Conference Proceedings*.
- Ghaddar, B., Naoum-Sawaya, J., Kishimoto, A., Taheri, N., and Eck, B., 2015. A Lagrangian decomposition approach for the pump scheduling problem in water networks. *European Journal of Operational Research*, 241(2), pp.490-501.
- Giacomello, C., Kapelan, Z., and Nicolini, M., 2013. Fast hybrid optimization method for effective pump scheduling. *Journal of Water Resources Planning and Management*, 139(2), pp.175-183.
- Hashemi, S.S., Tabesh, M., and Ataekia, B., 2014. Ant-colony optimization of pumping schedule to minimize the energy cost using variable-speed pumps in water distribution networks. *Urban Water Journal*, 11(5), pp.335-347.
- Housh, M., and Salomons, E., 2018. Optimal dynamic pump triggers for cost saving and robust water distribution system operations. *Journal of Water Resources Planning and Management*, 145(2), p.04018095.
- Jung, D., Kang, D., Kang, M., and Kim, B., 2014. Real-time pump scheduling for water transmission systems: Case study. *KSCE Journal of Civil Engineering*, 19(7), pp.1987-1993.
- Kougias, I.P., and Theodossiou, N.P., 2013. Multi-objective pump scheduling using harmony search algorithm (HAS) and polyphonic HSA. *Water Resources Management*, 27(5), pp.1249-1261.
- Kurian, V., Chinnusamy, S., Natarajan, A., Narasimhan, S., and Narasimhan, S., 2018. Optimal operation of water distribution networks with intermediate storage facilities. *Computer Aided Chemical Engineering*, 119, pp.215-227.
- León-Celi, C., Iglesias-Rey, P., Martínez-Solano, F., and Mora-Melia, D., 2016. A methodology for the optimization of flow rate injection to looped water distribution networks through multiple pumping stations. *Water*, 8(12), p.575.
- López-Ibáñez, M., 2009. *Operational Optimisation of Water Distribution Networks, Ph.D. Thesis*. Edinburgh Napier University, United Kingdom.
- López-Ibáñez, M., Prasad, T., and Paechter, B., 2008. Ant colony optimization for optimal control of pumps in water distribution networks. *Journal of Water Resources Planning and Management*, 134(4), pp.337-346.
- López-Ibáñez, M., Prasad, T.D., and Paechter, B., 2011. Representations and evolutionary operators for the scheduling of pump operations in water distribution networks. *Evolutionary Computation*, 19(3), pp.429-467.
- Makaremi, Y., Haghghi, A., and Ghafouri, H., 2017. Optimization of pump scheduling program in water supply systems using a self-adaptive NSGA-II; a review of theory to real application. *Water Resources Management*, 31(4), pp.1283-1304.
- Mala-Jetmarova, H., Barton, A., and Bagirov, A., 2015. Erratum for exploration of the trade-offs between water quality and pumping costs in optimal operation of regional multiquality water distribution systems. *Journal of Water Resources Planning and Management*, 141(2), p.08014001.
- Mala-Jetmarova, H., Sultanova, N., and Savic, D., 2017. Lost in optimisation of water distribution systems? A literature review of system operation. *Environmental Modelling and Software*, 93, pp.209-254.
- Mala-Jetmarova, H., Sultanova, N., and Savic, D., 2018. Lost in optimisation of water distribution systems? A literature review of system design. *Water*, 10(3), p.307.
- Marchi, A., Simpson, A., and Lambert, M., 2016. Optimization of pump operation using rule-based controls in EPANET2: New ETTAR toolkit and correction of energy computation. *Journal of Water Resources Planning and Management*, 142(7), p.04016012.
- Matott, L., Tolson, B., and Asadzadeh, M., 2012. A benchmarking framework for simulation-based Optimization of environmental models. *Environmental Modelling and Software*, 35, pp.19-30.
- Menke, R., Abraham, E., Parpas, P., and Stoianov, I., 2016. Exploring optimal pump scheduling in water distribution networks with branch and bound methods. *Water Resources Management*, 30(14), pp.5333-5349.
- Naoum-Sawaya, J., Ghaddar, B., Arandia, E., and Eck, B., 2015. Simulation-optimization approaches for water pump scheduling and pipe replacement problems. *European Journal of Operational Research*, 246(1), pp.293-306.
- Nowak, D., Krieg, H., Bortz, M., Geil, C., Knapp, A., Roclawski, H., and Böhle, M., 2018. Decision support for the design and operation of variable speed pumps in water supply systems. *Water*, 10, p.734.
- Odan, F., Ribeiro Reis, L., and Kapelan, Z., 2015. Real-time multiobjective optimization of operation of water supply systems. *Journal of Water Resources Planning and Management*, 141(9), p.04015011.
- PST, 2019. PST, Centre for Water Systems, University of Exeter. Available from: <http://www.emps.exeter.ac.uk/engineering/research/cws/resources/pst>. [Last accessed on 2019 Mar 02].
- Rao, Z., and Alvarruiz, F., 2007. Use of an artificial neural network to capture the domain knowledge of a conventional hydraulic simulation model. *Journal of Hydroinformatics*, 9(1), pp.15-24.
- Rao, Z., and Salomons, E., 2007. Development of a real-time, near-optimal control system for water-distribution networks. *Journal of Hydroinformatics*, 9(1), pp.25-38.
- Rossman, L., 1999. The EPANET programmer's toolkit for analysis of water distribution systems. In: Wilson, E.M., editors. *29th Annual Water Resources Planning and Management Conference No. 1-10*. American Society of Civil Engineering (ASCE), Tempe, Arizona, United States.
- Sadatiyan, A.S., and Miller, C., 2017. PEPSO: Reducing electricity usage and associated pollution emissions of water pumps. *Water*, 9(9), p.640.
- Sadatiyan, A.S., and Miller, C., 2019. PEPSO: Reducing electricity usage and associated pollution emissions of water pumps. *Water*, 9(9), p.640.
- Savić, D.A., Bicik, J., and Morley, M.S., 2013. A DSS generator for multi-objective optimisation of spreadsheet based models. *Environmental Modelling and Software*, 26(5), pp.551-561.
- Siew, C., Tanyimboh, T., and Seyoum, A., 2016. Penalty-free multi-objective evolutionary approach to optimisation of anytown water distribution network. *Water Resources Management*, 30(11), pp.3671-3688.
- Skworcow, P., Paluszczyszyn, D., Ulanicki, B., Rudek, R., and Belrain, T., 2014. Optimisation of pump and valve schedules in complex large-scale water distribution systems using GAMS modelling language. *Procedia Engineering*, 70, pp.1566-1574.

- Stokes, C., Simpson, A., and Maier, H., 2015. A computational software tool for the minimization of costs and greenhouse gas emissions associated with water distribution systems. *Environmental Modelling and Software*, 69, pp.452-467.
- Tsai, F., Katiyar, V., Toy, D., and Goff, R., 2008. Conjunctive management of large-scale pressurized water distribution and groundwater systems in semi-arid area with parallel genetic algorithm. *Water Resources Management*, 23(8), pp.1497-1517.
- Tsoukalas, I., Kossieris, P., Efstratiadis, A., and Makropoulos, C., 2016. Surrogate-enhanced evolutionary annealing simplex algorithm for effective and efficient optimization of water resources problems on a budget. *Environmental Modelling and Software*, 77, pp.122-142.
- van Zyl, J.E., Savić, D.A., and Walters, G.A., 2004. Operational optimization of water distribution systems using a hybrid genetic algorithm. *Journal of Water Resources Planning and Management*, 130(2), pp.160-170.
- Vieira, B., Mayerle, S., Campos, L., and Coelho, L., 2019. Optimizing drinking water distribution system operations. *European Journal of Operational Research*, 280(3), pp.1-34.
- Walski, T., Chase, D., and Savic, D., 2003. *Advance Water Distribution Modeling and Management*. 1st ed. Haestad Press, New York, USA.
- Walski, T.M., Brill, E.D., Gessler, J., Goulter, I.C., Jeppson, R.M., Lansey, K., Lee, H.L., Liebman, J.C., Mays, L., Morgan, D.R., and Ormsbee, L., 1987. Battle of the network models: Epilogue. *Journal of Water Resources Planning and Management*, 113(2), pp.191-203.
- Wang, J.Y., Chang, T.P., and Chen, J.S., 2019. An enhanced genetic algorithm for bi-objective pump scheduling in water supply. *Expert Systems with Applications*, 36, pp.10249-10258.
- Zhang, L., and Zhuan, X., 2018. Optimisation on the VFDs' operation for pump units. *Water Resources Management*, 33(1), pp.355-368.

General Information

ARO's Mission: ARO seeks to publish those papers that are most influential in their fields or across fields and that will significantly advance scientific understanding. Selected papers should present novel and broadly important data, syntheses, or concepts. They should merit the recognition by the scientific community and general public provided by publication in ARO, beyond that provided by specialty journals.

We welcome submissions from all fields of natural science and technology, and from any source. We are committed to the prompt evaluation and publication of submitted papers. ARO is published biannually; selected papers are published online ahead of print.

Submission

Manuscripts should be submitted by the correspondent authors of the manuscript via the on-line submission page. Regardless of the source of the word-processing tool, only electronic Word (.doc, .docx, .rtf) files can be submitted on-line. There is no page limit. Only online submissions are accepted to facilitate rapid publication and minimize administrative costs. Submissions by any other one but the authors will not be accepted. The submitting author takes responsibility for the paper during submission and peer review. If for some technical reason submission through the email is not possible, the author can contact aro.journal@koyauniversity.org for support. Before submitting please check ARO's guide to authors thoroughly to avoid any delay in the review and publication process.

Authors are explicitly responsible for the language of their texts. Paper should be submitted in a well written in understandable English. Authors should not expect the editor or editorial board to rewrite their paper. Prior to submission, authors should have their paper proofread by a possible academic native speaker of English.

- Submit the Article with contact Information
- File name should be your article title
- Don't submit your article in multiple journal, we are taking only minimum time for review process. please don't waste our time
- Once the paper is accepted, it can't be withdrawn
- Please follow publication ethics and regulation
- Avoid plagiarism and copied material
- Strictly Follow ARO's Template

Terms of Submission

Papers must be submitted on the understanding that they have not been published elsewhere and are not currently under consideration by another journal or any other publisher. ARO accepts original articles with novel impacts only. Post conference papers are not accepted "as is", however, regular papers on the same topic but with a different title can be submitted. The new paper should contain significant improvements in terms of extended content, analysis, comparisons with popular methods, results, figures, comments, etc. Please do not forget that the publication of the same or similar material in ARO constitutes the grounds for filing of an (auto) plagiarism case.

The submitting author is responsible for ensuring that the article's publication has been approved by all the other co-authors. It is also the authors' responsibility to ensure that the articles emanating from a particular institution are submitted with the approval of the necessary institution. Only an acknowledgement from the editorial office officially establishes the date of receipt. Further correspondence and proofs will be sent to the author(s) before publication unless otherwise indicated. It is a condition of submission of a paper that the authors permit editing of the paper for readability. All enquiries concerning the publication of accepted papers should be addressed to aro.journal@koyauniversity.org.

Peer Review

All manuscripts are subject to peer review and are expected to meet standards of academic excellence. Submissions will be considered by an editor and “if not rejected right away” by peer-reviewers, whose identities will remain anonymous to the authors.

Guide to Author

We welcome submissions from all fields of science and from any source. We are committed to the prompt evaluation and publication of submitted papers. Selected papers are published online ahead of print. Authors are encouraged to read the instructions below before submitting their manuscripts. This section arranged into an overview speedy guidelines below and more detailed at the bottom section of this page

Manuscript Preparation

Submitting your manuscript will be in two stages namely before final acceptance and after.

Stage one:

At the first stage manuscript needs to be prepared electronically and submitted online via the online submission page in a Word (.doc, .docx, .rtf) format of one column double-spaced page, Times New Roman font type, and 12 p font size. A pdf version of the submitted manuscript should be submitted too. All authors' names, affiliations, e-mail addresses, and mobile phone numbers should be typed on a cover page, indicating the correspondent author.

Stage two:

- File type: MS-Word version 2003 or later.
- Format: The preferred format of the manuscript two-column template with figures and captions included in the text. This template can be downloaded via the following link. Please follow instructions given in the template; <http://aro.koyauniversity.org/about/submissions#onlineSubmissions>
- Text: All text is in Times New Roman font. The main text is 10-point, abstract is 9-point font and tables, references and captions are 8-point font.
- Figures: Figures should be easily viewed on a computer screen.

Units of Measurement

Units of measurement should be presented simply and concisely using System International (SI) units.

Title and Authorship Information

The following information should be included;

- Paper title.
- Full author names.
- Affiliation.
- Email addresses.

Abstract

The manuscript should contain an abstract. The abstract should be self-contained and citation-free and should not exceed 200 words.

Introduction

This section should be succinct, with no subheadings.

Materials and Methods

This part should contain sufficient detail so that all procedures can be repeated. It can be divided into subsections if several methods are described.

Results and Discussion

This section may each be divided by subheadings or may be combined.

Conclusions

This should clearly explain the main conclusions of the work highlighting its importance and relevance.

Acknowledgements

All acknowledgements (if any) should be included at the very end of the paper before the references and may include supporting grants, presentations, and so forth.

References

References must be included in the manuscript and authors are responsible for the accuracy of references. Manuscripts without them will be returned. ARO is following Harvard System of Referencing. (Learn how to import and use Harvard Styling in your Microsoft Office by following this link:

<http://bibword.codeplex.com/releases/view/15852>)

Preparation of Figures

Upon submission of an article, authors are supposed to include all figures and tables in the PDF file of the manuscript. Figures and tables should be embedded in the manuscript. Figures should be supplied in either vector art formats (Illustrator, EPS, WMF, FreeHand, CorelDraw, PowerPoint, Excel, etc.) or bitmap formats (Photoshop, TIFF, GIF, JPEG, etc.). Bitmap images should be of 300 dpi resolution at least unless the resolution is intentionally set to a lower level for scientific reasons. If a bitmap image has labels, the image and labels should be embedded in separate layers.

Preparation of Tables

Tables should be cited consecutively in the text. Every table must have a descriptive title and if numerical measurements are given, the units should be included in the column heading. Vertical rules should not be used.

Copyright

Open Access authors retain the copyrights of their papers, and all open access articles are distributed under the terms of the Creative Commons Attribution License, which permits unrestricted use, distribution and reproduction in any medium, provided that the original work is properly cited.

The use of general descriptive names, trade names, trademarks, and so forth in this publication, even if not specifically identified, does not imply that these names are not protected by the relevant laws and regulations.

While the advice and information in this journal are believed to be true and accurate on the date of its going to press, neither the authors, the editors, nor the publisher can accept any legal responsibility for any errors or omissions that may be made. The publisher makes no warranty, express or implied, with respect to the material contained herein.

ARO Reviewer/Associate Editor Application Form

ARO is a scientific journal of Koya University (p-ISSN: 2410-9355, e-ISSN: 2307-549X) which aims to offer a novel contribution to the study of Science. The purpose of ARO is twofold: first, it will aim to become an ongoing forum for debate and discussion across the sciences and Engineering. We hope to advance our problem solving capacity and deepen our knowledge regarding a comprehensive range of collective actions. Second, ARO accepts the challenges brought about by multidisciplinary scientific areas and aspires to expand the community of academics who are able to learn from and help to produce advances in a variety of different disciplines.

The Journal is seeking reviewers who can provide constructive analysis of papers thus enhancing overall reputation of the Journal. If any expert is interested in participating of the review process, we highly encourage you to sign up as a reviewer for our Journal and help us improve our presence in domain of your expertise. Appropriate selection of reviewers who have expertise and interest in the domain relevant to each manuscript are essential elements that ensure a timely, productive peer review process. We require proficiency in English.

How to apply

To apply for becoming a reviewer of ARO, please submit the application form by following the link:

<http://aro.koyauniversity.org/user/register>

To apply for becoming a member of the Editorial Board of ARO, please submit the application form by following the link: <http://aro.koyauniversity.org/pages/view/AEB>

Both Associate Editor and Reviewers should specify their areas of research and expertise. Applicants must have a doctorate (or an equivalent degree), and if Master degree they need to have significant publishing experience. Please note that;

- You will need to write your full official name.
- Please provide an email which reflects your official name, such as nameOne.NameTwo@... , or your institute's official email.
- All data need to be written in English.

Note: For more information, kindly visit the following websites:

1. aro.koyauniversity.org.
2. <http://libweb.anglia.ac.uk/referencing/harvard.htm>.
3. <http://bibword.codeplex.com/releases/view/15852>.

INDEXING



Koya University is a young University established in 2003 and it is located in the city of Koya (Koysinjaq), short distance to the East of regional capital city of Erbil (Arbil, Hewlêr) in Kurdistan Region of Iraq. It is on the foothills of beautiful High Mountain. Its campus has been carefully laid out to embrace the beautiful mountainous nature. The Koya University has a Faculty system which enhances the interactions between similar academic fields. Today, Koya University has four Faculties: Engineering, Science and Health, Humanities and Social Sciences and Education in addition to the School of Medicine, which all consist of twenty-five scientific departments in different fields, such as Petroleum Engineering, Geotechnical Engineering, Software Engineering, Physics, Chemistry, Clinical Psychology, Social Science, Medical Microbiology and Sport Education.

ARO-The Scientific Journal of Koya University is a biannual journal of original scientific research, global news, and commentary in the areas of Science and Technology. ARO is a Peer-reviewed Open Access journal with CC BY-NC-SA 4.0 license. It provides immediate, worldwide and barrier-free access to the full text of research articles without requiring a subscription to the journal, and has no article processing charge (APC). ARO Journal seeks to publish those papers that are most influential in their fields or across fields and that will significantly advance scientific understanding. ARO Journal is a member of ROAD and Crossref agencies and has got ESCI, DOAJ seal, SHERPA/RoMEO deposit policy, and LOCKSS archiving policy.



ARO

The Scientific Journal of Koya University

Koya University (KOU)
University Park
Danielle Mitterrand Boulevard
Koya KOY45, Kurdistan Region - Iraq